A Study of the Origin and Applications of Nonlinear Polarization Rotation in Semiconductor Optical Amplifiers

A THESIS FOR THE DEGREE OF DOCTOR OF PHILOSOPHY

Presented to

Dublin City University (DCU)

By

Brendan F. Kennedy
B.Eng

School of Electronic Engineering
Faculty of Engineering and Computing
Dublin City University

Research Supervisor
Dr. Pascal Landais

November 2005

Approval

Name: Brendan Kennedy

Degree: Doctor of Philosophy

Title of Thesis: A Study of the Origin and Applications of Nonlinear Polarization Rotation in Semiconductor Optical Amplifiers

Examining Committee:

Mr. Stephen Daniels (Dublin City University)
Chair

____

Dr. Guillaume Huyet (University College Cork)
External Examiner

____

Dr. Liam Barry (Dublin City University)
Internal Examiner

____

Date Approved: ______________________________

Declaration

I hereby certify that this material, which I now submit for assessment on the programme of study leading to the award of Doctor of Philosophy is entirely my own work and has not been taken from the work of others save and to the extent that such work has been cited and acknowledged within the text of my work.

I.D. No.: 97543403
Signed: Breandan Kennedy
Date: 23\01\06

Dedication

To Mam, Dad and Magda - this is for you.

Acknowledgement

Firstly, I would like to extend my gratitude to my supervisor Dr. Pascal Landais, whose expertise and advice made this work possible. Pascal's door was always open if I had any questions.

I would like to thank my parents for the all encouragement and support they have given me over the years, I am truly lucky to have them. I would also like to thank my two sisters Catherine and Grainne, my brother Kevin, my nephew Daragh and my niece, and god-daughter, Katie. Without the support of you all, I believe the task of completing this work would have been infinitely greater.

The one person who understands what it took for me to complete this work is my beloved girlfriend, Magda. I am eternally grateful to you for being my guiding light during this time, you make it all worthwhile.

Numerous people have assisted me in the completion of this work, I would like to thank everyone who has helped me during the course of this project. In particular I would like to thank the following people: Dr. Louise Bradley, Dr. Liam Barry, Dr. Prince Anandarajah, Dr. Fred Surre, Severine Phillippe, Aisling Clarke, Dr. Miguel-Martinez Rosas, Paul Maguire, Frank Smyth and Louise-Phillipe Zebst.

I have made many friends during my time in DCU, with whom I spent a lot of the lighter moments. I know these friendships will be lasting ones, thanks guys: Paul Maguire, Damien O'Rourke, Frank Smyth, Dr. Eoin Kennedy, Dr. Prince Anandarajah, Dr. Aleksandra Kaszubowska, not forgetting Julia Anandarajah-Kaszubowska, Aisling Clarke, Antonia Danctha, Ciara Mulligan, Marc Rensing, Eoin Connolly, Ling Hu, Celine Guignard, Robert Maher and Krzysztof Bondarczuk.

List of Acronyms

AR Anti-Reflection

ASE Amplified Spontaneous Emission

BER Bit Error Rate

BERT Bit Error Rate Tester

BPF Band-Pass Filter

CDP Carrier Density Pulsations

CH Carrier Heating

CW Continuous-Wave

DISC Delayed Interference Signal Converter

DOP Degree Of Polarization

EDFA Erbium Doped Fibre Amplifier

FCA Free-Carrier Absorption

FP Fabry-Perot

FP-SOA Fabry-Perot SOA

FROG Frequency Resolved Optical Gating

FSR Free-Spectral Range

FWHM Full-Width Half Maximum

FWM Four-Wave Mixing

HH Heavy-Hole

HWP Half-Wave Plate

ISI Inter Symbol Interference

LCD Liquid Crystal Display

LED Light Emitting Diode

LEF Linewidth Enhancement Factor

LH Light-Hole

LI Light-Current

LOA Linear Optical Amplifier

MEMS Micro-Electro-Mechanical-Systems

MQW Multi-Quantum-Well

MZI Mach-Zehnder Interferometer

NA Numerical Aperture

NALM Nonlinear Amplifying Loop Mirror

NF Noise Figure

NOLM Nonlinear Optical Loop Mirror

NPR Nonlinear Polarization Rotation

NRZ Non-Return To Zero

OSA Optical Spectrum Analyzer

OXC Optical Cross-Connect

PBRS Pseudo-Random Bit Stream

PBS Polarizing Beam Polarizer

PC Polarization Controller

PM Polarization Maintaining

QWP Quarter-Wave Plate

SHB Spectral-Hole Burning

SHG Second-Harmonic Generation

SMF Single-Mode Fibre

SO Split-Off

SOA Semiconductor Optical Amplifier

SPM Self-Phase Modulation

SPR Self-Induced Polarization Rotation

TBP Time-Bandwidth Product

TE Transverse Electric

TM Transverse Magnetic

TOAD Terahertz Optical Asymmetric Demultiplexer

TPA Two Photon Absorption

TW-SOA Travelling-Wave SOA

WDM Wavelength Division Multiplexing

XGM Cross-Gain Modulation

XPM Cross-Phase Modulation

XPolM Cross-Polarization Modulation

XOR Exclusive OR

CONTENTS

Approval i
Declaration ii
Dedication iii
Acknowledgement iv
List of Acronyms v

Abstract x

1. Introduction 1

2. The Semiconductor Optical Amplifier (SOA) 5
- 2.1 Introduction 5
- 2.2 P-n junction 6
- 2.3 Photonic emission 9
- 2.4 Amplification and absorption 10
- 2.5 Theory of laser oscillation 11
  - 2.5.1 Gain saturation 12
- 2.6 Optical resonator 12
- 2.7 Suppression of cavity resonance 13
  - 2.7.1 Anti-reflection (AR) coatings 13
  - 2.7.2 Angled facets 14
  - 2.7.3 Window facet structure 16
- 2.8 Types of SOA's 16
  - 2.8.1 Bulk SOA's 16
  - 2.8.2 Quantum-well SOA's 17
  - 2.8.3 Quantum-dot SOA's 17
- 2.9 Bulk device structure 18
  - 2.9.1 Carrier recombinations 18
- 2.10 Gain dynamics in the SOA 21
  - 2.10.1 Carrier density pulsations (CDP) 21

2.10.2 Carrier heating (CH) 23

2.10.3 Spectral-hole burning (SHB) 23

2.10.4 Two-photon absorption (TPA) 24

2.10.5 Kerr nonlinearity 24

2.11 SOAs under test 24

2.12 Experimental characterization 25

2.12.1 Amplified spontaneous emission (ASE) 25

2.12.2 LI curve 27

2.12.3 Signal gain of the device 28

2.12.4 Experimental gain saturation 29

2.12.5 Noise figure (NF) 29

2.13 Conclusions 31

3. *SOA model* 37

3.1 Introduction 37

3.2 Overview of the model 38

3.3 Mathematical description of the model 38

3.3.1 Description of optical field travelling through the SOA 38

3.3.2 Description of the model used for the gain 41

3.3.3 Description of the carrier density, stimulated emission and spontaneous emission 42

3.3.4 Output power from the SOA and input power injected into the device 44

3.3.5 Dynamic model 44

3.4 Theoretical characterization of the SOA 45

3.4.1 Amplified spontaneous emission (ASE) 45

3.4.2 LI curve 48

3.4.3 Signal gain of the device 49

3.4.4 Gain saturation 50

3.4.5 Pulse propagation in the SOA 52

3.4.6 Self-phase modulation (SPM) in SOAs 54

3.5 Conclusions 57

4. *Characterization of NPR effect in the SOA* 63

4.1 Introduction 63

4.2 Polarization 64

4.3 Control and measurement of polarization in optical systems 67

4.3.1 Linear polarizer 67

4.3.2 Phase retarder 68
4.3.3 Polarization controller 68
4.3.4 Polarimeter 69
4.4 Optical axis of the SOA 71
4.5 Polarization sensitivity in SOAs 71
4.5.1 Asymmetric waveguides 71
4.5.2 Polarization dependence of gain dynamics 74
4.5.3 Modification of the waveguide axis 77
4.5.4 Anti-reflection (AR) coatings 77
4.6 Experiment to determine polarization dependence of SOA 78
4.6.1 Polarization dependent gain in SOA without injection 78
4.6.2 Nonlinear birefringence in SOA without injection 82
4.6.3 Polarization dependent gain and nonlinear birefringence in SOA with injection 83
4.7 Pump-probe experiment to determine NPR 88
4.7.1 Experimental setup 89
4.7.2 Effect of pump intensity and polarization on the change in polarization of the probe 90
4.7.3 Effect of initial probe polarization on NPR effect 91
4.8 Conclusions 93

5. *All-optical signal processing using the SOA* 99
5.1 Need for All-Optical Communication Systems 99
5.1.1 Summary of all-optical switching techniques 100
5.2 SOA nonlinearities 102
5.2.1 Cross-gain modulation (XGM) 102
5.2.2 Cross-phase modulation (XPM) 104
5.2.3 Four-wave mixing (FWM) 105
5.2.4 Nonlinear polarization rotation (NPR) 106
5.3 Wavelength conversion using NPR 110
5.3.1 Experimental setup for XPolM 112
5.3.2 Comparison of XPolM and XGM results 115
5.3.3 Suppression of noise on converted data 122
5.3.4 Polarization dependence of XPolM 123
5.4 Effect of gain-clamping in the SOA 124
5.5 Conclusions 126

6. *Ultra-fast all-optical signal processing using NPR in a bulk SOA* 133
- 6.1 Introduction 133
- 6.2 Polarization dependence of 2 ps pulses propagating through the SOA 134
  - 6.2.1 Frequency resolved optical gating (FROG) technique 135
  - 6.2.2 Experimental setup 136
  - 6.2.3 Results 138
- 6.3 Measurement of polarization dependent gain dynamics in bulk SOA 145
  - 6.3.1 Experimental setup and considerations 146
  - 6.3.2 Parameter extraction 149
  - 6.3.3 Analysis of results 151
- 6.4 Conclusions 154

7. *Conclusions* 161

Appendix 167

A. *Variables used in the model* 168

B. *Publications* 170
- B.1 Refereed journals 170
- B.2 Reviewed conference papers 170

LIST OF FIGURES

2.1 Block diagram of an SOA. 6

2.2 Illustration of the formation of a depletion region and corresponding barrier potential, V_D. 7

2.3 a) Band diagram in a double-heterostructure under forward bias showing carrier confinement. b) Refractive index profile that causes optical confinement. c) Waveguiding due to optical confinement. 8

2.4 Simplified band diagram illustrating a) spontaneous emission and b) stimulated emission. 10

2.5 Angled facet SOA. 15

2.6 Illustration of the top view of a window facet. 16

2.7 Band structure of a typical bulk SOA. 19

2.8 Illustration of CCCH Auger recombination. 20

2.9 Evolution of carrier distribution in the active region of a bulk SOA. Following stimulated emission due to a monochromatic optical signal the distribution recovers to equilibrium on several different timescales due to the different gain processes. 22

2.10 The ASE found experimentally showing a) full spectrum and b) ripples on the spectrum for the Optospeed device. 26

2.11 The ASE found experimentally showing a) full spectrum and b) ripples on the spectrum for the Avanex device. 26

2.12 LI curve found experimentally. 27

2.13 Experimentally measured gain as a function of bias current for -20 dBm and 0 dBm signal injection at a wavelength of 1515 nm. 29

2.14 Reduction of the gain as a function of injected intensity measured experimentally. 30

2.15 Noise figure as a function of wavelength measured experimentally. 31

3.1 Diagram illustrating a) all sections in the modelled SOA and b) parameters calculated in each section of the model. 39

3.2 ASE spectrum found for the Avanex device, using both simulated and experimental results. 45
3.3 The ASE calculated, as a function of current, using the model. 46
3.4 Spontaneous emission distribution in active region for a range of active region lengths, with a constant current density. 47
3.5 Carrier distribution in active region for a range of active region lengths, with a constant current density. 47
3.6 Comparison of the LI curve found both experimentally and theoretically. . . 48
3.7 Gain as a function of bias current for -20 dBm signal injection- Theory and experiment. 49
3.8 Illustration of the carrier evolution in active region, as a function of injection. 50
3.9 Comparison of the gain saturation found both experimentally and theoretically. 51
3.10 Simulated gain saturation for a range of bias currents. 51
3.11 Pulse propagation in each section of the SOA. 53
3.12 Recovery of the gain in each section of the SOA. 54
3.13 Simulation result illustrating the relationship between a) carrier density depletion and b) refractive index variation. 55
3.14 a) Simulated and experimental results illustrating the chirp introduced by the SOA and b) the simulated spectrum before the SOA and the simulated and theoretical spectra after propagation through the device. 57

4.1 Diagram illustrating the polarization ellipse. 65
4.2 Diagram illustrating the operation of a linear polarizer. 67
4.3 Diagram illustrating the operation of a phase retarder. 68
4.4 Diagram illustrating the Poincare sphere. 70
4.5 Simulated results showing the polarization dependence of a) gain and b) recovery time in a bulk SOA. 73
4.6 Simulated results showing the polarization dependence of a) chirp and b) spectrum in a bulk SOA. 74
4.7 Band structure for a) unstrained and b) tensile strained semiconductor material. 75
4.8 Transparency due to conduction band and valence band effective masses in the a) unstrained and b) strained cases. 76
4.9 Experimental setup used to measure the polarization dependent ASE spectrum. 79

4.10 Polarization resolved ASE spectra for the device under test and, inset, a close up of the Fabry-Perot gain ripples. 80
4.11 Polarization resolved gain spectra for a) I = 300 mA, b) 350 mA, c) I = 400 mA, d) I = 450 mA. 81
4.12 Experimental setup for NPR characterization experiment with injection. . . 85
4.13 Output ellipticity as a function of injection angle for a linearly polarized input at -10 dBm, -7 dBm, -6 dBm and -3 dBm. Solid lines represent experimental data and shapes represent fitted data. 86
4.14 Gain ratio between TE and TM modes, and phase difference as a function of input power. 88
4.15 Pump-probe experimental setup. 90
4.16 a) Ellipticity and b) orientation from pump-probe setup with a constant probe polarization of 45°. The pump polarization was varied between TE, 45° and TM. 92

5.1 Illustration of XGM. 103
5.2 Illustration of Mach-Zehnder used in XPM. 105
5.3 Illustration of FWM technique. 106
5.4 Schematic illustration of a Kerr shutter. 108
5.5 Polarization resolved gain saturation as a function of injected power. 112
5.6 Experimental setup for co-propagation. 113
5.7 Improvement of Q-factor as a function of injected probe intensity for non-inverted XPolM in contra-propagation. 114
5.8 Experimental setup for contra-propagation experiments. 116
5.9 Illustration of the conversion process where a) represents the input data signal, b) represents the suppression of the gain, c) represents the inverted XPolM signal and d) represents the non-inverted XPolM signal. 117
5.10 Power penalty for various techniques in co-propagation setup. 117
5.11 Power penalty for various techniques in contra-propagation setup. 118
5.12 Wavelength dependence of XGM and XPolM in co- and contra-propagation. 120
5.13 Wavelength converted data using XPolM for a) non-inverted and b) inverted techniques. 121
5.14 Regeneration of the signal after propagation through the SOA showing a) the degraded injected data signal and b) the converted probe signal. 123
5.15 Polarization dependence of the pump and the probe. 124

5.16 Gain clamping effect showing the pump after propagation through the SOA a) with and b) without the probe. 125

6.1 Experimental setup of the FROG device 136
6.2 Experimental setup used to determine the polarization dependence of 2 ps pulses injected into the SOA 137
6.3 a) Temporal and b) spectral data measured by the FROG for the source pulse. 139
6.4 Polarization dependence of of a) intensity and b) chirp when no CW signal is injected into the device. 141
6.5 Polarization dependence of of a) intensity and b) chirp when 1mW CW signal is injected into the device. 143
6.6 Polarization dependence of of a) intensity and b) chirp when 4mW CW signal is injected into the device. 144
6.7 Experimental setup for the FWM technique. 147
6.8 OSA spectrum showing a) pump, b) probe and c) conjugate signals. 148
6.9 Experimental data used and curves extracted from fitting for different gain processes at an angle of 30^o. 151
6.10 The extracted data for CDP: LEF (+) and recovery time (•) as a function of the angle of injection. 152
6.11 The extracted data for CH: LEF (+) and recovery time (•) as a function of the angle of injection. 153

LIST OF TABLES

2.1 Manufacturers specifications for the Optospeed and Avanex SOAs. 25

3.1 Simulated results for rise and fall times of pulses injected into the SOA with a maximum power of 1 mW and 0.1 mW, respectively 53

4.1 Ellipticity and orientation of probe signal as a function of pump intensity for several angles of initial probe polarization. 93

6.1 Chirp amplitude introduced by the SOA when no CW signal is injected. . . 142
6.2 Chirp amplitude introduced by the SOA when 1mW CW signal is injected. 143
6.3 Chirp amplitude introduced by the SOA when 4mW CW signal is injected. 145
6.4 Variance recorded between experimental and fitted curves as a function of polarization. 151

ABSTRACT

In order to fully exploit the capacity of optical networks it is necessary to develop all-optical signal processing techniques. One device which can be used for this purpose is the Semiconductor Optical Amplifier (SOA). A lot of research has been devoted to this device. This work concentrates mainly on the nonlinearities in the device to perform all-optical processes such as switching and wavelength conversion. The main nonlinearities that have been considered are cross-phase modulation, cross-gain modulation and four-wave mixing. However, another type of nonlinearity has recently come to attention, which is due to the intensity dependent rotation in the state of polarization of a signal injected into the SOA. This phenomenon is called Nonlinear Polarization Rotation (NPR). The exact physical origin of this effect is yet to be determined.

The physical origins behind the NPR effect are examined using several novel experimental techniques. Polarization dependence of the gain and birefringence are found to be contributing factors. A model is also presented in order to develop an understanding of the physical dynamics occurring in the SOA. This is used to assess the potential of the SOA as a wavelength converter based on NPR. For the first time a detailed investigation of the optimum experimental setup for such an operation is presented. Wavelength conversion based on NPR is shown to have several advantages over XGM. Results are presented to examine the polarization dependence of pulse propagation through the SOA using an accurate and complete measurement technique. A large polarization dependence is present at high intensities. The potential speed of NPR in the SOA is assessed using an original method. This work is based on polarization resolved four-wave mixing. The polarization dependence of several gain dynamics in the SOA are found using this technique. The potential of ultra-fast all-optical signal processing based on NPR in the SOA is demonstrated.

1. INTRODUCTION

The enormous volume of data used by modern society is driving the need to develop all-optical signal processing techniques. The volume of data crossing the internet every day in 2002 was 180 Petabit. It is forecast that this will reach 5000 Petabit per day by 2007. The growing demand for bandwidth will be fuelled by this phenomenal increase in internet traffic. With the continued explosive growth of the internet, as well as numerous other communication media, the limit is being reached on the capacity of the present networks. This limit is set largely by the use of electronic elements in optical networks to perform tasks such as switching and wavelength conversion. The limit for commercial electronic elements currently available is 40Gb/s. Electrical signal processing has been demonstrated at 100 Gbit/s, but it is clear that the limit of this technology is being reached.

It would be possible to perform these tasks at much higher bit rates if all-optical signal processing was used instead. In the immediate future techniques such as modulation and multiplexing can be improved in order to alleviate the problem. There are also many unused dark fibres that can be employed. However, due to the fundamental limit imposed by the electronics in these systems, it is inevitable that all-optical signal processing will be required as a long-term solution.

Numerous techniques exist to perform all-optical signal processing. Exploiting the nonlinearities of the Semiconductor Optical Amplifier (SOA) is one method which continues to receive a lot of attention. These nonlinearities, whilst a disadvantage for amplification, are an advantage for all-optical signal processing. The advantages of the SOA are its cost efficiency, small integratable size, wide spectral bandwidth, low power consumption and flexibility for implementation in numerous types of all-optical signal processing. The traditional techniques used to perform all-optical signal processing in the SOA are Cross-Gain Modulation (XGM), Cross-Phase Modulation (XPM) and Four-Wave Mixing (FWM). All of these techniques, however, are limited by their sensitivity to polarization.

The aim of the work presented in this thesis is to study Nonlinear Polarization Rotation (NPR) in the SOA, for use in all-optical signal processing. This nonlinearity in the SOA device has received considerable attention in the past ten years. The advantage of this technique is that instead of trying to remove the polarization sensitivity in SOAs, NPR utilizes the polarization in order to perform numerous forms of all-optical signal processing. Indeed, it is impossible due completely remove the polarization dependency due to asymmetry in the confinement factors and losses along orthogonal modes of the device

Much of the work related to NPR in the SOA continues to focus on the applications of the technique. For this reason a thorough and complete understanding of the physical mechanisms causing the effect has yet to be established. Two of the key causes of the polarization dependence of SOAs are a polarization dependence of the material gain and birefringence in the device. Several novel experimental techniques to investigate these mechanisms are presented in this thesis. The first of these experiments investigated the polarization sensitivity in the case where no external optical signal was injected into the device. After this, an experiment was performed to measure the impact on the NPR of injecting an optical signal into the device. These two experiments are in good agreement.

The insight into the cause of the NPR was then used to develop a wavelength converter based on Cross-Polarization Modulation (XPolM) in the SOA. The experimental setup for this technique is similar to that of XGM. A comparison between XGM and XPolM for wavelength conversion was performed. Wavelength conversion over a range of 35 nm is presented. XPolM was found to match the performance of XGM, in a device that is quoted as having low polarization sensitivity. If the polarization sensitivity were not suppressed it may be possible to achieve superior wavelength conversion using XPolM. In the XPolM wavelength converters presented to date both co- and contra-propagation have been used, but no definitive explanation has been given for this choice. A detailed comparison of both setups is presented in this thesis.

The impact of NPR on the propagation of picosecond pulses in an SOA was also investigated. The polarization dependence of this propagation was found to be significant when high intensity pulses, large enough to saturate the SOA, were injected into the device. An experiment is presented which demonstrates that the polarization of a signal injected into an SOA is an important parameter when assessing potential network performance of the device.

Recently a lot of attention has focused on performing optical processing at data rates above the limit due to carrier recombinations. A polarization dependence of the gain dynamics in the SOA could potentially be used to achieve such optical processing. An experiment is presented in this thesis to measure the polarization dependence of several of these gain dynamics. This experiment is based on polarization resolved FWM.

This thesis consists of six chapters, which are laid out as follows:

Chapter 2: The SOA device is introduced. The basic principles outlining the operation of the device are given. The similarities and differences between the SOA and the semiconductor laser are detailed. A description of the different types of SOA is given. The characteristics of the SOAs under test in this thesis are then outlined, before results on the experimental characterization of the devices are presented.

Chapter 3: A model based on the travelling-wave description of the SOA is presented. The optical signal propagating in the SOA is described by the plane-wave solution of the electric field in the SOA. The model is developed in both the steady-state and dynamic regimes of operation. The propagation of picosecond pulses in both the temporal and spectral domains is investigated. The characterization of the SOA using the model is compared with the experimental characterization performed. Excellent agreement is found between the two.

Chapter 4: The polarization dependence of the SOA is investigated. There are several physical mechanisms responsible for this dependence. These mechanisms are detailed with reference to previous work performed on each. The experimental investigation into the cause of NPR is then presented, for both the case where no light is injected into the SOA and the case when an optical signal is coupled into the device. Excellent agreement was found between both sets of experimental results. A pump-probe experiment is then described. The effect of the pump signal on the probe polarization is analyzed using a polarimeter.

Chapter 5: The standard techniques to perform all-optical signal processing in SOAs are presented, before a review of the NPR technique is given. The potential impact of NPR is investigated. Wavelength conversion using NPR is performed experimentally, over a span of 35 nm. A comparison between XGM and NPR in the device under test is presented. Results are taken for both co- and contra-propagation setups.

Chapter 6: The polarization dependent propagation of picosecond pulses through the SOA is examined experimentally. Results presented suggest a polarization dependence of the gain dynamics in the device. This dependence is then examined in more detail. An experiment is presented based on polarization resolved FWM. The recovery times and Linewidth Enhancement Factor (LEF)s of the gain dynamics are found using this technique. The dependence of these parameters on the angle of polarization results in the possibility to perform all-optical signal processing at speeds far in access of the limit due to carrier recombinations.

Chapter 7: A brief summary of the work performed in this thesis is given. The conclusions drawn from this work are also presented.

2. THE SEMICONDUCTOR OPTICAL AMPLIFIER (SOA)

2.1 Introduction

A Semiconductor Optical Amplifier (SOA) is a device that amplifies an optical signal injected into it. The SOA devices considered in this report are bulk SOA's. An SOA is very similar to a semiconductor laser, and is fabricated using the same material systems and techniques. The main difference between the two is that the purpose of an SOA is to amplify light and for this reason the resonance of the light in the active region is suppressed by using Anti-Reflection (AR) coatings and by angling the active region with respect to the facets of the device. An SOA may be described as a laser operating below threshold. There are two types of SOA. These are the Fabry-Perot SOA (FP-SOA), which have large reflections from the end facets of the device, and the Travelling-Wave SOA (TW-SOA), which have negligible reflections from the facets [1]. These devices have many advantages over other amplifiers available. The SOA has a high gain that is generally 20-30 dB, a large gain bandwidth in the order of 100 nm, and high saturation output power of over 10 dBm. Other advantages of the SOA are its small size and the ease with which it can be integrated into optical systems.

As well as being employed as an amplifier much work has focused on exploiting the strong nonlinearities in the SOA for use in all-optical switching and wavelength conversion. This feature of the SOA is of particular interest as the nonlinearities can be used together with the amplification in the device to produce, for example, a wavelength converted amplified optical signal. It is the study of the nonlinearities in the SOA that are of particular relevance to the work presented in this thesis. The SOA has several disadvantages compared to the Erbium Doped Fibre Amplifier (EDFA) or the Raman amplifier including a higher coupling loss, a larger polarization dependence and a higher Noise Figure (NF). However these competing techniques for optical amplification have weak nonlinearities, which reduces their ability to perform all-optical signal processing. The polarization dependence of the SOA, generally considered a disadvantage is exploited in this thesis for use as the nonlinearity to perform all-optical signal processing. In this way one of the disadvantages of the device is used in a positive manner. A diagram of a typical bulk SOA can be seen in Fig. 2.1. Energy

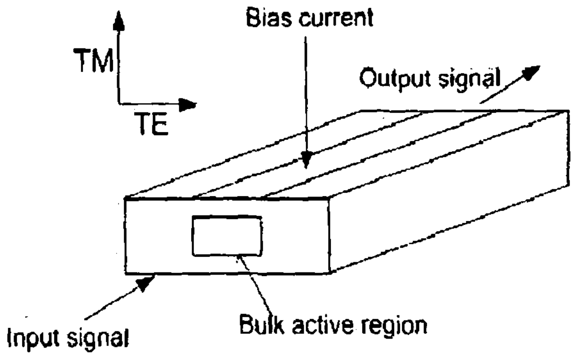

Fig. 2.1: Block diagram of an SOA.

is provided to the device by means of an electrical DC bias current. An optical signal is then injected into the device. This signal is resolved along the Transverse Electric (TE) and Transverse Magnetic (TM) modes of the waveguide, as illustrated in the figure. A large gain is imparted on the optical signal resulting in amplification. This single-pass operation of the SOA is in contrast to the oscillatory nature of the laser.

An introduction into the physics behind the SOA is presented in this chapter. This explanation begins with a definition of the SOA as a p-n junction designed in such a way as to maximize photonic emission. A description is then given of a semiconductor laser. An SOA is effectively a laser acting below threshold, where the cavity resonance has been suppressed. The techniques used to suppress the resonance are detailed. The physics of the SOA related to the carrier recombinations and the gain dynamics are also described. The specification of the SOAs under test, as well as the experimental characterization is then presented.

2.2 P-n junction

The operation of the SOA is outlined in this section. In order to understand the amplification process it is necessary to understand the mechanism by which the active region in the SOA is formed. In essence an SOA is a p-n junction modified in such a way as to cause the optimum amount of amplification to an electromagnetic wave of light which is injected into it. In a p-n junction, after an initial diffusion of holes to the n-region and electrons to the p-region, an electric field is set up which opposes the continued diffusion of minority carriers. The diffusion of carriers leads to the formation of a depletion region, as illustrated in Fig. 2.2. However, if an external voltage greater than the barrier potential, (V_D), is applied to the junction then the electric field is reduced and some carriers will have the energy required to overcome the electric field. This situation leads to a narrow region called the active region, where both free electrons and free holes are present. The free electrons reside in the conduction band and the free holes in the valence band. If an optical signal of suitable wavelength is injected into the active region, the interaction between electrons and holes can stimulate the emission or absorption of additional photons.

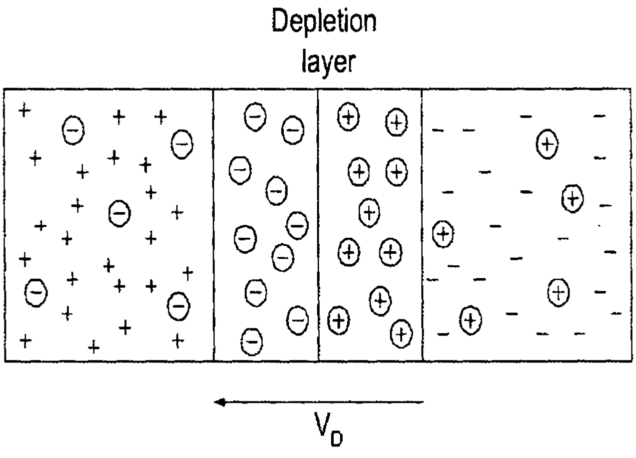

Fig. 2.2: Illustration of the formation of a depletion region and corresponding barrier potential, V_D.

The type of p-n junction that has been described is termed a homojunction. This is not the ideal situation because the active region where the gain is high is extremely small. A large amount of the injected carriers diffuse away from the junction, without the emission of a photon. The result is that a large injection current is needed to generate a significant quantity of light. To overcome this problem some mechanism of confining the carriers is required. Rather than diffusion it is desired that the carriers recombine in the active region, with the emission of a photon. The solution to this problem is to use a p-n double-heterojunction. The active region of this structure is made up of a semiconductor material with a lower band gap than the p-type and n-type cladding layers, which it lies between. Electrons and holes can now move freely to the active region under forward bias. However the potential barrier, which results from the band gap difference between the active region and the cladding layers, confines the carriers to the active region. This dramatically reduces diffusion of carriers from the active region. The second main advantage of the double heterojunction is that the cladding layers have a lower refractive index than the active region. This means that the optical beams injected into the material will be confined close to the active layer, which is desirable because this is the section of the material where the optical gain takes place. This index guiding helps to reduce the internal loss in the material. The carrier confinement and optical confinement are illustrated in Fig. 2.3. The band diagram of a typical p-n junction is illustrated in Fig. 2.3a) and it can be seen that a voltage of approx. 0.85 V is required to overcome the electric field in the depletion region and allow a linear increase in the current with respect to voltage. The reason for choosing a material where this specific voltage is required to overcome the electric field is because this voltage corresponds to a wavelength of $1.5\mu m$, which is the wavelength of interest for optical communications. The refractive index step resulting from the difference in bandgap between the active and cladding layers can be seen in Fig. 2.3b). The refraction caused by the larger refractive index in the active region leads to confinement of the light closer to the active region, which acts like a dielectric waveguide. This confinement is illustrated in Fig. 2.3c).

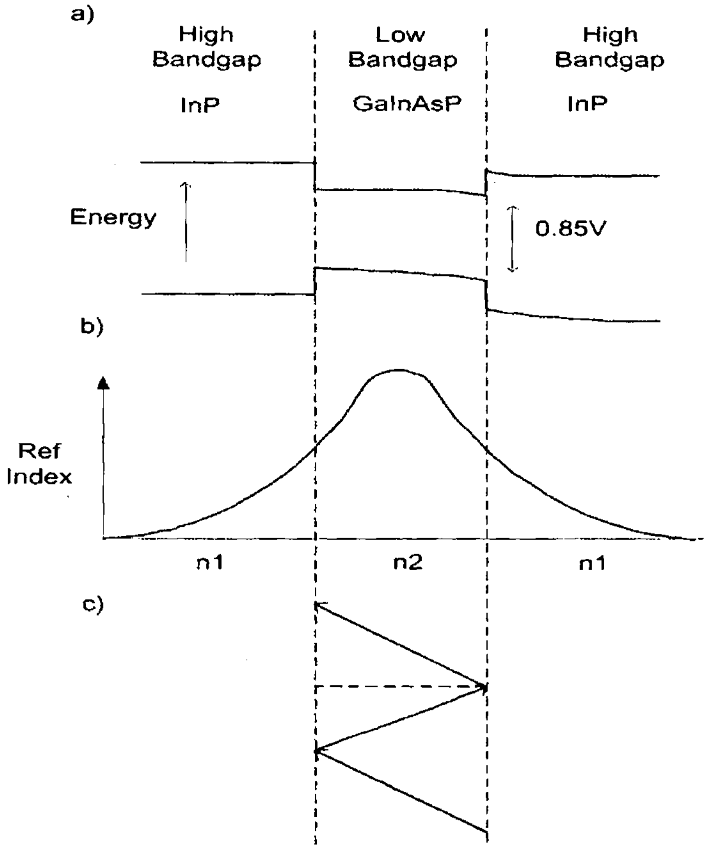

Fig. 2.3: a) Band diagram in a double-heterostructure under forward bias showing carrier confinement. b) Refractive index profile that causes optical confinement. c) Waveguiding due to optical confinement.

2.3 *Photonic emission*

In order for photonic emission to take place it is necessary to have radiative recombination. More specifically the types of radiative recombination that lead to photon emission are spontaneous emission and stimulated emission. Consider an electron that resides in the conduction band. Electrons are excited into this elevated energy state by means of electrical pumping in an SOA or a semiconductor laser. There is a finite probability that this electron will undergo a transition to the valence band where it recombines with a hole. This process is called spontaneous emission, as it occurs independently of an optical beam being injected into the active region. An illustration of spontaneous emission is presented in Fig. 2.4a). The energy of the emitted photon is equal to the difference between the electrons energy in the conduction band and the energy corresponding to its new position in the valence band. Spontaneously emitted photons have a random phase and direction. If a large number of electrons, N_2, that are in the conduction band due to electrical pumping are now considered, the following expression to define the average number of these electrons that will recombine radiatively with a hole in the valence band may be used [2]:

$$-(dN_2/(dt)) = A_{21}N_2 \tag{2.1}$$

where A_{21} is the spontaneous transmission rate and t represents time.

The second process by which photonic emission can occur is when an electron in the conduction band interacts with a photon of light from an injected electric field. If the energy of the light is the same as, or greater than, the difference in energy between electrons in the conduction band and holes in the valence band, then a second photon can be emitted. This photon has the same energy, phase and frequency as the incident photon. This process is stimulated emission and is illustrated in Fig. 2.4b). There is also a third process known as stimulated absorption. This is the reverse process where a electron in the valence band may undergo a transition to the conduction band with the absorption of a photons energy. The energy gained by the electron is equal to the energy of the photon. Expressions for these stimulated processes can also be defined:

$$W_{em} = B_{21}\rho(\mu) \tag{2.2}$$

$$W_{ab} = B_{12}\rho(\mu) \tag{2.3}$$

where $\rho(\mu)$ is the energy density per unit frequency and B_{21} and B_{12} define the rates of stimulated emission and stimulated absorption, respectively. The induced rates of stimu-

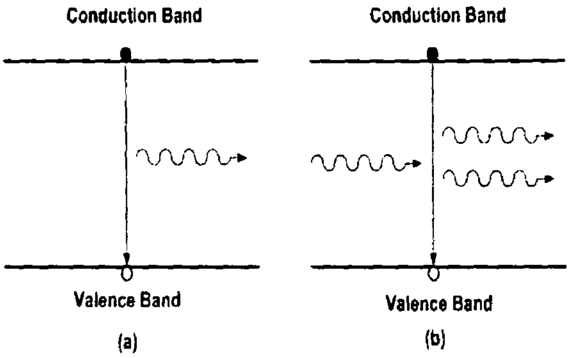

Fig. 2.4: Simplified band diagram illustrating a) spontaneous emission and b) stimulated emission.

lated emission and stimulated absorption, defined in Eqns. (2.2) and (2.3), are equal so whether net emission or absorption of photons occurs is determined by the carrier populations in each respective band. For amplification to exist it is necessary to have a larger carrier population in the conduction band. This is achieved in semiconductor lasers and amplifiers by pumping the active region with carriers by means of current injection. Population inversion occurs when there are more carriers in the conduction band than in the valence band; this is when photon emission exceeds photon absorption.

2.4 *Amplification and absorption*

Now that expressions have been defined for the rates of emission and absorption, it is possible to obtain an expression for the material gain in a semiconductor medium. If the propagation of a monochromatic plane wave is considered in the z-direction, through a gain medium with a cross-section area A and length steps of dz, it is possible to obtain an expression for the net power, dP_v, generated in the medium [3]:

$$dP_v = (W_{em} - W_{ab})hvAdz \tag{2.4}$$

where the power is expressed as the photon energy per unit volume. The net photonic emission is defined by the difference between the stimulated emission and absorption, $(W_{em} - W_{ab})$, hv is the energy of a photon, Adz defines the incremental volume. A related differential equation defines the change in power as a function of distance:

$$\frac{dP_v(z)}{dz} = (W_{em} - W_{ab})hvA = g_m(v)P_v \tag{2.5}$$

where g_m is the material gain coefficient, defined by:

$$g_m(v) = \frac{A_{21}c^2 l(v)(N_2 - N_1)}{8\pi {n_r}^2 v^2} \qquad (2.6)$$

this expression shows that the material gain in a semiconductor medium depends on the spontaneous emission, A_{21}, the refractive index, n_r, and the transition lineshape function, $l(v)$. In order to achieve a positive gain, the number of carriers in the conduction band, N_2, must exceed the number of carriers in the valence band, N_1. If N_1 is greater than N_2 then there is a negative gain and rather than amplification of the signal there will be absorption of the signal.

2.5 Theory of laser oscillation

As already stated, the SOA may be considered as a semiconductor laser operating below threshold, so in order to understand the operation of the SOA the semiconductor laser must be first examined. This section contains a brief explanation of the theory of operation of the semiconductor laser.

It has already been established that an atomic medium with population inversion is capable of amplifying an optical signal. But optical gain in itself is insufficient in the design of a semiconductor laser, optical feedback is also required to allow the light to oscillate in the active region of the device, otherwise the device would be a single-pass device and would amplify rather than lase. This optical feedback is provided by the cleaved facets in a semiconductor laser, which form an optical resonator. The signal is reflected at both ends of the resonator and is amplified as it propagates along the cavity. If this amplification exceeds the various losses and scattering effects then lasing occurs. When the rate of emission is equal to the rate of absorption optical transparency has been reached. Above transparency there is a net emission of photons, as this emission increases it eventually exceeds the losses in the system. Once the losses have been overcome the laser is said to be operating above threshold. This point is characterized by the threshold current. Above this current stimulated emission dominates and so the laser emits coherent light. This leads to a reduction in the amplification constant due to gain saturation. The oscillation level keeps increasing until such a time as the gain equals the losses. At this point the signal has reached its largest value and no further amplification is possible. The net gain per pass is unity and steady state oscillation has been obtained [2]. The gain is clamped in this situation as the carrier density is fixed due to the constant level of the optical signal in the cavity. The spectral range over which the laser emits light is determined by the material used. This parameter is the gain spectrum of the laser. Light is not continuously emitted over this range due to the presence of optical modes. These modes are caused by the interference between the signal oscillating in the cavity. This leads to the formation of standing waves.

2.5.1 Gain saturation

Gain saturation is a nonlinear effect in the semiconductor laser. As the optical power in the active region increases, more photons are available to stimulate further transitions from the conduction band to the valence band. However, the intensity cannot keep growing indefinitely for more and more cavity transit times. Every time one more photon is added to the field inside the cavity, the population inversion is decreased by 2. This is because when a photon is emitted it is due to an electron recombining with a hole, so the population of the conduction band has decreased by one, while the population of the valence band has increased by one. What may happen is that due to the amount of photons present, all the carriers in the conduction band recombine, which can lead to a situation in which there are no free carriers in the active region. When the electromagnetic field is so large that it causes carriers to give up their energy as fast as they are being pumped up the energy levels equilibrium has been reached. This situation causes gain saturation. The gain of the system must change to a lower value until the rate of production of the excess inverted population is balanced once again by the destruction rate by stimulated emission [2]. The gain will recover to its unsaturated value on a timescale defined by the carrier recovery time, a parameter that defines the time required for the carrier population in the conduction band to be replenished. The carrier recovery time will be analyzed in further detail in Sec. 2.10.

The result of the saturation effect is that the gain will decrease to a point where it is balanced by the losses in the cavity, this is the level at which the laser oscillates. The gain of the laser is thus clamped at the point where it balances the losses in the cavity. In reality, however, the gain will actually clamp at a value slightly lower than the loss, the slight difference being due to the effect of spontaneous emission. This is usually neglected. If the optical feedback is removed from the cavity then lasing will not take place and the device will always operate below threshold, and amplify the light injected into it. This is the case for the SOA.

2.6 Optical resonator

The most common type of resonator used in semiconductor devices is the Fabry-Perot (FP) etalon [4]. In a semiconductor laser the cleaved facets provide the reflections required for resonance. The oscillation of the light leads to the formation of standing waves in the cavity. Whether light appears at the output of the resonator depends on the interference between the multiple reflections of light present in the cavity. If the beams are in phase there is constructive interference, if they are out of phase the interference is destructive and no light appears at the output. The phase difference between reflections can be determined from the following expression [2]:

$$\delta = \left(\frac{2\pi}{\lambda}\right) 2nl\cos\theta \tag{2.7}$$

where λ is the wavelength of the light, l is the length of the cavity, θ is the angle at which the light travels through the cavity and n is the refractive index of the material. The interference in the cavity establishes longitudinal modes in the laser, which correspond to the transmission peaks for constructive interference. It is possible to determine the wavelength separation between the longitudinal modes, using the expression:

$$\Delta\lambda = \frac{\lambda_0^2}{2nl\cos\theta} \tag{2.8}$$

where λ_0 is the centre wavelength of the nearest transmission peak. This wavelength separation is known as the Free-Spectral Range (FSR) of the cavity.

2.7 *Suppression of cavity resonance*

A typical value for the semiconductor-air reflectivity at the facets of a semiconductor is 32%. It is this reflectivity of the signal at a particular wavelength which results the output of a laser to be coherent, so for the semiconductor laser it is desirable to have this high level of reflectivity at the facets of the device. However, for an SOA this is not the case. The requirement is to amplify the signal injected into the device. Rather than having a situation where there is a constant level of oscillation, it is required instead for an injected beam to have gain imparted on it, which is passed to the output of the device. The operation of an SOA can be thought of as being similar to a semiconductor laser operating below threshold. In order that the device stays below threshold, it is neccessary to suppress the reflections of the electric field. Generally, it is desirable to achieve effective reflectivities below 10^{-5}. This is achieved using three main techniques: Firstly AR coatings are used, secondly the active region can be set at an angle with respect to the facets, and thirdly a process involving a window region close to the end facets of the device is used.

2.7.1 *Anti-reflection (AR) coatings*

Applying an AR coating to the end facets of a semiconductor laser to reduce reflectivity was the first technique proposed to design an optical amplifier from a semiconductor laser and can be traced back as early as 1966 [5]. The level of reflectivity at the interface between two dielectrics is given by:

$$R = \left(\frac{n_2 - n_1}{n_2 + n_1}\right)^2 \tag{2.9}$$

where n_1 and n_2 are the dielectric refractive indices. If a plane wave of free-space wavelength λ_0 is incident on a material with a refractive index n_s then the optimal design conditions for an AR coating are [6]

$$n_f = \sqrt{n_s n_{air}} \tag{2.10}$$

$$d_f = \frac{\lambda_0}{4n_f} \tag{2.11}$$

where n_f and d_f are the refractive index and thickness of the AR coating. The thickness of the required AR coating is wavelength dependent and so a single AR coating is not suitable for operation over a large bandwidth. In order to obtain devices with wide bandwidth and low reflectivities, multilayer coatings must be used. Numerous dielectric materials can be used for AR coatings including SiO_2, SiN, $SiO_2 - Si_3N_4$ and $PbO - SiO_2$. They are applied to the facets of the SOA by means of evaporation or sputtering. The exact refractive index of the coating can be controlled in the evaporation or sputtering process. It is also possible to measure the reflectivity after the coating has been applied [7] - [8]. However care must be taken when applying the coating as it is possible to alter the device structure.

Another issue that needs to be considered for anti-reflection coatings is their polarization sensitivity, which leads to a polarization dependence of their performance. This issue is discussed in greater detail in Sec. 4.5.4.

2.7.2 *Angled facets*

A complementary technique used to reduce reflectivities involves slanting the active region away from the facet cleaved plane. This results in less reflected light being coupled into the active region. An important parameter for angled facet structures is the V-number:

$$V = \frac{\pi w}{\lambda_0}\sqrt{n_1^2 - n_2^2} \tag{2.12}$$

where w is the waveguide width and n_1 and n_2 are the effective refractive indices of the active and cladding regions respectively. V is a monomode criterion and $V < 2.4$ for single mode waveguide. A relationship between the TE mode full power width, ω_0, and the V-number is given by [9]:

$$\frac{\omega_0}{\omega} = \frac{1}{\sqrt{2}}\left(9.2063e-3+\frac{1.7265}{V}+\frac{0.38399}{V^3}-\frac{9.1691e-3}{V^5}\right) \qquad (2.13)$$

If a Gaussian distribution is assumed for the TE mode, the effective reflectivity of an angled facet is given by:

$$R_{ang}(\theta) = R_f(\theta)exp\left[-(\frac{2\pi n_2 \omega_{full}\theta}{\lambda_0})^2\right] \qquad (2.14)$$

θ is defined as the angle made between the beam propagation direction and the normal to the end facet. The Fresnel reflectivity, R_f, of the wave, at angled facet-air interface is given by:

$$R_f(\theta) = \frac{n_1 \cos\theta - (\sqrt{1-n_1{}^2}\sin^2\theta)}{n_1\cos\theta + \sqrt{(}1-n_1{}^2\sin^2\theta)} \qquad (2.15)$$

The effective reflectivity for the TM mode is very similar to the expression for the TE mode. An angled facet SOA can be seen in Fig.2.5. The mismatch between the reflected light and the tilted waveguide can be seen in this figure. It should be noted that there is a constraint on the angled facets technique for suppressing lasing in SOAs. This is due to the reduction in the coupling efficiency between an SOA and optical fibre as the facet angle increases, because of the far-field asymmetry. The optimum facet angle lies in the range 5^0-15^0. Alphonse *et. al.* [10] eliminated the reflected feedback by inclining the active region by 5% in order to make superluminescent diodes. The relative reflectivity will also decrease as the width of the waveguide increases. A drawback of this occurs if the waveguide is too wide because this will lead to higher order transverse modes appearing. A solution is to widen the waveguide near the end facets, a technique known as a flared waveguide. This maintains the single transverse mode condition [11].

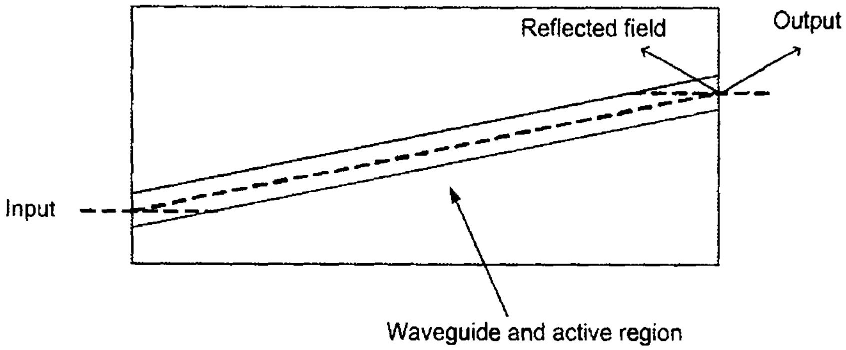

Fig. 2.5: Angled facet SOA.

2.7.3 Window facet structure

As already noted, AR coatings are generally polarization dependent. This polarization dependency can be reduced to less than 1 dB, along with further reduction in the effective facet reflectivity, by using a window close to the facet of the device [12], [13]. This area consists of a transparent region between the active region and the end facet. It is required that the transparent region has an energy bandgap greater than the signal photon energy. This removes the unwanted effect of stimulated absorption, although some intrinsic material absorption may be present. Diffraction will lead to the signal field travelling at some angle to the waveguide in the window region, this leads to only a partial reflection of the signal from the facet back into the waveguide. However, the coupling efficiency is inversely proportional to the length of the window region, which must be taken into consideration for long window regions. Fig. 2.6 illustrates the use of a window facet, where the length of the window region, L_w, is typically in the order of tens of μm. Average facet reflectivities of less than 0.06 % have been achieved using this technique, and when used in conjunction with AR coatings facet reflectivities below 10^{-5} are possible.

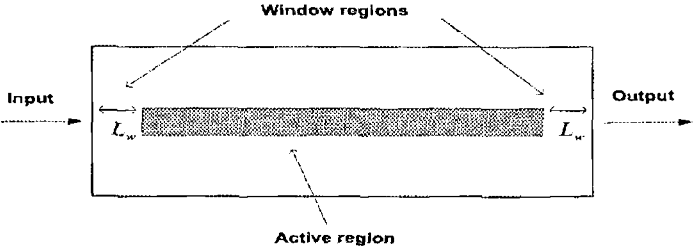

Fig. 2.6: Illustration of the top view of a window facet.

2.8 Types of SOA's

The type of material used in the active region of the SOA determines its operating characteristics. In this section bulk, quantum-well and quantum-dot materials are introduced. SOAs are mainly designed for operation in the low loss 1.3 μm and 1.55 μm regions. For this reason the materials used in SOA's are the III-IV semiconductors.

2.8.1 Bulk SOA's

Bulk materials are characterized by dimensions that are significantly greater than the de Broglie wavelength of carriers, λ_B. Devices with bulk material were the first devices used to develop semiconductor lasers and optical amplifiers and for this reason are well established and commercially available. The structure for bulk devices and the carrier recombinations associated with this material are discussed in Sec. 2.9.

2.8.2 Quantum-well SOA's

After the establishment of bulk material as the material of choice for semiconductor lasers and amplifiers, the quantum-well laser came to the fore [14]. The quantum-well SOA received a lot of attention in the early 1990's [15] - [17].
The thickness of the active layer defines whether a device is a bulk or a quantum-well device. In a quantum-well structure the thickness is approximately 10 nm while in a bulk material it is in the order of hundreds of nm. When the active layer thickness becomes comparable to the de Broglie wavelength of an electron the carriers are subjected to quantum confinement. An electron in the conduction band of a quantum-well device is free to move in both x and y directions, but is confined in the z direction, normal to the junction planes. In this situation the energy of a carrier is restricted to discrete values determined by quantum interference.

The main advantage in reducing the thickness of the active region is that the threshold current of the device is significantly reduced. However it should be stated that the confinement factor for the light is much smaller for the quantum-well case. The efficiency of a quantum-well laser is greater than that of a bulk laser because the stimulated emission occurs only at discrete energy levels. Rather than the band-gap energy being responsible for laser action it is the difference between quantum-well energy levels that is used. The wavelength of the light emitted can be tuned by altering the thickness of the laser. A common type of quantum-well SOA is the Multi-Quantum-Well (MQW) SOA. This device is fabricated by stacking a number of well and barrier layers. Quantum-well devices generally have a wider bandwidth and a smaller saturation output power. This smaller saturation power is advantageous in terms of exploiting the nonlinearities in the device. A lot of the experiments carried out to perform all-optical signal processing using SOAs now use the MQW device [18], [19]. There is a large asymmetry in the band structure of MWQ SOAs, leading to a large polarization dependence of the gain.

2.8.3 Quantum-dot SOA's

In the case of quantum-well devices, quantum confinement occurs in one spatial direction. For quantum-dot devices this confinement is in three spatial directions. This leads to the confinement of carriers to a region on the order of the electrons de Broglie wavelength. This results in discrete energy levels. Quantum-dots have received extensive study since 1994 [20] - [25]. Quantum-dots are fabricated using highly-mismatched epitaxy [22], where a material is grown on a substrate to which it is not lattice matched. Quantum-dot SOAs have numerous advantages over bulk and quantum-well devices. They require low current densities, have a small LEF [26], a high saturation power, broader bandwidth, lower noise figure and good temperature stability [22], [24]. The fast response time of quantum-dot SOAs make them suitable for very high speed optical signal processing applications. However quantum-dots have a lower modal gain than other devices. As the quantum-dot SOA is a relatively new device, it is behind the bulk and quantum-well devices in terms of commercial availability. The cost of fabrication is also greater than for bulk or quantum-well devices.

2.9 *Bulk device structure*

The SOAs under test in the work presented in this thesis are bulk devices. These devices were made from InP/GaInAsP which consists of a GaInAsP active region with bounding layers of InP. Other materials used in the design of SOAs are InGaAs, AlGaAs and InAlGaAs. The material that is used for SOAs has a direct bandgap. In this type of material the conduction band minimum and the valence band maximum have the same momentum vector. The probability of radiative transitions from the conduction band to the valence band is much greater for these materials, resulting in a higher device efficiency. A typical energy band structure in momentum, i.e E-k space, for an SOA is shown in Fig. 2.7 [27]. The conduction band and the valence band are separated by the energy gap, E_g. An incident photon must have an energy greater than this energy in order to induce the stimulated emission of a photon by the transition of a carrier from the conduction band to the valence band. The valence band may be further divided into three separate degenerate bands. These are the Heavy-Hole (HH) band, the Light-Hole (LH) band and the Split-Off (SO) band. The HH and LH bands are degenerate at the zone centre, Γ.

2.9.1 *Carrier recombinations*

There are two types of electron-hole recombination mechanisms that can occur in bulk SOAs, radiative and non-radiative recombinations. Radiative recombinations are characterized by the absorption or emission of a photon of light. There are three processes associated with this type of recombination: Spontaneous emission, stimulated emission and stimulated absorption, which were described in Sec. 2.3. The spontaneous radiative recombination rate is given by:

$$R_{rad} = B_{rad}N^2 \tag{2.16}$$

where B_{rad} is the bimolecular radiative recombination coefficient and N is the carrier density.

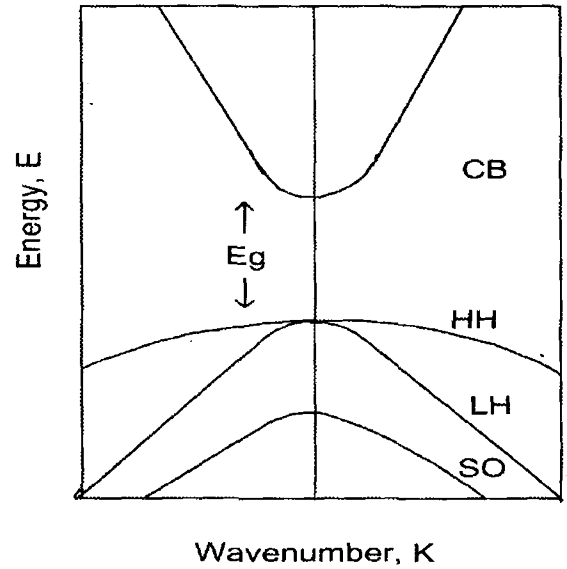

Fig. 2.7: Band structure of a typical bulk SOA.

The second form of carrier recombinations are the undesirable non-radiative recombinations, which act to deplete the carrier population without the emission of a photon and so reduce the efficiency of the device. The most important form of non-radiative recombination is Auger recombination. There are three Auger processes that can take place: CCCH, CHHS and CHHL. C represents the conduction band and H,L and S represent the HH, LH and SO valence bands, respectively. An example of CCCH Auger recombination is illustrated in Fig. 2.8.

A conduction band electron and a valence band hole recombine but instead of the resulting energy going into the emission of a photon, the energy is transferred to another conduction band electron. This electron is then excited into a higher energy level in the conduction band, thus reducing the amount of carriers available for the generation of photons. The process illustrated in Fig. 2.8 is termed CCCH as it involves three electrons in the conduction band and one heavy-hole in the valence band. It has been estimated that Auger recombination accounts for 80 % of the total current in a semiconductor laser at room temperature [28]. The Auger recombination rate is given by:

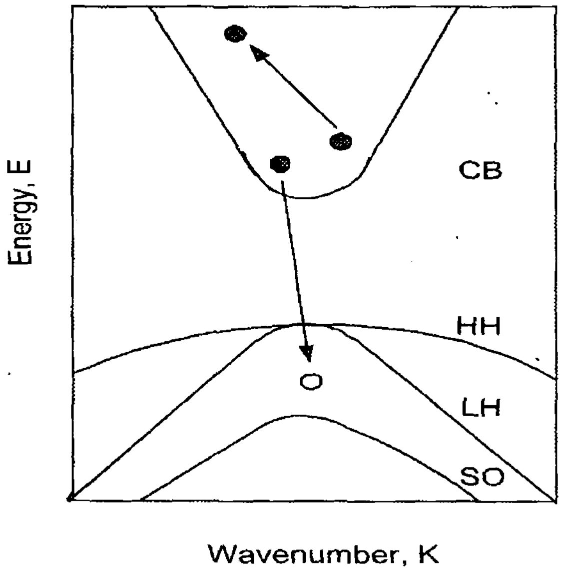

Fig. 2.8: Illustration of CCCH Auger recombination.

$$R_{aug} = CN^3 \tag{2.17}$$

where C is the Auger coefficient, representing the total contribution from all Auger processes.

Another source of nonradiative recombination is material defects. These defects or traps can be introduced to the active region of the device during the fabrication process and worsen as the device ages. Impurities from the air absorbed by the end facets and surface effects can also add to the nonradiative recombination. The contribution of the material defects to the recombination rate is given by:

$$R_{tr} = A_N \tag{2.18}$$

where A is the Schockley-Read-Hall leakage coefficient. A final source of nonradiative recombination is due to carrier leakage, which occurs when carriers leak across the heterojunction, leading to a diffusion or drift of carriers. The leakage recombination is given by:

$$R_{leak} = DN^{3.5} \tag{2.19}$$

for diffusion or

$$R_{leak} = DN^{5.5} \tag{2.20}$$

for drift, where D is the leakage coefficient. Carrier leakage effects only become significant at high carrier densities. The total recombination rate can be expressed as:

$$R(N) = AN + BN^2 + CN^3 + DN^{5.5} \tag{2.21}$$

if it is assumed that carrier drift is the primary source of current leakage current. In the model presented in Chapter 3, the leakage current, $DN^{5.5}$, is also omitted as it is negligible at the current densities considered.

2.10 Gain dynamics in the SOA

When an optical beam is injected into an amplifier, electrons in excited states are depleted due to the stimulated emission that leads to the generation of photons. This depletion of the carriers leads to a reduction of the gain. There is also a variation in the refractive index, which is determined by the LEF, usually represented by α [29]. After depletion of the carriers there is a recovery of the gain to the initial undepleted value. This recovery is determined by several processes with a certain timeframe associated with each one. The main processes involved in the recovery of the gain to its initial value are Carrier Density Pulsations (CDP),Carrier Heating (CH), Spectral-Hole Burning (SHB), Two Photon Absorption (TPA) and ultra-fast Kerr effects. A separate LEF can also be associated with each process, due to the different carrier dynamics in each case. The LEF is of interest in this work as it results in a frequency chirping effect that can limit the performance of optical signals in communication systems. A diagram of the evolution of the carrier distribution as a function of energy is given in Fig. 2.9, showing the different processes that occur at different timeframes. The switching speed of systems based on SOAs therefore depends on the particular gain process, or processes, visible to the optical data signal injected into the device, which depends on the speed of the data signal.

2.10.1 Carrier density pulsations (CDP)

The timeframe associated with this process is related to the relaxation time required for the transition of carriers from the valence band to the conduction band. It is the well-known interband relaxation time, that is described by the equation [30]:

$$\tau_s^{-1} = \frac{\partial R(N)}{\partial N} = A + 2BN + 3CN^2 \tag{2.22}$$

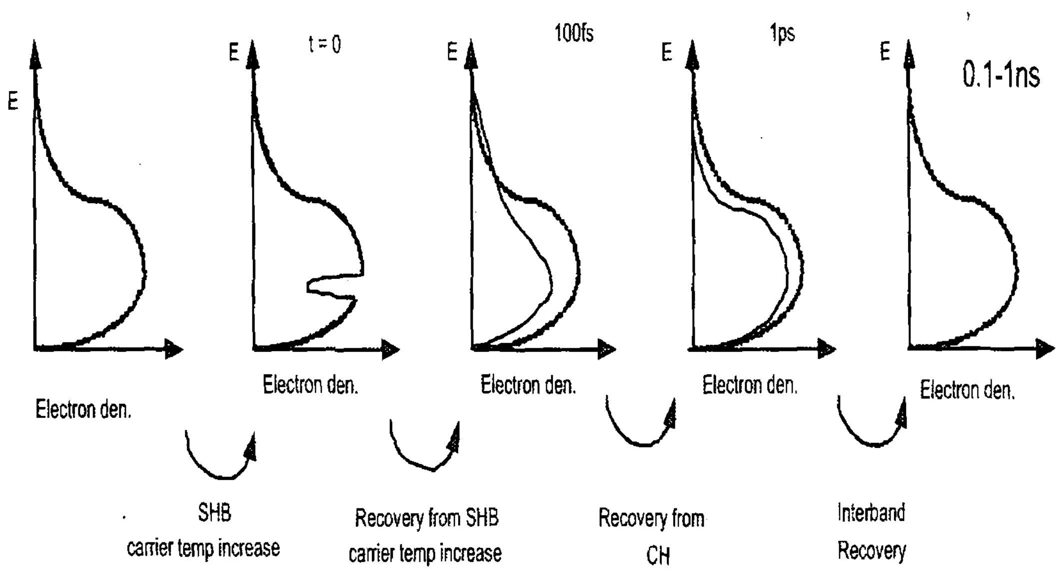

Fig. 2.9: Evolution of carrier distribution in the active region of a bulk SOA. Following stimulated emission due to a monochromatic optical signal the distribution recovers to equilibrium on several different timescales due to the different gain processes.

where τ_s is the inter-band carrier lifetime, $R(N)$ is the total carrier recombination rate defined in Eqn. (2.21), where A, B and C represent the same parameters. τ_s decreases for increasing SOA length, bias current and injected optical power. Typical times associated with this process are in the order of hundreds of picoseconds, the exact value varies between devices. The LEF for the interband recombination is given by the following expression [29]:

$$\alpha = \frac{-4\pi}{\lambda} \frac{\frac{\partial n}{\partial N}}{\frac{\partial g_m}{\partial N}} \tag{2.23}$$

where n is the refractive index, N is the carrier density and g_m is the material gain. This expression is a measure of the ratio between the rate of change of refractive index with respect to carrier density and the rate of change of material gain with respect to carrier density. It is a magnitude describing the variation of the refractive index due to the inter band transitions. The LEF defines the strength of the coupling between the gain and the phase in the SOA. Typical values for the LEF in bulk SOAs are in the range 3-8. The LEF determines the Self-Phase Modulation (SPM) and the level of frequency chirp introduced by the SOA. These parameters are important in terms of optical communication systems and will be explained in greater detail in Chapters 3 and 6, respectively.

2.10.2 Carrier heating (CH)

CH refers to several processes by which the temperature of the carrier distribution increases beyond the lattice temperature. The heated carriers relax to the temperature of the lattice by the emission of phonons. The characteristic lifetime of CH is generally between 0.5-1 ps. The main processes causing CH are stimulated emission and Free-Carrier Absorption (FCA). The main effect of CH is to suppress the gain in the SOA [31].

When an optical signal is injected into an SOA, carriers at the energy corresponding to the signal are depleted due to stimulated emission. The carriers that are removed by this process are those near to the band-edge. They are referred to as 'cold carriers'. The removal of these carriers leads to the increase of the average energy of the remaining carriers after carrier-carrier scattering has redistributed the energy of the carriers. FCA also leads to CH. FCA, known as the plasma effect, is a process where an electron absorbs a photon within the conduction or valence band and transits to a higher energy level [32]. The LEF originating from CH can be defined in both the conduction band and the valence band, and is given by [33]:

$$\alpha_{ch} = \frac{-4\pi}{\lambda} \frac{\frac{\partial n}{\partial T_{(c,v)}}}{\frac{\partial g_m}{\partial T_{(c,v)}}}; \tag{2.24}$$

where n is the refractive index, $T_{(c,v)}$ is the carrier temperature in the conduction and valence bands, respectively, and g_m is the material gain. Experimental investigations have found that the SPM due to CH is far less than that due to CDP [34]. This indicates that the LEF for CH is far less than for CDP. An experiment to measure the recovery time and LEF associated with CH is presented in Chapter 6.

2.10.3 Spectral-hole burning (SHB)

SHB refers to a localized reduction in the number of carriers at the transition energies. It occurs due to the intense stimulated emission which is localized to the wavelength of a signal injected into an SOA. This signal depletes carriers close to its wavelength faster than injection can replenish the carrier level. The depth of the spectral hole is dependent on the amount of carrier transitions from the conduction to the valence band. The recovery time associated with SHB is defined by the finite intraband relaxation time of the carriers, i.e. the carrier-carrier scattering time. The timeframe associate with SHB is generally around 100 fs, although this value is variable for different devices. The LEF for SHB is considered to be 0 because a spectral hole symmetrically depletes the gain around the emission wavelength, in such a situation no refractive index change results [35]. Therefore there is no SPM originating from SHB.

2.10.4 Two-photon absorption (TPA)

TPA is a process whereby a carrier absorbs the energy of two photons and transits to a higher energy level, corresponding to the combined energy of the two photons. This leads to a further suppression of the gain. The recovery time associated with this process is in the order of tens of femtoseconds. This effect only becomes significant in SOAs subjected to high signal intensity operating near transparency [36] - [37]. TPA can also lead to CH for high power optical signals.

2.10.5 Kerr nonlinearity

The Kerr effect is an ultra-fast phase change that is dependent on the SOA gain due to injection of an optical signal and also the TPA effect [38]. The recovery time associated with this process is below 100 fs. Large phase variations have been measured using this effect, demonstrating the potential to design ultrafast all-optical switches based on femtosecond pulses [38] - [39].

2.11 SOAs under test

In this section the specifications of the SOAs used in the experimental work are detailed. Two devices where used to perform the experiments presented in this thesis. Both devices were grown using the InP/InGaAsP material system. In the case of the Avanex device, a tensile strained bulk material was used. Both SOAs used are chip devices i.e. there was no fibre coupled to the device during packaging. This allowed for control of the polarization that would not be possible if the devices were packaged with Single-Mode Fibre (SMF). The specifications for both the Optospeed and Avanex devices are given in Table 2.1.

It can be observed from the specifications that the gain is 10 dB greater for the longer Optospeed device. This is because the longer cavity allows for more amplification of the signal as it propagates along the cavity. The longer device is also more sensitive to polarization, because it is more difficult to match the TE and TM mode gains. This makes the Optospeed device the more suitable one for measuring the NPR effect. Another interesting difference between the two devices is the 3 dB spectral bandwidth, which is far greater for the shorter Avanex device. The reason for this is also related to the device length and will be presented in the next chapter. The Amplified Spontaneous Emission (ASE) ripple parameter is due to the presence of the FP modes even after the suppression of these modes using

Device parameter	Optospeed	Avanex
Length, mm	1.5	0.6
Waveguide tilt	12^o	12^o
Bias current, mA	500	200
Typ. Gain, dB	30	20
Max pol. depen., dBm	6	1.5
3 dB bandwidth, nm	25	70
Peak gain wavelength, nm	1572	1515
3 dB sat. power, dBm	9	9.6
ASE Ripple, dB	0.65	0.1
Noise figure, dB	17	9

Tab. 2.1: Manufacturers specifications for the Optospeed and Avanex SOAs.

the techniques described in Sec. 2.7 . The variation in the magnitude of the FP modes, i.e. the ASE ripple, is small with values of 0.65 dB and 0.1 dB, respectively. The waveguides of both of the devices were tilted by 12^o in order to suppress the longitudinal modes.

2.12 Experimental characterization

2.12.1 Amplified spontaneous emission (ASE)

As already discussed in Sec. 2.3, carriers that reside in the conduction band have a finite probability of being emitted as photons independently of any injected optical signal. The quantity of spontaneously emitted photons is given by Eqn. (2.1). A fraction of this light, β, will be coupled into one of the modes of the optical resonator [40]. β typically has a value in the order of 10^{-5}. A percentage of these photons are reflected from the end facets due to the residual reflectivity, also in the order of 10^{-5} [41], which although very low can become significant for large amounts of generated photons. As these spontaneously emitted photons are guided through the cavity they may have the energy required for recombination to occur between additional carriers in the conduction band and holes in the valence band, with the emission of a photon of light with the same characteristics as the original photon. This process is known as ASE.

The spectrum of the ASE was measured experimentally, using an Optical Spectrum Analyzer (OSA) with a spectral resolution of 0.07 nm. Carriers were injected into the conduction band by means of electrical pumping. This current source is generally omitted from experimental setups, its presence is to be assumed throughout this thesis. After the current was applied the ASE was emitted in equal quantities at either end of the device. A lensed fibre was positioned at one end of the SOA in order to collect the ASE and guide it down an SMF. The working distance of this lensed fibre was 1.5 mm, and the coupling efficiency was estimated as being 50%.

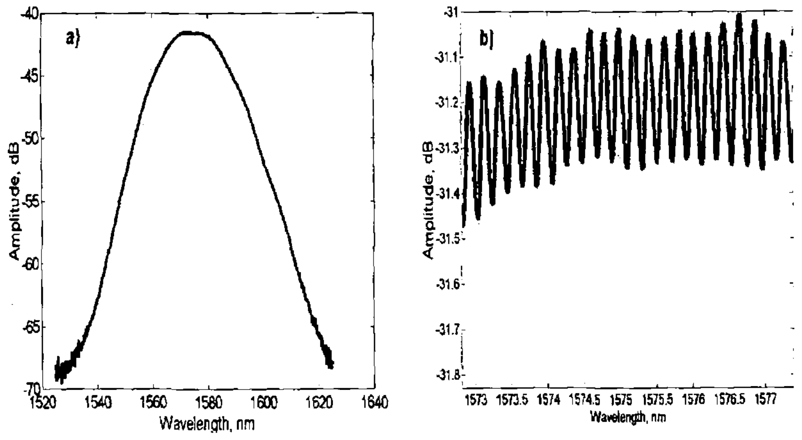

Fig. 2.10: The ASE found experimentally showing a) full spectrum and b) ripples on the spectrum for the Optospeed device.

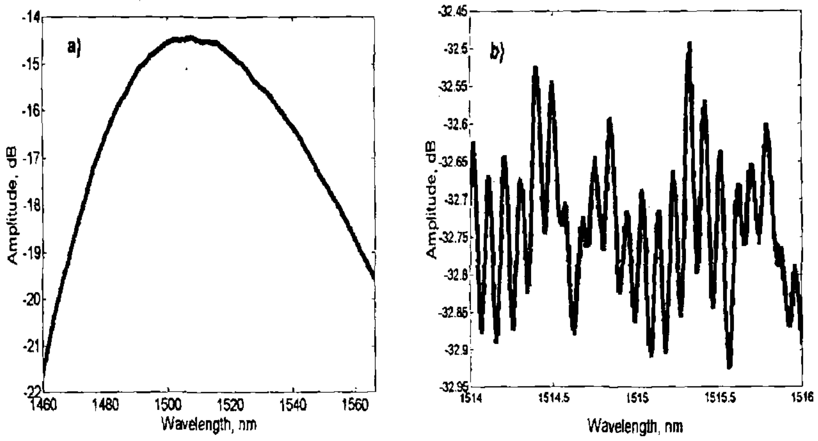

Fig. 2.11: The ASE found experimentally showing a) full spectrum and b) ripples on the spectrum for the Avanex device.

The ASE spectra found experimentally for both devices under test are shown in Fig. 2.10a) and Fig. 2.11a). The 3 dB spectral bandwidth of both devices is quite different. The Optospeed device has a value of approximately 25 nm whereas the Avanex device has a value of approximately 70 nm. This variation is attributed to the different material gains of both devices due to the different levels of doping used in the fabrication process.

Fig. 2.10b) and Fig. 2.11b) show that the longitudinal FP modes still have an impact on the spectrum. These ripples remain from the residual reflectivity still present in the waveguide even after suppression using the techniques described in Sec. 2.7. The difference in the ripples introduced to each device is due to the lengths of the respective devices. The longer Optospeed device has a larger amount of reflected light due to the larger amplification of the light coupled to the waveguide modes. This is because of the additional distance over which the signal has travelled. From Fig. 2.10b) and Fig. 2.11b) it can be seen that the Avanex device has less periodical ripples than the Optospeed device. Again this may be attributed to the shorter length of the Avanex device, which results in less well defined ASE ripples. A wavelength dependence of the AR coating of the Avanex device may also cause larger ASE ripples. The ASE ripple quoted for the Avanex device is consistent with that measured experimentally. The ripple measured for the Optospeed device, however, is far lower than the value quoted by the manufacturer. It should be noted that the reflectivity of both SOAs is similar.

2.12.2 Light-Current (LI) curve

The LI curve is a plot of the average power emitted due to ASE as a function of the bias current in the SOA. Below a certain current there is very little amplification of the spontaneous emission and the SOA will act like a Light Emitting Diode (LED), where the emitted light is pure spontaneous emission.

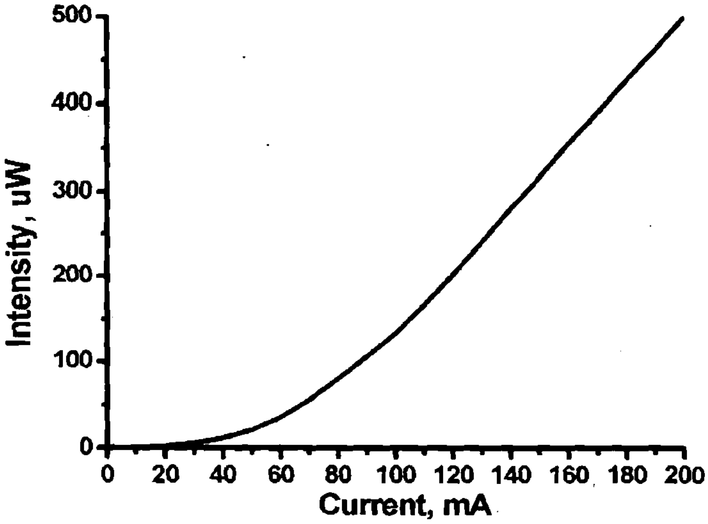

Fig. 2.12: LI curve found experimentally.

As the current is increased there is a point at which the amplification of the spontaneous emission starts to dominate the emission from the SOA. This can be seen in Fig. 2.12, where it can be seen that above a current of approximately 50 mA the ASE increases exponentially. This result was taken for the Avanex device. Spontaneous emission is not the only mechanism by which these carriers can recombine however. The non-radiative recombinations, discussed in Sec. 2.9.1, are also present and act to reduce the carriers that contribute to ASE.

2.12.3 Signal gain of the device

The signal gain of an SOA is the ratio of the power measured at the output of the device to the power injected into the device. It is important to take coupling losses into consideration for this measurement. This gain differs from the material gain as optical confinement and losses are also taken into account. The signal gain is calculated experimentally using the following expression:

$$G = 10log[P_{out}/P_{in}] \tag{2.25}$$

where P_{out} is the power of the signal measured at the output of the device and P_{in} is the power of the signal injected into the device, taking coupling losses into consideration. The ASE was subtracted from P_{out} in order to accurately measure the contribution of the signal power on the output power.

Lensed fibres are used to couple an optical signal into the SOA and to collect the amplified signal at the output of the device. The gain as a function of current measured experimentally for the Avanex device is shown in Fig. 2.13 for injected intensities of -20 dBm and 0 dBm. As the intensity is increased there is a reduction in gain of the device. This is related to the gain saturation phenomenon, discussed in Sec. 2.5.1.

Ideally it is desirable to have as high an optical gain as possible. There is as limit to the level the gain can reach, however, and as the bias current increases the rate of increase of the gain levels off. This effect, visible in Fig. 2.13 for bias currents above 100 mA, is due to the device becoming fully inverted as it cannot infinitely pump carriers into the conduction band. At a certain bias current the maximum number of carriers contributing to photonic emission have been injected into the conduction band, and so the gain has reached its maximum value at this point. It should be noted that the gain in Fig. 2.13 starts to increase at approximately the same current where the ASE starts to dominate the LI curve as can be observed in Fig. 2.12. This is because both the gain and the ASE are determined by the quantity of carriers excited into the conduction band, and at a current of

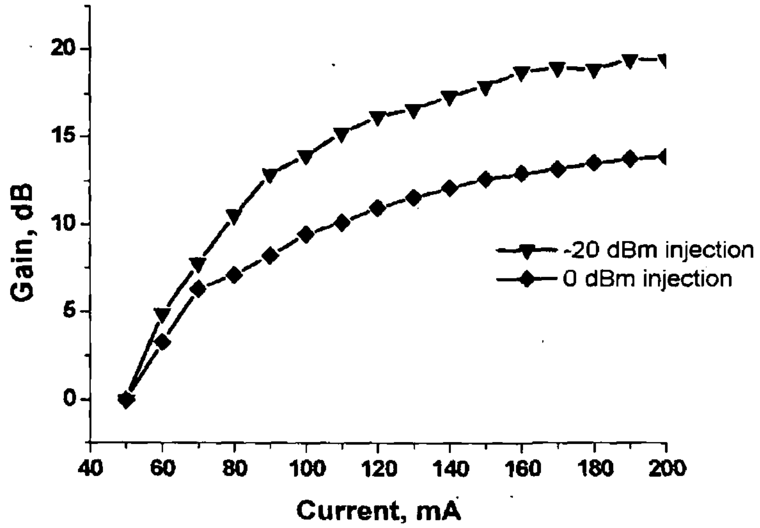

Fig. 2.13: Experimentally measured gain as a function of bias current for -20 dBm and 0 dBm signal injection at a wavelength of 1515 nm.

approx. 50 mA there are enough carriers in the conduction band so that stimulated emission starts to dominate the emission from the device.

2.12.4 Experimental gain saturation

The gain saturation was described in Sec. 2.5.1. Experimentally the gain saturation is often characterized by the input or output intensity corresponding to a 3 dB reduction in the gain.

This effect is undesirable if the SOA is to be used as an amplifier, as it limits the gain of the device. However, it is a very useful nonlinearity that can be exploited for use directly in XGM and indirectly through the LEF in XPM. Both these processes can be used to perform all-optical signal processing, which will be discussed in detail in Chapters 5 and 6. The gain saturation was measured experimentally and is shown in Fig. 2.14 for the Avanex device. The device was biased at 200 mA for this measurement. The relatively short length of this SOA results in the gain saturation occurring at a low injection power of approximately -7 dBm.

2.12.5 Noise figure (NF)

The predominant source of noise, limiting device performance, in all optical amplifiers is spontaneous emission. As already discussed, a fraction of these photons will be emitted

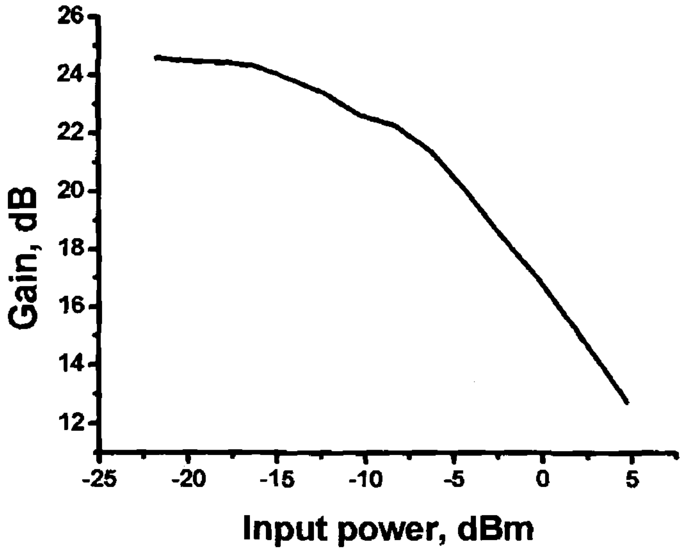

Fig. 2.14: Reduction of the gain as a function of injected intensity measured experimentally.

with a direction close to the direction of the signal photons. These photons will be amplified as they travel along the amplifier towards the output. The result is that at the output of the device both the signal and the noise will be amplified, the output power can be given by [42]:

$$P_{out} = GP_{in} + P_n \tag{2.26}$$

where P_n represents the ASE signal. The degradation of the signal to noise ,(S/N), ratio from input to output of the optical amplifier is given by the NF of the device:

$$F = \frac{(S/N)_i}{(S/N)_o} \tag{2.27}$$

where $(S/N)_i$ is the (S/N) at the input of the device and $(S/N)_o$ is the (S/N) at the output of the device. Typical values for the NF of a practical SOA are 7 to 14 dB. This parameter was measured experimentally as a function of wavelength. The results are shown in Fig. 2.15. The wavelength was varied from 1490 nm to 1590 nm. The experiment was performed on the Avanex device, which was biased at 200 mA. It is observed that the NF shows little variation over the span from 1490 nm to 1550 nm. The NF was measured to be approx. 11.2 over this range.

As the wavelength increases beyond 1550 nm the NF starts to increase and was measured to be 13.5 at 1590 nm. This increase coincides with the 3 dB gain bandwidth as can

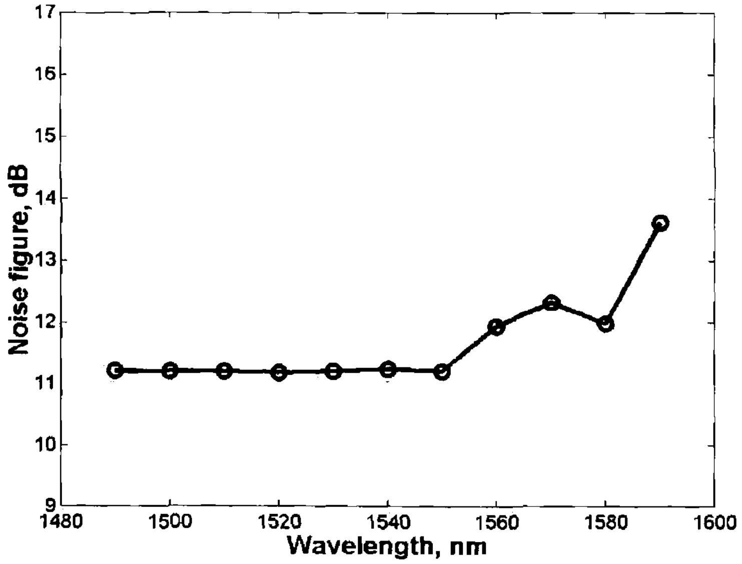

Fig. 2.15: Noise figure as a function of wavelength measured experimentally.

be seen from the ASE spectrum of Fig. 2.11, i.e. the NF is at its lowest when the signal receives greatest gain. As the gain reduces $(S/N)_o$ also reduces leading to the increase in the NF. This factor should to be taken into consideration when amplifying signals in an SOA.

2.13 *Conclusions*

The SOA was introduced in this chapter. The physics behind the operation of this device were described in a methodical manner. The SOA is essentially a p-n junction designed in such a way that photonic emission occurs. The processes of amplification and absorption were then described. The operation of the SOA is very similar to the operation of the semiconductor laser. The key difference is that in an SOA the lasing condition is never reached. The SOA may be described as a modified semiconductor laser. The laser is adjusted to suppress lasing by several techniques, including the application of AR coatings and angling the facets of the device. There are different types of SOA devices. Bulk SOAs are used in the work presented in this thesis. The key physics related to the SOA, including carrier recombinations and gain dynamics were also discussed before the specifications of the two devices used in this work were given. The two SOAs under test were obtained from Optospeed and Avanex, respectively. The experimental characterization measured using these devices was detailed in this chapter. Good agreement was found between this characterization and the specifications provided. The Optospeed device was used in the experiments presented in Chapter 4, whilst the Avanex device was used in obtaining the experimental results presented in Chapters 5 and 6. There are large differences in the performance of these devices which should be noted from the specification presented. These variations are due to different device parameters such as length, gain, bias current and saturation power. This basic understanding of the SOA was used to develop a detailed theoretical model, which is presented in the next chapter.

BIBLIOGRAPHY

[1] H. Ghafouri-Shiraz. "The principles of semiconductor laser diodes and amplifiers". *Imperial College Press*, pages 64–68, 2004.

[2] A. Yariv. "Optical electronics". *Saunders college publishing*, 1991.

[3] M.J. Connelly. "Semiconductor optical amplifiers". *Kluwer Academic Publishers*, pages pg. 10–12, 2003.

[4] C. Fabry, A. Perot. "Theorie et applications d'une nouvelle methode de spectroscopie interferentielle". *Ann. Chim. Phys.*, vol.16:pp.115, 1899.

[5] W.J. Crowe, and W.E. Aheam. "Semiconductor laser amplifier". *IEEE J. Quantum Electronics*, vol.2(no.8):pp.283–289, 1966.

[6] H.A. Macleod. "Thin-film optical filters ". *Institute of physics pub.*, 2001.

[7] S.A. Merritt, C. Dauga, S. Fox, I-F. Wu and M. Dagenis. "Measurement of the facet modal reflectivity spectrum in high quality semiconductor travelling wave amplifiers". *IEEE J. Lightwave Tech.*, vol.13(no.3):pp.430–433, 1995.

[8] L. Jungkeun, and T. Kamiya. "Improved characterization of multilayer antireflection coatings for broad-band semiconductor optical amplifiers". *IEEE J. Lightwave Tech.*, vol.18:pp.2158–2166, 2001.

[9] D. Marcuse. "Reflection loss of laser mode from tilted end mirror". *J. Lightwave Technol.*, vol.7:pp.336–339, 1989.

[10] G.A. Alphonse, D.B. Gilbert, M.G. Harvey, and M. Ettenberg. "High-power superluminescent diodes". *IEEE J. Quantum Electronics*, 24(12):pp.2454–2457, 1988.

[11] C.E. Zah, R. Bhat, S.G. Menocal, N. Andreadakis, F. Favire, C. Caneau, M.A. Koza, T.P. Lee. "1.5 μm GaInAsP angled-facet flared-waveguide traveling-wave laser amplifiers". *IEEE Photonics Tech. Letters*, vol.2(no.1):pp.46–47, 1990.

[12] I. Cha, M. Kitamura, H. Honmou, and I. Mito. "1.5 μm band travelling-wave semiconductor optical amplifier with window facet structure". *IEE Electronic Letters*, vol.25:pp.1241–1242, 1989.

[13] N. A. Olsson, R.F. Kazarinov, N.A. Nordland, C.H. Henry, M.G. Oberg, H.G. White, P.A. Garbinski, and A. Savage. "Polarization-independent configuration optical amplifier with buried facets". *IEE Electronic Letters*, vol.25:pp.1048–1049, 1989.

[14] J.P. Van der Ziel, R. Dingle, R.C. Miller, W. Wiegmann, and Jr. W.A. Nordland. "Laser oscillation from quantum states in very thin GaAs-AlGaAs multilayer structures". *Appl. Phys. Lett.*, vol.26:pp.170, 1975.

[15] G. Eisenstein, U. Koren, G. Raybon, T.L. Koch, J.M. Weisenfeld, M. Wegener, R.S. Tucker, B.I. Miller. "Large and small signal gain characteristics of $1.5\mu m$ multiple quantum well optical amplifiers". *IEEE Photonics Tech. Letters*, vol.4(no.6):pp.1201–1203, 1992.

[16] K.S. Jepsen, B. Mikkelsen, J.H. Povlsen, M. Yamaguchi, and K.E. Stubkjaer. "Wavelength dependence of noise figure in InGaAs/InGaAsP multiple-quantum-well laser amplifier". *IEEE Photonics Tech. Letters*, vol.4(no.2):pp.550–553, 1992.

[17] T. Saitoh, Y. Suzuki, and H. Tanaka. "Low noise characteristics of a GaAs-AlGaAs multiple-quantum-well semiconductor laser amplifier". *IEEE Photonics Tech. Letters*, vol.2(no.11):pp.794–796, 1990.

[18] A.K. Mishra, X. Yang, D. Lenstra, G.D. Khoe, and H.J.S. Dorren. "Ultrafast all-optical wavelength conversion using nonlinear polarization rotation in a semiconductor optical amplifier". *ICTON 2004*, pages pp.322–325, 2004.

[19] T. Keating, J. Minch, C.S. Chang, P. Enders, W. Fang, S.L. Chuang, T. Tanbun ek, Y.K. Chen, and M. Sergent. "Optical gain and refractive index of a laser amplifier in the presence of pump light for cross-gain and cross-phase modulation". *IEEE Photonics Tech. Letters*, vol.9(no.10):pp.1358–1360, 1997.

[20] N. Kirstaeder, N.N. Ledentsov, M. Grundmann, D. Bimberg, V.M. Ustinov, S.S. Ruvimov, M.V. Maximov, P.S. Kop'ev, Zh.I. Alferov, U.Richter, P.Werner, U. Gosele, J. Heydenreich. "Low threshold large t_0 injection laser emission from InGaAs quantum dots". *IEE Electronics Letters*, vol.30:pp.1416, 1994.

[21] M. Sugawara. "Self-assembled InGaAs/GaAs quantum dots". *Academic press*, page pp.209, 1999.

[22] M. Sugawara. "Quantum-dot semiconductor optical amplifiers". *OFC 2003*, pages pp.537–538, 2003.

[23] M. Grundmann. "The present status of quantum dot lasers". *Physica E*, vol.5:pp.167–184, 1999.

[24] T.W. Berg, and J. Mørk. "Saturation and noise properties of quantum-dot optical amplifiers". *IEEE J. Quantum Electronics*, vol.40(no.11):pp.1527–1539, 2004.

[25] D. O'Brien, S.P. Hegarty, and G. Huyet. "Sensitivity of quantum-dot semiconductor lasers to optical feedback". *Optics Letters*, vol.29(no.10):pp.1072–1074, 2004.

[26] S.P. Hegarty, B. Corbett, J.G. McInerney, and G. Huyet. "Free-carrier effect on index change in 1.3 μm quantum-dot lasers". *IEE Electronic Letters*, vol.41(no.7):pp.416–418, 2005.

[27] E.P. O'Reilly, and A.R. Adams. "Band-structure engineering in strained semiconductor lasers". *IEEE J. Quantum Electronics*, vol.30:pp.366–379, 1994.

[28] M. Silver, and E.P. O'Reilly. "Gain and radiative current density in InGaAs/InGaAsP lasers with electrostatically confined electron states". *IEEE Journal of Quantum Electronics*, vol.30(no.2):pp.547–553, 1994.

[29] C.H. Henry. "Theory of the linewidth of semiconductor lasers". *IEEE J. Quantum Electronics*, vol.18(no.2):pp.259–264, 1982.

[30] S. Ruiz-Moreno, J. Guitart. "Practical method for modelling the nonlinear behaviour of a travelling wave semiconductor optical amplifier". *IEE Proceedings*, vol.140(no.1):pp.39–42, 1993.

[31] M. Willatzen, A. Uskov, J. Mørk, H. Olesen, B. Tromborg, and A.-P. Jauho. "Nonlinear gain suppression in semiconductor lasers due to carrier heating". *IEEE Photonic Tech. Letters*, vol.3(no.7):pp.606–609, 1991.

[32] C-Y. Tsai, C-Y. Tsai, C-H. Chen, T-L. Sung, T-Y. Wu, F-P. Shih. "Theoretical model for intravalley and intervalley free-carrier absorption in semiconductor lasers: Beyond the classical drude model". *IEEE J. Quantum Electronics*, vol.34(no.3):pp.552–559, 1998.

[33] M.Y. Hong, Y.H. Chang, A. Dienes, J.P. Heritage, and P.J. Delfyett. "Subpicosecond pulse amplification in semiconductor laser amplifiers: Theory and experiments". *IEEE J. Quantum Electronics*, vol.30(no.4):pp.1122–1131, 1994.

[34] L. Schares, C. Schubert, C. Schmidt, H.G. Weber, L. Occhi, and G. Guekos. "Phase dynamics of semiconductor optical amplifiers at 10-40 GHz". *IEEE J. Quantum Electronics*, vol.39:pp.1394–1408, 2003.

[35] R.P. Schreieck, M.H. Kwakernaak, H. Jackel, and H. Melchior. "All-optical switching at multi-100-Gb/s data rates with Mach-Zehnder interferometer switches". *IEEE J. Quantum Electronics*, vol.38(no.8):pp.1053–1061, 2002.

[36] Y.-H. Kao, T.J. Xia, M.N. Islam, and G. Raybon. "Limitations on ultrafast optical switching in a semiconductor laser amplifier operating at transparency current". *J. of Appl. Physics*, vol.86(no.9):pp.4740–4747, 1999.

[37] J.M. Tang, and K.A. Shore. "Strong picosecond optical pulse propagation in semiconductor optical amplifiers at transparency". *IEEE J. Quantum Electronics*, vol.34(no.7):pp.1263–1269, 1998.

[38] H.J.S Dorren, X.Yang, D.Lenstra, H. de Waardt, G.D Khoe, T. Simoyama, H. Ishikawa, H. Kawashima, and T. Hasama. "Ultrafast refractive-index dynamics in a multiquantum-well semiconductor optical amplifier". *IEEE J. Quantum Electronics*, vol.15(no.6):pp.792–794, 2003.

[39] H.J.S Dorren, X.Yang, A.K. Mishra, Z. Li, H. Ju, H. de Waardt, G.D Khoe, T. Simoyama, H. Ishikawa, H. Kawashima, and T. Hasama. "All-optical logic based on ultrafast gain and index dynamics in a semiconductor optical amplifier". *IEEE J. Sel. Areas Quantum Electronics*, vol.10(no.5):pp.1079–1091, 2004.

[40] G. Giuliani, and D. D'Alessandro. "Noise analysis of conventional and gain-clamped semiconductor optical amplifiers". *IEEE J. Lightwave Tech.*, vol.18(no.9):pp.1256–1263, 2000.

[41] T. Durhuus, B. Mikkelsen and K.E. Stubkjaer. "Detailed dynamic model for semiconductor optical amplifiers and their crosstalk and intermodulation distortion". *IEEE J. Lightwave Tech.*, vol.10(no.8):pp.1056–1064, 1992.

[42] H. Ghafouri-Shiraz. "The principles of semiconductor laser diodes and amplifiers". *Imperial College Press*, page 29, 2004.

3. SOA MODEL

3.1 Introduction

A numerical model is presented in this chapter which describes the propagation of an optical signal through an SOA. The main purpose of this model is to qualitatively describe physical trends associated with the SOA, particularly those that cannot be measured experimentally. Models for SOAs have received considerable attention since SOAs were first viewed as useful optical components [1] - [17]. The model may be used to validate results obtained experimentally and to provide a deeper understanding to these results. It was initially developed for operation in steady-state regime and was then extended to the dynamic regime, enabling the propagation of pulses in the order of tens of picoseconds to be described. In recent years the now well-established techniques for modelling SOAs have been used to model the dynamic response of the SOA [18] - [22]. The dynamic analysis of the SOA model is important in order to assess their potential performance in optical networks employing all-optical signal processing techniques. This is the approach which was taken with the model presented in this chapter.

The model is based on a numerical solution of travelling wave equations in the active region of an SOA [2] - [4], [6], [12], [13] and [17]. The active region is divided into a number of sections, 10 in this case. Initially there is a constant carrier density in each section. The travelling wave rate equation is solved in each section of the device. This sectioning technique provides a more accurate description of the SOA than a single section model. The variation in carrier density as a function of distance in the longitudinal direction can be modelled, unlike many of the initial models presented [3], [6] and [8]. The propagation of the optical signal, and ASE, from section to section was described using boundary conditions between each section, with spurious facet reflectivities at either end of the device accounting for the small reflections still present after suppression of lasing.

There are many techniques available to model SOAs. The rate equation model presented has the advantage over certain techniques in that the spatial dependence of the light is included [1]. The chapter begins with an introduction to the equations used in establishing the model. These equations were solved in order to describe the operation of the SOA.

After this the theoretical characterization performed using these equations is presented and compared to the same characterization performed experimentally in order to validate the operation of the model. This theoretical characterization, provided by the model, gives a good indication as to the value of device parameters which could not be measured experimentally.

3.2 Overview of the model

The model predicts the behaviour of an SOA by dividing the device into a number of sections. Initially there was a constant carrier density in each section. The electric field, which was modelled as a travelling-wave, and the ASE were solved in each section of the device. Consistency between sections was maintained by including boundary conditions which allow for the propagation of the electric field from section-to-section. The sectioning of the active region is illustrated in Fig. 3.1a). The electric field was defined in both left and right travelling fields. There is a field propagating in the direction opposite to injection due to the presence of weak facet reflectivities even after the anti-guiding techniques have been applied, as discussed in Sec. 2.7. The model is based on results previously presented in the literature [12]. A diagram illustrating the sectioned SOA is shown in Fig. 3.1b) [23]. As well as the forward and backward propagating signal field in each section, $E_m^{(+/-)}$, the intensity of spontaneously emitted photons, $I_{sp}^{(+/-)}$, propagating in both forward and backward directions was also included. The reflectivity of each end facet is represented in Fig. 3.1b) by r_1 and r_2 respectively. It is important to have a point of reference within each section, for this reason the variables z_m^- and z_m^+ were included to represent the position at the beginning and end of each section. The propagating electric field and spontaneous intensity were then used to solve the carrier density rate equation, $\frac{\partial N}{\partial t}$. The bias current is represented by I_{Bias} and the input and output optical powers are represented by P_{in} and P_{out} respectively. Each variable used in the model is defined in Appendix A of this thesis.

3.3 Mathematical description of the model

3.3.1 Description of optical field travelling through the SOA

As can be seen in Fig. 3.1b) the electric field travelling through the active region, $E_m(w, z)$, can be decomposed as follows:

$$E_m(w, z) = E_m^+(w, z) + E_m^-(w, z) \qquad (3.1)$$

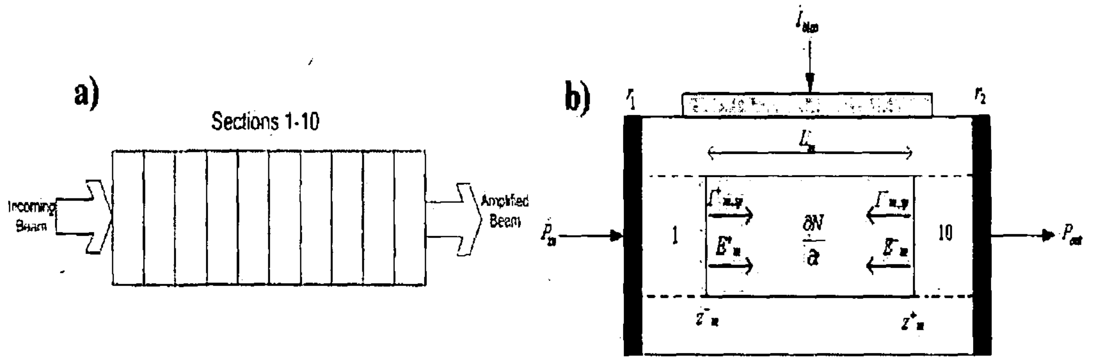

Fig. 3.1: Diagram illustrating a) all sections in the modelled SOA and b) parameters calculated in each section of the model.

where $+$ and $-$ represent right and left-travelling fields, respectively. w represents the angular frequency and z is the position in the cavity of the device. The E-field is considered to be a linearly polarized signal aligned along the TE axis of the device. Due to the continuity between the sections, the boundary conditions which define propagation between each section, m, may be written as:

$$E^+_m(w, z^-_m) = E^+_{m-1}(w, z^+_{m-1}), \qquad m = 2 \cdots n \tag{3.2}$$

$$E^-_m(w, z^+_m) = E^-_{m+1}(w, z^-_{m+1}), \qquad m = 1 \cdots n-1 \tag{3.3}$$

In the case of the first and last sections where m equals 1 and n respectively, the boundary conditions are

$$E^+_1(w, z^-_1) = r_1 E^-_1(w, z_1) + E^{in}(w), \qquad m = 1 \tag{3.4}$$

$$E^-_n(w, z^+_n) = r_2 E^+_n(w, z^+_n), \qquad m = n \tag{3.5}$$

where the initial input field E^{in} was taken at the point immediately inside the amplifier, just after the input facet, which was defined in the model to be the left-hand side facet. The next step was to find an equation that describes the field evolution inside each section. The one-dimensional Helmholtz wave equation was used. This equation represents the propagation of an electromagnetic wave as a function of distance travelled in the device:

$$\frac{\partial^2 E^\pm_m(w, z)}{\partial z^2} + K^2_m(w, N_m) E^\pm_m(w, z) = 0 \tag{3.6}$$

solving this equation, the following result was obtained:

$$E_m^{\pm}(w, z) = E_m^{\pm}(w, z_m^{\mp})e^{\mp iK_m(w,N_m)(z-z_m^{\mp})} \tag{3.7}$$

which represents the plane wave solution of the electric field, under the condition that the wavenumber, K_m, defined as:

$$K_m(w, N_m) = \frac{w}{c}n_e(w, N_m) + i\frac{1}{2}(\Gamma g_m(w, N_m) - \alpha_i) \tag{3.8}$$

is constant along the direction of propagation. The carrier density, N_m, is assumed to be constant in each section, which results in a constant wavenumber in each section. $n_e(w, N_m)$ is the effective refractive index in section m, Γ is the confinement factor, α_i is the internal loss per unit length, and $g_m(w, N_m)$ is the material gain in a section which will be described in the next section.

The signal frequencies are assumed to be appreciable only in a narrow band around the optical frequency, w_{k0}, so the wavenumber can be replaced with its first-order Taylor expansion around w_{k0}:

$$K(w, N) = K(w_{k0}, N) + \frac{\partial K(w, N)}{\partial w}(w - w_{k0}) \tag{3.9}$$

where

$$\frac{\partial K(w, N)}{\partial w} = \frac{n_g}{c} + i\frac{1}{2}\Gamma\frac{\partial g_m(w, N)}{\partial w} \tag{3.10}$$

the group refractive index n_g is given by:

$$n_g = n_e(w_{k0}, N) + w_{k0}\frac{\partial n_e(w, N)}{\partial w} \tag{3.11}$$

Eqn. (3.7) and Eqns. (3.9)-(3.11) were used to get an expression for the field in the frequency domain at the output of section m in terms of the input field to that section, where the propagation between the different sections is defined by Eqns. (3.2)-(3.5):

$$E_m^{\pm}(w, z_m^{\pm}) = E_m^{\pm}(w, z^{\mp}).e^{iK_m(w_{k0},N_m)L_m}.e^{-i\frac{n_g}{c}(w-w_{k0})L_m}.e^{\frac{1}{2}\Gamma\frac{\partial g_m(w,N_m)}{\partial w}(w-w_{k0})L_m} \tag{3.12}$$

A representation of the field in the time domain was then obtained by using the inverse Fourier transform:

$$F_m^{\pm}(t, z_m^{\pm}) = \sqrt{G_{s,m}}e^{i\phi_m}[1 - i\frac{\Gamma}{2}\frac{\partial g_m(w, N)}{\partial w}L_m\frac{\partial}{\partial t}].F_m^{\pm}(t - \tau_m, z_m^{\mp}) \tag{3.13}$$

this equation describes the evolution of the field as it passes through a section, where $\tau_m = \frac{L_m n_g(w, N_m)}{c}$ is the transit time for a section and $G_{s,m}$ is the single-pass gain in a section, defined as:

$$G_{s,m} = e^{(\Gamma g_m(w_{k0}, N_m) - \alpha_i) L_m} \tag{3.14}$$

The phase shift, ϕ_m, induced by propagation through a section m is:

$$\phi_m = \frac{w_{p0}}{c} n_{e,0} L_m + \frac{n_{g,0}}{c}(w_{k0} - w_{p0}) L_m + \frac{w_{p0}}{c} \frac{\partial n_e(w, n)}{\partial N}(N - N_r) L_m \tag{3.15}$$

The evolution of the field between sections was established , in the time domain, by defining boundary conditions in a similar manner to Eqns. (3.2)-(3.5):

$$F_m^+(t, z_m^-) = F_{m-1}^+(t, z_{m-1}^+), \qquad m \neq 1 \tag{3.16}$$

$$F_m^-(t, z_m^+) = F_{m+1}^-(t, z_{m+1}^-), \qquad m \neq n \tag{3.17}$$

$$F_1^+(t, z_1^-) = r_1 F_1^-(t, z_1^-) + F^{in}(t) e^{i(w_{p0} - w_{k0})t}, \qquad m = 1 \tag{3.18}$$

$$F_n^-(t, z_n^+) = r_2 F_n^+(t, z_n^+), \qquad m = n \tag{3.19}$$

In order to model the interaction between light and matter it was essential to solve these equations to describe the propagation of the signal through the active region. When equations were in place to calculate the time-resolved propagation of the electric field, F, time varying phenomena with durations down to a section transit time could be modelled, where this transit time was approximately 0.6 ps. This meant that there was a restriction on the validity of this model. The ultra-fast gain dynamics that happen on the order of a couple of hundred femtoseconds could not be described using this model.

3.3.2 Description of the model used for the gain

This section describes the equation used to calculate the gain in the model [17]. The material gain for a direct bandgap bulk material was calculated by analysis of the energy band structure in the SOA and is given by the following expression:

$$g_m = \frac{c^2}{4\sqrt{2}\pi^{3/2}n_1^2\tau {f_{k0}}^2}\left(\frac{2m_e m_{hh}}{\hbar(m_e + m_{hh})}\right)^{3/2} \times \sqrt{f_{k0} - \frac{E_g(n)}{h}}(f_c(f_{k0}) - f_v(f_{k0})) \tag{3.20}$$

where c is the speed of light in a vacuum, n_1 is the active region refractive index, τ is the radiative carrier recombination lifetime, f_{k0} is the optical frequency, m_e and m_{hh} represent the conduction band electron and heavy-hole (HH) masses, respectively. $\hbar$ represents Planck's constant divided by 2π, and f_c and f_v represent the Fermi-Dirac distributions for the conduction band and valence band, respectively. This expression for the material gain, g_m, is composed of two elements, a gain coefficient and an absorption coefficient.

3.3.3 *Description of the carrier density, stimulated emission and spontaneous emission*

The rate of change of the carrier density with respect to time was calculated in each section of the SOA. The rate equation used to model this behaviour is given by the following expression:

$$\frac{dN_m}{dt} = \frac{I_m}{eV_m} - R(N_m) - [g(w, N_m)S_{m,sig} + a_m(N_m - N_0)S_{m,spon}]\frac{c}{n_{g,0}} \tag{3.21}$$

where I_m is defined as the bias current injected into each section, e and V_m are the elementary charge and volume of the active region, respectively. $R(N)$ describes the carrier recombination rate defined in Eqn. (2.21). The last term in Eqn. (3.21) accounts for the amplified optical signal and the ASE. The amplified signal, $S_{m,sig}$, is defined by:

$$S_{m,sig} = \frac{G_{s,m} - 1}{ln(G_{s,m})}\cdot\frac{\pi n_{g,0}}{c\zeta}\left[\left(|\frac{1}{\sqrt{hw_{k0}}}F_m^+(t, z_m^-)|\right)^2 + \left(|\frac{1}{\sqrt{hw_{k0}}}F_m^-(t, z_m^+)|\right)^2\right] \tag{3.22}$$

In this equation h is Planck's constant, $\zeta = \frac{\sqrt{\frac{\mu_0}{\epsilon_0}}}{n_{e,0}}$ is the wave impedance, where ϵ_0 is the vacuum permittivity and μ_0 is the vacuum permeability.

In order to obtain an expression for the value of the average photon density originating from spontaneous emission an expression for the spontaneous intensity was first defined:

$$\frac{dI_{m,sp}^{\pm}(w, z)}{dz} = \pm\left[\Gamma g(w, N_m) - \alpha_i\right] I_{m,sp}^{\pm}(w, z) \pm \frac{\beta(w)R(N_m)hw}{4\pi} \tag{3.23}$$

where $\beta(w)$ defines the fraction of the spontaneous emission that is coupled into ones of the modes of the device and is thus available for amplification. Eqn. (3.23) has the following solution:

$$I^{\pm}_{m,sp}(w, z^{\pm}) = I^{\pm}_{m,sp}(w, z^{\mp})G_{s,m} + \frac{\beta R(N_m)\hbar w_s L_m}{2ln(G_{s,m})}G_{s,m} - 1 \qquad (3.24)$$

As was the case for the signal field it was necessary to have boundary conditions between sections in order to account for the propagation of the spontaneous intensity through the device. These conditions can be written as:

$$I^{+}_{m,sp}(w, z^{-}_{m}) = I^{+}_{m-1,sp}(w, z^{+}_{m-1}), \qquad m \neq 1 \qquad (3.25)$$

$$I^{-}_{m,sp}(w, z^{+}_{m}) = I^{-}_{m+1,sp}(w, z^{-}_{m+1}), \qquad m \neq n \qquad (3.26)$$

$$I^{+}_{1,sp}(w, z^{-}_{1}) = r_1^2 I^{-}_{1,sp}(w, z^{-}_{1}), \qquad m = 1 \qquad (3.27)$$

$$I^{-}_{n,sp}(w, z^{+}_{n}) = r_2^2 I^{+}_{n,sp}(w, z^{+}_{n}), \qquad m = n \qquad (3.28)$$

An initial value for spontaneous intensity was needed before the above equations were implemented. The negative going intensity was defined just inside the left facet of the device [23]:

$$I_1^{-}(z_1^{-}) = \frac{r_1^2 r_2^2 G S_1 E_1 \prod_{k=2}^{n} G_k^2 + r_2^2 \prod_{k=2}^{n} G_k [\sum_{l=1}^{n-1} (SE_l \prod_{p=l+1}^{n} G_p) + SE_n]}{1 - r_1^2 r_2^2 \prod_{k=1}^{n} G_k^2} \times \frac{\sum_{k=2}^{n-1} (SE_{n-k+2} \prod_{p=2}^{n-k+1} G_p) + SE_2}{1 - r_1^2 r_2^2 \prod_{k=1}^{n} G_k^2} \qquad (3.29)$$

where

$$SE_m = \frac{\beta R_{sp}(N_m)\hbar\omega_s L_m}{2ln(G_{sm})}(G_{sm} - 1) \qquad (3.30)$$

Using Eqns. (3.24)-(3.29) the spontaneous intensity was defined in each section of the device. This was used to define the spontaneous photon density in each section:

$$S_{m,spon} = \frac{4\pi n_{g,0}}{hw_{p0}c}\left\{(I^{+}_{m,sp}(z^{-}_{m}) + I^{-}_{m,sp}(z^{+}_{m}) + \frac{\beta R_r(N_m)hw_{p0}}{2\pi(\Gamma g(w_{p0},N_m)-\alpha_i)}).\left(\frac{G_{s,m}-1}{lnG_{s,m}}\right)\right\} \\ - \frac{2\beta R_r(N_m)n_{g0}}{(\Gamma g(w_{p0},N_m)-\alpha_i)c} \tag{3.31}$$

3.3.4 Output power from the SOA and input power injected into the device

To simplify the comparison between experimental and modelling work it is important to calculate parameters with the model which are easily measured experimentally. The output power and the input power expressed in mW are such parameters, which can readily be compared to experimental data. The output power is expressed in terms of the electric field:

$$P_{out}(t) = \frac{(1-r_2^2)|F_n^+(t,z_n^+)|^2Wd}{2\zeta\Gamma} \tag{3.32}$$

where W represents the active region width and d represents the active layer thickness. A similar expression is used to describe the input power, which is expressed in terms of the injected electric field:

$$P_{in}(t) = \frac{|F_{in}(t)|^2Wd}{2\zeta(1-r_1^2)\Gamma} \tag{3.33}$$

3.3.5 Dynamic model

The model defined up to this point represents the steady-state situation in which a Continuous-Wave (CW) signal was described by using a constant value for $F_{in}(t)$. This CW signal was replaced by an expression for a super-Gaussian pulse, with a pulsewidth in the order of tens of picoseconds. The power in the pulse is given by:

$$P_{pulse} = P_0 \exp\left(\frac{-|t|-T_b/2}{T_b}\right)^{T_b/T_r} \tag{3.34}$$

where P_0 represents the maximum power of the pulse, t represents time, T_b represents the pulsewidth and T_r represents the risetime of the pulse. As already stated the section transit time limits the capability of the model to the description of time-varying phenomena above approximately 0.6 ps. However, in order to obtain as realistic results as possible, the propagation of pulses below 10 ps were not modelled in this work as it has been demonstrated experimentally that below 10 ps the ultra-fast gain dynamics dominate the recovery of the gain. The additional equation to describe the pulse power was the only alteration that needed to be made in order to model pulse propagation in the SOA. The other equations remained unchanged from the steady-state case, as they have already been defined as functions of time.

3.4 Theoretical characterization of the SOA

In the following section a theoretical characterization of the SOA is presented with emphasis on the model described in the previous section. The experimental characterization performed on the Avanex device is used to verify the results obtained using the model. As the exact device parameters were unavailable, estimations for these parameters were used based on models presented in the literature.

3.4.1 Amplified spontaneous emission (ASE)

The spectrum of the ASE found both from the model and experimentally for the Avanex device can be seen in Fig. 3.2, for a bias current of 200 mA. The intensity of both spectrums was normalized in order to facilitate comparison. The 3 dB bandwidth of both spectra was found to be approximately 70 nm. On the long wavelength side of the spectrum there is a very close approximation between the model and the experiment, with nearly identical profiles from 1500 nm to 1700 nm. On the low wavelength side, however, there is an increasingly larger difference between both cases as the wavelength decreases. This variation is due to the parabolic assumption in the band structure taken for the model, discussed in Sec. 2.9.

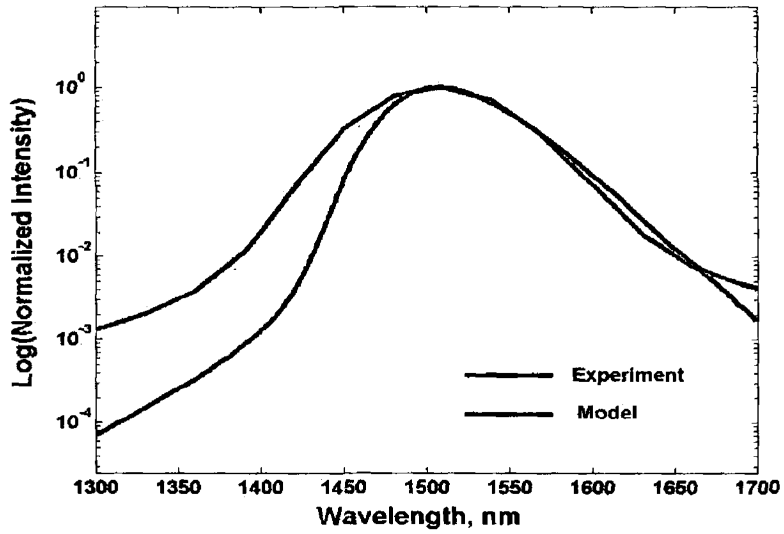

Fig. 3.2: ASE spectrum found for the Avanex device, using both simulated and experimental results.

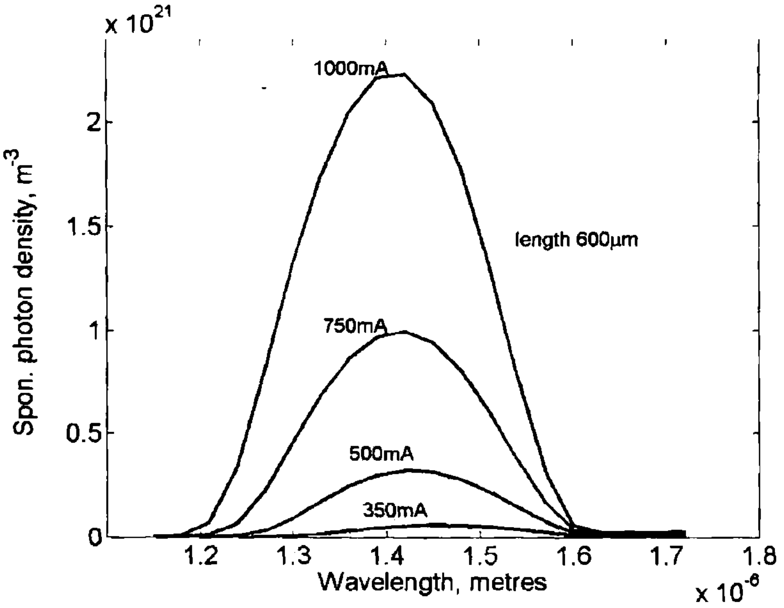

Fig. 3.3: The ASE calculated, as a function of current, using the model.

Fig. 3.3 shows the ASE spectrum as a function of bias current, obtained using the model. It can be seen that there is a shift in the ASE spectrum toward lower wavelength as the bias is increased. This is because increasing the bias causes the carriers to occupy higher energy levels. The resulting recombination causes emission at lower wavelengths. A shift of 60 nm was found as the bias current was increased from 350 mA to 1000 mA. This procedure could not be repeated experimentally because of the high bias currents applied to the SOA, which would damage the device. However a shift in the spectrum, towards lower wavelengths, of approximately 3 nm was measured when the bias current was increased from 350 mA to 500 mA using the Optospeed device, as opposed to a 25 nm shift obtained over the same range using the model. This result confirms that the trend observed in Fig. 3.3 is accurately describing the SOA behaviour. The variation in the magnitude of the shift in wavelength between theory and experiment underlines the qualitative nature of the model. This is due to the mismatch between the real device parameters and those used in the model.

Fig. 3.4 shows the ASE as a function of section number for a range of different active region lengths. The ASE considered in this figure is for the case where there is no optical injection. The current density in the active region is kept constant, at 400 mA/mm, as the active region length is increased so that the impact of varying the device length may be assessed. The ASE has a symmetrical shape because of the equal probability of amplification of a spontaneously emitted photon in either direction. As the device length increases

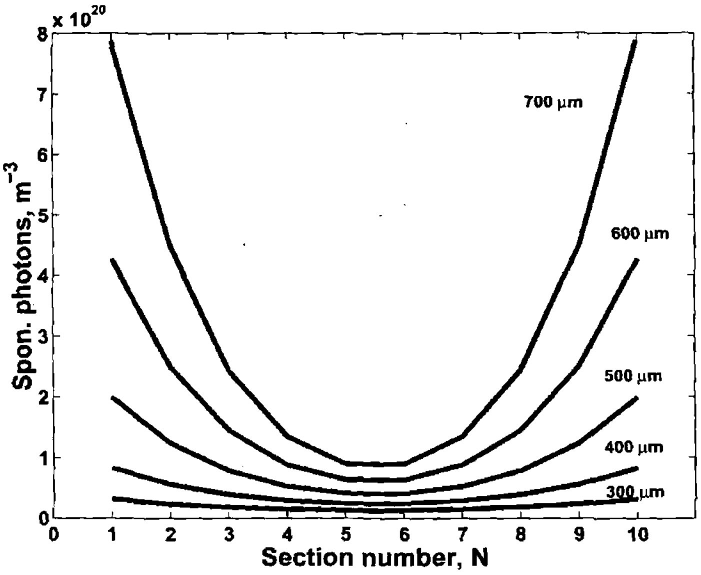

Fig. 3.4: Spontaneous emission distribution in active region for a range of active region lengths, with a constant current density.

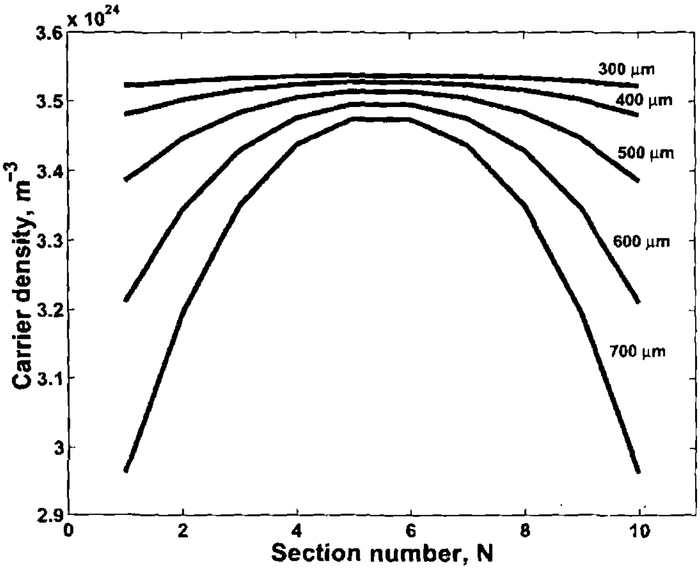

Fig. 3.5: Carrier distribution in active region for a range of active region lengths, with a constant current density.

there are higher levels of ASE at either end of the device. This is expected as the extra length allows additional recombinations to take place. The corresponding effect on the carrier density can be observed in Fig. 3.5. As no optical signal is injected into the device the variation in the carrier density is primarily due to the ASE. For this reason, the carrier density also has a symmetrical profile. As the device length increases the carrier density is reduced because of relationship between carrier density and ASE.

The more amplification that occurs the greater the depletion in the carrier density, due to the fact that amplification of an optical signal in a semiconductor material can only take place at the expense of carriers. This explains why the greater the length is, the greater the level of ASE and the lower the level of carrier density. For example the largest amount of ASE exists for a device of length 700 μm. This also corresponds to the lowest carrier density.

3.4.2 LI curve

The LI curve found using the model is shown in Fig. 3.6. A comparison with the experimentally measured LI curve can be seen in this figure and a good match between the experiment and model can be observed. The results in Fig. 3.6 were taken for the Avanex device. The different slope of the curve for the experimental and theoretical cases is attributed to a mismatch between the recombination rate used in the model and the actual rate. This parameter was unknown for the SOAs under test, so a standard value was used. Furthermore, the parabolic approximation used in the definition of the gain model, defined in Eqn. (3.20), causes a variation between LI curves measured theoretically and experimentally.

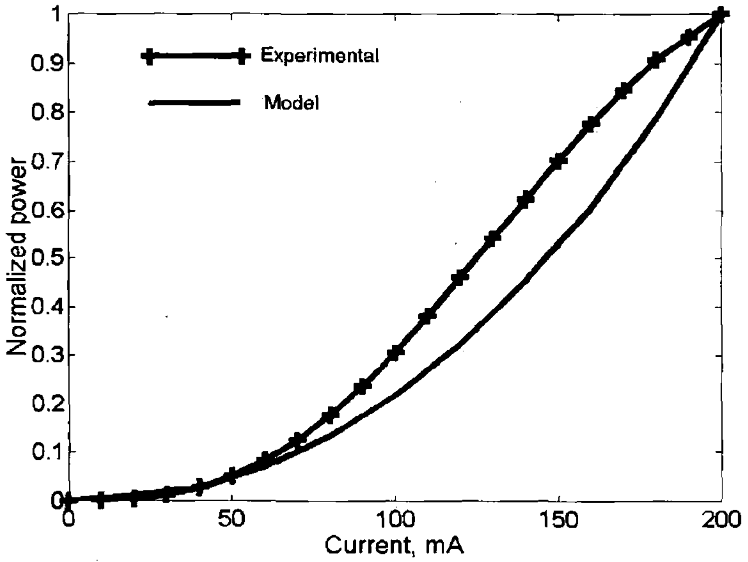

Fig. 3.6: Comparison of the LI curve found both experimentally and theoretically.

3.4.3 Signal gain of the device

A comparison between the experimentally measured and theoretically calculated gain as a function of bias current can be seen in Fig. 3.7. The experimental results were taken using the Avanex device , which was biased at 200 mA. The large difference between the plots is attributed to the fact that the exact device parameters of the SOA under test were unknown. Nonetheless, it can be seen that the behaviour of the simulated SOA is similar to the experimental case.

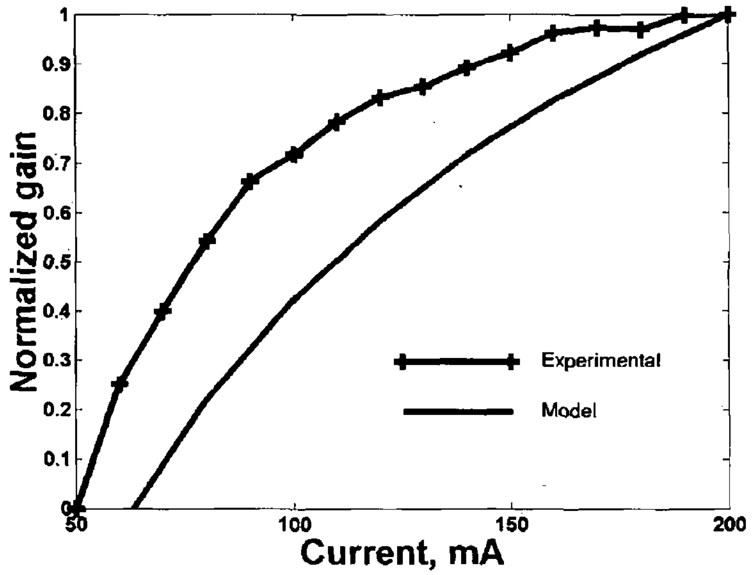

Fig. 3.7: Gain as a function of bias current for -20 dBm signal injection- Theory and experiment.

Fig. 3.8 shows the effect in each section on the carrier density of injecting a CW signal into the SOA. The bias current was set at 500 mA. This effect is presented for a range of injection powers. As already stated the carrier density is smaller at the facets of the device due to the fact that the ASE has reached its largest value due to amplification at this point. Upon injection of an optical signal into the active region of the device there is a shift in the peak of the ASE profile toward the input facet and a large decrease toward the output, due to the fact that the injected signal is amplified, thus increasingly more carriers are depleted towards the output of the device. This leads to a smaller carrier density at the output and because of this there is a reduction in the ASE at this point. This means that the back-propagating ASE is smaller due to its reduced level to start with. This leads to the net intensity of light near the input of the device being lower with injection than is the case when there is no injection. This result is in agreement with previously reported

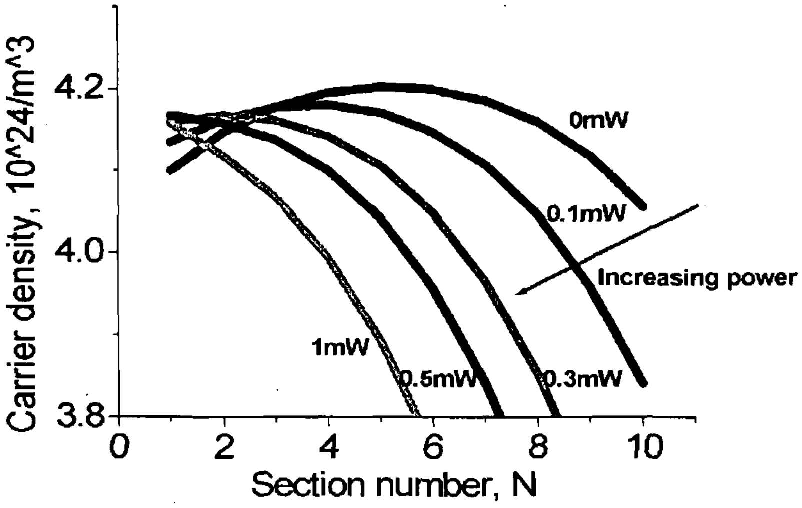

Fig. 3.8: Illustration of the carrier evolution in active region, as a function of injection.

experimental results [24]. From Fig. 3.8 it can be observed that the level of carrier density increases at the input upon injection of light. This continues up the point where 0.5 mW of light is injected. When 1 mW is injected the carrier density again starts to decrease at the input of the device. This level of injection corresponds to the point at which the gain becomes saturated, i.e. the gain is reduced by 3 dB from its small-signal value. This can be seen in Fig. 3.10, for the 500 mA case, which shows the gain saturation calculated using the model with the same parameters.

3.4.4 Gain saturation

The gain saturation was discussed in detail in Sec. 2.5.1. The theoretically calculated gain saturation is shown in Fig. 3.9, where a comparison with the experimental result for the Avanex device can be seen. The device was biased at 200 mA in this case. There is a slight variation between the experimental and theoretical results which is due to both experimental error in measuring the gain and also due to a mismatch between the rate of change of gain with carrier density for both techniques. This results in a small difference in the slope of the gain as a function of input power, for the experimental and theoretical cases.

Fig. 3.10 shows the gain saturation calculated using the model, for a device of length 1.5 mm with similar parameters as the Optospeed device. The gain saturation in this figure is shown for a range of bias currents from 150 mA to 500 mA in steps of 50 mA. The level of

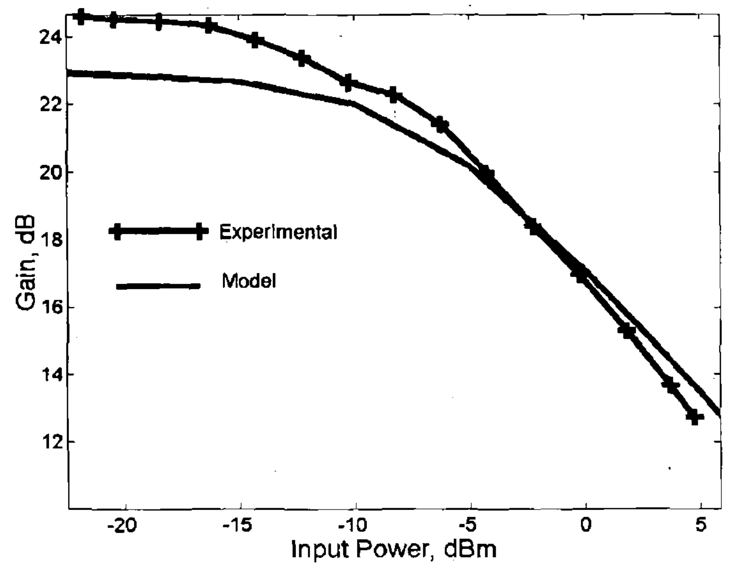

Fig. 3.9: Comparison of the gain saturation found both experimentally and theoretically.

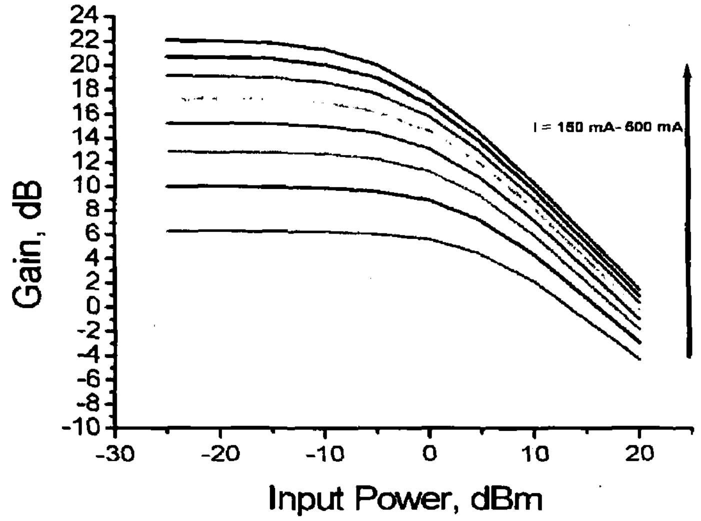

Fig. 3.10: Simulated gain saturation for a range of bias currents.

optical signal required to saturate the device is measured as the input power corresponding to a drop of 3 dB in the gain. From the simulation results shown in Fig. 3.10 it can be seen that the 3 dB gain saturation is a function of the bias current. When the bias current is at 150 mA the gain saturation occurs at an input power of 9 dBm. As the bias current is increased the gain saturation reduces at every increment until it reaches a value of -0.5 dBm at 500 mA. When the bias current is 150 mA the gain in the SOA is low with a value of 6 dB for the small-signal case. This means that a high level of injection is required to deplete enough carriers so that there is a reduction in this gain. As the bias is increased, the gain in the SOA also increases, this results in less optical injection being required to deplete the carrier density. Added to this is the fact that as the bias current increases there is a large increase in the level of ASE in the device. The ASE results in a further depletion of carriers, which also serves to reduce the 3 dB gain saturation point.

3.4.5 *Pulse propagation in the SOA*

The propagation of picosecond super-Gaussian pulses was modelled in each section of the SOA. The model is limited to the measurement of inter-band effects. The calculated power of the pulse in each section is shown in Fig. 3.11. The pulses have an initial pulsewidth of 15 ps. The input power at the peak of these pulses was 1 mW. It should be noted from Fig. 3.9 that this level of injection causes a large suppression of the gain. The evolution of the pulse along the length of the SOA, shown in Fig. 3.11, cannot be measured experimentally. This figure may be used to describe a typical phenomenon that occurs when amplifying high intensity pulses in an SOA. Initially, in the first few sections of the device, the pulse propagating through the SOA has a symmetrical shape, similar to the shape of the injected signal. As the signal continues to be amplified an asymmetry is introduced to the pulse shape. With the increase in section number, m, the rise time of the pulse becomes increasingly shorter than the fall time. This is related to the gain experienced by the leading and falling edges of the pulse. As the optical intensity increases, the gain becomes saturated by the leading edge of the pulse. This means that the leading edge sees the unsaturated gain of the device, but the falling edge sees the gain remaining after it has been depleted by the leading edge of the pulse. This effect causes the pulses to broaden in time. The temporal response of the SOA for high intensity signals is well-established [25], [26].

Table 3.1 shows the rise time and the fall time of the pulse in each section of the SOA for two levels of injected intensity, corresponding to 1 mW and 0.1 mw injection. In the case of 1 mW injected power it can be seen that initially the rise and fall time are within a fraction of a picosecond of each other, but in the last three sections of the device the fall time becomes much larger than the rise time, due to the saturation of the gain in these sections. In the last section of the device the fall time is over 11 ps longer than the rise time. This can be a problem when using SOAs in optical networks, if the injected signal is large enough to deplete the gain of the device. For example if a series of '1's' are being transmitted, the broadening of the pulses may lead to temporal overlap, thus degrading the

	1 mW max. power		0.1 mW max. power	
Section number	Rise time (ps)	Fall time (ps)	Rise time (ps)	Fall time (ps)
1	5.75	5.5	5.75	5.5
2	5.75	5.25	5.75	5.25
3	5.75	5.25	5.25	5.25
4	5.75	5.5	6.5	5.25
5	5.5	5.75	7	5
6	5.25	6.5	7.75	5
7	4.75	9.5	8	5
8	4.75	12.5	8.5	5
9	4.25	14.5	8.25	5
10	4	15.25	7.5	5

Tab. 3.1: Simulated results for rise and fall times of pulses injected into the SOA with a maximum power of 1 mW and 0.1 mW, respectively

operation of the network. The rise and fall times corresponding to the propagation of pulses with an intensity of 0.1 mW is also shown in Table. 3.1. This level of injection is not large enough to deplete the gain of the device, as can be seen from Fig. 3.9. The leading and falling edges of the pulse are subjected to an approximately equal level of gain. The result is that the rise and fall times are very similar as the pulse propagates along the length of the device.

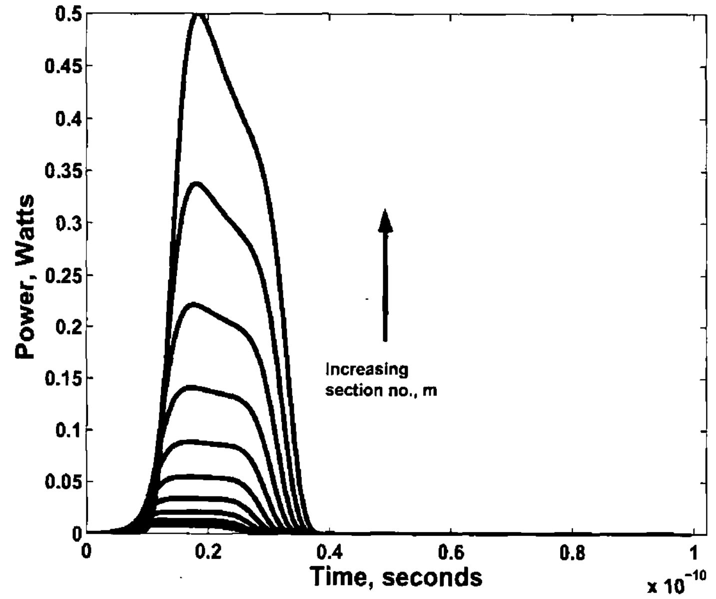

Fig. 3.11: Pulse propagation in each section of the SOA.

A parameter related to the saturation of a device is its carrier recovery time, defined by the speed at which carriers depleted from the conduction band are replenished. This parameter may be calculated from Eqn. (2.22). Fig. 3.12 shows the recovery times corresponding to the pulses amplified in each section shown in Fig. 3.11. A huge variation in recovery time as a function of section number is visible. The recovery time is much longer in the sections at the end of the device, as these are the sections where the carrier depletion is greatest. The recovery time varies from 173 ps in the first section to 450 ps in the last section. These values have a similar magnitude to those previously reported for bulk SOAs [14].

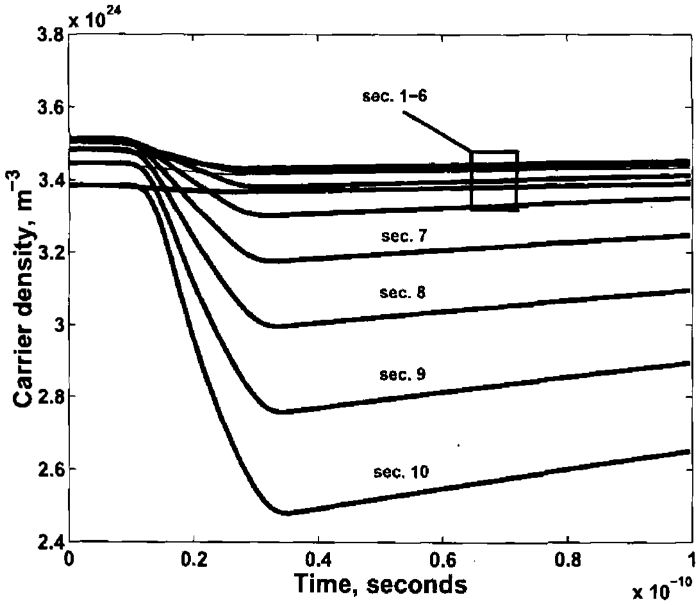

Fig. 3.12: Recovery of the gain in each section of the SOA.

3.4.6 *Self-phase modulation (SPM) in SOAs*

A considerable volume of work has concentrated on the temporal and spectral broadening introduced to pulses after propagation through SOAs [25] - [30]. This broadening is due to the nonlinear effects of gain saturation and SPM, which occur when a signal large enough to significantly deplete the carriers is injected into the SOA, resulting in a suppression of the gain. This results in a corresponding variation in the refractive index, the strength of which is related to the LEF defined in Eqn. (2.23). In this equation $\frac{\partial n}{\partial N}$ represents the variation of the refractive index with respect to carrier density and $\frac{\partial g_m}{\partial N}$ represents the variation of the material gain with respect to carrier density. $\frac{\partial n}{\partial N}$ was assumed to be primarily due to a carrier induced shift of the absorption edge. The contribution from the FCA was also taken into consideration [31]. The calculation of the relationship between $\frac{\partial n}{\partial N}$ and $\frac{\partial g_m}{\partial N}$ was based on the Kramers-Kronig theory.

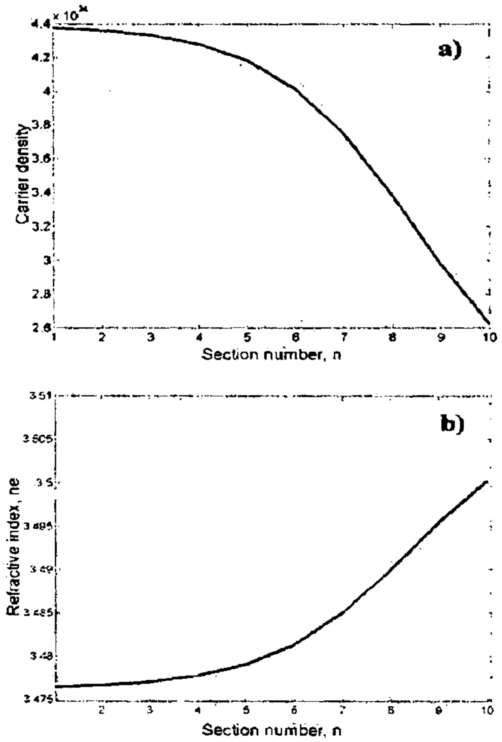

Fig. 3.13: Simulation result illustrating the relationship between a) carrier density depletion and b) refractive index variation.

Simulation results shown in Fig. 3.13 illustrate how the refractive index varies along the length of the SOA as the carrier density is depleted. A LEF of 7.5 was calculated from this simulation, which is within the range typically found for SOA devices [28]. The SPM is defined by the variation in phase induced by the modulation of the refractive index. If a pulse is injected in the linear region of the gain it is possible to amplify the signal without significant distortion of the pulse. The temporal response of the SOA when a high intensity signal is injected has been discussed in section 3.4.6. The spectral broadening introduced due to SPM in an SOA is a more complex effect. This topic has been the subject of a lot of research [27] - [30]. These results reported a shift of the spectrum towards longer wavelengths after injection into an SOA. This result has been attributed to SPM induced negative frequency chirp being introduced to the pulses. The chirp is defined as the instantaneous frequency variation across the pulse, due to SPM, which results in new frequency components contributing to the spectrum. It may be defined using the following expression:

$$\Delta\nu(\tau) = -\frac{1}{2\pi}\frac{\partial\phi}{\partial t} \tag{3.35}$$

Fig. 3.14a) shows a comparison between the chirp profile found both experimentally and theoretically with an intensity of 1 mW injected into the SOA. In this experiment the pulse was measured in both the temporal and spectral domains using the Frequency Resolved Optical Gating (FROG) technique, which is discussed in greater detail in Sec. 6.2.1. The effect on 15 ps gain-switched pulses of propagating through the Avanex SOA was investigated. The pulses were injected into the device with an intensity large enough to bring the gain of the device into the nonlinear regime. The red-shift of the induced chirp can be seen in this figure. Good agreement is found between results. The difference in the shape of the profile, between theory and experiment, is attributed to the difference in the shape of the injected pulses. This may also explain the different magnitudes of the chirp introduced by the SOA. Results have been presented in the literature which demonstrate the dependence of the chirp on the shape of the injected pulses [28]. The shape of the chirp profile shown in Fig. 3.14a) follows the shape of the pulse intensity, but is reflected in the x-axis. This type of profile, introduced by the SOA, has been explained in the literature [27]. The gain is depleted following the integral of the pulse intensity. The refractive index experiences a similar temporal variation to the gain but with an inverse relationship, as shown in Fig. 3.13, thus causing the chirp introduced by the SOA to have an inverse relationship with the pulse intensity.

It has been reported that the spectrum develops a multi-peak structure after propagation through the SOA, due to an interference effect common to nonlinear media [28]. This is related to the same value of instantaneous frequency existing at two points within the profile of a pulse, leading to the possibility of constructive or destructive interference occurring, causing the oscillatory nature of the spectra found in the literature [32]. Simulation results for an unchirped super-Gaussian pulse can be seen in Fig. 3.14b). The signal was injected into an SOA, with a similar specification to the Avanex device, at an intensity of 1 mW. The red-shift of the spectrum as well as the development of a multi-peak structure are clearly visible in the spectrum after the SOA. This figure also shows the spectrum recorded experimentally for a pulse with similar characteristics. Again good agreement between the experimental and simulated spectras is observed. The difference in the magnitude of the ripples in the spectrum may be related to the difference in the chirp profiles shown in Fig. 3.14a). The finite resolution of the OSA used to measure the experimental spectra may also be a factor limiting the comparison.

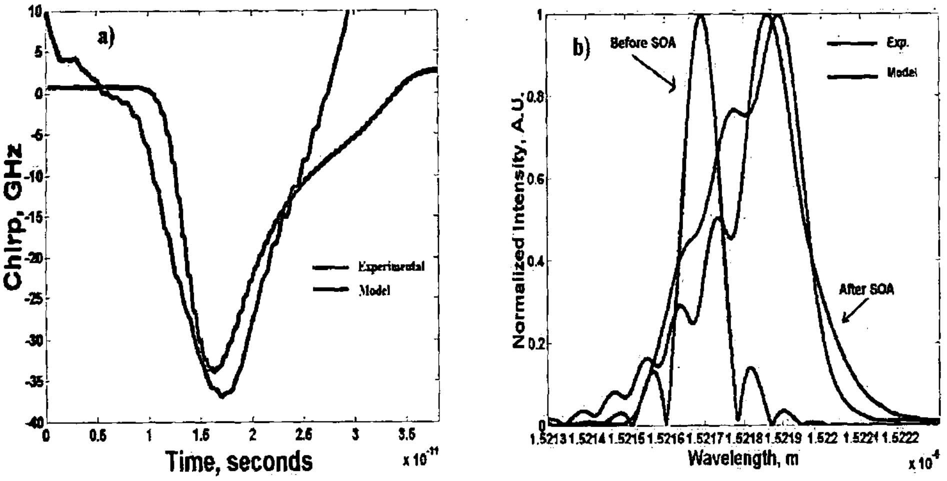

Fig. 3.14: a) Simulated and experimental results illustrating the chirp introduced by the SOA and b) the simulated spectrum before the SOA and the simulated and theoretical spectra after propagation through the device.

3.5 Conclusions

A numerical model was introduced in this chapter, which was based on the plane wave solution of an electric field. The model was developed in order to provide a deeper understanding of the dynamics of the SOA device, thus providing a platform on which the polarization effects of the SOA could be investigated. The SOA active region was divided into a number of sections with constant carrier density in order to develop as accurate a model as possible. The carrier density rate equation was solved in each section of the device. The model was initially developed in the steady-state regime, in order to model the injection of CW signals into the device. The model was then extended to describe the dynamics of pulse propagation in the SOA. A comparison with experimental data was performed in order to validate the accuracy of the model. Good agreement was found. An accurate description of phenomena caused by the inter-band carrier recombinations was determined using the model. In order to model phenomena caused by the intra-band gain dynamics it would be necessary only to replace the gain model described in Eqn. (3.20). Expressions for the gain which are capable of describing these ultra-fast phenomena have been presented in the literature [33], [34], and [35].

The model described in this chapter does not include a Langevin noise term in the travelling-wave equation, unlike other modelling techniques. The Langevin noise term accounts for fluctuations in noise caused by spontaneous emissions. Work has been performed to include this noise term in the travelling-wave equations [36]. This leads to very complex results, to which solutions have yet to be found [37]. For this reason the Langevin noise term was omitted from the model to be presented in this chapter.

The model was also used to describe the propagation of pulses polarized along orthogonal axes of the SOA. These results are presented in Sec. 4.5 of the next chapter. This polarization dependence is limited to the case when the signal is polarized along either axis of the device. A more complete description of the polarization dependence of the SOA could be modelled using an approach similar to [38]. It should be stated that the inaccuracies between results obtained experimentally and theoretically are due to a mismatch between the set of device parameters used in the model and those corresponding to the devices under test. Estimations were used for these parameters, as they were not supplied by the SOA manufacturers. The model presented in this chapter provided a detailed analysis of the SOA, which was necessary before consideration could be given to the NPR in the device. Having established this understanding, the polarization sensitivity of the SOA will be introduced in the next chapter.

BIBLIOGRAPHY

[1] T. Mukai, and Y. Yamamoto. "Noise in AlGaAs semiconductor optical amplifier". *IEEE J. Quantum Electronics*, vol.18(no.4):pp.564–575, 1982.

[2] D. Marcuse. "Computer model of an injection laser amplifier". *IEEE J. Quantum Electronics*, vol.19(no.1):pp.63–73, 1983.

[3] M.J. Adams, J.V. Collins, I.D. Henning. "Analysis of semiconductor laser optical amplifiers". *IEE Proc.*, vol.132(no.1):pp.58–63, 1985.

[4] I.D. Henning, M.J. Adams, and J.V. Collins. "Performance predictions from a new optical amplifier model". *IEEE J. Quantum Electronics*, vol.21(no.6):pp.609–613, 1985.

[5] J. Buus, and R. Plastow. "A theoretical and experimental investigation of Fabry-Perot semiconductor laser amplifiers". *IEEE J. Quantum Electronics*, vol.21(no.6):pp.614–618, 1985.

[6] B. Tromborg, H. Olesen, X. Pan, and S. Saito. "Transmission line description of optical feedback and injection locking for Fabry-Perot and DFB lasers". *IEEE J. Quantum Electronics*, vol.23(no.11):pp.1875–1889, 1987.

[7] A.A.M. Saleh. "Nonlinear models of travelling-wave optical amplifiers". *IEE Electronic Letters*, vol.24(no.14):pp.835–837, 1988.

[8] R.M. Jobson, and T.E. Darcie. "Calculation of multicarrier intermodulation distortion in semiconductor optical amplifiers". *IEE Electronic Letters*; vol.24(no.22):pp.1372–1374, 1988.

[9] L. Gillner, E. Goobar, L. Thylen, and M. Gustavsson. "Semiconductor laser amplifier optimization: An analytical and experimental study". *IEEE J. Quantum Electronics*, vol.25(no.8):pp.1822–1827, 1989.

[10] A.J. Lowery. "Amplified spontaneous emission in semiconductor laser amplifiers: Validity of the transmission-line laser model". *IEE proceedings*, vol.137(no.4):pp.241–247, 1990.

[11] M.J. Connolly, and R.F. O'Dowd. "Theory of signal degradation in semiconductor laser amplifiers with finite facet reflectivities". *IEEE J. Quantum Electronics*, vol.27(no.11):pp.2397–2403, 1991.

[12] T. Durhuus, B. Mikkelsen and K.E. Stubkjaer. "Detailed dynamic model for semiconductor optical amplifiers and their crosstalk and intermodulation distortion". *IEEE J. Lightwave Tech.*, vol.10(no.8):pp.1056–1064, 1992.

[13] L. Gillner. "Comparitive study of some travelling-wave semiconductor laser amplifier models". *IEE Proceedings in Optoelectronics*, vol.139(no.5):pp.339–347, 1992.

[14] S. Ruiz-Moreno, J. Guitart. "Practical method for modelling the nonlinear behaviour of a travelling wave semiconductor optical amplifier". *IEE Proceedings*, vol.140(no.1):pp.39–42, 1993.

[15] C.Y.J. Chu, and H. Ghafouri-Shiraz. "A simple method to determine carrier recombinations in a semiconductor laser optical amplifier". *IEEE Photonics Tech. Letters*, vol.5(no.10):pp.1182–1185, 1993.

[16] P. Brosson. "Analytical model of a semiconductor optical amplifier". *IEEE J. Lightwave Tech.*, vol.12(no.1):pp.49–54, 1994.

[17] M.J. Connolly. "Wideband semiconductor optical amplifier steady-state numerical model". *IEEE J. Quantum Electronics*, vol.37(no.3):pp.439–447, 2001.

[18] D. Cassioli, S. Scotti, and A. Mecozzi. "A time-domain computer simulation of the nonlinear response of semiconductor optical amplifiers". *IEEE J. Quantum Electronics*, vol.36(no.9):pp.1072–1080, 2000.

[19] R. Gutierrez-Castrejon, L. Schares, L. Occhi, G. Guekos. "Modelling and measurement of longitudinal gain dynamics in saturated semiconductor optical amplifiers of different length". *IEEE J. Quantum Electronics*, vol.36(no.12):pp.1476–1484, 2000.

[20] F. Ginovart, and J.C. Simon. "Gain dynamic studies of a semiconductor optical amplifier". *Journal of Optics A: Pure and Applied Optics*, vol.4:pp.283–287, 2002.

[21] F. Ginovart, and J.C. Simon. "Semiconductor optical amplifier length effects on gain dynamics". *Journal of Physics D: Applied Physics*, vol.36:pp.1473–1476, 2003.

[22] A. Bogoni, L. Poti, and A. Bizzi. "Effective model for the design of ultrafast all-optical signal processors based on semiconductor optical amplifiers". *IEEE Photonics Tech. Letters*, vol.15(no.11):pp.1576–1578, 2003.

[23] H. Soto. "Dynamique des amplificateurs optiques a' semi-conducteurs massifs". *PhD Thesis, Paris, France*, page 32, 1994.

[24] J-N. Fehr, M-A. Dupertuis, T.P. Hessler, L. Kappei, D. Marti, F. Salleras, M.S. Nomura, B. Deveaud, J-Y. Emery, and B. Dagens. "Hot phonons and Auger related carrier heating in semiconductor optical amplifiers". *IEEE J. Quantum Electronics*, vol.38(no.6):pp.674–681, 2002.

[25] L.M. Frantz and J.S. Nodvik. "Theory of pulse propagation in a laser amplifier". *J. Appl. Phys.*, vol.34:pp.2346–2349, 1963.

[26] J.P. Wittke and P.J. Warter. "Pulse propagation in a laser amplifier". *J. Appl. Phys.*, vol.35:pp.460–461, 1964.

[27] P.J. Delfyett, H. Shi, S. Gee, I. Nitta, J.C. Connolly, and G.A. Alphonse. "Joint time-frequency measurements of mode-locked semiconductor diode lasers and dynamics using frequency resolved optical gating". *IEEE J. Quantum Electronics*, vol.35(no.4):pp.487–500, 1999.

[28] G.P. Agrawal, and N. A. Olsson. "Self-phase modulation and spectral broadening of optical pulses in semiconductor laser amplifiers". *IEEE J. Quantum Electronics*, vol.25(no.11):pp.2297–2306, 1989.

[29] G.P. Agrawal, and N. A. Olsson. "Amplification and compression of weak picosecond optical pulses by using semiconductor optical amplifiers". *Optics Letters*, vol.14(no.10):pp.500–503, 1989.

[30] N. A. Olsson, and G.P. Agrawal. "Spectral shift and distortion due to self-phase modulation of picosecond pulses in 1.5 μm optical amplifiers". *Appl. Phys. Lett.*, vol.55(no.1):pp.13–15, 1989.

[31] J. Manning, R. Olshansky, C.B. Su. "The carrier-induced index change in AlGaAs and 1.3 μm InGaAsP diode lasers'. *IEEE J. Quantum Electronics*, vol.19(no.10):pp.1525–1530, 1983.

[32] Y.R. Shen. "The principles of nonlinear optics". *Wiley*, pages 325–329, 1984.

[33] J. Mark, J. Mørk. "Subpicosecond gain dynamics in InGaAsP optical amplifiers: Experiment and theory". *Appl. Physics Letters*, vol.61(no.19):pp.2281–2283, 1992.

[34] M.Y. Hong, Y.H. Chang, A. Dienes, J.P. Heritage, and P.J. Delfyett. "Subpicosecond pulse amplification in semiconductor laser amplifiers: Theory and experiments". *IEEE J. Quantum Electronics*, vol.30(no.4):pp.1122–1131, 1994.

[35] J.M. Tang, P.S. Spencer, and K.A. Shore. "Analysis of operating characteristics of TOADs using gain saturation and nonlinear gain in SOAs". *IEE proc. Optoelectronics*, vol.145(no.1):pp.83–87, 1998.

[36] K. Hinton. "Optical carrier linewidth broadening in a travelling wave semiconductor laser amplifier". *IEEE J. Quantum Electronics*, vol.26(no.7):pp.1176–1182, 1990.

[37] H. Ghafouri-Shiraz. "The principles of semiconductor laser diodes and amplifiers". *Imperial College Press*, page 199, 2004.

[38] H.J.S. Dorren, D. Lenstra, Y. Liu, M.T. Hill and G.D. Khoe. "Nonlinear polarization rotation in semiconductor optical amplifiers: Theory and application to all-optical flip-flop memories". *IEEE J. Quantum Electronics*, vol.39(no.1):pp.141–148, 2003.

4. CHARACTERIZATION OF NPR EFFECT IN THE SOA

4.1 Introduction

The nonlinear rotation of the state of polarization of a signal injected into an SOA is examined in this chapter. This effect could potentially be used to perform all-optical signal processing in SOAs. The physical mechanisms behind the effect are detailed as well as the techniques used to remove the polarization dependence in these devices.

The chapter begins with a general description of the polarization of light, which is important to establish before proceeding to the particular case of the polarization of a signal amplified in an SOA. Since SOAs were first studied the issue of polarization dependency has existed [1], [2]. In general, this dependence is unwanted and numerous techniques exist to remove polarization sensitivity in SOAs [3] - [5]. All commercially available devices have been optimized to minimize the polarization dependency. Despite this a large polarization dependency still exists, as shown by the experiments presented in this chapter [6]. These experiments measure the level of polarization dependency as well as examining the physical mechanisms causing the effect. Consistency is found between each independent set of experiments presented. An experiment is also presented which looks at the standard setup used to perform wavelength conversion using NPR, but the focus of this experiment is on examining the exact change in the state of polarization using a polarimeter, in order to gain insight into the polarization dynamics of the effect. These results help in the design of optical switching systems based on NPR in SOAs, as shall be seen in Chapter 5. As NPR is virtually impossible to completely remove, it may be beneficial to try and exploit this effect for all-optical processing applications such as wavelength conversion and demultiplexing. The applications of NPR in all-optical signal processing will be discussed in detail in Chapters 5 and 6. The purpose of this chapter is to introduce the effect and to discuss the physical reasons behind it.

4.2 Polarization

Polarization of light describes the direction the electric field takes as a function of time, i.e. displacement. All light consists of variations in electric and magnetic fields, polarization is the direction of the fields. From Maxwells equations it is known that they are always perpendicular, therefore it is only necessary to know the direction of one field. The convention is that the polarization of light describes the direction of the electric field. The concern of the work presented in this thesis is the polarization of light in a waveguide, i.e. the SOA. In this circumstance a plane wave propagating in the z-direction may be considered. The electric field, which determines the direction of polarization, is orientated in the x-y plane. Generally the amplitude and phase of the components in the x and y planes will be different, this leads to the light tracing an ellipse as it propagates down the waveguide in the z-direction.

The parameters used to determine the state of polarization are the orientation and the ellipticity. The orientation refers to the angle of displacement of the light and may vary from $0^o - 360^o$. The ellipticity refers to how elliptical the shape of the polarized signal is. The ellipticity is determined by the relationship, in terms of intensity and phase, of orthogonal components of the electric field. The ellipticity and orientation are clearly illustrated in Fig. 4.1. The orientation of the ellipse is defined by α. The ellipticity, e, is defined as the ratio of the major axis, A_{max}, of the ellipse to the minor axis, A_{min}:

$$e = \frac{A_{min}}{A_{max}} \tag{4.1}$$

In the figure the orientation is 45° and the ellipticity is 0.375. As already mentioned the state of the ellipse is determined by the relationship between the orthogonal x and y components of the electric field. The two extremes exist when the ellipse degenerates to a line or to a circle, defined by an ellipticity of 1 and 0, respectively. These conditions describe linear and circular polarization.

The plane wave travelling in the z-direction can be described using the following expression:

$$\vec{E} = E_0 e^{i(\omega t - kz + \phi)} \tag{4.2}$$

where E_0 is the complex amplitude, ω is the angular frequency, k is the wavevector, z represents distance and ϕ is the phase. If the propagation of the electric field is considered as being due to the propagation of the x and y components the following expression is obtained:

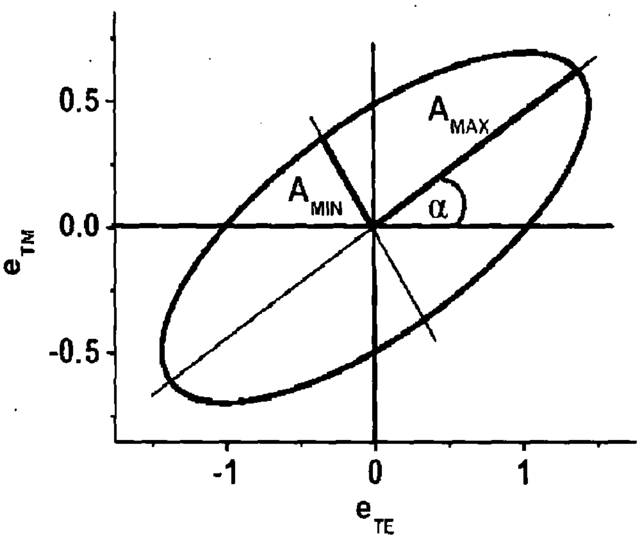

Fig. 4.1: Diagram illustrating the polarization ellipse.

$$\vec{E} = E_{0x}e^{i(\omega t-kz+\phi_1)}\hat{\imath} + E_{0y}e^{i(\omega t-kz+\phi_2)}\hat{\jmath} \tag{4.3}$$

where E_{0x} is the projection of E_0 on $\hat{\imath}$ and E_{0y} is the projection of E_0 on $\hat{\jmath}$. Now considering only the real part of E, expressions for the normalized components of the electric field are found by dividing the electric field by the maximum values, E_{0x} and E_{0y}:

$$\frac{E_x}{E_{0x}} = cos(\omega t - kz + \phi_1) = cos(\omega t - kz)cos(\phi_1) - sin(\omega t - kz)sin(\phi_1) \tag{4.4}$$

$$\frac{E_y}{E_{0y}} = cos(\omega t - kz + \phi_2) = cos(\omega t - kz)cos(\phi_2) - sin(\omega t - kz)sin(\phi_2) \tag{4.5}$$

These unit vectors may be added together to obtain figures known as Lissajous' figures which determine the shape of the ellipse by projecting a circle of diameter E_{0x} onto the x-axis and a circle of diameter E_{0y} onto the y-axis. The contribution of each of these components allows a description of E to be obtained. Although these components have the same frequency, $(\omega t - kz)$, they have different phases, $\delta = \phi_2 - \phi_1$. It is possible to obtain an expression describing the ellipse defined by the Lissajous' figure:

$$(\frac{E_x}{E_{0x}})^2 + (\frac{E_y}{E_{0y}})^2 - (\frac{2E_xE_y}{E_{0x}E_{0y}})cos\delta = sin^2\delta \tag{4.6}$$

This ellipse is called the polarization ellipse. The orientation of the ellipse can be determined from:

$$tan2\alpha = \frac{2E_{0x}E_{0y}cos\delta}{E_{0x}^2 - E_{0y}^2} \tag{4.7}$$

The other parameter used to define the ellipse, the ellipticity may also be determined using the following expression:

$$tan(e) = \frac{E_{0x}sin\alpha_1 sin\alpha - E_{0y}sin\alpha_2 cos\alpha}{E_{0x}cos\alpha_1 cos\alpha + E_{0y}cos\alpha_2 sin\alpha} \tag{4.8}$$

These two parameters allow for complete characterization of a waves polarization. If the case is considered when δ, the phase difference, is equal to 0 or π Eqn. (4.6) becomes:

$$(\frac{E_x}{E_{0x}})^2 + (\frac{E_y}{E_{0y}})^2 - (\frac{2E_xE_y}{E_{0x}E_{0y}}) = 0 \tag{4.9}$$

This results in the ellipse collapsing into a straight line and defines the case of linear polarization. The equation of this straight line is given by:

$$\frac{E_x}{E_{0x}} = \pm\frac{E_y}{E_{0y}} \tag{4.10}$$

Because the polarization is linear. In this situation the orientation parameter, α, is defined by the slope of this line, allowing the expression in Eqn. (4.7) to be calculated for the linear case:

$$tan2\alpha = \frac{2tan\alpha}{1 - tan^2\alpha} = \frac{2E_{0x}E_{0y}}{E_{0x}^2 - E_{0y}^2} \tag{4.11}$$

The expression for the ellipticity from Eqn. (4.8) is equal to 0, for the linear case, which makes sense as there is no ellipse present.

A second case occurs if $E_{0x} = E_{0y} = E_0$ and $\delta = \pm\pi/2$. Eqn. (4.6) can now be expressed as:

$$\frac{(E_x)^2}{E_0} + \frac{(E_y)^2}{E_0} = 1 \tag{4.12}$$

This defines the equation of a circle and for these conditions the ellipse becomes a circle and the displacement of the light traces a circular path. This condition is known as circular polarization. In this case the orientation, α, is indeterminate and the ellipticity is equal to

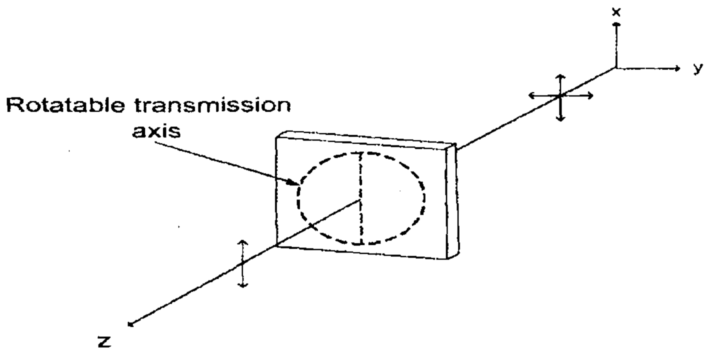

Fig. 4.2: Diagram illustrating the operation of a linear polarizer.

unity. This explanation of circular polarization is incomplete, as the light may be displaced in a clockwise or an anticlockwise direction depending on whether $\delta = \pi/2$ or $\delta = -\pi/2$. If the light is displaced in a clockwise direction it is termed right-circularly polarized light, if the light is displaced in an anticlockwise direction it is termed left-circularly polarized light.

4.3 *Control and measurement of polarization in optical systems*

When talking about polarization in optical systems it is essential to understand the techniques used to control and measure the polarization of a signal. This section introduces several of the components used to control the polarization of signals in optical networks, as well as the polarimeter, which can be used to measure the polarization of a signal.

4.3.1 *Linear polarizer*

A linear polarizer only allows transmission of linear polarized light injected perpendicularly to its axis. The remaining light is absorbed in the polarizer and so is not transmitted. One type of polarizer consists of an elastic sheet containing numerous crystals which absorb the horizontal components but transmit the vertical components. The axis along which the light is transmitted is called the transmission axis. Generally the removal of the undesired components is not 100% efficient so the transmitted light is partially polarized. If the signal field, E, makes an angle of θ with the transmission axis, the transmitted field will have a magnitude $E_T = Ecos\theta$. The intensity of the signal is then given by $I_T = I_0 cos^2\theta$.

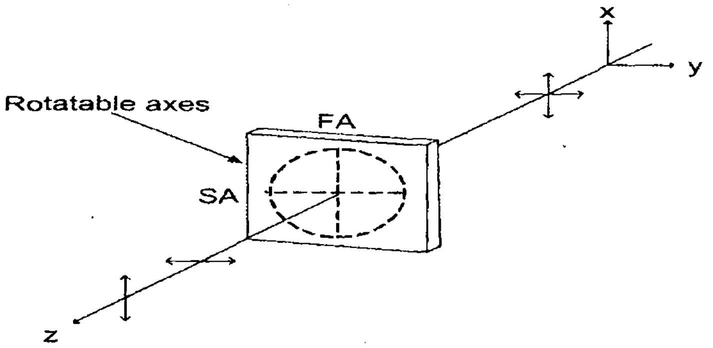

Fig. 4.3: Diagram illustrating the operation of a phase retarder.

4.3.2 Phase retarder

Another optical component which varies the polarization of an injected signal is the phase retarder. Retardance is a measure of the differential phase shift between the eigenmodes, or fast and slow axes, of a signal. This component does not remove any of the light from the signal, instead it introduces a phase difference between orthogonal components. The material used for a phase retarder is a birefringent material that allows one component to travel through the plate faster than the other. When unpolarized light is injected into the plate the amount of birefringence determines the phase difference introduced. If the phase difference is 90° the plate is termed a Quarter-Wave Plate (QWP), when it is 180° it is called a Half-Wave Plate (HWP). The signal should not be injected with an angle of polarization corresponding to the optical axis of the device. In this case no birefringence is induced in the phase retarder material.

4.3.3 Polarization controller

The Polarization Controller (PC) is a component which allows for the control of the state of polarization of light propagating in single-mode fibre. Stress introduced to SMF can cause birefringence in the fibre which is used to induce a phase shift between orthogonal components of the light. The stress in the fibre is caused by looping the fibre into coils. The birefringence is inversely proportional to the square of the diameter of the coil. Control of the diameter and the number of turns allows for the creation of any fiber wave-plate desired. The PCs used in this work were based on a design which contained three loops in a length of optical fibre, where each loop was positioned on a movable paddle [7]. The first paddle consists of one turn and the stress introduced leads to the creation of a QWP. The pressure on the loop was varied by adjusting the position of the paddle thus varying the delay between orthogonal components. This allows the injected signal to be adjusted to have any polarization between the two extremes of linear and circular. The second coil contains two turns and causes the action of a HWP, allowing for a maximum phase shift of 180°. So the orientation of the signal could be controlled with this wave-plate. A second QWP is then required to once again control the ellipticity of the signal after propagation through the HWP. The combination of wave plates allows for complete control of the polarization of a signal simply by adjusting the paddles of each wave-plate. This type of PC cannot be used with multimode or Polarization Maintaining (PM) fibre, only with SMF.

4.3.4 Polarimeter

A polarimeter is a device used to measure the state of polarization of a signal. The measurement is performed by evaluating the Stokes parameters. The Stokes parameters are four real numbers that are related to the intensity of light [8]:

$$\begin{aligned} S_0 &= I_0, \\ S_1 &= I_x - I_y, \\ S_2 &= I_{45^o} - I_{-45^o}, \\ S_3 &= I_{RCP} - I_{LCP} \end{aligned} \tag{4.13}$$

where S_0 represents total intensity, S_1 represents the difference between the horizontally and vertically linear polarized component, S_2 represents the difference in intensity between linearly polarized components of the signal at $+45^o$ and -45^o and S_3 refers to the difference in intensity between left- and right-circularly polarized components. S_0 can be measured directly using a photodetector. Measurement of S_1 and S_2 is straightforward as it only requires a polarizer, and S_3 may be measured using a QWP. Polarimeters generally fall into two categories, those involving either temporal or spatial measurements. In both cases at least 4 measurements are required, one for each of the Stokes parameters. For spatial measurements the injected signal is split along four paths, each beam is passed through the required optics to determine each respective parameter.

The Stokes parameters may be expressed in terms of the parameters of the polarization ellipse, θ and φ:

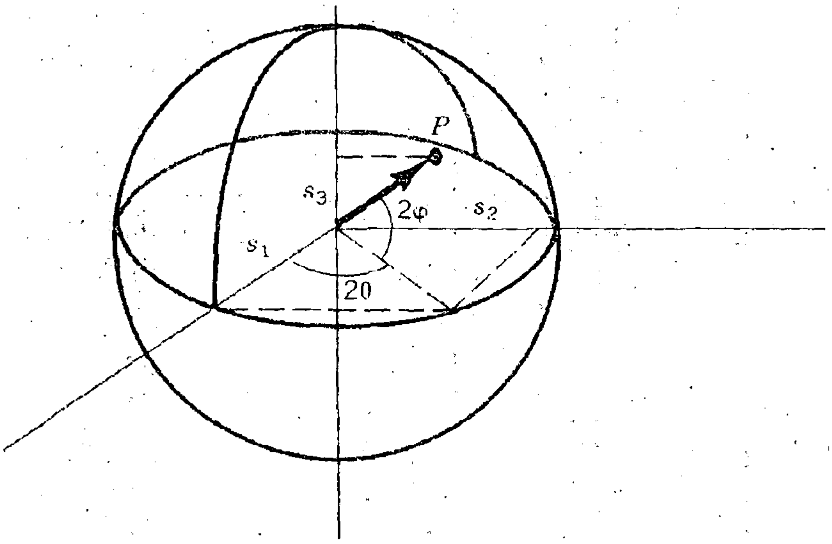

Fig. 4.4: Diagram illustrating the Poincare sphere.

$$\begin{aligned} S_1 &= S_0 cos2\varphi cos2\theta, \\ S_2 &= S_0 cos2\varphi sin2\theta, \\ S_3 &= S_0 sin2\varphi \end{aligned} \tag{4.14}$$

these expressions allow for the polarization to be expressed using the more intuitive parameters of θ and φ. A measurement of the quantity of light in a signal which is polarized can be found using the polarimeter and is called the Degree Of Polarization (DOP):

$$V = \frac{1}{S_0}\sqrt{S_1^2 + S_2^2 + S_3^2} \tag{4.15}$$

One representation of the Stokes parameters often used in a polarimeter is the Poincare sphere, which is illustrated in Fig. 4.4 [9]. In this sphere S_1, S_2, S_3 are coordinates on a sphere of radius S_0. Points on the equator of this sphere represent linearly polarized components, the north and south poles represent right and left circularly polarized light respectively, where the position in the upper and lower hemispheres determines the degree of right and left elliptically polarized states. Completely unpolarized light is represented by the origin whilst 100% polarized light is located on the surface of the sphere. Orthogonally polarized signals are represented by antipodal points on the Poincare sphere.

4.4 Optical axis of the SOA

A polarized optical signal may be decomposed into a TE and a TM component. These two components are perpendicular to each other and are also mutually perpendicular to the propagation axis of the waveguide. They correspond to the propagation axis of the semiconductor waveguide, also called the eigenmodes. The propagation axis defines the input polarization which is maintained after propagation through the device.

4.5 Polarization sensitivity in SOAs

As early as 1988 a technique had been developed to design a polarization insensitive lightwave receiver [1]. This system used two SOAs in order to achieve a polarization-insensitivity of $-29.2dBm$. The need for two SOAs as well as two photodiodes made this setup both expensive and complex. Around this time another scheme was developed to use a single SOA [2]. This technique required a double-pass of a signal through an amplifier. For the second pass the polarization was rotated by 90°, leading to the overall amplification of the signal by an amount equal to the average of the TE and TM gain. Polarization sensitivity was reduced from 4dB to 0.2dB using this technique. Although some success in reducing polarization sensitivity in optical networks employing SOAs was found with these methods, no understanding of the physical mechanisms causing the polarization sensitivity was developed. In the following discussion the key phenomena that are thought to cause a polarization dependent response of the SOA will be discussed.

4.5.1 Asymmetric waveguides

An early publication speculated that the difference in optical mode confinement factors for TE and TM modes was the cause of the signal gain variations along these orthogonal modes [10]. Because TE and TM modes are orthogonal to each other the TE will propagate in the transverse direction whilst the TM will propagate in the lateral direction.

The confinement factor is defined by the following expressions in the transverse and lateral directions [11]:

$$\Gamma_T \cong \frac{D^2}{2+D^2} \tag{4.16}$$

for the transverse direction and

$$\Gamma_L \cong \frac{W^2}{2+W^2} \tag{4.17}$$

for the lateral direction. From these equations it can be seen that in the case where the normalized waveguide thickness, D, is equal to the normalized width, W, i.e. the case of a square waveguide, then the confinement for TE and TM polarized signals is equal causing no polarization dependence of the propagation of a signal through an SOA. However, if the waveguide is rectangular in geometry, as is the case with many commercially available devices, including those under test, then there will be a polarization dependence of the confinement factor and so a polarization dependence of the modal gain of the device, from the equation:

$$G = (\Gamma g_m - \alpha)L \tag{4.18}$$

where Γ represents the confinement factor, g_m represents the material gain, α represents the optical losses and L is the length of the device. A major difficulty in obtaining a square waveguide is that it requires a control of the photolithograhic technology on a sub-micron level. If the waveguide is perfectly square polarization-independent devices can be achieved. These devices, however, have a large far-field divergence, which results in a poor coupling efficiency between the SOA and external optical fibre. A technique developed to improve the coupling is to introduce passive tapered regions, causing a strong confinement in the central active region but less confinement in the tapered region, which leads to an increase in the output mode size thus reducing the far-field divergence, increasing the coupling efficiency. Polarization sensitivity of $< 1dB$ has been achieved using this technique [3].

Another significant type of polarization dependence introduced to an SOA with an asymmetric waveguide is due to the birefringence introduced to the device. This asymmetry causes two propagation constants to exist corresponding to the orthogonal TE and TM modes. The effective refractive indices typically differ by 2×10^{-2} [12]. The difference in refractive index causes the TE and TM modes to propagate through the device at different speeds causing a phase difference to be introduced between the signals. An index difference as small as 2×10^{-4} has been reported as being sufficiently high to induce a phase shift between the TE/TM modes of $\pi/2$ [13]. Many of the initial publications based on NPR justified the effect as being solely due to the asymmetric waveguide [13] - [15]. These papers also report an increase in the NPR due to birefringence as a function of injected power in the SOA. This modulation of the refractive index through modulation of the gain of the device is defined by the SPM [16] and is quantified using the LEF [17].

Simulations were performed in order to demonstrate the effect on the propagation of 15 ps pulses of an asymmetric waveguide in a bulk unstrained SOA. This effect was modelled by introducing a polarization dependence to the confinement factor and refractive index.

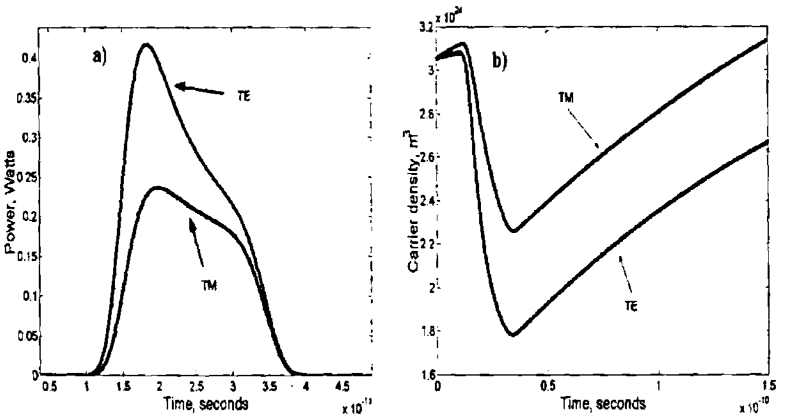

Fig. 4.5: Simulated results showing the polarization dependence of a) gain and b) recovery time in a bulk SOA.

The confinement along the TE axis was 0.31 whilst along the TM axis the confinement factor was 0.26. This difference of 0.05 is similar to the difference used by other groups in modelling NPR [18]. A refractive index difference of 8×10^{-2} was also modelled, with an index value of 3.5 along the TE mode and 3.42 along the TM mode. This magnitude of polarization dependent refractive index is justified from experimental measurements of this effect [6]. The propagation of two independent signals polarized along the TE and TM axes of the device were simulated. The intensity of the injected signal was 1 mW in each case. The polarization dependence of the amplified signal, introduced due to the asymmetric waveguide can be seen in Fig. 4.5a). The higher confinement along the TE axis leads to a larger amplification of the signal. This larger gain along the TE axis also leads to a larger asymmetry in the pulse due to the rising edge of the pulse experiencing a larger gain than the falling edge. The larger TE gain causes a larger depletion of the carriers that in turn leads to a longer recovery time for the signal polarized along the TE axis. This can be seen in Fig. 4.5b). The recovery time, at the output of the device, for the TE polarized signal was measured as 447 ps, whilst the recovery time for the TM polarized signal was measured as 324 ps.

The polarization dependence of the gain leads to a polarization dependence of the chirp introduced to the signal after propagation through the SOA. The relationship between the gain and the chirp was discussed in Sec. 3.4.6. The chirp is shown in Fig. 4.6a). The larger TE gain leads to a larger phase shift for light aligned with this axis, causing a larger magnitude of chirp to be introduced for the TE polarized signal. The magnitude of the chirp is similar to previously reported experimental measurements [19]. As expected the SOA induced chirp is predominantly red-shifted. The polarization dependence of the spectrum,

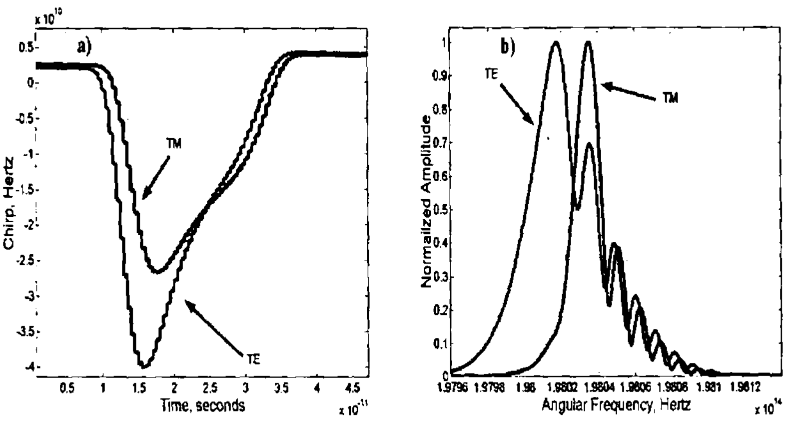

Fig. 4.6: Simulated results showing the polarization dependence of a) chirp and b) spectrum in a bulk SOA.

introduced due to the chirp can be seen in Fig. 4.6b). In this figure the effect of the larger negative frequency components introduced to the TE mode can be seen as the TE spectrum undergoes a larger shift towards lower frequencies than the TM spectrum. The ripples on the high frequency section of the spectrum, introduced due to interference effects, also receive a larger shift towards lower frequencies for the TE mode. This is because of interference occuring at larger magnitudes of instantaneous frequency variations, i.e. chirp, for light polarized along this axis.

4.5.2 Polarization dependence of gain dynamics

Because of the fact that the overall device gain is generally larger for the case of TE polarization, due to the difficulties in designing a completely square waveguide [3], a technique generally used is to introduce tensile strain to enhance the LH transitions, and therefore the TM transitions, in order to minimize the variation in gain between TE and TM axes. In this way the TM gain is increased to a level where it compensates for the higher TE gain. This balancing of the gains can be understood by considering the following expression [4]:

$$\Delta G_{TE-TM}(dB) = (1 - (\Gamma_{TM}/\Gamma_{TE})(g_{TM}/g_{TE}))G_{TE}(dB) \tag{4.19}$$

where G represents the modal gain, Γ represents the confinement factor and g represents the material gain. From this expression it is clear that increasing g_{TM} over g_{TE} can compensate for the larger confinement along the TE axis. Polarization sensitivity as low as 0.3 dB has been achieved for a strain value of $\approx$0.15% [5]. This is effective and although complete polarization insensitivity has never been achieved, it is an effective technique in compensating for the higher TE gain. It should be noted that the measurements performed to test this technique, from the literature, only consider the static steady-state gain and not the dynamic gain processes, which are governed by the material gain. It is not possible, using tensile strain, to achieve polarization independence of both the device gain and the material gain.

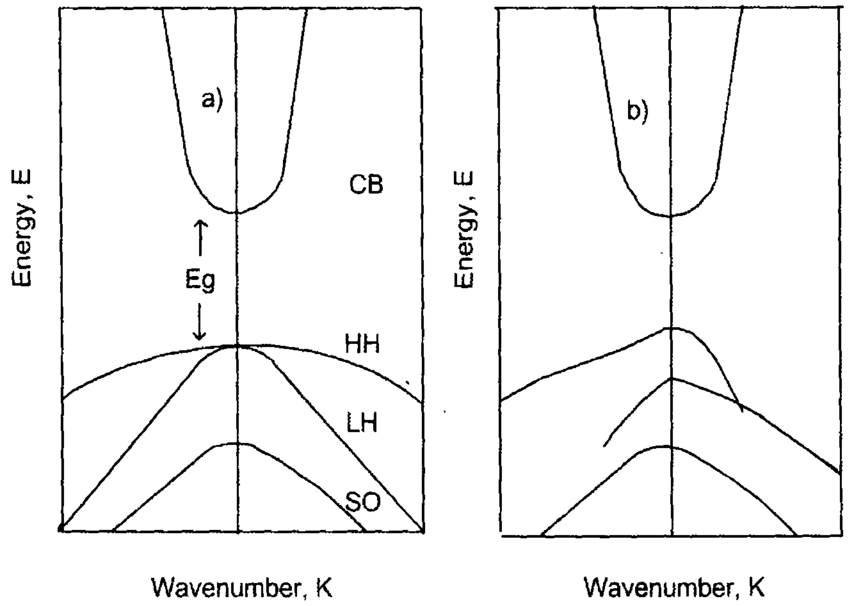

Fig. 4.7: Band structure for a) unstrained and b) tensile strained semiconductor material.

The reason for a polarization dependence of the dynamic gain processes in the SOA originates in the band structure. For the case of an unstrained waveguide there is complete symmetry in the material gain of the device and there is no polarization dependence of the material gain. This situation is represented in Fig. 4.7a). The valence band may be sub-divided into a HH band and a LH band, where the TE transitions predominantly occur with the HHs and the TM transitions occur predominantly with the LH [18]. The effect of introducing a tensile strain to the device is shown in Fig. 4.7b). In terms of the gain dynamics in the device, the situation under tensile strain is that there are effectively two material gains in the device which couple to two different reservoirs of holes. This is due to the degeneracy being removed from the valence band. The result is that there are also two different gain dynamics in the device, with different timescales associated with each. A polarization dependency may be expected due to the mixing of the two gain dynamics. If a signal is injected off-axis, i.e. with a combination of TE and TM light then the amount of light which couples to each mode will determine the overall time constant associated with each process.

The application of tensile strain is also beneficial in SOAs for a second reason. This strain leads to a large reduction in the threshold current for a semiconductor laser and reduces the bias current required to obtain a given gain in an SOA. This is due to the broad energy bands in semiconductor devices. For the unstrained case, the conduction band has a low effective mass, m_c, whilst the valence band has a large effective mass, m_h. As carriers are injected into the device, this causes the quasi-Fermi level for holes, F_v, to move down into the valence band at a much slower rate than the quasi-Fermi level for electrons, F_c, moves upwards in the conduction band. The transparency condition is reached when these quasi-Fermi levels are separated by more than the band-gap energy [20]. This situation is depicted in Fig. 4.8a) [21]. The carriers in the conduction band occupy a large range of energies in this case, however the carriers that contribute to the amplification of an injected signal have a narrow range of energies, therefore only a small percentage of the excited carriers can contribute to the amplification of the signal. Furthermore, these higher energy carriers that cannot contribute to the amplification process can, however, contribute to the nonradiative loss processes such as spontaneous emission which also reduces the efficiency of the device. The situation in the valence band is that due to the high effective mass, the valence band states are almost completely full.

When strain is applied to the device the degeneracy of the HH and LH bands are removed,

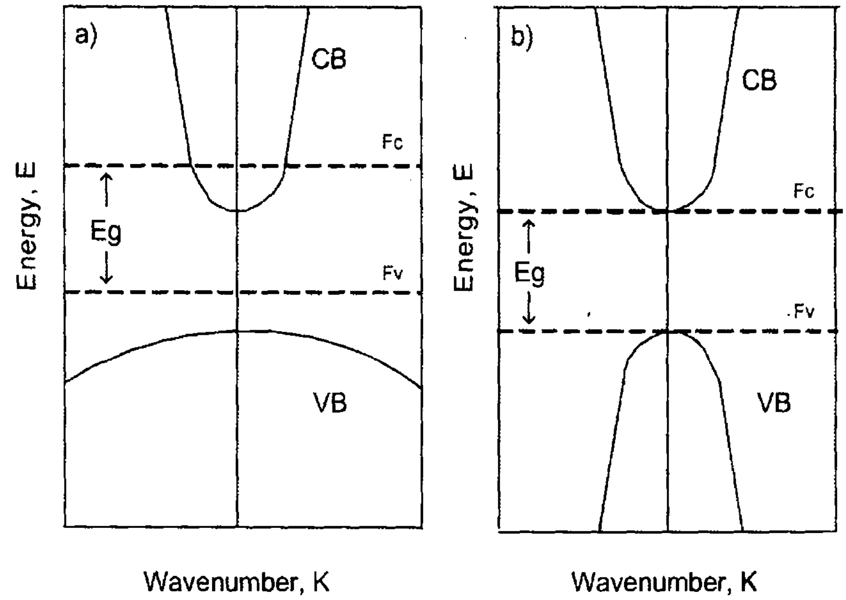

Fig. 4.8: Transparency due to conduction band and valence band effective masses in the a) unstrained and b) strained cases.

and a large reduction in the hole mass can result, leading to a balance between conduction band and valence band effective masses. This can result in the transparency being reached at the same energy in the conduction and valence bands and the higher level energy states in the conduction band not being occupied at this transparency point, whilst at the same time the valence band is not full [22]. This vastly reduces the required bias current and reduces the rate of non-radiative recombination. This is illustrated in Fig. 4.8b).

A recent publication has shown experimental results that eliminate the confinement factor as being the primary cause of polarization dependence in bulk SOAs [23]. This group observed a discrepancy with this theory in the case where the bias current was varied. Instead they suggest a gain anistrophy due to an inherent stress introduced due to the heterostructure nature of the device.

4.5.3 Modification of the waveguide axis

The studies of one group point to a modification of the eigenmodes of the device as being a cause of NPR in the SOA [13], [24]. This modification of the waveguide is brought about by a high intensity signal injected into the device causing a nonlinear birefringent effect. It was noticed that the TE and TM eigenmodes of the device at low injection powers were no longer the eigenmodes when the power was increased to high intensity values. One simple experiment used to test this waveguide modification experimentally involved injecting a single TE or TM signal into an SOA device and observing if there is any variation in the polarization of the signal at the output of the device as the intensity of the signal is increased.

4.5.4 Anti-reflection (AR) coatings

AR coatings are generally polarization dependent, with reflectivity varying along orthogonal TE and TM modes. This was considered the main cause of polarization dependence in early SOA devices [25]. A polarization dependence as high as 10 dB was measured in this work. This soon led to the development of polarization-insensitive AR coatings based on multi-layer coatings [26]. With these multi-layer coatings it was possible to achieve reflectivity below 10^{-4} for both TE and TM directions over a wavelength range of 100 nm. The AR coating has thus been minimized as a large factor determining polarization sensitivity in the SOA, some degree of sensitivity still remains though and this point should be noted. Measurement techniques exist to determine the reflectivity from the end facets, but these techniques involve measurements both prior to and after the application of the anti-reflection coating [27], [28]. The devices under test in this work were purchased commercially, therefore it was not possible to perform measurements prior to the application of the coating.

4.6 *Experiment to determine polarization dependence of SOA*

Several novel techniques to examine the cause of the NPR effect in the SOA under test, i.e. the Optospeed device, are presented in this chapter. The experiments presented in this section are broken into two parts. Firstly experiments were performed in the absence of a signal being injected into the SOA, in order to obtain information about the inherent linear polarization rotation due to the design of the SOA. These experiments were based on analysis of the ASE spectrum of the device. Secondly, the nonlinear rotation in the state of polarization was examined by injecting an optical signal into the SOA. The overall NPR is a combination of both linear and nonlinear rotations in the state of polarization. In all experiments discussed in this section, the Optospeed device was the SOA under test. The device had a bias current between 300 mA and 450 mA and was temperature controlled by means of a Peltier cooler at 20°C.

The experiments were performed in free space in order that complete control of the polarization was maintained. It is not possible to control accurately and, just as importantly, to know exactly the angle of polarization when using SMF. Many groups use SMF taped in position so that the polarization is fixed. The major disadvantage of this technique is that the exact angle of polarization is unknown making the repeatability of experiments difficult as the same angle of polarization cannot be reproduced easily. The second disadvantage is that if the fibre happens to move at any position in the system then the polarization will fluctuate due to the movement of the fibre, further degrading results. Another option is to use PM fibre, whereby the polarization is maintained along the axis of the fibre. In order to obtain any benefit from using PM fibre the whole system needs to use PM fibre, any SMF in the system would result in the loss of control of the polarization, thus removing the benefit of the PM fibre in the first place. It was impossible to design a system with the available equipment that exclusively used PM fibre, due to many of the commercially designed optical components in use being pigtailed to SMF.

4.6.1 *Polarization dependent gain in SOA without injection*

The experimental setup used to measure the polarization dependence of the gain and birefringence without injection is shown in Fig. 4.9. The ASE at the output of the device was collected by a 0.25 Numerical Aperture (NA) AR coated microscope objective. At 400 mA an ASE intensity of 2.8 mW was found experimentally, compared with an intensity of

7 mW recorded by the manufacturer at the same bias current, thus indicating a coupling efficiency of 40% using the microscope objective lenses.

After the ASE was collected by the microscope objectives, the light was passed through a Polarizing Beam Polarizer (PBS) with an extinction ratio of 50 dB. The PBS was aligned along the optical axes of the device. In this way it was possible to obtain polarization resolved ASE spectra using an OSA with a resolution of 0.07 nm. The eigenmodes are referred to as TE (horizontal) and TM (vertical) for all the experiments discussed in this thesis, not only the experiments presented in this chapter.

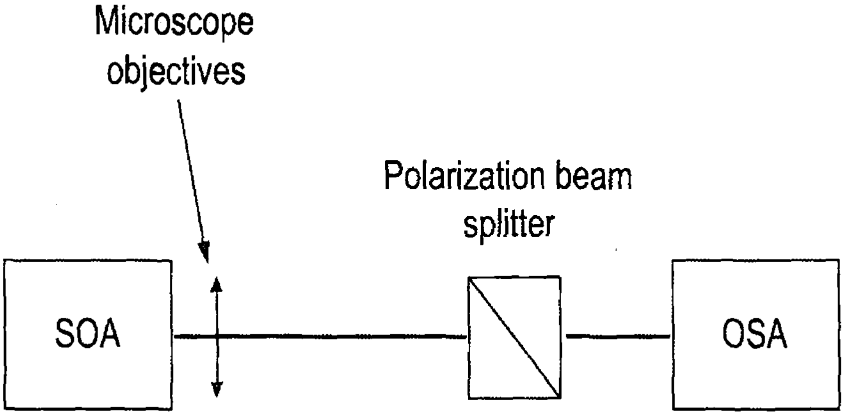

Fig. 4.9: Experimental setup used to measure the polarization dependent ASE spectrum.

Firstly it was desirable to calculate the single-mode gain along orthogonal modes of the SOA in order to observe if there were any discrepancies between the gain along the TE mode and the gain along the TM mode. As discussed in section 4.5.1, due to waveguide asymmetry the single-pass gain will generally be polarization dependent [14].

The polarization resolved single-pass gain was calculated using the ASE spectrum. In an ideal TW-SOA, the ASE spectrum is completely smooth and there is no noise or ripples on the spectrum. From observation of Fig. 4.10 it is obvious that there were ripples in the spectrum of the device under test. These ripples are caused by spurious reflections from the end facets of an SOA, even after the application of the AR coating and after tilting the active region with respect to the end mirrors. The reflections are typically below 10^{-4} [29] but are sufficient to induce interference between the forward propagating and weak backward propagating signals. The ripples originate because the SOA comprises a FP etalon. Whether the interference is constructive or destructive determines whether a maximum or minimum of the ripple results. If the reflectivities were further reduced the ripples would also be reduced.

The presence of these ripples allowed parameters associated with the SOA to be deter-

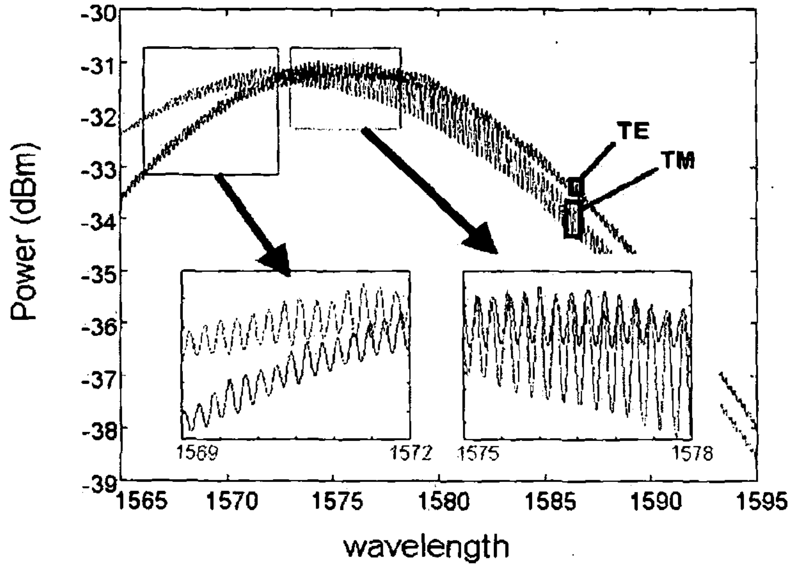

Fig. 4.10: Polarization resolved ASE spectra for the device under test and, inset, a close up of the Fabry-Perot gain ripples.

mined. The wavelength dependence of the gain was determined from the FP ripples in the ASE spectrum. The relationship between the depth of modulation of the FP ripples and the single-pass gain of the device has received considerable attention [28], [30] and [31]. The depth of modulation of the ripples, r, was defined as the average between two consecutive peaks, $\frac{1}{2}(P_i + P_{i+1})$, divided by the valley, V_i, which lies between them, yielding the following equation:

$$r_i = \frac{P_i + P_{i+1}}{2V_i} \tag{4.20}$$

The gain-reflectivity spectrum, γ, was then obtained using the formula [28]:

$$\gamma(\lambda) = \frac{\sqrt{r(\lambda)} - 1}{\sqrt{r(\lambda)} + 1} \tag{4.21}$$

The gain-reflectivity spectrum may also linked to the single-pass gain of the SOA through the following expression:

$$\gamma = \sqrt{R_1(\lambda)R_2(\lambda)}G(\lambda) \tag{4.22}$$

where R_1 and R_2 are the reflectivities of the end facets of the SOA. For the purpose of this study it was assumed that the reflectivities were equal and constant over the wavelength range used for this experiment in the same manner as in the literature [32]. The gain-reflectivity spectrum was calculated over a large spectral range, resulting in the possibility of calculating the gain over a large spectral range as well. As the ASE spectra were polarization resolved, it was possible to obtain the polarization resolved single-pass gain, using Eqns. (4.20)-(4.22). These ASE spectra can be seen in Fig. 4.10.

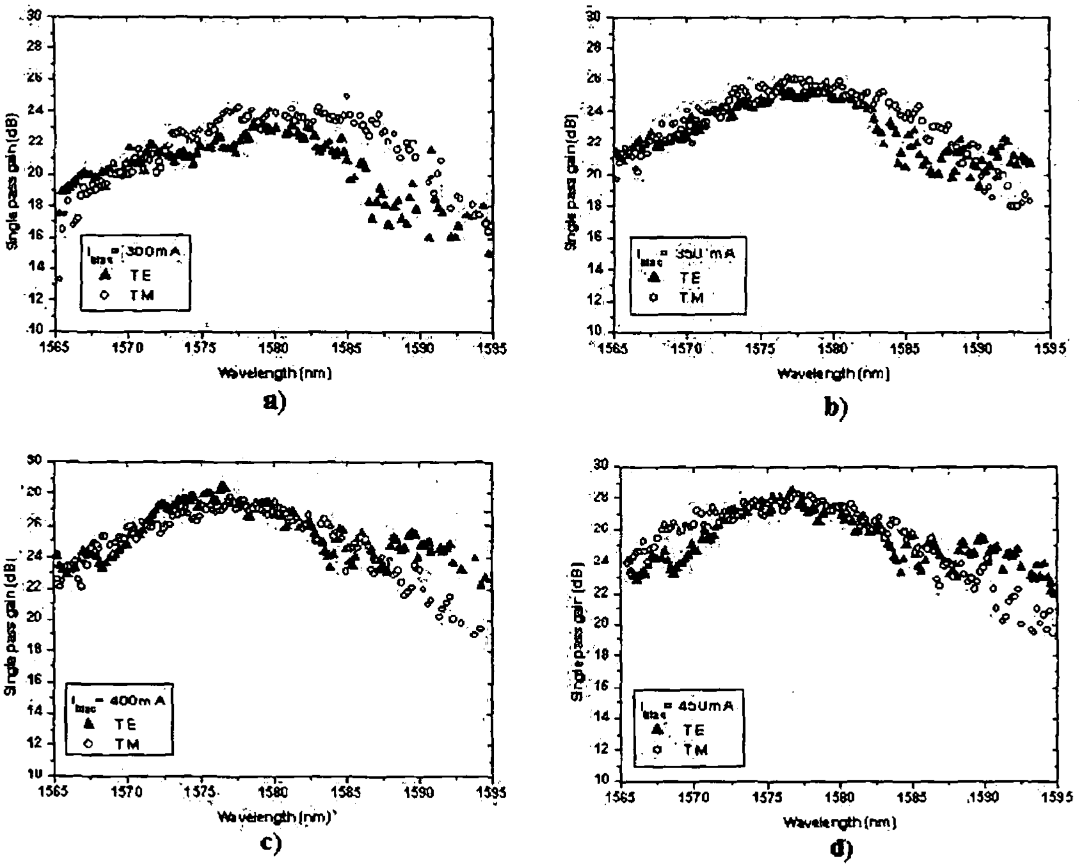

a)

b)

c)

d)

Fig. 4.11: Polarization resolved gain spectra for a) I = 300 mA, b) 350 mA, c) I = 400 mA, d) I = 450 mA.

A close-up of the FP ripples can be observed in the inset of Fig. 4.10. The ripples may be studied as a function of bias current also. However, in this study the results were limited to a bias current above 300 mA because the reflectivities were so low, due to the application of AR coatings and waveguide tilting, that the ripples were very weak below this current. Fig. 4.11 shows the TE and TM single-pass gain calculated using the polarization resolved ASE spectra. The gain was calculated at bias currents of 300 mA, 350 mA, 400 mA and 450 mA over the spectral range from 1565 nm to 1595 nm. It can also be seen that as the bias current increased the gain also increased along both modes, with a levelling off of the gain apparent at 450 mA. From Fig. 4.11 the maximum single-pass gain along the TE mode and the maximum single-pass gain along the TM mode are approximately equal. There is evidence of a small dip in the TE gain spectra at 1585 nm. This arises because of a decrease in the ripple modulation depth, possibly due to a imperfect AR coating, which later recovers. It should be noted for later reference that the TE and TM gains at 1580 nm under bias of 400 mA are equal within error of the graph, and that the spectra obtained here are dependent on the value of the reflectivity. A change in these parameters would lead to a vertical shift in the spectra obtained, but would not change their profile. The peak gain at each bias current is in agreement with the single-pass gain measured.

4.6.2 *Nonlinear birefringence in SOA without injection*

The second main cause of NPR in SOAs is birefringence. In fact originally it was put forward as the primary cause of NPR due to the asymmetric nature of the SOA waveguide [12], [14] and [15]. Birefringence results in orthogonal signals in the device propagating at different speeds. There are two refractive indices in the device along the TE and the TM modes, respectively. The FP modulation ripples from the polarization resolved ASE spectrum were used once again, in order to calculate the refractive indices along orthogonal modes. The principle behind this calculation is that if the signals are travelling at different speeds then the periods of the ripples will be different, because the period is related to the round-trip time in the cavity. The result is that the ripples along orthogonal modes come in and out of phase with respect to each other due to the small difference in the periods of the ripples [33]. This effect can be seen from observation of the inset of Fig. 4.10.

In the first case, between 1569 nm and 1572 nm the ripples are out of phase with each other, with a maximum along the TE mode corresponding to a minimum along the TM mode. However, between 1575 nm and 1578 nm the ripples are in phase. This proves that there are indeed different refractive indices in this device and that there must be birefringence in the device. As already stated, the same ASE spectra used to calculate the polarization dependent gain were used to calculate the polarization resolved refractive index. In order to do this the definition of the FSR in a FP resonator was used to calculate the refractive index for both modes:

$$\Delta\lambda = \frac{2n_{g,eff}L}{k} - \frac{2n_{g,eff}L}{k+1} = \frac{2n_{g,eff}L}{k(k+1)} \approx \frac{\lambda^2}{2n_{g,eff}L} \qquad (4.23)$$

where λ is the wavelength, $n_{g,eff}$ is the effective group refractive index, L is the length of the device and k is the wavevector. From this expression it was possible to extract $n_{g,eff}$ as a function of wavelength. $\Delta\lambda$ was calculated as the wavelength separation from trough-to-trough. λ was taken as the central wavelength in each calculation. Using this technique a refractive index was calculated for each central wavelength. The TE effective refractive index was found to be 4.03 whilst the TM mode effective refractive index was found to be 3.95. These results were obtained by averaging the effective refractive index values for each mode over the wavelength range from 1560 nm to 1590 nm. The results obtained here verify experimentally that birefringence is indeed present in the device under test. The values of the refractive index found correspond well with previously documented results [34].

As well as determining the birefringence in the device, attempts were made to extract the dispersion parameter for each mode using the following expression [34]:

$$n_{g,eff} = n_{eff} - \lambda\frac{\partial n}{\partial\lambda} \tag{4.24}$$

where $n_{g,eff}$ corresponds to the refractive index determined using the FSR, n_{eff} is the wavelength independent effective refractive index and $\partial n/\partial\lambda$ is the dispersive term to be determined. However, the scatter of the refractive index data was too large to extract any reliable data.

4.6.3 *Polarization dependent gain and nonlinear birefringence in SOA with injection*

In the previous section experimental techniques were presented to determine the polarization rotation originating from the design of the waveguide, i.e. in the absence of an injected signal. These experiments provided valuable information on the origin of the NPR effect but from a practical point of view their relevance is limited. In general terms an SOA is operated in a system by injecting an external signal into the device. The experiment to be presented in this section outlines a technique to measure both the polarization dependent gain and the nonlinear birefringence in the case when a signal is injected into the device. Again the experiment was performed in a CW setup. The output state of polarization of the signal was examined as a function of input polarization and intensity of the injected signal. Most of the reports on NPR to date use a pump-probe setup where the polarization of the probe is controlled by a high intensity pump signal injected either in co- or contra-propagation [12] - [15], [18] and [35]. The experiment presented in this section did not operate in a pump-probe setup. There was only one signal injected into the device. This technique has been termed Self-Induced Polarization Rotation (SPR), and can be found in the literature [36]. However, regardless of whether a SPR or a pump-probe setup is used

the physics determining the rotation of the state of polarization are the same.
The setup used for this experiment is shown in Fig. 4.12. In a similar manner to the experiment presented in the previous section, the experiment is performed in free space in order to allow easy and more effective control of the state of polarization. The signal injected into the SOA was provided by a HP8168F tunable laser source. Several components were required in order to control the polarization of the free-space signal. Firstly, a polarizer was used to ensure that the signal from the tunable laser was linearly polarized prior to injection into the SOA device. As well as having a linearly polarized signal it was desired to rotate the angle of linearly polarized light and for this reason a HWP was used. Lastly, a QWP was used in order to compensate for the mismatch between the operating wavelength of the laser and the operating wavelength of the plates. After this series of plates, the optical signal was launched into the SOA via a 0.25 NA AR microscope objective. As explained in the previous section a coupling efficiency of 40% was estimated. The launching conditions were optimized using the two mirrors and the micro-control lens mount. A Band-Pass Filter (BPF) centred at 1580 nm with a bandwidth of 10 nm was placed in front of the polarimeter in order to reduce the randomly polarized ASE injected into the polarimeter, thus improving the accuracy in the measurement of the polarization of the injected signal. The polarimeter operates by measuring the Stokes parameters and converting them to ellipticity and orientation, which are the parameters displayed on the polarimeter. An ellipticty of zero corressponds to a a linear polarization. An ellipticity of -1 corressponds to a circular polarization, the negative sign is a convention to define left-handed rotation, which defines the direction, clockwise or anti-clockwise, in which the circularly polarized light is rotating.

Fig. 4.13 shows a plot of the ellipticity of the output signal plotted against the orientation of the injected signal. The device was biased at 350 mA for this measurement. The wavelength of the injected signal was 1580 nm, this wavelength was chosen as it corresponds to the peak gain wavelength, of both TE and TM modes, measured in the experiment with no injection, as shown in Fig. 4.11. The output ellipticity was recorded for several different values of injected power. These values were 83.3 μW, 166 μW, 208 μW and 413 μW. This was the optical power of the signal generated by the tunable laser cavity. If a coupling efficiency of 40% is assumed, as was justified already, then the actual optical power injected into the SOA was 33.3 μW, 66.4 μW, 83.2 μW and 165.2 μW. Initally when the input orientation is 0^o, the ellipticity is 0, indicating that the light is linearly polarized and that 0^o is an axis of the device. As the input orientation increases there is a large decrease in the value of the ellipticity. At 90^o, however, the ellipticity returns to 0, indicating that 90^o is the second axis of the device. These two angles of input orientation

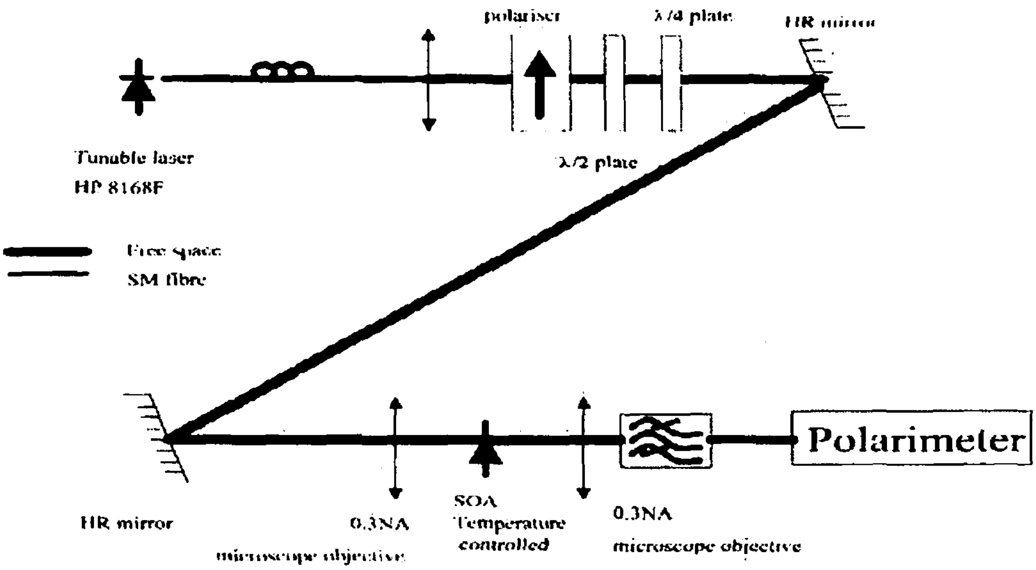

Fig. 4.12: Experimental setup for NPR characterization experiment with injection.

0^o and 90^o, corresspond to the optical axes of the device for each of the optical powers injected into the device. From this result it may be stated that there is no modification of the waveguide axis due to the carrier induced variation of the refractive index, as has been reported in the literature [24]. It should be pointed out that this result is for the Optospeed device only.

As already stated, when the input orientation is increased the ellipticity decreases to a minimum value of -0.94 at 48^o. At this minimum value the output signal is approaching a circular polarization, if the input orientation is increased further, the polarization begins to return to a linear polarization. For circular polarization the magnitude of the TE and the TM components are equal, it is the difference in phase of $\pi/2$ which causes the circularly polarized light. If the TE and TM gain were equal it would be expected that this minimum in the ellipticity would occur at 45^o, however, in this case the minimum occurs at 48^o, which implies that the TE gain must be higher than the TM gain. The reason for this is that at this angle there will be more light injected into the TM mode and in order that the output approach circular polarization the gain in the TE mode must be larger in order to compensate for the lower level of injected power. The negative sign on the ellipticity is the convention to denote that the output polarization is left-handed polarization, this result indicates that the TE axis is slower than the TM axis, which is consistent with the result from the previous experiment in this chapter, the case with no injection.

The electric field may be split into two components, each representing the orthogonal

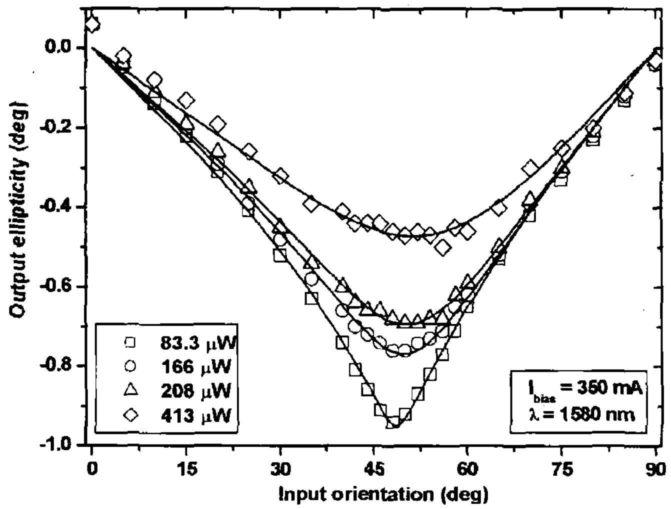

Fig. 4.13: Output ellipticity as a function of injection angle for a linearly polarized input at -10 dBm, -7 dBm, -6 dBm and -3 dBm. Solid lines represent experimental data and shapes represent fitted data.

modes of the device:

$$E = e^{i(\omega t-kz)}(E_{0TE}e^{i\phi_{TE}} + E_{0TM}e^{i\phi_{TM}}) \tag{4.25}$$

where $E_{0TE(TM)}$ is the E component along the TE (TM) direction and its phase is $\phi_{TE(TM)}$. E_{TE} and E_{TM} are expressed as:

$$\begin{aligned} E_{0TE} &= \rho E cos(\theta)\vec{u}_{TE}, \\ E_{0TM} &= E sin(\theta)\vec{u}_{TM} \end{aligned} \tag{4.26}$$

where ρ is the ratio of the single-pass gain in the TE mode to the single-pass gain in the TM mode, θ is the input angle and $u_{TE(TM)}$ is the unit vector along the horizontal (vertical) axis. For the purpose of the model the amplitude of the input field, E, is taken to be unity. The phases of the input field may be defined as follows:

$$\phi_{TE} = \frac{2\pi L n_{TE}}{\lambda},$$
$$\phi_{TM} = \frac{2\pi L n_{TM}}{\lambda} \tag{4.27}$$

From Fig. 4.13 it can be seen that this simple theory can be used to accurately model the experimental data using only two parameters ρ and the phase difference, $\delta\phi = \phi_{TM} - \phi_{TE}$. The ellipticity as a function of orientation was fitted using only one value of ρ and $\delta\phi$ for each value of injected power. Fig. 4.14 shows the variation of the two model parameters as a function of injected power. It can be seen that initially the gain ratio is 1.12 indicating that the TE gain is initially slightly larger than the TM gain. In the previous experiment with no injection the gains were found to be equal, but this was within the resolution of the experiment, which was limited by the high level of noise in the ASE spectrum which hindered the decision process in determining the analysis of the modulation ripples. It can be seen from Fig. 4.14 that as the level of injected power was increased up to 413 μW the gain ratio increased to 1.25 indicating that the single-pass TE gain became even larger with respect to the single-pass TM gain. This increased difference between the orthogonally polarized gains, as a function of intensity, leads to a larger polarization rotation, due to NPR, of the injected signal. The nonlinear nature of the birefringence may also be seen in Fig. 4.14, from observation of the phase difference as a function of injected power. Firstly, the phase difference $\delta\phi$ is negative, indicating the n_{TE} is larger than n_{TM}. As the injected power is increased $\delta\phi$ also increases. Due to the fact that the refractive index is proportional to the phase, which can be seen from Eqn. (4.27), an increase in the phase difference along orthogonal modes also points to an increase in the difference between the refractive indices along orthogonal modes. This increased variation in refractive indices also leads to an increase in the polarization rotation, due to NPR, as a function of injected power.

From the experiments performed in this section it may be concluded that there is an polarization rotation inherent to the SOA under test. This rotation is thought to be primarily due to the asymmetric shape of the waveguide. This manifests itself as a birefringent effect as found experimentally using the polarization resolved ASE spectra. There is also a possible rotation of the polarization occurring due to a polarization dependent single-pass gain in the device, although this gain was found to be equal, within the large resolution of the measurement technique, along orthogonal modes of the device under test. The injection of an optical signal into the device was also studied from an experimental point of view. The polarization dependent gain and the birefringence where found to increase as a function of

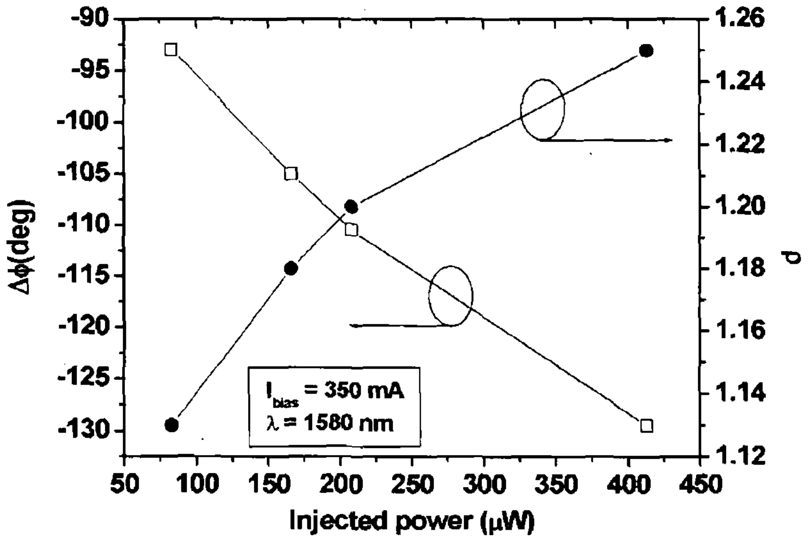

Fig. 4.14: Gain ratio between TE and TM modes, and phase difference as a function of input power.

this injected power, demonstrating an increase in the polarization rotation. Finally, comparing the two techniques, the experiment with injection is thought to be the more reliable measurement as no assumptions were made in order to obtain the fitting, whereas the facet reflectivity was given an approximate value in the analysis of the gain spectrum. However, the experiment with injection is also limited due to the fact that in the gain analysis it is only a relative gain that can be extracted. It is felt that the two experiments complement each other well, with the limitations of each being overcome by their combined analysis. Consistency is also found between the two experiments.

4.7 Pump-probe experiment to determine NPR

The aim of the experiments presented so far in this chapter were to examine the underlying physical mechanisms behind the effect of NPR. While essential from the point of view of understanding the effect, these experiments were not performed in a setup that would be used in a practical optical system. If all-optical processing techniques, particularly wavelength conversion, are to be performed in bulk SOAs it will be necessary to inject two optical signals, a pump and a probe, into the device in order to transfer the data at one wavelength onto the wavelength of the second signal. With regards to the NPR effect a detailed analysis of the state of polarization of both pump and probe signals is required in order to design the best possible optical system using NPR.

An experiment was performed to observe the change in polarization of a probe signal brought about by the injection, in a contra-propagating setup, of a pump signal. This experiment was performed in a CW setup, where the polarization was measured directly using a polarimeter. The experiment was performed in the steady-state case in order to provide a focus for the experiment. If pulses were to be considered in such an experiment, the complexity would be greatly increased, as the nonlinear gain dynamics would need to be accounted for under these conditions. The high intensity pump signal acted to vary the gain and birefringence of the device such that the NPR of the probe signal was effected by the pump signal. This technique may be used to perform all-optical signal processing such as wavelength conversion. In this initial experiment, however, it was desirable to examine the strength of the probe variation originating from the pump signal. This experiment was performed in free-space in order to allow easy control of the state of polarization of the signals. The aim of this experiment was to determine the plausibility of designing a system to perform all-optical signal processing using NPR, by obtaining exact measurements of the change in polarization of the probe signal induced by the pump signal. Both the polarization and the intensity of the pump signal were varied in order to observe the effect these experimental conditions had on the NPR, so that the optimum rotation could be achieved. The initial polarization of the probe signal was also varied and it was found that the NPR was dependent on this initial value.

Several groups have investigated the NPR effect in SOAs using a pump-probe setup, but these groups measured the polarization indirectly by recording changes in optical output power as a function of injected pump power and polarization [12], [15] and [35]. These groups focussed on exploiting the NPR effect from an optical systems point of view, rather than try to understand the physics of the effect. This technique, whilst easier to implement, does not reveal much about the polarization dynamics in the device. The pump-probe experiment presented in this section gives a much more detailed insight into the exact change in the polarization, in terms of orientation and ellipticity, than work previously carried out. This leads to a more complete understanding of the NPR effect, which should facilitate the design of a wavelength converter based on this effect.

4.7.1 *Experimental setup*

The experimental setup is shown in Fig. 4.15. The SOA under test was biased at 200 mA and temperature controlled by means of a Peltier cooler at 23^oC. The unbroken lines represent the signals propagating in free space whilst the dotted lines represent the signals propagating in SMF. The pump and probe laser signals were provided by 2 external cavity HP8168F sources at wavelengths of 1575 nm and 1580 nm, respectively. These wavelengths lie very close to the peak gain wavelength of the device, ensuring maximum gain upon amplification in the SOA. The wavelength difference of 5 nm was required in order to discriminate between the pump and probe signals at the detection stage. The microscope objectives were used to collimate the signals from the sources in free space. A polarizer and PBS were used to ensure the signals were linearly polarized. The orientation of this linear polarization was controlled by a HWP in each arm of the setup. A QWP was also used in order to compensate for the mismatch between the wavelength of the laser and the operating wavelength of the HWP. The signals were then injected into the SOA using two further microscope objectives. The probe signal was detected by using a beam splitter to redirect a portion of the beam and a filter to isolate the signal under test. The signal was detected using a polarimeter, in order to obtain the ellipticity and orientation of the signal, thus fully characterizing the polarization of the signal in question.

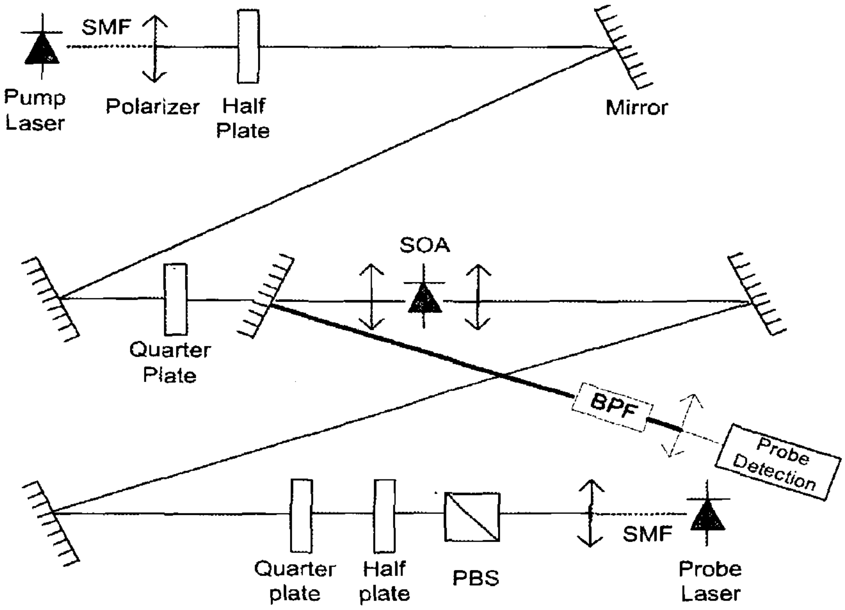

Fig. 4.15: Pump-probe experimental setup.

4.7.2 Effect of pump intensity and polarization on the change in polarization of the probe

With the experimental setup just discussed, the probe polarization was fixed at 45°, using the wave plate configuration. The intensity was constant at -12 dBm, ensuring that the gain of the SOA due to the probe signal was in the linear regime. The probe polarization was fixed at 45° as there should be large contributions from the TE and TM modes at this orientation [6]. The intensity of the pump was varied from -20 dBm to 0 dBm, this variation in intensity was performed for 3 separate angles of polarization, TE, 45° and TM.

The results of this experiment can be observed in Fig. 4.16. Both the ellipticity and orientation are represented in this figure. The ellipticity varies from approximately 0.56 at -20 dBm to approximately 0.3 at 0 dBm when the pump polarization was aligned along the TM axis. The orientation of the probe at the output for this setup varied from approximately 83^o at -20 dBm to approximately 101^o at 0 dBm again with the pump signal aligned along the TM axis of the device. The effect of varying the polarization of the pump may also be observed in Fig. 4.16. Irrespective of the angle of the pump polarization, the ellipticity and orientation follow the same trend. The large modulations of the ellipticity and orientation visible as the intensity increases may be attributed to the nonlinear birefringence and nonlinear gain which were determined experimentally in Sec. 4.6.

There are variations between the probe responses for different angles of pump polarization but these variations are minimal and are down to limitations in the experiment due to varying coupling efficiency and imperfect polarizers. The main conclusion from this initial experiment is that the primary contribution of the pump is to deplete carriers in the device thus modulating the gain and inducing nonlinear birefringence in the device. This information is important in considering the design of a system to perform all-optical signal processing using NPR in the SOA as it indicates that it is not critical to control the polarization of the pump signal in such a system. Furthermore, it may be concluded that NPR in the SOA under test has a large effect and becomes significant for large levels of injected powers, which may be observed from the variation of the ellipticity and orientation as a function of injected optical power in Fig. 4.16. This power dependency of NPR was also found in the experiment presented in Sec. 4.6.3, providing consistency between the results.

4.7.3 *Effect of initial probe polarization on NPR effect*

The experimental setup of Fig. 4.15 was also used in this experiment. The polarization of the pump signal was fixed and was randomly selected to be orientated in the TM direction. The polarization of the probe was varied between TE, 45° and TM. The nonlinear rotation of the polarization was observed by recording the polarization of the probe as the pump intensity was increased. Table 4.1 shows the ellipticity and orientation of the probe as a function of injected pump power, for 3 separate initial probe polarizations, TE, 45° and TM. The results reveal that the initial polarization of the probe plays a crucial role in determining the extent of the NPR observed. For example considering the case where the probe is initially orientated along the TM axis it can be seen that the signal remains linearly polarized, as the ellipticity is negligible, and also there is very little variation in the orientation of the signal, with a maximum swing in the orientation of less than 2^o. A similar situation is observed when the probe is orientated along the TE axis, again there is

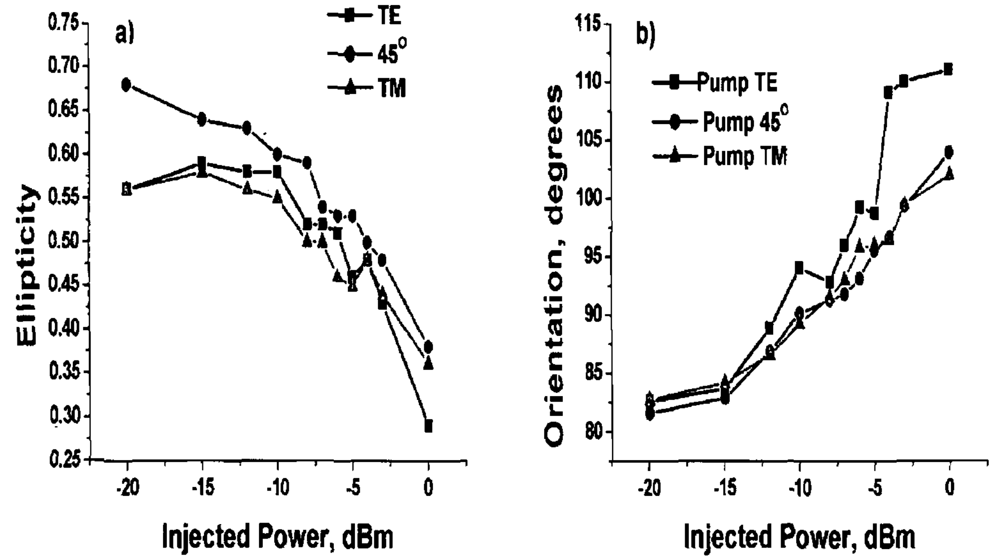

Fig. 4.16: a) Ellipticity and b) orientation from pump-probe setup with a constant probe polarization of 45°. The pump polarization was varied between TE, 45° and TM.

a negligible ellipticity, indicating linearly polarized light, and the orientation varies by less than 2°. The reason for the polarization remaining constant at these angles of polarization is that the TE and TM modes correspond to the optical axes' of the device, resulting in the polarization at the output remaining unchanged with respect to the polarization that was injected into the device. If light is injected along one of the axes' then there will be no effect from nonlinear birefringence or from the nonlinear gain. It may also be concluded from this experiment that there is no modification of the waveguide axis for this level of injected power, if there was then the polarization of the signal injected along the original axis of the device would vary at the output of the SOA. This result is consistent with the results found in the Sec. 4.6.3. In order to induce NPR in the probe signal, the initial probe signal must be polarized such that there is a TE and a TM component in the signal. In this way the nonlinear birefringence will result in one signal travelling at a slower speed with respect to the other, and the different gains will lead to one component having a higher gain imparted on it than the other. When the probe signal was orientated at 45° a large effect from NPR can be observed with the ellipticity varying from 0.55 at -20 dBm to 0.37 at 0 dBm, and the orientation varying from 79.8° to 100.29°.

A pump-probe experiment has been presented whereby the effect of the pump power and polarization on the output polarization of the probe were studied. The effect of varying the probe polarization was also studied. It was found that the output polarization of the probe

Probe TM			**Probe** 45^o			**Probe TE**		
Pump TM	Ellip.	Orien.	Pump TM	Ellip.	Orien.	Pump TM	Ellip.	Orien.
probe	0.02	87.99	probe	0.55	79.8	probe	-0.04	-1.2
-20	0.02	87.91	-20	0.55	80.07	-20	-0.04	-1.5
-15	0.02	88.29	-15	0.56	82.68	-15	-0.04	-1.5
-12	0.01	88.67	-12	0.52	84.64	-12	-0.05	-1.5
-10	0.01	88.78	-10	0.51	87.33	-10	-0.05	-1.6
-8	0	89.18	-8	0.5	89.57	-8	-0.05	-1.9
-7	0	88.62	-7	0.49	91.06	-7	-0.05	-1.9
-6	0	88.81	-6	0.49	92.51	-6	-0.05	-1.7
-5	0.01	88.6	-5	0.47	95.79	-5	-0.05	-1.5
-4	0.02	88.94	-4	0.49	95.72	-4	-0.05	-1
-3	0	89.44	-3	0.42	99.52	-3	-0.05	-0.5
-2	0	89.95	-2	0.46	100.15	-2	-0.06	-0.2
-1	0.02	89.72	-1	0.43	100.93	-1	-0.06	-0.3
0	0	89.41	0	0.37	100.29	0	-0.06	0.06

Tab. 4.1: Ellipticity and orientation of probe signal as a function of pump intensity for several angles of initial probe polarization.

was highly dependent on the input power of the pump, indicating the contribution of the nonlinear gain and birefringence on the polarization of the probe. The effect of varying the polarization of the pump signal was very small and did not significantly vary the polarization of the probe signal. The second experiment examined the dependence of the output probe polarization on the orientation of the injected probe signal. It was observed that the initial orientation is critical in a system based on NPR. If the probe signal is injected along one of the principal axes of the device, there is no rotation of the state of polarization and the injected state of polarization is preserved at the output. A large rotation of the polarization was observed by injecting the probe signal at some angle to the axis of the device. This result also indicated the absence of a modification of the axes of the SOA. These experiments would help in the design of a practical optical system as it has been determined that control of the polarization of the pump is not necessary, thus simplifying the design.

4.8 Conclusions

In conclusion, the phenomenon of polarization has been introduced in this chapter, with particular reference to the polarization state of signals injected into the SOA. The key components used to control the state of polarization of signals in optical systems were introduced. These components are key to both the design of optical systems based on polarization effects and to the measurement of the polarization of an optical signal. The polarization sensitivity of the SOA was then introduced, with the key causes of this sensitivity explained along with several techniques which have been used to reduce this sensitivity. After this introduction to the NPR effect in the SOA, experiments carried out to establish the physical mechanisms behind the effect were detailed. The exact level of gain and phase changes induced both due to the waveguide design and due to an injected signal was determined, using several novel experimental techniques. These experiments were carried out with and without the presence of injected optical signals. Consistency was found between the two sets of experiments. Finally, a third set of experiments were carried out whereby the SOA was placed in a CW pump-probe setup, which is the setup typically used to perform all-optical signal processing with SOAs. The experimental results presented, however, looked at this setup as a means to understanding the causes of the NPR, rather than simply exploiting the effect for signal processing, as other groups have done. The experimental results found in this chapter were used to facilitate the design of the NPR wavelength converter, to be presented in the next chapter. This approach was chosen so that a more complete understanding of the effect, from both a physical and application point of view, could be obtained. The results presented in this chapter give exact values of the change in the state of polarization induced by a pump signal. All other results presented in the literature to date discuss the change in intensity induced by NPR. These results do not detail a direct measurement of NPR.

BIBLIOGRAPHY

[1] R.E. Tench, N.A. Olsson, L.D. Tzeng, T.W. Cline, M. Dixon. "Polarization-insensitive lightwave receiver using optical amplifiers". *IEE Electronic Letters*, vol.24(no.24):pp.1497–1499, 1988.

[2] N. A. Olsson. "Polarization-independent configuration optical amplifier ". *IEE Electronic Letters*, vol.24(no.17):pp.1075–1076, 1988.

[3] P. Dousiere, P. Garabedian, C. Graver, D. Bonnevie, T. Fillion, E. Derouin, M. Monnot, J.G. Provost, D. Leclerc, M. Klenk. "1.55μm polarization independent semiconductor optical amplifier with 25 db fiber to fiber gain". *IEEE Photonics-Tech. Letters*, vol.6(no.2):pp.170–172, 1994.

[4] M. Itoh, Y. Shibata, T. Kakitsuka, Y. Kadota, and Y. Tohmori. "Polarization-insensitive SOA with a strained bulk active layer for network device application". *IEEE Photonics Tech. Letters*, vol.14(no.6):pp.765–767, 2002.

[5] J.-Y. Emery, T. Ducellier, M. Bachmann, P. Doussiere, F. Pommereau, R. Ngo, F. Gaborit, L. Goldstein, G. Laube, and J. Barrau. "High performance 1.55μm polarisation-insensitive semiconductor optical amplifier based on low-tensile-strained bulk GaInAsP". *IEE Electronic Letters*, vol.33(no.12):pp.1083–1084, 1997.

[6] B.F. Kennedy, S. Philippe, P. Landais, A.L.Bradley, and H. Soto. "Experimental investigation of polarization rotation in semiconductor optical amplifiers". *IEE Proc. Optoelectronics*, vol.151(no.2):pp.114–118, 2004.

[7] H.C. Lefevre. "Single mode fibre fractional wave devices and polarization controllers". *IEE Electronic Letters*, vol.16(no.20):pp.778–780, 1980.

[8] G.G. Stokes. *Trans. Cambridge. Phil. Soc.*, vol.9:pp.309, 1852.

[9] R. Guenther. "Modern optics". *John Wiley and sons*, page 47, 1990.

[10] T. Saitoh, and T. Mukai. "1.55 μm GaInAsP travelling-wave semiconductor laser amplifier". *IEEE J. Quantum Electronics*, vol.23(no.6):pp.1010–1020, 1987.

[11] G.P. Agrawal. "Long-wavelength semiconductor lasers". *Van Nostrand Reinhold, first edition*, pages pp.41–49, 1986.

[12] R.J. Manning, A. Antonopoulos, R. Le Roux, and A.E. Kelly. "Experimental measurement of nonlinear polarisation rotation in semiconductor optical amplifiers". *IEE Electronic Letters*, vol.37(no.4):pp.229–231, 2001.

[13] H. Soto, D. Erasme and G. Guekos. "Cross polarization modulation in semiconductor optical amplifiers". *IEEE Photonics Tech. Letters*, vol.11:pp.970–972, 1999.

[14] M.F.C. Stephens , M. Asghari, R.V. Penty and I.H. White. "Demonstration of ultrafast all-optical wavelength conversion utilizing birefringence in semiconductor optical amplifiers". *IEEE Photonics Tech. Letters*, vol.9(no.4):pp.449–451, 1997.

[15] D.M. Patrick, A.D. Ellis, D.A.O Davies, M.C. Tatham and G. Sherlock. "Demultiplexing using polarization rotation in a semiconductor laser amplifier". *IEE Electronic Letters*, vol.30(no.4):pp.341–342, 1994.

[16] G.P. Agrawal, and N. A. Olsson. "Self-phase modulation and spectral broadening of optical pulses in semiconductor laser amplifiers". *IEEE J. Quantum Electronics*, vol.25(no.11):pp.2297–2306, 1989.

[17] C.H. Henry. "Theory of the linewidth of semiconductor lasers". *IEEE J. Quantum Electronics*, vol.18(no.2):pp.259–264, 1982.

[18] H.J.S. Dorren, D. Lenstra, Y. Liu, M.T. Hill and G.D. Khoe. "Nonlinear polarization rotation in semiconductor optical amplifiers: Theory and application to all-optical flip-flop memories". *IEEE J. Quantum Electronics*, vol.39(no.1):pp.141–148, 2003.

[19] B.F. Kennedy, S. Philippe, H. Soto , A.L.Bradley, and P. Landais. "Measurement of the chirp introduced to a picosecond pulse injected into an SOA as a function of input polarization". *Proc. ETOS, Cork, Ireland*, 2004.

[20] M.G.A. Bernard, and B. Douraffourg. "Laser conditions in semiconductors". *Phys. Stat. Sol.*, vol.1:pp.699–703, 1961.

[21] E.P. O'Reilly, and A.R. Adams. "Band-structure engineering in strained semiconductor lasers". *IEEE J. Quantum Electronics*, vol.30:pp.366–379, 1994.

[22] E. Yablonovitch, and E.O. Kane. "Reduction of lasing threshold current density by lowering of valence band effective mass". *IEEE J. Lightwave Tech.*, vol.4(no.5):pp.504–506, 1986.

[23] W. Wang, K. Allaart, and D. Lenstra. “Semiconductor optical amplifier gain and anisotrophy”. *IEE Electronic Letters*, vol.40(no.25):pp.1602–1603, 2004.

[24] H. Soto, J.C. Dominguez, D. Erasme and G.Guekos. “Demonstration of an all-optical switch using cross polarization modulation in semiconductor optical amplifiers”. *Microw. and Optic. Tech. Letters*, vol.29(no.3):pp.205–209, 2001.

[25] J.C. Simon. “GaInAsP laser amplifiers for single-mode fiber communications”. *IEEE Journal of Lightwave Tech.*, vol.LT-5(no.9):pp.1286–1295, 1987.

[26] C. Vassallo. “Polarization-independent antireflection coatings for semiconductor optical amplifiers”. *IEE Electronic Letters*, vol.24(no.1):pp.61–62, 1988.

[27] I.P. Kaminow. “Measurement of the modal reflectivity of an antireflection coating on a superluminescent diode”. *IEEE J. Quantum Electronics*, vol.19(no.4):pp.493–495, 1983.

[28] S.A. Merritt, C. Dauga, S. Fox, I-F. Wu and M. Dagenis. “Measurement of the facet modal reflectivity spectrum in high quality semiconductor travelling wave amplifiers”. *IEEE J. Lightwave Tech.*, vol.13(no.3):pp.430–433, 1995.

[29] L. Jungkeun, and T. Kamiya. “Improved characterization of multilayer antireflection coatings for broad-band semiconductor optical amplifiers”. *IEEE J. Lightwave Tech.*, vol.18:pp.2158–2166, 2001.

[30] B.W. Hakki, and T.L. Paoli. “CW degradation at 300 K of GaAs double-heterostructure junction lasers. Electronic gain”. *J. of Applied Physics*, vol.44(no.9):pp.4113–4119, 1973.

[31] B. Hakki, and T. Paoli. “Gain spectra in GaAs double-heterostructure injection lasers”. *J. of Applied Physics.*, vol.46(no.3):pp.1299–1306, 1975.

[32] G. Guekos. “Photonic devices for telecommunications”. *Editor Springer-Verlag*, page pp.329, 1999.

[33] S. Diez, C. Schimt, R Ludwig, H.G. Weber, P. Doussiere, and T. Duceiller. “Effect of birefringence in bulk semiconductor optical amplifiers on FWM”. *IEEE Photonics Tech. Letters*, vol.10(no.2):pp.212–214, 1998.

[34] G. Guekos. “Photonic devices for telecommunications”. *Editor Springer-Verlag*, pages pp.143–145, 1999.

[35] G. Liu, M.Y. Hill, E. Tangdiongga, H. de Waardt, N. Calabretta, G.D. Khoe , and H.J.S. Dorren. "Wavelength conversion using nonlinear polarization rotation in a semiconductor optical amplifier ". *IEEE J. Quantum Electronics*, vol.15(no.1):pp.90–92, 2003.

[36] N. Calabretta, Y. Liu, F.M. Huijskens, M.T. Hill, H. de Waardt, G.D. Khoe, and H.J.S. Dorren. "Optical signal processing based on self-induced polarization rotation in a semiconductor optical amplifier". *IEEE Photonics Tech. Letters*, vol.22(no.2):pp.372–381, 2004.

5. ALL-OPTICAL SIGNAL PROCESSING USING THE SOA

5.1 Need for All-Optical Communication Systems

The recent explosive growth in internet traffic continues to increase with no sign of a leveling off in internet usage. In developed countries like Ireland user penetration now exceeds half the population. The percentage growth of internet users in Ireland increased by 168% between 2000 and 2005. Densely populated countries with rapidly developing economies, for example India and China, will fuel the continued development of the internet. In the same five year period between 2000 and 2005, India's user growth was 684% resulting in a user penetration of only 3% whilst China's user growth was 358% resulting in a user penetration of only 7.9% [1]. As well as this, there is a continued rapid growth in the demand for new bandwidth hungry multimedia services. These facts indicate a future demand for faster switching capabilities than existing network infrastructure can provide.

In long-haul telecommunications systems data propagates along optical fibre in optical format. The current systems, however, do not operate solely in the optical domain, as switching needs to be performed in the electronic domain. This involves conversion of the optical data to electronic data in order for the switching to take place and then conversion back to optical data after the switching operation has been performed. Commercial systems are currently restricted by the maximum speed at which the electronics can operate, which is 10Gb/s (OC-192) [2], with the latest improved electronics operating at 40Gb/s (OC-768) [3]. As the overall data transmission obtainable in the optical domain far exceeds this maximum, electronic bottlenecks may occur in future systems at the multiplexer, electronic to optical converter, optical to electronic converter and at the demultiplexer. This would have the effect of limiting the maximum transmission rate of the system. In order to avoid these bottlenecks, at some point it will likely be necessary for high-speed telecommunication networks to operate solely in the optical domain. In order for this to be realised, techniques to perform this all-optical switching need to be developed.

This chapter commences by briefly introducing several of the techniques proposed to do this. The focus of the chapter is on exploiting the nonlinearities in the SOA to achieve all-optical signal processing, and specifically on the use of NPR in the SOA as a technique to perform all-optical data manipulation. The potential of NPR as a technique to perform all-optical signal processing is investigated experimentally, and comparison with a more mature technique, i.e. XGM, is given. The information obtained from the experiments presented in Chapter 4 is used to perform this switching. The experiment presented investigates wavelength conversion in both co- and contra-propagating setups in order to establish the optimum wavelength converter.

5.1.1 Summary of all-optical switching techniques

Numerous techniques have been proposed to implement all-optical switches. These methods use very different technology in order to perform the switching operation. For example, thermo-optic, electro-optic, acousto-optic, opto-mechanical and micro-mechanical techniques have all been developed, with varying levels of success. These all-optical functions could remove the 'electronic bottleneck', where optical networks would potentially be slowed down by the signal processing that is carried out in the electrical domain.

Opto-mechanical switching

One such technique is the use of opto-mechanical switching. This technique involves mechanical maneuvering of the fibre in order to select the desired switching path. This is the first all-optical switching technology to become commercially available. The fact that the switching involves the mechanical motion of the fibre means that this method is slow, with a switching speed of 2 ms [4], and is unsuitable to complex switching schemes [5].

Micro-Electro-Mechanical-Systems (MEMS)

Micro-Electro-Mechanical-Systems (MEMS) are silicon micro-machines that have the same design process as a typical silicon integrated circuit. In the design process small movable mirrors are created. These mirrors are moved in such a way as to direct incoming light toward a desired output. The fact that the direction of the mirror can be selected means that switching between different outputs can be performed. The advantage of using MEMS for all-optical switching are their small size and use as add-drop multiplexers. Disadvantages are their unreliability, a 3 dB insertion loss introduced at the mirror surface [6] and a sub-millisecond speed. A 8 X 8 bidirectional switch using the MEMS switching principle has been demonstrated [7]. These devices have a relatively large footprint, which increases as a function of the number of mirrors in the device.

Bubble switches

This technique involves two optical waveguides intersecting with each other at a given angle. At the point of intersection is a trench containing a liquid with the same refractive index as the waveguide. Because of the fact that the refractive indices are the same, injected light will pass through the liquid and continue along its path unhindered. However, a heater is placed beside the trench which is used to heat the liquid, creating an air bubble in the liquid. The bubble has a lower refractive index than the waveguide which leads to total internal reflection, causing the light to be directed along a different waveguide thus switching the data [8]. A 32 X 32 bubble switch-based Optical Cross-Connect (OXC) has been developed [9]. The switching time for this technique is below 10 ms, with insertion losses of 8 dB. It should be noted that the bubbles need to be maintained over the entire distance of the switched path.

Liquid crystal

This technique is based on the same technology used in Liquid Crystal Display (LCD) computer monitors. Light may be switched based on the polarization of the incoming signal. The polarization is varied by using the Pockels effect coming from the application of an electric field to the crystal. After the polarization is varied the signal is injected into a birefringent material, where the walk-off due to the birefringent effect as well as the material's thickness are used to displace the beam at the output [10]. A 64 X 64 Benes OXC based on liquid crystals has been demonstrated [11]. The insertion loss in this technique was 9-10 dB. A disadvantage of liquid crystals is that they have a switching speed in the millisecond range.

Optical fibre nonlinearities

One technique of this nature uses the Sagnac interferometer which takes advantage of the nonlinear phase shift inherent in optical fibres, to perform switching. This interferometer uses a long length of fibre connected between the two output ports of a coupler, forming a fibre loop. A pulse injected into the interferometer is split in two. The ratio of this splitting is dependent on the coupler used. If the power along each arm is the same then both pulses will experience the exact same linear and nonlinear phase shift and no phase difference is introduced, leading to the input beam being reflected. The relative phase difference between the two beams is used to determine if the input beam is transmitted or reflected. There are several techniques used to obtain this phase shift. Different types of optical switches which employ Sagnac interferometers are: Nonlinear Optical Loop Mirror

(NOLM), Nonlinear Amplifying Loop Mirror (NALM) and Terahertz Optical Asymmetric Demultiplexer (TOAD) [12] - [14]. Extremely fast switching on a femtosecond timescale can be obtained using these techniques, due to the ultrafast nature of the fibre nonlinearities. Disadvantages of these techniques include the long length of fibre required, temperature fluctuations affecting performance, difficulties in integrating the switch in a network and the high level of power that is generally needed to induce the nonlinearities.

5.2 SOA nonlinearities

As well as being used as an amplifier the SOA has huge potential for use in optically transparent networks [15]. Many all-optical functions such as switching and wavelength conversion can be performed using the nonlinearities in the SOA. The SOA is an attractive device for all-optical switching as it is much faster than mechanical switching techniques, easy to integrate to optical networks and relatively straightforward to implement in a switching scheme. As well as this the temperature of the device can be controlled without difficulty, ensuring stable operation, and the SOA does not degrade over time, unlike mechanical switching techniques. It is true that it is possible to achieve faster switching using fibre nonlinearities but recent work has shown the possibility to perform optical switching using the SOA close to the THz range [16]. Furthermore, the nonlinearities in optical fibre are very weak, in comparison to the SOA, which means that either very high intensity signals must be used or very long lengths of fibre.

The main cause of nonlinearities in SOA's is due to changes in the carrier dynamics and associated refractive index variations, induced by an input signal. The three main types of nonlinearity exploited for all-optical signal processing are: XGM, XPM and FWM. Switching rates in access of 100 Gbit/s can be easily achieved using these techniques, with the possibility to achieve speeds in access of 1 Tbit/s [16]. A new method called NPR has recently emerged as a potential competitor to these more established techniques. NPR, discussed in detail in Chapter 4, has received significant attention in recent years [17] - [23]. The focus of this chapter is on NPR and in using the understanding of this effect, gained from Chapter 4, to assess the possibilities and limitations of using NPR to perform all-optical functions. In particular an experiment is presented to perform wavelength conversion.

5.2.1 Cross-gain modulation (XGM)

XGM occurs because of the interaction of two optical signals via the carrier population in the SOA. This technique can be used to perform numerous types of all-optical signal processing, e.g. wavelength conversion, all-optical switching and signal reshaping. As the power injected into the SOA increases the gain is reduced through the gain reduction due to the carrier consumption of the amplified signal. Using this gain depletion it is possible to modulate the amplifier gain with an input signal. When a '1' level is injected into the device the gain is minimized and when a '0' level is injected the gain is maximized. This gain modulation can be encoded on another signal travelling at a different wavelength through the device. A CW probe beam is injected into the SOA at a different wavelength to the pump and its amplitude and phase are changed due to the depletion of the gain. This leads to inverted wavelength conversion from the data wavelength to the CW wavelength. This process is illustrated in Fig. 5.1. XGM in a travelling-wave SOA was first demonstrated at 1 Gb/s [24]. The maximum processing speed that can be obtained using this process is equal to the inverse of the gain recovery time. The gain recovery time is the time taken for the carriers in the conduction band to be replenished following saturation of the carriers due to high intensity signal injection. This time is defined by Eqn. (2.22). It is possible to measure the gain recovery time experimentally [25]. Values for this parameter are dependent on the experimental conditions, e.g. bias current, device geometry. Typical values lie in the range 100 ps to 1 ns, limiting the maximum processing speed to approximately 10 GHz. It is possible to suppress the recovery time by injecting a CW holding beam into the device. Recovery times as low as 10 ps have been measured using this technique [26], [27], suggesting that it is possible to switch at data rates up to 100 GHz, due to the inter-band carrier recovery dynamics [28]. Indeed, wavelength conversion at this data rate was later shown experimentally [29].

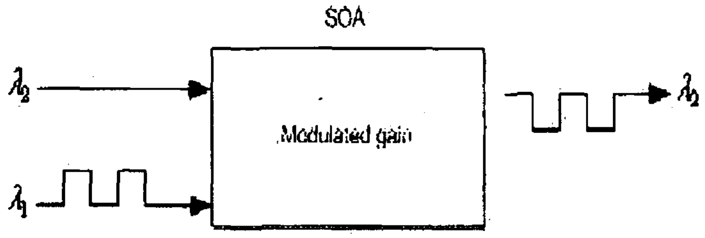

Fig. 5.1: Illustration of XGM.

XGM is a simple and stable form of wavelength conversion, with switching possible over a large range of up to approximately 70 nm. The main disadvantage of this technique is the reduction of the signal-to-noise ratio due to the spontaneous emission. Amplitude distortion and chirping can also reduce the efficiency of this process. Chirp was introduced in Sec. 3.4.6 and is defined by Eqn. (3.35). Phase modulation leads to this chirping of the pulses, with a red-shifted chirp introduced to the leading edge and a blue-shifted chirp on the trailing edge [30]. The chirping effect is generally large as the phase modulation is maximized due to the large carrier density modulation.

5.2.2 Cross-phase modulation (XPM)

The modulation of the phase that leads to the unwanted chirp in XGM is used constructively in XPM to perform wavelength conversion. A diagram of a typical interferometer is shown in Fig. 5.2. In this setup the light to be switched, i.e. the probe, is split into two paths both containing SOAs. The phase of the signal in one of these arms is modulated by injecting the high intensity data signal into this arm. This signal modulates the gain, and so the phase, of the device. There is a coupling between the phase and gain in an SOA, the extent of which is related to the LEF, defined in Chapter 2. When the signals in both arms recombine, constructive or destructive interference results, depending on the phase difference between the two paths. This phase difference in turn depends on whether there is a '1' or a '0' on the data signal, due to the dependence of the phase modulation on the gain modulation. The interference of the signals in the absence of pump light can be set either to be constructive or destructive, leading to inverted or non-inverted operation. This is an advantage over XGM, where only inverted operation is possible. The interference between the two signals can be controlled by varying the bias current to the SOAs. The duration of the trailing edges of these converted pulses is directly related to the carrier recovery time of the SOA. At high data rates the trailing edges may lead to an overlap between successive bits, leading to Inter Symbol Interference (ISI). There are various types of interferometers that can be used to take advantage of XPM. The most popular are the Mach-Zehnder Interferometer (MZI), Michelson interferometer and Sagnac interferometer. The MZI is generally considered to be the superior interferometer as the other techniques rely on counter-propagation, which limits the bandwidth. Wavelength conversion at 168 Gbit/s has been demonstrated using a variation of the MZI [31]. This technique is referred to as the Delayed Interference Signal Converter (DISC), and consists of a single SOA in series with a passive MZI. The maximum data rate achievable with this technique is also restricted by the carrier recovery time, because it is the carrier modulation which effectively modulates the phase. However a recent publication demonstrates the possibility to perform XPM at data rates beyond 600 Gb/s, using the ultra-fast gain processes discussed in Chapter 2. The possibility of using these processes to achieve all-optical signal processing is discussed in detail in Chapter 6.

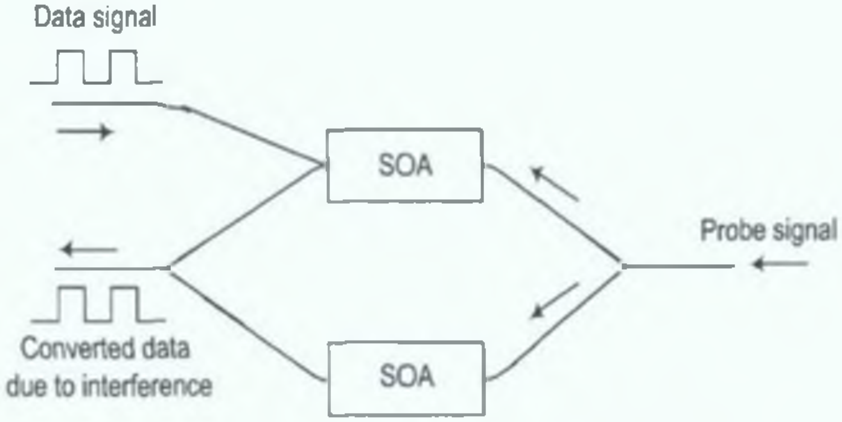

Fig. 5.2: Illustration of Mach-Zehnder used in XPM.

5.2.3 Four-wave mixing (FWM)

FWM is another phenomenon that can be used to achieve all-optical signal processing using the nonlinearities in an SOA. The principle of FWM is illustrated in Fig. 5.3. A strong pump at an angular frequency ω_0 interacts with a second weaker probe signal at an angular frequency ω_1 to produce conjugate signals at angular frequencies given by $|2\omega_0 - \omega_1|$, i.e. the new frequency components are generated on either side of the injected signals with a spacing determined by the beat frequency. Ω represents the angular frequency detuning between the signals. The new field is called the conjugate because its phase is opposite to the signal phase. The pump and probe signals must be co-polarized in order to generate the beating required for FWM. It should be noted that multiple conjugate signals are produced using this technique. Fig. 5.3 illustrates the conjugate signals located nearest to the injected pump and probe signals.

This beating of the pump and probe signals leads to a modulation of various parameters associated with the dynamic gain processes in the device. Their is a separate cut-off frequency associated with each gain process. Therefore, as the frequency detuning is increased it is possible to observe the contribution from each of the gain processes. These processes occur at different frequency detunings [32]. The FWM parameter that is recorded to determine which gain parameter is being modulated is the conversion efficiency, defined as the conjugate power divided by the probe power, P_{conj}/P_{probe} at the output of the SOA. If the conjugate signal is generated at higher frequencies than the pump and the probe then the conversion is defined as a frequency up-converted signal, if the conjugate is generated at lower frequencies than the pump and the probe then it is defined as a frequency down-converted signal. For small detunings, corresponding to relatively large timescales, the

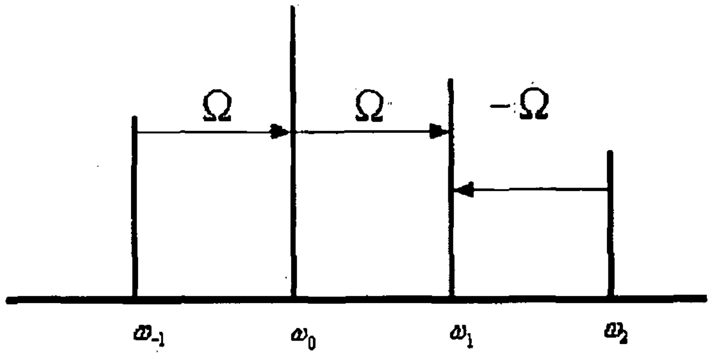

Fig. 5.3: Illustration of FWM technique.

interband carrier density is able to follow the optical beating and induces the desired gain fluctuations. As the detuning is increased this interband carrier density effect is too slow to follow the variations and the faster intra-band gain dynamics, introduced in Sec. 2.10, follow the optical beating. This modulation of the intraband effects is the cause of one of the main disadvantages of the FWM technique. The efficiency for these effects is considerably less than for the interband modulation, so the performance of FWM deteriorates as the wavelength is detuned, reducing the maximum switching speed. The polarization sensitivity of FWM is another factor that needs to be considered before its implementation. Polarization independent FWM has received considerable attention recently [33]. One advantage that FWM has over XGM and XPM is due to the preservation of both amplitude and phase. This means that FWM is the only nonlinear process that is strictly transparent. Another benefit of using FWM is that it is independent of modulation format due to it being a coherent process, unlike the other techniques, which are restricted to amplitude modulation formats. FWM can operate at high speed without a degradation in the extinction ratio. All-optical encoding and wavelength conversion at 160 Gbit/s have been shown experimentally using FWM in a gain-clamped SOA [34], [35]. A gain-clamped device was used in order to increase the carrier recovery time in the device, thus reducing pattern effects in the data.

5.2.4 Nonlinear polarization rotation (NPR)

A new nonlinear technique that has emerged is NPR. The physical reasons behind this effect were discussed in detail in Chapter 4, along with experimental characterization of the effect. Traditionally the polarization dependence of the SOA to injected signals has been an unwanted effect and the focus has been on developing polarization insensitive devices [36], as discussed in Sec. 4.5. Recently more attention has been paid to the NPR effect as a means to achieve all-optical switching [17]. The motivation to study this effect in SOA's grew from work previously carried out which looked at the NPR effect in optical fibres. This technique is based on a nonlinear birefringence induced by a discrepancy between the change in the refractive index of orthogonal modes in an optical fibre as a function of intensity. The nonlinear birefringence manifests itself as a NPR of a signal injected into the waveguide. So if a signal is injected with a known polarization, the nonlinear birefringence leads to orthogonal components travelling at different speeds resulting in a rotation of the state of polarization of the signal measured at the output of the fibre. This effect is induced by a strong optical pump beam and is referred to as the Kerr effect. It was first observed in 1973 and has received considerable attention since this time [37].

The basic component used to perform all-optical signal processing using NPR in optical fibres is the Kerr shutter. The operation of this component can be understood from Fig. 5.4. Two optical signals are linearly polarized with a 45^o angle between their respective polarizations. These two signals represent the pump and probe beams. A polarizer at the output of the fibre is adjusted so that the probe transmission is blocked in the absence of the pump beam. When the pump is applied the pump induced birefringence leads to a different variation of the refractive indices along orthogonal polarization directions. This leads to a variation of the probe polarization, which allows part of the probe beam to be transmitted through the polarizer. So whether or not there is light at the output of the polarizer is dependent on the application of the pump beam. Also, the quantity of the probe signal that is transmitted through the polarizer may be controlled by varying the pump power, as this leads to an intensity dependent NPR of the probe beam. This Kerr shutter has been proposed for use in many aspects of all-optical signal processing. It has been proposed for use as an optical switch [38], for optical logic gates [39], multiplexers [40], intensity discriminators [41], nonlinear filters [42], and pulse shapers [43]. However, an inherent problem with this effect is due to the instability of the output polarization, due to temperature fluctuations and drafts in the environment surrounding the fibre. Another disadvantage of this effect is the huge peak powers of the pump signal and large lengths of fibre are required in order to induce nonlinear birefringence, due to the fact that this nonlinearity is weak. In [44] peak powers of up to 6 Watts were used.

The SOA can remove the disadvantages associated with the NPR in optical fibres. Its small size also makes it much more efficient for implementation in optical networks. The small size of its active region and its higher dielectric constant means that the required peak power is much lower and although there may be some issues related to temperature fluctuations, these variations are on a much smaller scale and can be controlled in a more efficient

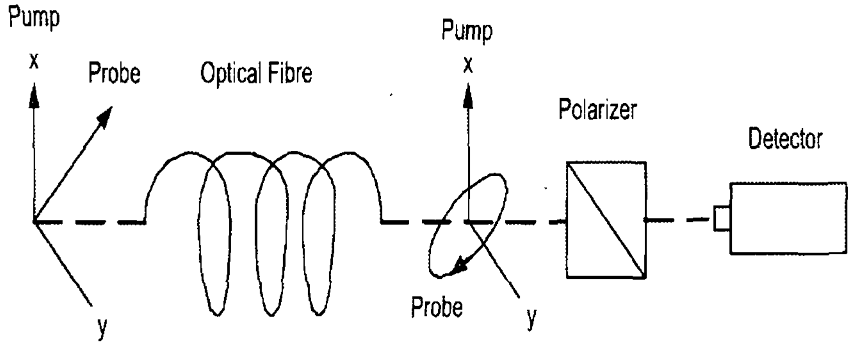

Fig. 5.4: Schematic illustration of a Kerr shutter.

manner than is the case for fibre. Patrick *et. al.* [17] were the first to consider the effect of NPR in an SOA device. In this work, a demultiplexing technique is presented which allows a 10 Gbit/s channel to be extracted from a 20 Gbit/s data channel. They attributed the effect solely to a variation in the propagation constants for TE and TM modes, analogously to the origin of the effect in optical fibres. The first experiments exploiting wavelength conversion using NPR were published by Stephens *et. al.* [18]. The experimental setup used in these experiments is based on a pump-probe approach, where the polarization of a CW probe beam is modulated by a high intensity pulsed pump beam, in a similar setup to the Kerr shutter. This setup also uses a polarizer after the nonlinear medium in order to allow transmission based on the polarization of the light at the output of the medium. If the polarizer is aligned to allow transmission of the probe only when the pump beam is on, then there is a conversion of the data from the pump wavelength to the probe wavelength due to the SOA becoming modulated by the pump beam. This experiment concentrated on performing the wavelength conversion and the authors did not focus on the cause of this effect to any great extent. Again they attributed the NPR to the birefringence in the device, mentioning that the polarization dependence of the confinement factors accentuated the effect. Lee *et. al.* [45] proposed a technique for improved wavelength conversion using XGM that was based on the birefringence introduced in the SOA. This experiment showed an improved extinction ratio for wavelength conversion but the problems of high NF and chirping still remained.

The next group to look at the physical reasons behind the effect was Soto *et. al.* [20]. This work concentrated on the origin of NPR more than any other group to that point. Jones matrices were used in order to study the evolution of the polarization in the SOA as a function of the angle of injection and also, critically, as a function of intensity. They found that at high intensities the TE and TM axes were no longer the axes of the device, this implies that there was a modification of the waveguide brought about by the carrier depletion occurring due to the high intensity of the injected beam. This is due to the relationship between the carrier density and the refractive index, as the carriers are depleted there is a modulation of the refractive indices which results in the axis of the device shifting. Further studies were performed to understand the effect of NPR as a function of injected intensity [21]. It was found that NPR leads to a reduction in the contrast ratio in a TOAD configuration. The variation of the birefringence with intensity is attributed to the modulation of the gain. Soto *et. al.* expanded on their previous work related to the modification of the waveguide at high intensities [46]. Again the Jones matrices were used in this analysis. An all-optical switch was developed based on this technique whose operation was tested using a Non-Return To Zero (NRZ) 2.5 Gb/s data signal with a $2^{23} - 1$ Pseudo-Random Bit Stream (PBRS). An extinction ratio of 30 dB was found using this all-optical switch.

As well as its implementation in wavelength conversion and all-optical switching, NPR in an SOA has also been proposed as a means to implement all-optical logic gates, which are of vital importance if the prospect of optical computing and all-optical switching nodes are to be realized. Work has been carried out on Exclusive OR (XOR) gates [47] operating at 5 Gb/s and AND gates [48] using NPR in an SOA. As in [18] a polarizer is used after the SOA to allow transmission only for a specific polarization. In the case of the XOR gate the polarizer is adjusted so that there is transmission at the output of the SOA only when one of the two input beams is in the 'on' state [47]. In order for this setup to work as an XOR gate, the polarization at the output of the device due to each individual beam must be the same or very close to each other. So if one of the beams is 'on' some of the light at the output will be transmitted through the polarizer, for the case where both beams are 'off' or both beams are 'on', the polarization at the output of the SOA is such that no light passes through the polarizer. This is the function of an XOR gate. An extinction ratio of 20 dB was found using this technique. The AND gate operates in a similar setup [48]. Again a polarizer is used, but this time the polarizer is aligned so that there is maximum transmission when two control beams are in the 'on' state. These two control signals modulate the polarization of a third signal, a CW beam, which acts as the probe in the setup. So when the two control beams are 'on' the polarization of the probe is such that it is transmitted through the polarizer, a filter is then used to isolate the probe signal wavelength. An extinction ratio of 16 dB was found using this technique.

The current focus of several groups is related to the applications of NPR in terms of all-optical signal processing. Recently wavelength conversion at 10 Gb/s has been demonstrated independently by two separate groups, [22] and [49]. A new application has concentrated on all-optical 2R regeneration, which is the retiming and reshaping of optical pulses, using NPR in an SOA [50]. An Linear Optical Amplifier (LOA) was used in this work. An LOA is similar to a gain-clamped SOA, when operated in the linear regime, its gain and thus carrier density is clamped at a particular value. However, when the linear power range is exceeded, the standard saturation effects take place. The difference between an LOA and a gain-clamped SOA is that in an LOA a laser is integrated with the amplifier on the semiconductor substrate [51]. This arrangement allows for very fast switching windows to be achieved. Using a degraded input signal a receiver sensitivity improvement of over 3 dB at a Bit Error Rate (BER) of 10^{-9} is achieved for 2.5 Gb/s. In a publication by Calabretta *et. al.* attention is paid for the first time to a self-induced NPR, rather than the effect being introduced to a weak signal by a strong control beam [52]. Numerous novel all-optical signal processing techniques are demonstrated using this technique. An all-optical header processing system, an all-optical seed pulse generator for packet synchronization and an all-optical arbiter that can be used for optical buffering are demonstrated. An experiment has recently been presented demonstrating wavelength conversion using NPR in an SOA employing 120 fs optical pulses [53]. This work concentrated on the polarization of the ultrafast gain dynamics, which will be discussed in detail in Chapter 6. Another paper, presented by the same group, demonstrates the possibility to perform mode-locking at a repetition rate of 28 GHz using NPR in an SOA [54]

NPR can provide inverted and non-inverted wavelength conversion, similar to XPM, but with an experimental setup that is as simple as XGM. As well as this, NPR takes advantage of the inherent polarization dependence of commercial SOAs instead of trying to minimize its effect. The variety of applications found for NPR make it a very promising all-optical signal processing technique.

5.3 Wavelength conversion using NPR

An experiment is presented in this section to perform wavelength conversion using NPR in an SOA at a frequency of 2.5 GHz. This technique is known as XPolM. The purpose of the experiment is to optimize the experimental setup in order to obtain the most efficient wavelength converter. A lot of attention is paid to the carrier dynamics occurring in the device in order to fully understand the wavelength conversion process. Wavelength conversion is demonstrated over a range of 35 nm.

A comparison between co-propagation and contra-propagation setups in performing wavelength conversion using XPolM is presented in this chapter. The contra-propagation scheme has been used in several recent publications concerned with switching data using XPolM [55] and [56]. The co-propagation setup has also been widely used to perform switching based on this technique [17], [18] and [48]. No detailed explanation for the preference of either co- or contra-propagation is given in any of these publications, and no comparison between setups has been presented for XPolM. A paper has been presented, however, that compares the two setups for XPM [57]. It highlights the fact that the maximum bandwidth of the conversion is far less in the contra-propagation setup due to the fact that the beams are propagating in opposite directions in the device. This bandwidth limitation exists because of the transit time of a signal in the device. This limitation has also been studied in the case of XGM [58]. One advantage of the contra-propagation setup is that no filter is required at the output of the device. It is also possible to convert data to the same wavelength using contra-propagation, this is not possible using co-propagation [58].

A detailed comparison between the two setups for XPolM is presented in this section. The wavelength conversion is recorded as a function of probe wavelength, pump polarization and probe polarization. The power penalty and Q-factor were calculated as a function of these variables. As well as performing the wavelength conversion in both co- and contra-propagation setups, the XPolM experiment was performed using both inverted and non-inverted conversion techniques. The experimental setup was adjusted so that wavelength conversion using XGM could also be performed, in order that XPolM could be compared with this more established switching technique. The regenerative properties of the SOA were also examined for the case when a degraded data signal was injected into the device. The Avanex SOA was used for this experiment. The device was biased at 200 mA and temperature controlled at 23^oC.

The polarization dependent gain depletion was measured experimentally for this device and can be seen in Fig. 5.5. For low levels of injected power, below approximately -15 dBm, there is very little suppression of the gain and the TE and TM gains are equal. As the injected power is increased, there is a suppression of the gain due to gain saturation. This suppression of the gain is polarization dependent. An increasingly larger variation between the TE and TM gain is introduced as the injected power is increased. There is a difference of approximately 3 dB in the gain along orthogonal axes at an injected power of 5 dBm. This polarization dependent gain depletion is the key to performing wavelength conversion based on this technique.

The performance of the wavelength conversion was analyzed by measuring the Q-factor and the BER of the converted signal. The Q-factor is defined as the optical signal-to-noise ratio. It can be measured directly using the oscilloscope. The Q-factor is calculated by the oscilloscope using the following expression:

$$Q = \frac{I_1 - I_0}{\sigma_1 + \sigma_0} \tag{5.1}$$

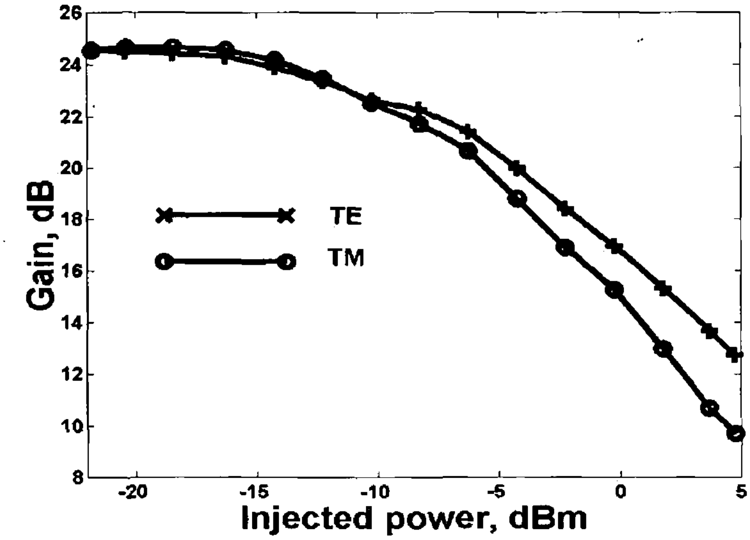

Fig. 5.5: Polarization resolved gain saturation as a function of injected power.

where I_1 and I_0 represent the mean signal level at '1' and '0', σ_1 and σ_0 represent the standard deviation of the noise on the '1' and '0' level. The BER was measured using the Bit Error Rate Tester (BERT). This parameter indicates the probability that a bit will be received in error. It was also possible to calculate the BER from the Q-factor using the equation:

$$BER \cong \frac{e^{\frac{-Q^2}{2}}}{Q\sqrt{2}} \tag{5.2}$$

This equation gives accurate results, if the noise is assumed to be Gaussian. The power penalty plot was obtained, for each of the experimental setups, by varying the received power falling on the photodetector and measuring the BER in each case.

5.3.1 Experimental setup for XPolM

Wavelength conversion was performed using XPolM at a data rate of 2.5 GHz and a PBRS of $2^7 - 1$. The co-propagation setup is shown in Fig.5.6. The data signal was obtained from a pseudo random data generator. Two optical signals were simultaneously injected into the SOA. Both optical signals were generated using external cavity tunable lasers. The wavelength of the pump signal was 1538 nm and the wavelength of the probe was varied between 1535 nm and 1570 nm. The pump signal was modulated at 2.5 GHz and then amplified to an average power of approximately 7 dBm prior to injection in the SOA, in order to saturate the gain of the device.

In [55], a large probe power of 1.58 dBm was injected into the device. This high level of

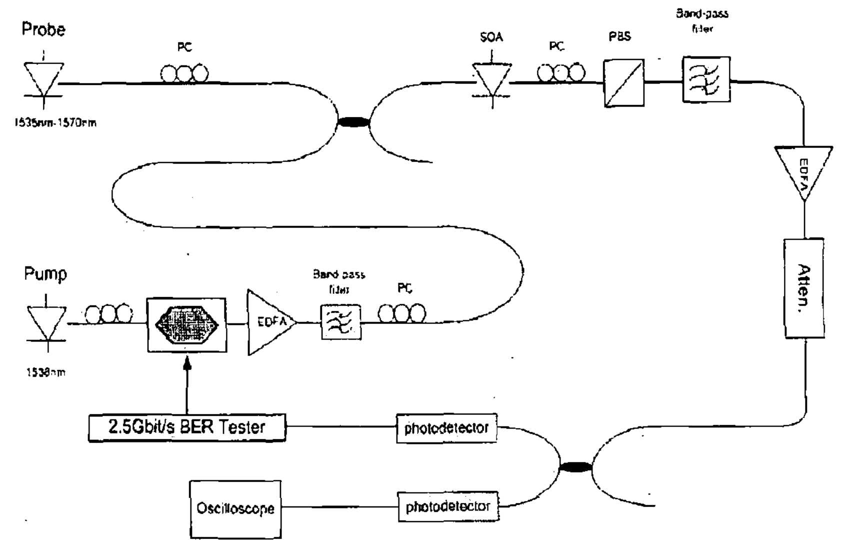

Fig. 5.6: Experimental setup for co-propagation.

injection was large enough to deplete the gain of the device, thus inducing a polarization dependence due to the probe. This is in contrast to most other publications in which the probe is kept low so as the gain depletion, and the NPR, is solely due to the pump signal in order that the largest impact of the pump is obtained. The logic is that if the probe does not induce variations in the gain along orthogonal axes, then any NPR is solely due to the pump signal, leading to the largest extinction ratio. As can be seen from the experimental results shown in Fig. 5.7, this is not the case for the experimental setup shown in Fig. 5.6. This figure shows the Q-factor obtained from non-inverted XPolM wavelength conversion as a function of the probe power. The probe power was varied from -12.2 dBm to -3.56 dBm and the Q-factor was recorded at each power. It is observed that the highest Q-factor was recorded when the probe power was maximized. The result may be explained from observation of the polarization dependent gain variation as a function of input power, shown in Fig. 5.5. The key to the argument is the nonlinear increase in the polarization dependence as a function of input power. The critical parameter to consider when performing wavelength conversion based on NPR is not the polarization dependence induced solely by the pump, rather it is the increase in polarization dependence induced by the pump which is of most relevance. As can be seen from Fig. 5.5 the polarization dependence increases as a function of intensity. The fact that the biggest extinction ratio was found when the probe signal was large implies that this additional power coupled with the pump power caused a larger variation in polarization dependence. This resulted in a larger impact of the pump power on the polarization dependence. The intensity of the probe signal defines the section of the gain saturation curve that the device is operating in upon injection of the pump. The maximum pump induced polarization dependence occurs when the probe is large due to the nonlinear increase in polarization dependence with power. This result is in agreement with the experimental setup presented in [55]. For this reason the probe signal was injected with a power of -3.56 dBm. At this level of intensity there is a difference in gain along orthogonal axes of approximately 1 dBm, as can be observed in Fig. 5.5. This was the largest probe intensity that could be injected into the SOA, after all coupling losses were considered, using the available tunable laser source. If higher probe signal intensity was required, it would be possible to further amplify the probe signal using an EDFA.

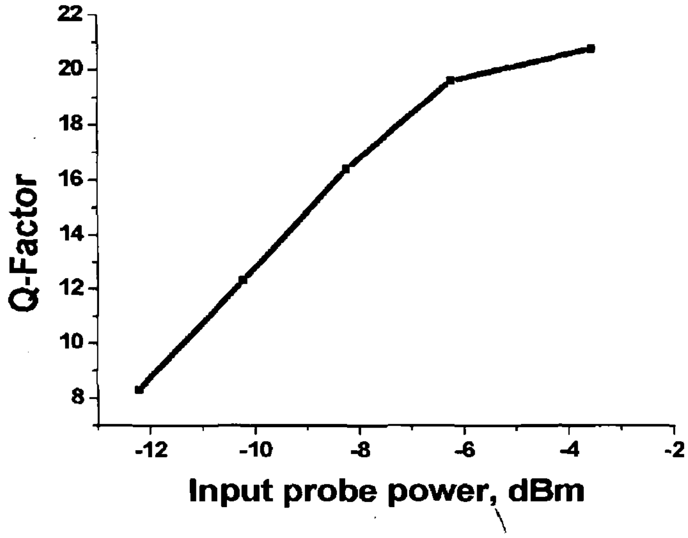

Fig. 5.7: Improvement of Q-factor as a function of injected probe intensity for non-inverted XPolM in contra-propagation.

The state of polarization of both input signals was controlled using PCs. At the output of the SOA a PC and PBS acted to control the transmission of the amplified signal, based on the polarization of the signal. It is the combination of these two components that distinguishes this setup from that of XGM. The wavelength conversion due to the polarization of the signal is based on the fact that the polarization rotation is a nonlinear process. Both inverted XPolM and non-inverted XPolM can be performed using this setup, depending on the initial transmission of the probe signal through the PBS, in the absence of the pump signal. The PC at the output of the SOA is used to maximize or minimize this transmission. In the case of inverted XPolM, the probe transmission is maximized before injection of the pump. So if the data signal transmits a '0', then the probe transmission through the PBS is maximized and inverted wavelength conversion of the '0' occurs. In the presence of a pump signal '1' level, the high intensity causes the rotation of the state of polarization of the co-propagating probe signal leading to a misalignment between the polarization of the probe signal and the polarization axis of the PBS. This results in a drop in the intensity after the PBS, the new level corresponding the '0' level. It was necessary to have a BPF after the PBS in order to select the probe signal wavelength. It is also possible to perform non-inverted XPolM, simply by minimizing the initial transmission of the probe in the absence of the pump, this leads to a '0' on the pump corresponding to a '0' on the probe. A second EDFA is used to amplify the wavelength converted signal and an attenuator is used to vary the received power falling on the photodetector. The signal can then be observed on an oscilloscope and BERT.

The second setup, that of contra-propagation, is shown in Fig.5.8. In this setup the pump and probe were injected into the device in opposite directions. A circulator was used for this purpose, without disturbing the measurement of the probe. An isolation of over 35 dB was provided by the circulator. An isolator was used at the probe end of the device to ensure that the pump signal was not injected into the probe laser. Using this setup it was possible to convert data to the same wavelength. Because the signals are injected at opposite ends of the device it was not necessary to select the correct wavelength using a BPF, but there was one included in the setup to remove any ASE that may have been transmitted through the PBS.

5.3.2 Comparison of XPolM and XGM results

Fig. 5.10 shows a comparison of the performance of inverted and non-inverted XPolM to XGM with respect to the back to back measurement, which is a plot of the received power versus the BER measured directly from the source, bypassing the wavelength converter. The experimental setup for XGM is exactly the same as the setup for XPolM, shown in Figs. 5.6 and 5.8, except that the PC and the PBS at the output of the SOA are removed in the case of XGM.

The results shown in Fig. 5.10 are for the co-propagation setup. A penalty of approximately 1 dB is introduced by both the XGM and the inverted XPolM in this setup. The power penalty plots for both techniques are almost identical. In order to achieve a BER of 10^{-9} using these two techniques, a received power of -12 dBm is required. This result suggests that inverted XPolM can match the performance of XGM in a device designed to be polarization insensitive.

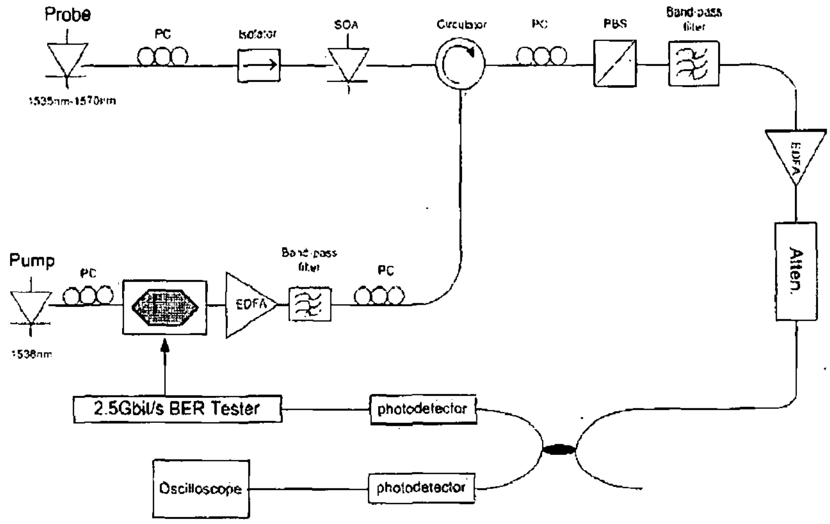

Fig. 5.8: Experimental setup for contra-propagation experiments.

The non-inverted XPolM for this setup introduces a much larger penalty than the other two techniques. From Fig. 5.10 it can be seen that a penalty of 5 dB is introduced for non-inverted XPolM. The inverted XPolM occurs simultaneously with the inherent XGM, which is also an inverted technique [22]. This is not the case for non-inverted XPolM which is reduced due to the XGM which acts to minimize its effect. This is because the non-inverted conversion occurs when the gain of the device is at its minimum due to the high intensity pump signal, leading to a weaker converted signal. In other words, the non-inverted XPolM is due to NPR in the SOA with reduced gain whereas the inverted XPolM is due to NPR occurring at the maximum unsaturated level of the gain. For this reason the Q-factor for the non-inverted conversion will not be as large as for the inverted XPolM technique and consequently the power penalty is much larger. This may be explained with the aid of Fig. 5.9. The input data is represented in Fig. 5.9a). If this signal is large enough to suppress the gain then the gain will become modulated following the inverse of the data signal, as shown in Fig. 5.9b). This process is the basis for XGM. However for XPolM this gain modulation effect is also occurring, as it is inherent to the SOA device. If inverted XPolM, represented in Fig. 5.9c), is now considered, it can be seen that the '1' level occurs when the gain of the SOA is at its peak value, i.e. there is no suppression of the gain and the converted signal is amplified by the maximum amount. Finally non-inverted XPolM is illustrated in Fig. 5.9d). In this case the '1' level occurs when the gain is suppressed due to the input data signal. This means that the converted signal receives less amplification than if the gain was not suppressed.

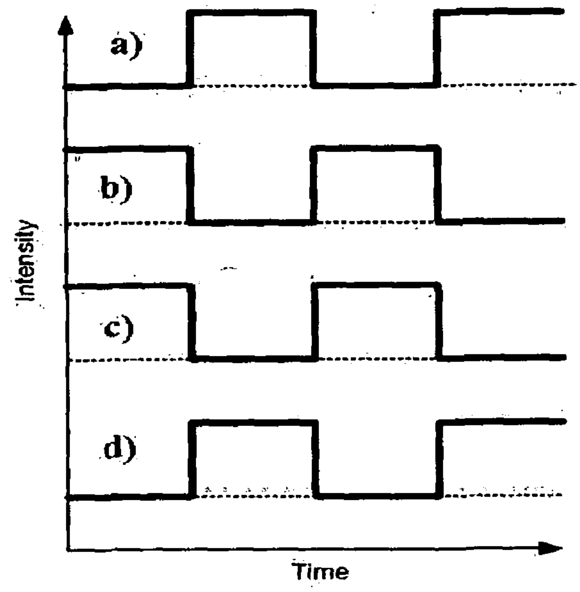

Fig. 5.9: Illustration of the conversion process where a) represents the input data signal, b) represents the suppression of the gain, c) represents the inverted XPolM signal and d) represents the non-inverted XPolM signal.

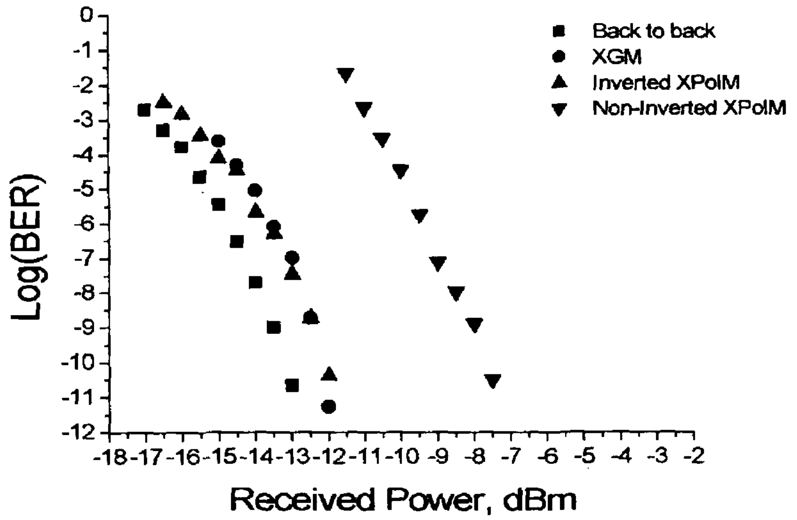

Fig. 5.10: Power penalty for various techniques in co-propagation setup.

The same results were taken for the contra-propagation setup and are illustrated in Fig. 5.11. As was found with the co-propagation setup, the performance of XGM and inverted XPolM are very similar. In the contra-propagation setup, however, the power penalty introduced by these techniques is reduced to less than 0.5 dBm. This improved performance indicates that the nonlinearities in both techniques are maximized for contra-propagation. For this setup, the intensity of the pump signal is largest after propagation through the device. For this reason the probe is injected to the SOA when the nonlinearities due to the pump are strongest. The probe then propagates through the device increasing the nonlinearities in the device to an even larger level. This is not the case for co-propagation where the initial nonlinearities of the gain are weak and the maximum nonlinearities due to the pump are not present until the point where the probe is passed to the output of the device. This full utilization of the pump power for the contra-propagation setup has been reported in the literature for XGM [59].

The most interesting difference between Fig. 5.10 and Fig. 5.11 is related to the non-inverted XPolM. In the contra-propagation technique the penalty introduced for this technique is less than 1 dB as opposed to 5 dB in the co-propagation technique. This large variation between the techniques may also be attributed to the increased nonlinearity in the contra-propagation setup. Even though the gain is saturated for the non-inverted technique, the increased nonlinearity in the polarization rotation leads to an almost identical performance of the inverted and non-inverted techniques in this set up. The fact that the inverted XPolM and the XGM still give identical performance for the contra-propagation technique indicates that the inverted XPolM performance is limited by the PBS, which has an extinction ratio of 20 dB. If this were not the case then the increased nonlinearity for the contra-propagation setup should lead to an improved performance of the inverted XPolM, as can clearly be seen for the non-inverted case.

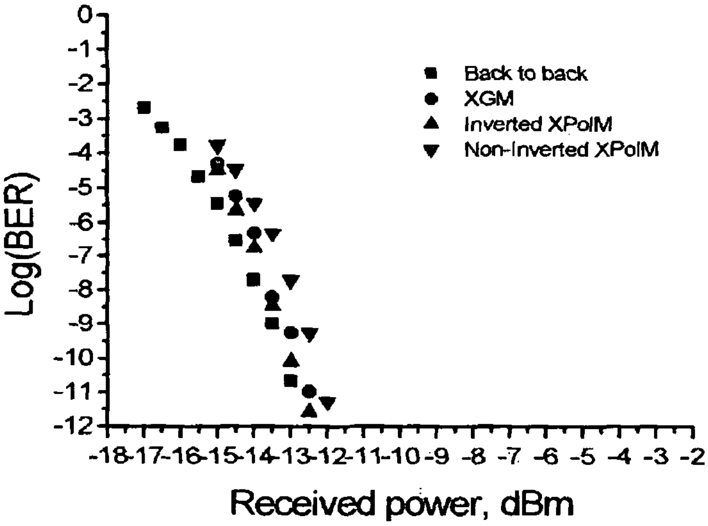

Fig. 5.11: Power penalty for various techniques in contra-propagation setup.

A more detailed comparison between XGM, inverted XPolM and non-inverted XPolM can be seen in Fig. 5.12, where the wavelength dependence of the various techniques can be seen. The wavelength of the probe signal was varied from 1535 nm to 1570 nm, whilst the pump signal wavelength was constant at 1538 nm. This is an important factor for Wavelength Division Multiplexing (WDM) systems, which are required to convert signals at different wavelengths. The key to the wavelength dependence is that the gain depletion is wavelength dependent, due to the gain spectrum of the SOA. As the probe wavelength is increased the converted signal receives less amplification, as the wavelength is moving further from the peak gain wavelength. This results in an increase in the received power required to obtain the same BER. The wavelength dependence is greatest for inverted and non-inverted XPolM in the contra-propagation setup.

Non-inverted XPolM in the co-propagation setup is wavelength independent, although a much larger received power is required for this technique, as already stated. The non-inverted XPolM conversion, for the '1' level, takes place when the gain is at its lowest level, due to gain suppression as illustrated in Fig. 5.9. The reduction of the gain is greatest at 1535 nm, as this is the wavelength closest to the peak gain wavelength. At 1535 nm, however, the effect of NPR is also greatest. As the wavelength is moved to longer wavelengths, further from the gain peak, the depletion of the gain is reduced, and so the '1' level of the non-inverted conversion reaches a higher level. The gain suppression is reduced because the gain is wavelength dependent. At the same time however, the NPR is reduced. This is also due to the wavelength being moved further from the gain peak. So as the wavelength is increased the reduced gain suppression increases the level of the converted signal, but the NPR reduces the level of the converted signal. This causes a trade-off, where the two effects balance each other, causing a negligible dependence of the wavelength conversion on the wavelength of the signal onto which the data is to be switched. For non-inverted wavelength conversion there are two factors which will determine the extinction ratio at the output of the SOA. Firstly the stronger the NPR effect then the larger the change in the state of polarization and the more light will pass through the PBS at the output of the SOA. Secondly, if it is taken that light has passed through the PBS then the amplitude of that light is determined by the gain in the SOA. These two factors oppose each other in non-inverted XPolM, leading to the wavelength independence for the co-propagation setup.

A wavelength dependence of approximately 2.5 dB is introduced to the non-inverted wavelength conversion in the contra-propagation setup. This indicates that the nonlinearities are enhanced, with the contribution from the NPR now having a larger contribution, as a function of wavelength, than the depleted gain. This additional contribution from NPR is evident as approximately 3 dBm less received power is needed in contra-propagation non-inverted XPolM as opposed to co-propagation at a wavelength of 1535 nm.

XGM has a wavelength dependence of approximately 2 dBm in the co-propagation setup as opposed to approximately 1.5 dBm for inverted XPolM in the same setup. In the contra-propagation setup, the wavelength dependence is greatest for inverted XPolM with a wavelength dependence of 3.5 dBm compared with a wavelength dependence of approximately 2 dBm for XGM in the contra-propagation setup. The increased wavelength dependence for inverted XPolM is further evidence of an increase in the impact of NPR for the contra-propagation setup. Furthermore, it can be seen that for XGM there is a relatively small variation of approximately 0.5 dBm in the wavelength dependence between the co- and contra-propagation setups.

It may be concluded from these results that the effect of NPR is maximized for the contra-propagation setup. A large wavelength dependence is observed for this setup and is attributed to the wavelength dependent gain. A smaller wavelength dependence is observed for XGM. This wavelength dependence does not vary significantly between the co- and contra-propagation setups.

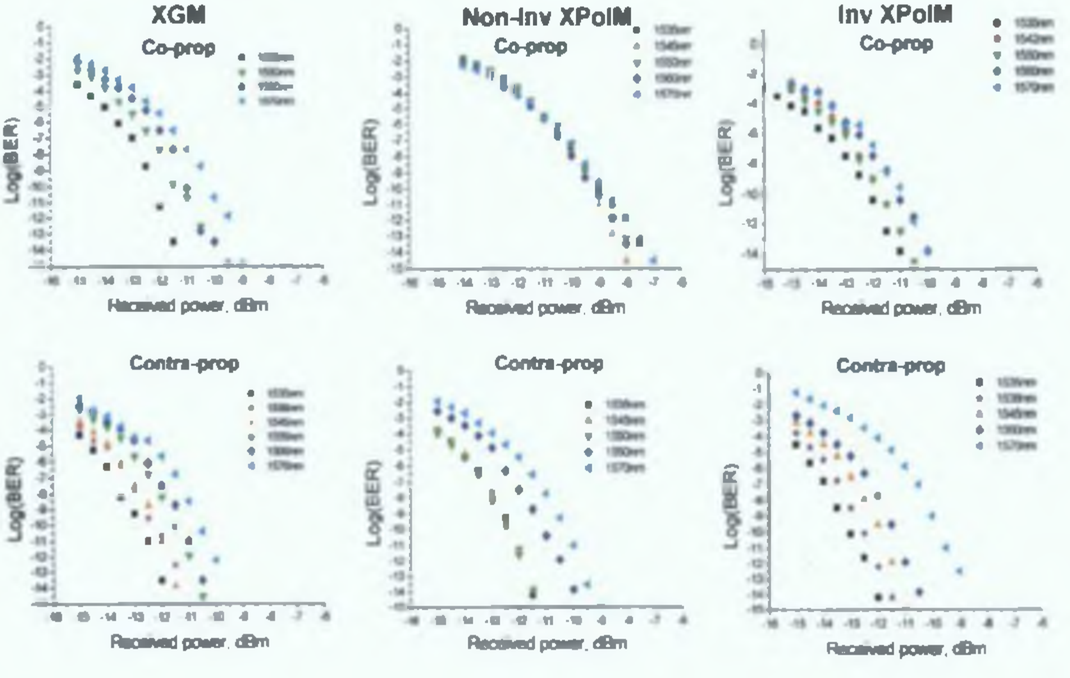

Fig. 5.12: Wavelength dependence of XGM and XPolM in co- and contra-propagation.

Fig. 5.13 shows time traces of wavelength converted data signals performed using the XPolM co-propagation setup. This data was converted from 1538nm to 1545nm. The superior performance of the inverted conversion is visible from this diagram. The non-inverted conversion has much larger amplitude noise and extinction ratio degradation.

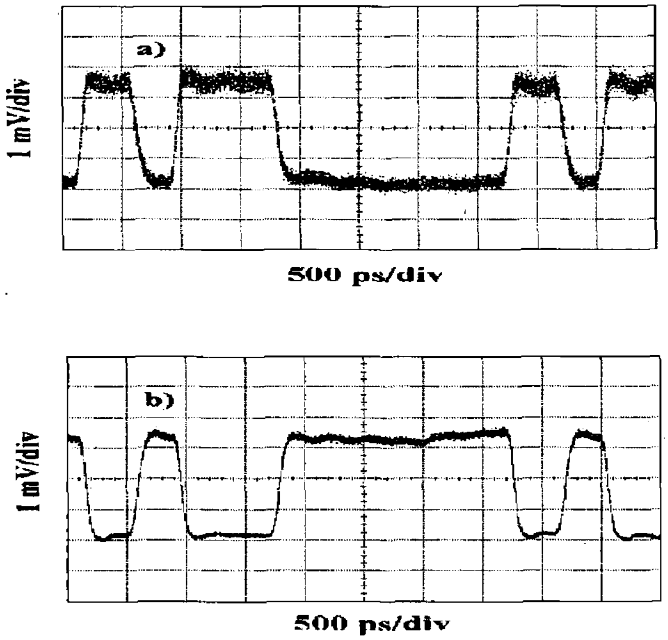

Fig. 5.13: Wavelength converted data using XPolM for a) non-inverted and b) inverted techniques.

The results in this section show that wavelength conversion due to NPR can closely match that due to XGM in a device that is designed to be polarization independent. Wavelength conversion over a range of 35 nm was demonstrated for XPolM and XGM with a maximum wavelength dependence of 3 dB. It is important to state that the restriction of the wavelength conversion to 35 nm was due to the EDFA used in the experimental setup, rather than the SOA. The EDFA was limited to amplification over the C-band. However, the SOA studied had a 3 dB spectral bandwidth of approximately 70 nm, as discussed in Sec. 2.12.1. A virtual wavelength independence was observed for non-inverted XPolM in the co-propagation setup. If devices were designed to take advantage of the inherent polarization dependence of rectangular waveguide tensile strained devices it is reasonable to expect that the performance of XPolM could be superior to that of XGM. The question of whether to use a co- or contra-propagation setup depends very much on the requirements of the system. If wavelength independence is a critical factor then non-inverted XPolM in the co-propagation setup would be most desirable, whereas if minimum received power is required XGM or XPolM in the contra-propagation setup would be favourable. In order to improve the comparison between the two techniques it would be very interesting to perform the same set of experiments using a PBS with a higher extinction ratio, in order to see if superior wavelength conversion can be obtained using inverted XPolM as opposed to XGM, using the same device as was used in the experiment presented. Furthermore, the model presented in Chapter 3 could be extended to describe this experiment. This would give details of pulse and carrier dynamics occuring in the device.

5.3.3 Suppression of noise on converted data

Noise suppression has previously been reported in bulk SOAs for XGM [59] - [62]. However, this effect has never been reported for XPolM. Wavelength conversion performed using the experimental setups of Fig. 5.6 and Fig. 5.8, using either XGM or XPolM, is accompanied by noise suppression in the converted data due to the inherent physics of the SOA. Fig. 5.14 illustrates this suppression for inverted XPolM. The input pump data was purposely degraded leading to a large amount of noise on the '1' level, introduced to the signal through noise in the electrical amplifiers and the data modulator in the experimental setup. The noise was introduced to the signal in order to imitate the degradation that may occur to a signal after propagation through long lengths of fibre. The data had a Q-factor of 13.5 before the SOA. The regeneration in the SOA resulted in a Q-factor of 21.9 for the wavelength converted data at the output of the SOA. The regeneration works by removing a large proportion of the noise on the '1' level of the injected signal. When the noisy '1' level is injected into the device, the gain of the device becomes depleted, because the pump signal is of high intensity. If the high intensity pump signal is large enough to fully deplete the gain, the noise will be transparent to the gain modulation. This will occur if the SOA is fully depleted before the noise on the signal can impact on the carrier transitions, in this way the noise can have no effect of the depletion of the gain, or the wavelength converted signal [59]. This effect occurs for XGM and also for XPolM, because XPolM occurs due to a nonlinear polarization dependence of the device gain. Fig. 5.14 illustrates inverted XPolM, so the '1' level on the pump corresponds to the '0' level on the converted signal. The reduction of the noise on the converted signal is clearly visible from the figure. The noise on the '0' level of the injected data, however, occurs in the linear region of the gain, and is thus amplified by the SOA. This can be seen in the figure as there is a larger noise on the '1' level of the converted signal than on the '0' level of the injected signal. The reduction of the gain on the '1' level, of the injected data, is far greater than this amplification of the noise resulting in a dramatic improvement of the Q-factor after propagation through the SOA.

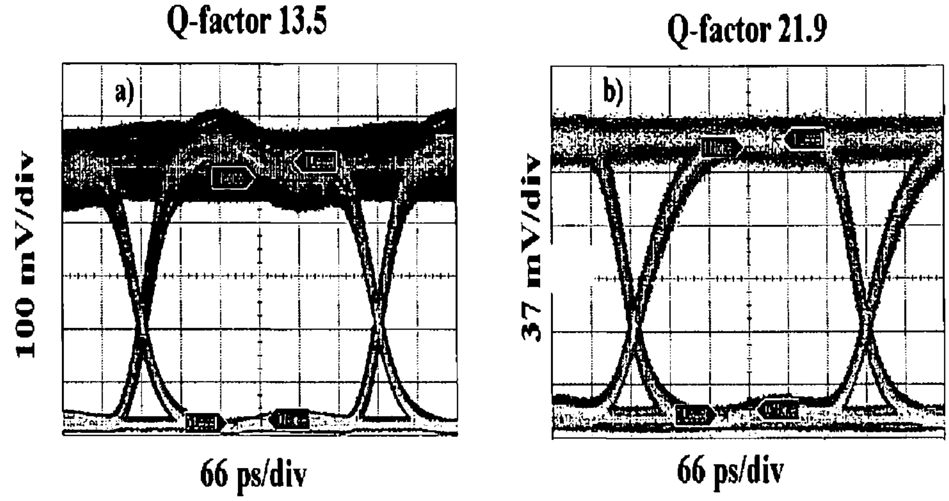

Fig. 5.14: Regeneration of the signal after propagation through the SOA showing a) the degraded injected data signal and b) the converted probe signal.

5.3.4 Polarization dependence of XPolM

The dependence of the wavelength conversion on the polarization of the probe and the pump in XPolM was measured. This was carried out in both co- and contra-propagation for the probe and in contra-propagation for the pump. The measurement was performed by placing a polarizer in series with a PC in both the pump and probe arm of the experimental setup of Fig. 5.8 and by placing the same components in the probe arm of the experimental setup of Fig. 5.6. The polarization of the light was varied by adjusting the axis of the polarizer and the PC was used to maintain a constant intensity as a function of polarization. SMF was used in this experiment, so the exact state of polarization of the light injected into the device is unknown, the important fact is that the polarization of the light was varying as the angle of injection was varied. The fibre was fixed in position for the duration of this experiment in order to have consistency between the results taken at different angles of polarization.

From observation of Fig. 5.15 it can be seen that there is a far greater variation of the Q-factor with polarization in the contra-propagation setup than in the co-propagation setup. As was discussed in previous sections of this chapter the NPR effect is greater in contra-propagation due to the additional length over which the effect can build up. This results in a larger Q-factor with a variation in the Q-factor from 23 to 17 as the angle of the polarizer is rotated from 0° to 210°, compared with a smaller Q-factor in co-propagation with a maximum of 20.5 and a minimum at 18, over the same range of polarization angles.

The dependence of the conversion on the polarization of the pump is small. Over the same polarization range the Q-factor varies from 13.25 to 12, implying that the main contribution of the pump is in terms of its high intensity. Fig. 5.15 shows the pump polarization dependence in the contra-propagation setup. A similar small pump polarization dependence was found for the co-propagation setup. The large reduction in the Q-factor when the polarization in the pump arm is controlled is due to the large reduction in the intensity of the pump due to the polarizer, which acts as a filter.

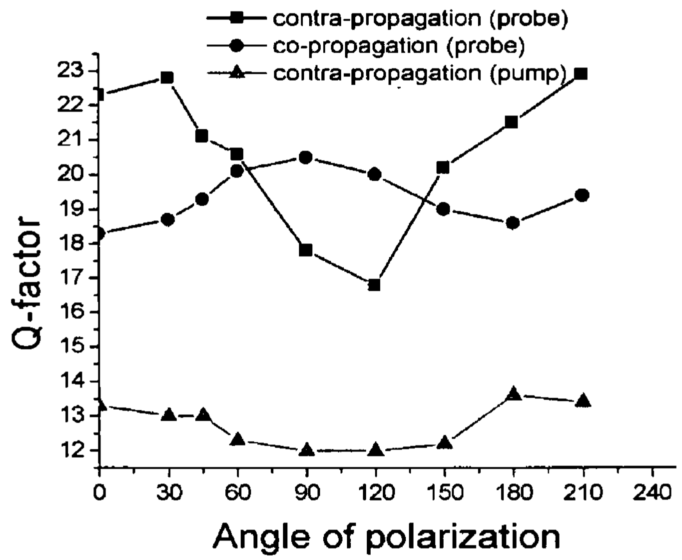

Fig. 5.15: Polarization dependence of the pump and the probe.

5.4 *Effect of gain-clamping in the SOA*

An interesting observation was made regarding the amplification of the pump data in the SOA, with relevance to XGM and XPolM. The amplified pump signal is shown in Fig. 5.16a). A large overshoot is present on the rising edge of the data signal after amplification through the device. This overshoot occurs due to the gain becoming saturated in the device [63]. Initially the data is amplified by the maximum level of gain, but as the carriers become depleted faster than they can be replenished, the gain has to reduce until the carriers recover. In Fig. 5.16a) it is observed that after a decay in the '1' level of the data signal a steady state level for the '1' level occurs. The time between the initial high level for the '1' and this steady-state value is approximately 300 ps. This is the conduction-valence band transit time, or the time it takes to stimulate the emission of all excited carriers in the conduction band. This technique could be used in order to approximate this transit time. Fig. 5.16b) also shows the amplified pump at the output of the SOA, but in this case the probe signal is also injected, in co-propagation, into the device. It can now be observed that the large overshoot that was present in the absence of the probe is now reduced dramatically. The reason for this is that the pump signal is unable to drive the device deep into depletion because the probe also contributes to the removal of carriers from the conduction band and the pump can only deplete those carriers remaining after the probe has been amplified. This results in the gain becoming clamped at a level that is determined by the level of the probe signal. In this case, the extinction ratio is improved from approximately 9.56 in the pump only setup to approximately 13.1 in the pump and probe setup. This is a somewhat counter-intuitive result, as one would assume there would be a greater extinction when the signal is injected into the device on its own. Again the gain-clamping can explain this result. When the probe is injected into the device the pump signal is unable to force the device into saturation and so the gain is maintained at a higher level than in the absence of the probe. This leads to a higher amplification of the signal. This effect occurs for XGM, but also for XPolM, as gain suppression occurs inherently in the SOA, regardless of the conversion scheme employed. The gain clamping effect is very useful in understanding the dynamics of the SOA and in understanding wavelength conversion using XGM and XPolM. These techniques are effectively performing two operations at once. Firstly they are converting data to a new wavelength and, secondly, the CW probe signal is clamping the gain so that the device never operates deep in saturation.

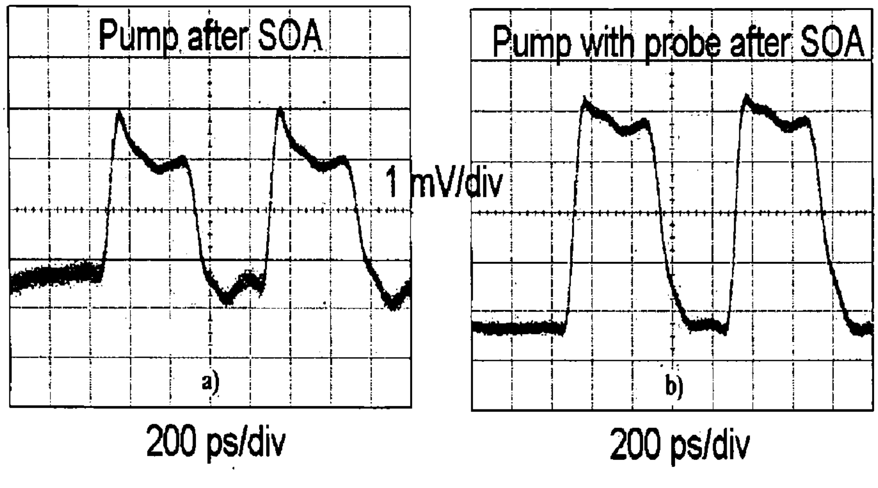

Fig. 5.16: Gain clamping effect showing the pump after propagation through the SOA a) with and b) without the probe.

5.5 Conclusions

In conclusion, the SOA was analyzed for use in all-optical signal processing systems. Wavelength conversion, using the NPR effect, was investigated experimentally over a range of 35 nm. The span of the conversion was limited by the EDFA, which was designed for operation in the C-band. The SOA used in this experiment had a spectral bandwidth of 70 nm, which suggests that it would be possible to extend the span beyond 35 nm. This technique was compared to XGM in the same device. XPolM was found to match the performance of XGM in the inverted case. Non-inverted wavelength conversion, which cannot be obtained using XGM, was demonstrated using XPolM. The experiments were carried out in both co- and contra-propagation. A larger wavelength dependence was observed for the contra-propagation setup, although this configuration required less received power at wavelengths close to the peak gain wavelength.

Regeneration of the converted signal was also found experimentally, with an improvement in Q-factor from 13.5 to 21.9 due to the gain dynamics in the SOA. The polarization dependence of the pump and of the probe was tested using a polarizer in series with a PC. A large polarization dependence of the Q-factor was found for the probe, with a much smaller dependence found for the pump. This indicates that the primary function of the pump in this setup is to provide enough intensity to saturate the gain of the amplifier. Finally the clamping of the gain in an SOA was investigated. This effect occurs when two signals are propagating in the device. From the results of these experiments it can be concluded that the polarization dependence of SOAs is a feature of these devices that can be exploited for use in optical systems.

The XPolM presented in this chapter was caused by the interband carrier recombinations. There is a fundamental limit of approximately 200 GHz in the speed at which this conversion can operate [16]. In order to extend the operation of all-optical signal processing into the THz range it is necessary to consider other possibilities. The intra-band gain processes have been proposed as a means to obtain THz operation. Experimental results are presented in the next chapter which investigate the polarization dependence of these intra-band processes in order to assess the potential to perform XPoLM in the THz range.

BIBLIOGRAPHY

[1] "http://www.internetworldstats.com".

[2] S. Tariq, M.K. Dhodhi, J.C. Palais, and R.E. Ahmed. "Next generation DWDM networks: Demands,capabilities and limitations". *IEEE Canadian Conf. on Elec. and Comp. Eng. 2000,* vol.2:pp.1003–1007, 2000.

[3] G. Held. "On the road to OC-768". *IT Professional*, vol.3:pp.46–48, 2001.

[4] S. Nagaoka, and Y. Suzuki. "'Compact optomechanical switches and their applications in optical communication and testing systems'. *Proc. IEEE MEMS'97*, pages pp.366–371, 1997.

[5] P. De Dobbelaere. "Digital MEMS for optical switching". *IEEE communications magazine*, vol.40(no.3):pp.88–95, 2002.

[6] Xiaohua ma, G.S. Kuo. "Optical switching technology comparison: Optical MEMS vs. other technologies". *IEEE Optical Communications*, pages pp.16–23, November 2003.

[7] L.Y. Lin. "High-density connection-symmetric free-space micromachined polygon optical cross-connects with low loss for WDM networks". *Proc. OFC'98*, page PD24, 1998.

[8] S. Hengstler, J.J. Uebbing, and P. McGuire. "Laser-activated optical bubble switch element ". *IEEE LEOS*, pages pp.117–118, 2003.

[9] Agilent photonic switching platform: N3565a 32 x 32 photonic switch, tech spec, www.agilent.com.

[10] J.J. Prisco. "A low-crosstalk liquid crystal optical switch". *IEEE J. Lightwave Technology*, vol.3(no.1):pp.37–38, 1985.

[11] K. Noguchi. "Optical multichannel switch composed of liquid-crystal light-modulator arrays and birefringent crystals". *IEEE J. Sel. Top. in Quantum Electronics*, vol.33:pp.1627–1629, 1997.

[12] J.W. Lou, J.K. Andersen, J.C. Stocker, M.N. Islam, and D.A. Nolan. "Polarization insensitive demultiplexing of 100Gb/s words using a twisted fiber nonlinear optical loop mirror". *IEEE Photonics Tech. Lett.*, vol.11(no.12):pp.1602–1604, 1999.

[13] E. Yamada, and M. Nakazawa. "Reduction of amplified spontaneous emission from a transmitted soliton signal using a nonlinear amplifying loop mirror and a nonlinear optical loop mirror". *IEEE J. Quantum Electronics*, vol.30(no.8):pp.1842–1850, 1994.

[14] J.M. Tang, P.S. Spencer, and K.A. Shore. "Analysis of operating characteristics of TOADs using gain saturation and nonlinear gain in SOAs". *IEE proc. Optoelectronics*, vol.145(no.1):pp.83–87, 1998.

[15] R.J. Manning, A.E. Kelly, I.D. Philips, A.D. Ellis, A.J. Postie, and K.J. Blow. "Recent advances in all-optical signal processing using semiconductor optical amplifiers". *IEEE LEOS*, vol.2:pp.447–448, 1999.

[16] D. Cotter, R.J. Manning, K.J. Blow, A.D. Ellis, A.E. Kelly, D. Nesset, I.D. Phillips, A.J. Poustie, D.C. Rogers. "Nonlinear optics for high-speed digital information processing". *Science*, vol.286:pp.1523–1528, 1999.

[17] D.M. Patrick, A.D. Ellis, D.A.O Davies, M.C. Tatham and G. Sherlock. "Demultiplexing using polarization rotation in a semiconductor laser amplifier". *IEE Electronic Letters*, vol.30(no.4):pp.341–342, 1994.

[18] M.F.C. Stephens , M. Asghari, R.V. Penty and I.H. White. "Demonstration of ultrafast all-optical wavelength conversion utilizing birefringence in semiconductor optical amplifiers". *IEEE Photonics Tech. Letters*, vol.9(no.4):pp.449–451, 1997.

[19] M. Asghari, I.H. White and R.V. Penty. "Wavelength conversion using semiconductor optical amplifiers". *Journal of Light. Tech.*, pages pp.1181–1190, 1997.

[20] H. Soto, D. Erasme and G. Guekos. "Cross polarization modulation in semiconductor optical amplifiers". *IEEE Photonics Tech. Letters*, vol.11:pp.970–972, 1999.

[21] R.J. Manning, A. Antonopoulos, R. Le Roux, and A.E. Kelly. "Experimental measurement of nonlinear polarisation rotation in semiconductor optical amplifiers". *IEE Electronic Letters*, vol.37(no.4):pp.229–231, 2001.

[22] Y. Liu, M.T. Hill, E. Tangdiongga, H. de Waardt, N. Calabretta, G.D. Khoe and H.J.S. Dorren. "Wavelength conversion using nonlinear polarization rotation in a single

semiconductor optical amplifier". *IEEE Photonics Tech. Letters*, vol.15(no.1):pp.90–92, 2003.

[23] H.J.S. Dorren, D. Lenstra, Y. Liu, M.T. Hill and G.D. Khoe. "Nonlinear polarization rotation in semiconductor optical amplifiers: Theory and application to all-optical flip-flop memories". *IEEE J. Quantum Electronics*, vol.39(no.1):pp.141–148, 2003.

[24] B. Glance, J.M. Wiesenfeld, U. Koren, A.H. Gnauck, H.M. Presby, and A. Jourdan. "High performance optical wavelength shifter". *IEE Electronic Letters*, vol.28(no.18):pp.1714–1715, 1992.

[25] F. Girardin, G. Guekos, and A. Houbavlis. "Gain recovery of bulk semiconductor optical amplifiers". *IEEE Photonics Tech. Letters*, vol.10(no.6):pp.784–786, 1998.

[26] R.J. Manning, D.A.O. Davies, D. Cotter, and J.K. Lucek. "Enhanced recovery rates in semiconductor laser amplifiers using optical pumping'. *IEE Electronic Letters*, vol.30(no.10):pp.787–788, 1994.

[27] R.J. Manning, D.A.O. Davies, and J.K. Lucek. "Recovery rates in semiconductor laser amplifiers: Optical and electrical bias dependencies'. *IEE Electronic Letters*, vol.30(no.15):pp.1233–1235, 1994.

[28] R.J. Manning, D.A.O. Davies. "Three-wavelength device for all-optical signal processing'. *Optics Letters*, vol.19(no.12):pp.889–891, 1994.

[29] A.D. Ellis, A.E. Kelly, D. Nesset, D. Pitcher, D.G. Moodie, and R. Kashyap. "Error free 100Gbit/s wavelength conversion using grating assisted cross-gain modulation in 2mm long semiconductor amplifiers". *IEE Electronic Letters*, vol.34(no.34):pp.1958–1959, 1998.

[30] J. Mørk, M.L. Nielsen, and T.W. Berg. "The dynamics of semiconductor optical amplifiers". *Optics and Photonic News*, pages pp.43–48, July 2003.

[31] S. Nakamura, Y. Ueno, and K. Tajima. "'168-Gb/s all-optical wavelength conversion with a symmetric Mach-Zehnder type switch'. *IEEE Photonics Tech. Lett.*, vol.13(no.10):pp.1091–1093, 2001.

[32] A. Uskov, J. Mørk, and J. Mark. "Wavelength mixing in semiconductor laser amplifiers due to carrier heating and spectral-hole burning". *IEEE J. Quantum Electronics*, vol.30(no.8):pp.1769–1781, 1994.

[33] D.I Forsyth, and M.J. Connelly. “Dual semiconductor optical amplifier polarization independent wavelength conversion using four-wave mixing with optoelectronic feedback”. *IEEE LEOS*, vol.1:pp.396–397, 2004.

[34] S. Arahira, and Y. Ogawa. “160-Gb/s all optical encoding experiments by four-wave mixing in a gain-clamped SOA with assist-light injection”. *IEEE Photonics Tech. Letters*, 16(2):pp.653–655, 2004.

[35] H. Kawaguchi. “Ultrafast all-optical switching using four-wave mixing in semiconductor optical amplifiers for wavelength routing”. *Transparent Optical Networks Conf.*, vol.2:pp.33–36, 2004.

[36] T. Kakitsuka, Y. Shibata, M. Itoh, Y. Kadota, Y. Tohmori, and Y. Yoshikuni. “Influence of buried structure on polarization sensitivity in strained bulk semiconductor optical amplifiers”. *IEEE J. Quantum Electronics*, vol.38(no.1):pp.85–92, 2002.

[37] R.H. Stolen, and A. Ashkin. “Optical kerr effect in glass waveguide”. *Appl. Phys. Lett.*, vol.22:pp.294–296, 1973.

[38] B.E. Olsson, and P.A. Andrekson,. “Polarization independent Kerr-switch using a polarization diversity loop”. *ECOC’98*, pages pp.185–186, 1998.

[39] K. Kitayama, Y. Kimura, and S. Seikai. “Fibre-optic logic gate”. *Appl. Phys. Lett.*, vol.46:pp.317–319, 1985.

[40] T. Morioka, M. Saruwatari, and A. Takada. “Ultrafast optical multi/demultiplexer utilizing optical Kerr effect in polarization-maintaining single-mode fibres”. *IEE Electronic Letters*, vol.23:pp.453–454, 1987.

[41] R.H. Stolen, J. Botineau, and A. Ashkin. “Intensity discrimanation of optical pulses with birefringent fibres”. *Optical Letters*, vol.7:pp.512–514, 1982.

[42] M. Horowitz, and Y. Silberberg. “Nonlinear filtering by use of intensity-dependent polarization rotation in birefringent fibres”. *Optical Letters*, vol.22:pp.1760–1762, 1997.

[43] M. Hofer, M.E. Fermann, F. Haberl, M.H. Ober, and A.J. Schmidt. “Mode locking with cross-phase and self-phase modulation”. *Optical Letters*, vol.16:pp.502–504, 1991.

[44] C. Vinegoni, M. Wegmuller, B. Huttner, and N. Gisin. "Measurement of nonlinear polarization rotation in a highly birefringent optical fibre using a Faraday mirror". *J. Opt. A: Pure Appl. Opt.*, vol.2:pp.314–318, 2000.

[45] H.J. Lee, M. Sohn, K. Kim, and H.G. Kim. "Wavelength dependent performance of a wavelength converter based on cross-gain modulation and birefringence of a semiconductor optical amplifier". *IEEE Photonics Tech. Letters*, vol.11(no.2):pp.185–187, 1999.

[46] H. Soto, J.C. Dominguez, D. Erasme and G.Guekos. "Demonstration of an all-optical switch using cross polarization modulation in semiconductor optical amplifiers". *Microw. and Optic. Tech. Letters*, vol.29(no.3):pp.205–209, 2001.

[47] H. Soto, D. Erasme, and G. Guekos. "5-Gb/s XOR optical gate based on cross-polarization modulation in semiconductor optical amplifiers". *IEEE Photonics Tech. Letters*, vol.13(no.4):pp.335–337, 2001.

[48] H. Soto, C.A. Diaz, J. Topomondzo, D. Erasme, L. Schares, and G. Guekos. "All-optical AND gate implementation using cross-polarization modulation in a semiconductor optical amplifier". *IEEE Photonics Tech. Letters*, vol.14(no.4):pp.498–500, 2002.

[49] C.S. Wong, and H.K. Tsang. "Polarization-independent wavelength conversion at 10 Gb/s using birefringence switching in a semiconductor optical amplifier". *IEEE Photonic Tech. Letters*, vol.15(no.1):pp.87–89, 2003.

[50] M. Zhao, J. de Merlier, G. Morthier, and R. Baets. "All-optical 2R regeneration based on polarization rotation in a linear optical amplifier". *IEEE Photonics Tech. Letters*, vol.15(no.2):pp.305–307, 2003.

[51] D.A. Francis, S.P. DiJaili, and J.D. Walker. "A single-chip linear optical amplifier". *OFC 2001*, vol.35:pp.414–415, 2001.

[52] N. Calabretta, Y. Liu, F.M. Huijskens, M.T. Hill, H. de Waardt, G.D. Khoe, and H.J.S. Dorren. "Optical signal processing based on self-induced polarization rotation in a semiconductor optical amplifier". *IEEE Photonics Tech. Letters*, vol.22(no.2):pp.372–381, 2004.

[53] A.K. Mishra, X. Yang, D. Lenstra, G.D. Khoe, and H.J.S. Dorren. "Wavelength conversion employing 120-fs optical pulses in an SOA-based nonlinear polarization switch". *IEEE J. Sel. Top. Quantum Electronics*, vol.10(no.5):pp.1180–1186, 2005.

[54] Z. Li, X. Yang, E. Tangdiongga, H. Ju, G.D. Khoe, H.J.S. Dorren, and D. Lenstra. "Simulation of mode-locking by nonlinear polarization in a semiconductor optical amplifier". *IEEE J. Quantum Electronics*, vol.41(no.6):pp.808–816, 2005.

[55] G. Liu, M.Y. Hill, E. Tangdiongga, H. de Waardt, N. Calabretta, G.D. Khoe , and H.J.S. Dorren. "Wavelength conversion using nonlinear polarization rotation in a semiconductor optical amplifier ". *IEEE J. Quantum Electronics*, vol.15(no.1):pp.90–92, 2003.

[56] L.Q. Guo, and M.J. Connelly. "All optical AND using nonlinear polarization rotation in a semiconductor optical amplifier". *OSA, Optical amp. and their appl.*, 2005.

[57] S. Bischoff, A. Buxens, S.T. Fischer, M. Dulk, A.T. Clausen, H.N. Poulsen, and J. Mørk. "Comparison of all-optical co- and counter-propagating high-speed signal processing in SOA-based Mach-Zehnder interferometers". *Kluwer Optical and Quantum electronics*, vol.33:pp.907–926, 2001.

[58] D. Nesset, T. Kelly, and D. Marcenac. "All-optical wavelength conversion using SOA nonlinearities". *IEEE Comm. magazine*, pages pp.56–61, 1998.

[59] K. Inoue. "Noise transfer characteristics in wavelength conversion based on cross-gain saturation in a semiconductor optical amplifier". *IEEE Photonics Tech. Letters*, vol.8(no.7):pp.888–890, 1996.

[60] I. White, R. Penty, M. Webster, Y.J. Chai, A. Wonfor, and S. Shahkooh. "Wavelength switching components for future photonic networks". *IEEE Comms magazine*, vol.40(no.9):pp.74–81, 2002.

[61] S.I. Pegg, M.J. Fice, M.J. Adams, and A. Hadjifotiou. "Noise in wavelength conversion by cross-gain modulation in a semiconductor optical amplifier". *IEEE Photonics Tech. Lett.*, vol.11(no.6):pp.724–726, 1999.

[62] S-J. Kim, J-H. Han, J-S Lee, and C-S Park. "Intensity noise suppression in spectrum-sliced incoherent light communications systems using a gain-saturated semiconductor optical amplifier". *IEEE Photonics Tech. Lett.*, vol.11(no.8):pp.1042–1044, 1999.

[63] D.D. Marcenac, A.E. Kelly, D. Nesset, and D.A.O. Davies. "Bandwidth enhancement of wavelength conversion via cross-gain modulation by semiconductor optical amplifier cascade". *IEE Electronic letters*, vol.31(no.17):pp.1442–1443, 1995.

6. ULTRA-FAST ALL-OPTICAL SIGNAL PROCESSING USING NPR IN A BULK SOA.

6.1 Introduction

As the development of all-optical signal processing continues, higher and higher data rates will be achieved. From [1] the relatively small carrier density change required for a differential phase shift, $\partial\phi$, equal to π and the high rate at which carriers are replenished due to the injection current lead to the possibility of performing switching using asymmetric interferometers at data rates higher than 100 GHz. The ultimate limit on the speed of such interferometers is the time required to recover the equilibrium Fermi-Dirac distribution of the carriers. This is believed to be 5 ps [2]. In order to achieve switching speeds higher than this fundamental limit of approximately 200 GHz it is therefore necessary to employ a mechanism other than the carrier recombination between conduction and valence bands. The intra-band gain dynamics, introduced in Sec. 2.10, can be used to achieve even higher data rates. These processes recover on time scales in the picosecond and sub-picosecond range, leading to a potential performance of all-optical switching in the THz range.

The possibility to operate a MZI, employing SOAs, at data rates of 640 GHz has been demonstrated in the literature [3]. There is a drawback however. The on/off ratio is severely degraded for this speed due to the increased gain suppression and reduced LEF caused by the intra-band gain nonlinearities. In the last chapter the techniques of XGM, XPM, NPR and FWM were discussed. The first three of these switching techniques were discussed as originating solely from the inter-band carrier recombinations whilst the FWM technique was described as being fundamentally limited due to the intra-band recombinations, for large wavelength detuning between the pump and the probe. The intra-band gain dynamics have recently received a lot of attention from various groups as a means to extend the speed of optical networks using these techniques [3] - [7].

The NPR effect has been discussed in the preceding chapters as a possible alternative to XGM, XPM and FWM. In order that interest be maintained in this technique it is critical that the NPR technique can compete with the performance of the more established techniques. The impact of NPR on femtosecond pulses has been investigated recently both

theoretically and experimentally [8] and [9]. These are the first studies concerned with the polarization dependence of the ultra-fast gain dynamics. It is also vital to measure the polarization dependence of the gain dynamics in order to determine their effect on high speed optical networks employing SOAs in general. A large polarization dependence would limit the speed of XGM, XPM and FWM. This is due to the random polarization in SMF.
Little attention is paid in the literature to the impact of the intraband effects on the propagation of pulses in the order of several picoseconds, only a few studies have been presented [7] - [11]. This is despite a separate experiment in which a critical pulsewidth of 10 ps was measured and calculated below which the effects of intra-band gain dynamics dominate the gain saturation [12]. An experiment is presented in this chapter in which the polarization dependence of 2 ps pulses propagating in an SOA is studied. This dependence was analyzed in both the temporal and spectral domains using the FROG technique. A polarization dependence in the propagation of these pulses was found, indicating a polarization dependence of the ultra-fast gain processes. A second experiment is then presented in which the polarization dependent recovery times and LEFs, associated with the gain dynamics, were measured. This experiment is based on varying the detuning between the pump and the probe in a FWM setup.

6.2 Polarization dependence of 2 ps pulses propagating through the SOA

Due to the fact that the ultra-fast gain dynamics are dominant for pulsewidths below 10 ps [12], it is an interesting experiment to look at the polarization dependence of 2 ps pulses propagating through the SOA. If optical networks are to operate above the limiting speed due to carrier recombinations, then it is important to investigate the polarization dependence of sub-10 ps pulse propagation, because the standard fibre in use in such systems is SMF. The polarization of light propagating through this fibre is continually varying and is therefore unknown at the point where it is injected into the SOA. Any polarization dependence of the SOA is thus a limiting factor on the performance of the system.

Several groups have investigated the propagation of 2 ps pulses through the SOA [11], [13] and [14]. These groups injected high intensity signals into the SOA and identified TPA as being the dominant gain dynamic for these pulses. A detailed study of the propagation of 2 ps pulses in the femtojoule range is reported in this chapter. For these energies TPA may be considered negligible and CDP, CH and SHB are considered to be the main factors determining the gain recovery. A recent study of the ultrafast phase dynamics in the SOA showed that the LEFs associated with CH and SHB are much lower than that due to the CDP [7]. This result indicates that the main contribution of CH and SHB is to suppress the gain in the device. Much larger phase variations can be found if the pulsewidth is shorter, i.e. in the hundreds of femtoseconds range, in which case the ultrafast Kerr effect becomes important [5].

Interest in the NPR effect on sub-picosecond pulses has also received a lot of attention in recent years [8] and [9]. In the literature a model has been presented which accounts for the propagation of sub-picosecond pulses in an SOA. This model accounts for CDP, CH, SHB and TPA in the device. The polarization dependence of these parameters is explained by the tensile strain introduced to the device. The experiment presented in this section aims to measure the polarization dependence of 2 ps passively mode-locked pulses propagating through an SOA using the FROG technique. This technique has been used before to study the propagation of femtosecond pulses through an SOA [15], but it has only recently been used to measure pulses in the order of 2 ps [16] - [18].

6.2.1 Frequency resolved optical gating (FROG) technique

FROG is a technique used to measure optical pulses of pulsewidth in the range from tens of femtoseconds to tens of picoseconds. The outstanding feature of this technique is that the measurement is resolved in both the time and frequency domains, giving complete characterization of a pulse [19] - [22]. FROG is similar to autocorrelation in the sense that the measurement is performed by overlapping a pulse with a delayed version of itself in some nonlinear optical medium [23]. A Second-Harmonic Generation (SHG) crystal was the nonlinearity used in this experiment. It should be noted that the SHG process involves generating signals at twice the frequency of the injected signal. The key difference is that for autocorrelation the overlapped pulses are measured using a photodetector whereas for FROG a spectrometer is used. Instead of measuring the signal energy vs. delay, which yields an autocorrelation, FROG involves measuring the signal spectrum vs. delay. A diagram of the experimental setup used for the SHG FROG technique is shown in Fig. 6.1. A beam splitter splits the beam and passes one beam to a variable delay line, which delays one pulse with respect to the other. The pulses are then combined in the SHG crystal. The parameter that is measured with this setup is the spectrogram of the pulse, which for the SHG FROG case may be written as follows:

$$I_{FROG}(\omega,\tau) = \left| \int_{-\infty}^{\infty} E(t)E(t-\tau)exp(-i\omega t) \right|^2 \tag{6.1}$$

where $E(t)$ is a representation of the signal electric field in time and $E(t-\tau)$ represents the electric field in time delayed by τ seconds. The information on the phase is known due to the exponential phase term in the expression. This spectrogram is in a hybrid time-frequency domain. It contains spectral information at each point of overlap between the pulse and the delayed version of itself. In order to obtain all the relevant information in each domain, separately, the two-dimensional phase-retrieval problem is solved. There are several ambiguities associated with this solution, such as in absolute phase and with respect to translation in time. These ambiguities are trivial and can be resolved through analysis of the pulse. The temporal and spectral resolutions of the FROG used in this experiment are 100 fs and 0.1 nm at 1550 nm, respectively.

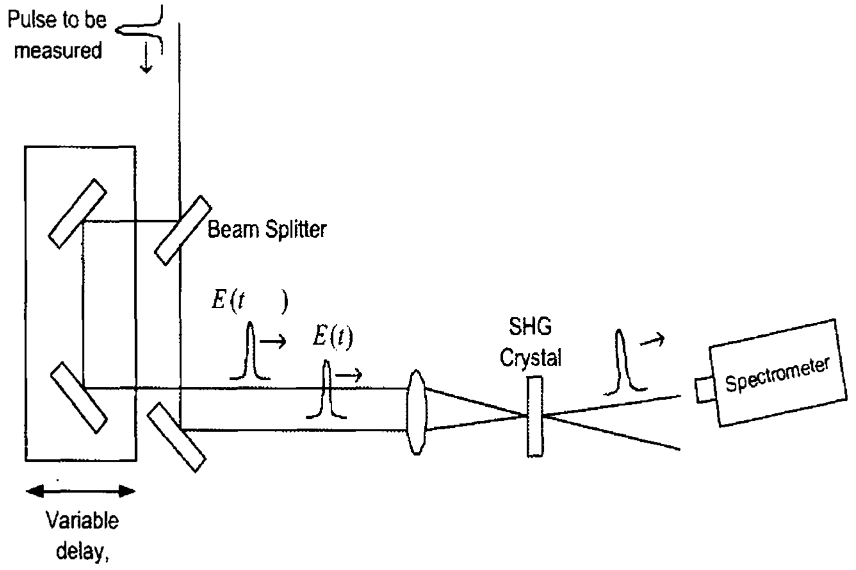

Fig. 6.1: Experimental setup of the FROG device

6.2.2 Experimental setup

The experimental setup is shown in Fig. 6.2. The Avanex SOA was used for this experiment. The device was biased at 200 mA and temperature regulated at 23 $^\circ C$. 2 ps pulses were generated from a passively mode-locked laser, centred at 1540 nm, with a repetition frequency of 10 GHz. The peak power of the pulses was 30 mW, corresponding to a pulse energy of approximately 60 fJ and an average power of 600 μW. The pulses were injected into the SOA using PM lensed fibre. A polarizer was used to align the light along the axis of the PM fibre, in order to ensure a linear state of polarization for the light injected into the device. The PC before the polarizer allowed control of the intensity of the light polarized in this direction. The angle that the linearly polarized light made with respect to the axis of the device was controlled by physically rotating the lensed fibre. A CW laser was also injected into the SOA at a wavelength of 1538 nm, only 2 nm from the signal wavelength.

The purpose of this signal was to deplete carriers in the device in order to observe the polarization dependence of the pulses in the nonlinear gain regime of the SOA. This signal was also polarized along the axis of the PM lensed fibre and a PC was placed in the CW arm in order to control its intensity. A BPF, centred at 1540 nm, removed the amplified CW signal at the output of the device. The Full-Width Half Maximum (FWHM) of the filter was 1.75 nm. The signal was positioned spectrally close to the pulses so that the induced carrier depletion would have the largest impact on the pulses. It would also be possible to deplete carriers in the device by amplifying the pulses using an EDFA. However, for the pulsewidths used in this experiment significant temporal and spectral broadening result from the amplification of 2 ps pulses in standard EDFAs, due to the long length of the doped fibre. An EDFA was used, prior to injection into the FROG, to amplify the pulses to a level large enough for analysis with the FROG. This EDFA differed from the standard device in that it was specifically designed for the amplification of pulses with a width in the order of 2 ps. This involved designing the amplifier with a much shorter length of doped fibre, significantly reducing the temporal and spectral broadening introduced.

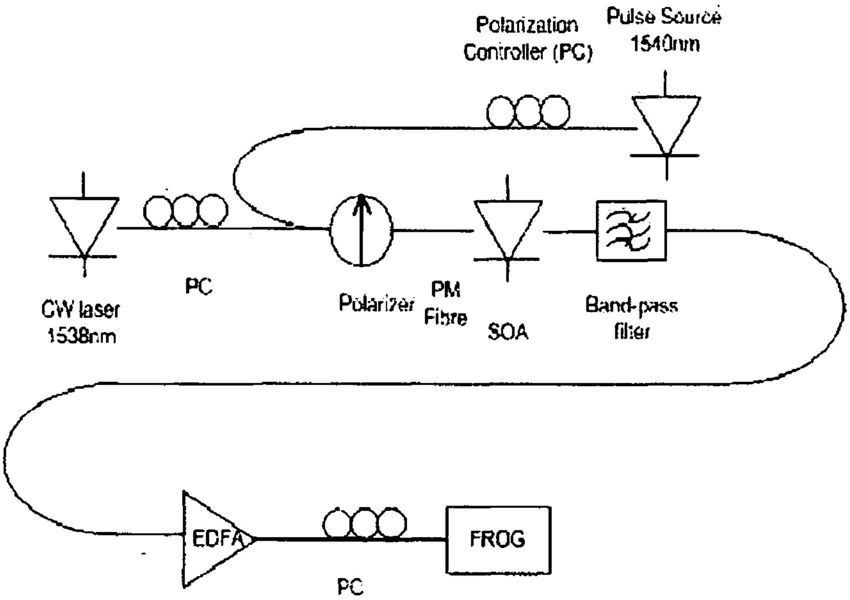

Fig. 6.2: Experimental setup used to determine the polarization dependence of 2 ps pulses injected into the SOA

6.2.3 Results

The polarization dependence of the pulses was recorded after propagation through the SOA for several values of CW injection. The pulse energy was kept constant at approximately 60 fJ, in each case. The intensity and chirp were recorded using the FROG. The polarization was varied in steps of 15° from 0° to 90°, although the figures presented in this section illustrate the results at the most significant angles, in order to preserve clarity. These results show the polarization dependence of the propagation for levels of CW injection of 0 mW, 1 mW and 4 mW.

The filter after the SOA limits the spectrum of the data measured with the FROG to a spectral width of 1.5 nm. As the spectrum of the pulses is wider than this the spectrum is not presented for the pulses after amplification in the SOA. The spectral results measured using the FROG were limited to the response function of the filter. The BPF spectral width of 1.75 nm corresponds to a frequency variation of approx. 220 GHz. This means that chirp with a magnitude in the region of 220 GHz can be recorded with the FROG in this experimental setup. The error between the experimental data and the data measured using the FROG retrieval program was below ≈ 0.007, indicating accurate retrievals [24] for the results presented in this chapter.

Prior to the presentation of these results the mechanism used to generate the 2 ps pulses, passive mode-locking, is discussed in order to explain the characteristics of the pulse which are visible from the measurements of the FROG.

Mode-locked pulses

In order to understand the properties of the pulse after propagation through the SOA, it is first necessary to understand the pulse characteristics before injection into the device. For this reason a description of the mode-locking technique is given prior to analyzing the amplified pulses. The pulses used in this experiment were generated using passive mode-locking [25]. This technique is based on a conventional gain medium and an absorption region inside a resonant cavity. The saturable absorber has a constant high absorption at low intensities, which saturates and reduces to low values at high intensities. When pumping of the gain medium begins the absorption is usually larger than the gain, so no signal can build up in the laser cavity. Gradually the round-trip gain in the cavity increases until it exceeds all the losses, saturable and non-saturable, in the system. At this point a weak laser oscillation begins to build up from the noise. If a particularly large intensity noise spike is present, the loss of the saturable absorber decreases allowing further amplification of the spike. This leads to the selective amplification of the noise spike and the absorption of the remaining low intensity light. So the noise spike experiences less round trip loss than the rest of the noise in the cavity and after numerous round trips, becomes the dominant signal in the system. The continued build-up of the laser oscillation results in the formation of a short pulse which is transmitted in the cavity, reducing the loss in the saturable absorber on each round trip. This results in a train of pulses with a repetition frequency that is determined by the length of the cavity. This is one disadvantage of passive mode-locking, the repetition frequency is fixed by the length of the cavity. This problem may be overcome using active mode-locking with an external signal. However, this technique was not used in this experiment.

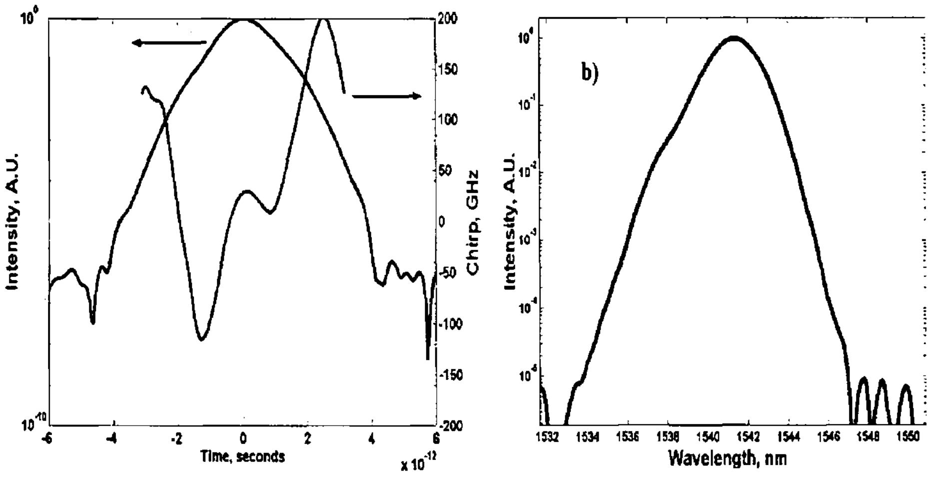

Fig. 6.3: a) Temporal and b) spectral data measured by the FROG for the source pulse.

The intensity and the chirp of a 2 ps pulse, generated from passive mode-locking are illustrated in Fig. 6.3a). The pulses are approximately $sech^2$ in shape, for which transform limited pulses have a Time-Bandwidth Product (TBP) of 0.31. The TBP of the measured pulses was 0.36, indicating excellent pulse quality. The generated pulses were symmetrical in nature, with an extinction ratio of approximately 50 dB. The FROG results, however, are unreliable for intensities more than approximately 35 dB below the peak. So it would be more accurate to say that the injected pulses have an extinction ratio in excess of 35 dB. The chirp introduced due to the mode-locking process can also be observed in Fig. 6.3a). The chirp is shown across the central portion of the pulse. There is an abrupt end in the profile of the chirp at the edges of the pulse. The chirp was not considered at these points because of the inaccuracies in measuring the chirp using the FROG when the pulse intensity is very low. The chirp has a highly nonlinear profile, with the maximum chirp introduced to the rising edge of the pulse. This chirp is attributed to the large carrier density fluctuations occurring in the laser cavity during pulse formation, due to the relationship between carrier density and refractive index. The wide spectrum of the mode-locked pulses is shown in Fig. 6.3b). The FWHM spectral width of these pulses was found to be 2.25 nm.

The absence of any pedestals on the temporal pulse shown in Fig. 6.3a) should be noted. Such pedestals may be introduced to the pulse due to reflections between the saturable absorber and the gain medium of the mode-locked source. As already discussed, however, there is uncertainty in the FROG measurement for intensities more than 35 dB below the pulse peak. This could lead to a masking of the pulse pedestals, which has been reported in the literature [17].

Polarization dependence with no CW injection

As already stated the energy of the pulses generated from the mode-locking process was 60 fJ. These pulses were injected into the SOA and the polarization was varied. Fig. 6.4 shows the intensity and the chirp of the amplified pulses as a function of the angle of linear polarization. The chirp introduced by the SOA was found experimentally by subtracting the overall chirp from the chirp on the source pulse, as demonstrated in the literature [26], using the following expression:

$$\Delta\nu_{out}(\tau) = \Delta\nu_{in}(\tau) - \Delta\nu_{SOA}(\tau) \tag{6.2}$$

where the second term on the right-hand side represents the chirp introduced by the SOA. From Fig. 6.4 it can be seen that there is no significant variation in the temporal response of the SOA as a function of polarization. For the pulse energy considered in this experiment, i.e. 60 fJ, the device is operating in the linear regime. The saturation energy of the device is given by [27]:

$$E_{sat(in)} = \frac{hfW_{in}d}{a\Gamma} \tag{6.3}$$

where W_{in} is the width at the input of the device, hf is the photon energy, d is the active layer thickness, a is the gain coefficient and Γ is the confinement factor. Using typical values for these parameters a saturation energy in the pJ range is estimated.

In the linear gain regime the TE and TM modes are well-matched, leading to very little polarization dependence. This can be observed in the steady-state case from Fig. 5.5. The chirp introduced by the SOA, shown in Fig. 6.4, has a similar shape to that reported in the literature [26]. Again it should be noted that the chirp is not considered away from the central portion of the pulse. This chirp is predominantly red-shifted, indicating that the

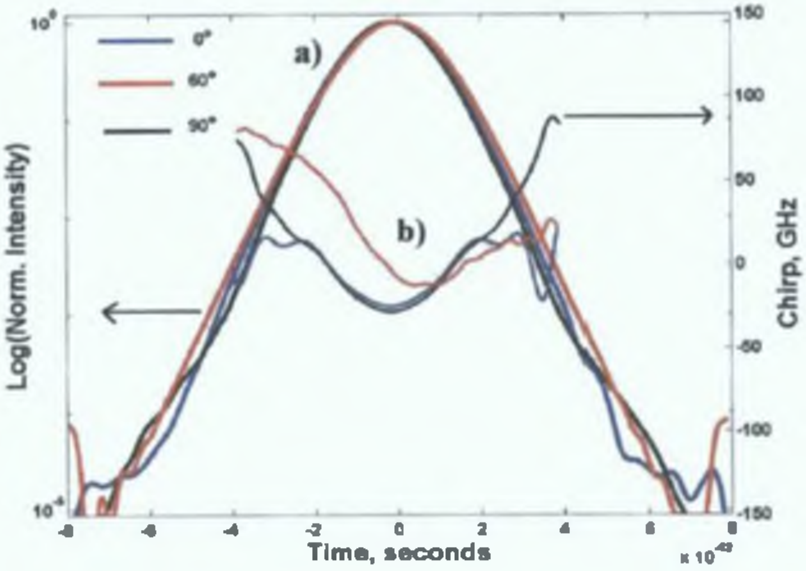

Fig. 6.4: Polarization dependence of of a) intensity and b) chirp when no CW signal is injected into the device.

effect of the chirp introduced is to shift the spectrum of the pulse to longer wavelengths. In Sec. 3.4.6 experimental and simulation results were presented which show that the chirp introduced by 15 ps pulses is also predominantly red-shifted. The shape of the chirp profile is directly related to the shape of the pulse, following the inverse of the pulse shape. This is due to SPM in the device which was also discussed in detail in Sec. 3.4.6. The polarization dependence of the chirp is therefore linked to the polarization dependence of the pulse shape, which is very small in this case. The magnitude of the chirp introduced by the SOA is comparable with previous independent measurements for a similar experimental setup [17]. The peak to peak chirp introduced by the SOA over the central portion of the pulse is shown in Table 6.1. This value indicates the magnitude of the frequency variation introduced to the pulse. The chirp amplitude varies by less than 10 GHz, as a function of polarization, in this case. This variation corresponds to a variation in wavelength of 0.08 nm, which is close to the resolution of the FROG.

It may be concluded from these results that polarization dependence is not significant when amplifying 2 ps pulses in a bulk SOA, for the case when the gain of the device is in the linear unsaturated regime.

Angle	Chirp amplitude (GHz)
0°	11.2
15°	14.5
30°	16.9
45°	18.7
60°	20.77
75°	12.96
90°	14.37

Tab. 6.1: Chirp amplitude introduced by the SOA when no CW signal is injected.

Polarization dependence with 1 mW CW injection

A CW signal was next injected into the device with an intensity of 1 mW in order to observe the temporal and spectral effect of passing 2 ps pulses through the device in the case when the SOA is operated in the nonlinear region of the gain. From Fig. 5.5 it can be seen that this level of injected signal is sufficient to cause a large variation in the gain along orthogonal axes. The purpose of the CW signal was to deplete carriers thus bringing the gain of the SOA into the nonlinear regime of operation. The intensity and chirp at the output of the device can be seen in Fig. 6.5. In the temporal domain large pedestals are visible in the pulse. The amplification of these pedestals in bulk SOAs has been documented [17].

It has been reported that the pedestals exist on the pulses injected into the SOA. The reason they are absent from the FROG results shown in Fig. 6.3 is that the amplitude of the pedestals in this case is below the noise level of the measurement system. The pedestals become more significant after propagation through the SOA due to gain saturation in the device. This causes the pedestal present on the rising edge of the injected pulse to receive a much larger gain with respect to the centre and falling edge of the pulse, so it becomes much more pronounced. In this case the pedestal is located only approx. 17 dB from the peak of the pulse for an angle of 60°.

There are pedestals present on the falling edge of the pulse as well as the rising edge. Those present on the falling edge of the pulse are visible after the SOA as they occur approximately 4 ps after the peak of the pulse, by which time the gain has recovered significantly. The gain has not, however, recovered to its full unsaturated value, as can be seen from the fact that the pedestal on the falling edge does not receive as much amplification as the pedestal on the rising edge, with a difference of approximately 3 dB between rising and falling edge pedestals visible at 60^0. Due to SPM the phase also varies with larger negative frequency components introduced, as can be seen from the chirp profile in Fig. 6.5.

A large polarization dependence in the amplification of the pedestals is observed, with

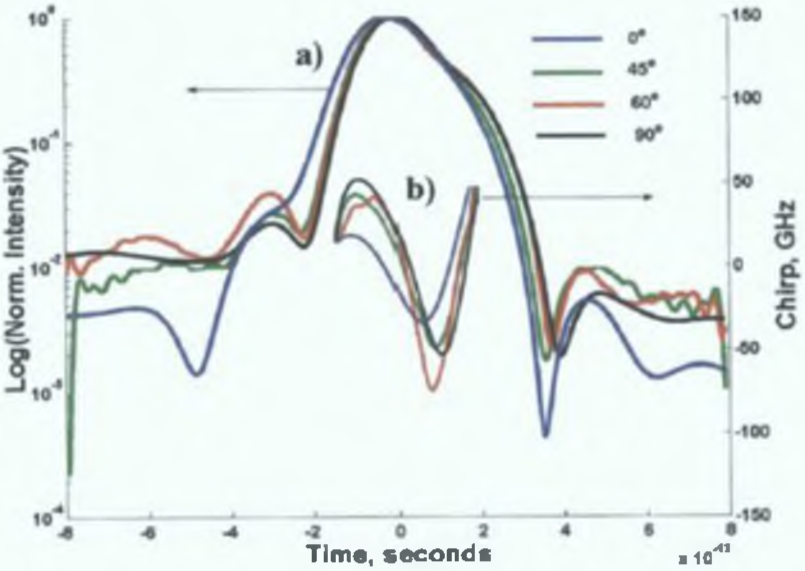

Fig. 6.5: Polarization dependence of of a) intensity and b) chirp when 1mW CW signal is injected into the device.

Angle	Chirp amplitude (GHz)
0°	69
15°	64
30°	64
45°	131
60°	132
75°	89
90°	109

Tab. 6.2: Chirp amplitude introduced by the SOA when 1mW CW signal is injected.

their largest amplification occurring at 60°. A variation in the amplitude of the pedestals of approximately 2 dB can be observed between angles of 60° and 90°. This indicates that there is a variation in the suppression of the gain as a function of polarization for pulses of length 2 ps. As the ultra-fast gain processes are dominant for pulses of length 2 ps [12], the results indicate a polarization dependence in the saturation of the gain due to these ultra-fast processes. The chirp amplitude introduced to the pulses, as a function of polarization, for a CW intensity of 1 mW is shown in Table 6.2. A large polarization dependence is introduced to the chirp for this level of CW intensity, due to the increased SPM. A maximum polarization dependence of 68 GHz is introduced to the pulses.

Polarization dependence with 4 mW CW injection

The level of CW injection was further increased to 4 mW, in order to observe the polarization dependent amplification of the 2 ps pulses in the SOA at even higher levels of injection. The increased depletion of the gain, visible from Fig. 5.5, leads to a larger significance of the pedestals on the rising and falling edges of the pulse as can be seen in Fig. 6.6. From this figure it can be seen that the pulses have an intensity only 12 dB from the peak of the pulse at 60°. This gain suppression also leads to an increase in the negative frequency chirp introduced due to SPM that can be seen in the figure.

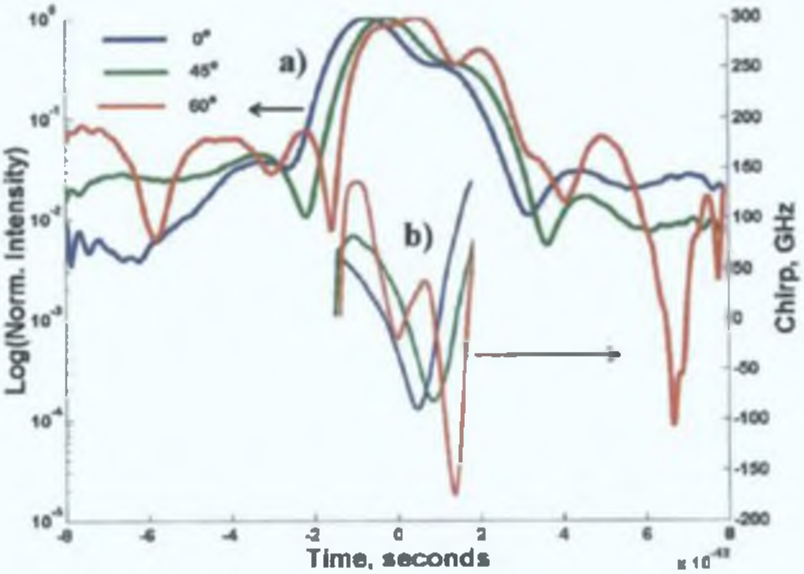

Fig. 6.6: Polarization dependence of of a) intensity and b) chirp when 4mW CW signal is injected into the device.

There is a larger polarization dependence for this high intensity signal, with the maximum nonlinearity again located at 60°. An increase in the polarization dependence of the gain suppression is also indicated with over 4 dB variation in the amplitude of the pedestals between 0° and 60°. This in turn leads to an increase in the polarization dependence of the chirp, with a large negative frequency component introduced at 60°. This indicates a larger shift of the spectrum to longer wavelengths at this angle. The increase in the polarization dependence of the chirp amplitude may be seen in Table 6.3, where there is a maximum variation of 143 GHz between angles of 30° and 60°. This large polarization dependence may lead to unstable performance in SOA based optical networks employing SMF.

Another development in the temporal domain for this level of injection is the introduction of a second peak in the profile of the pulse. This new pulse is most prominent at an

Angle	Chirp amplitude (GHz)
0°	182
30°	168
45°	182
60°	311
90°	207

Tab. 6.3: Chirp amplitude introduced by the SOA when 4mW CW signal is injected.

angle of 60° and occurs approx. 1.5 ps from the main peak of the pulse. It may be stated that this new peak is not caused by birefringence as this would imply a refractive index variation of 0.75. This value is two orders of magnitude larger than previously reported refractive index variations in SOAs [28]. A similar development of a multi-peak pulse after propagation through an SOA has been reported in the literature. This work was carried out on pulses with a similar width as those used in the experiment presented in this chapter [11].

From the experiment presented in this section it is observed that the polarization dependence of the pulses amplified in the SOA increase as a function of the level of gain depletion. As the ultra-fast gain processes are dominant for 2 ps pulses, the results of this experiment indicate a possible nonlinear saturation of the gain along orthogonal modes for these ultra-fast gain processes. The results of this experiment show that if mode-locked pulse sources, of this pulsewidth, are to be used in optical communications systems, it is very important to test the polarization dependent propagation through the SOA in order to avoid such effects as ISI between channels in WDM networks. As well as this, the results show experimentally the existence of a polarization dependence of the ultra-fast gain processes in an SOA, which could potentially be exploited for use in an optical network employing NPR as an all-optical signal processing technique.

6.3 Measurement of polarization dependent gain dynamics in bulk SOA

The experiment performed in the last section indicated a polarization dependence of the gain dynamics in the SOA. In this experiment, however, no measurement was made to characterize this dependence. Experimental and theoretical work has been performed by other groups which also indicate the existence of such a polarization dependence but no experimental work has been presented which measures this effect directly [8], [9] and [29]. To date studies of the NPR effect have mainly focused on the effect due to the interband recombinations. This fundamentally limits the speed to 200 GHz [2]. A polarization dependence of the ultra-fast gain dynamics could extend the operation of optical networks into the THz range.

An experiment is presented in this section which measures the polarization dependence of several processes associated with the gain dynamics in the SOA. The main processes effecting the recovery of the gain are CDP, CH, SHB, TPA and the ultra-fast Kerr effect, as discussed in Chapter 2. The polarization dependence of CDP and CH are considered in the experiment presented in this section. This experiment is based on a FWM setup. The frequency detuning between the pump and the probe is used to retrieve information related to the recovery time of the gain. The gain of the SOA is modulated at the beat frequency between the pump and the probe signals. Therefore, as the detuning is increased the gain of the SOA is modulated at increasingly smaller timeframes. Recovery from the different gain processes in the SOA occurs at separate times. So, increasing the detuning makes it possible to observe the contribution of each of the gain processes as a function of time.

Experimental results related to the efficiency of FWM as a function of detuning were compared to theoretical expressions in order to retrieve parameters associated with CDP and CH. The use of such frequency domain results in order to measure time domain phenomena has received extensive study in the literature [30] - [39] [40] [41] [42]. However, this technique has never been used to measure the polarization dependence of different gain processes.

6.3.1 Experimental setup and considerations

The experimental setup is shown in Fig. 6.7. In order to maintain consistency with the experimental results presented in Sec. 6.2 the Avanex device was also used in this experiment. The device was biased at 200 mA and temperature regulated at $23^{o}C$.

Two external cavity tunable lasers were used to perform the FWM. The wavelength of the pump was 1535 nm, which is within the 3 dB gain bandwidth of the device. Ideally it would be preferable to have the pump wavelength closer to the gain peak of the device, which occurs at 1515 nm, but there was a restriction due to the EDFA which does not amplify the signal significantly, below 1535 nm. The choice of wavelengths used for the pump and the probe thus involved a trade-off between the gain spectrum of the EDFA, which operates in the C-band, and the gain spectrum of the SOA, respectively.

The wavelength of the probe was varied from 1535 nm to 1560 nm in steps as low as 0.1 nm. This allowed for the measurement of time-varying phenomena recovering on timescales greater than 300 fs. The cause of this limitation is discussed later in this section. From the literature CDP and CH have recovery times greater than this value [37], [38]. Typical values for these parameters are 500 ps and 1 ps, respectively. It was not possible to measure the polarization dependency of the faster gain processes of SHB, TPA and ultra-

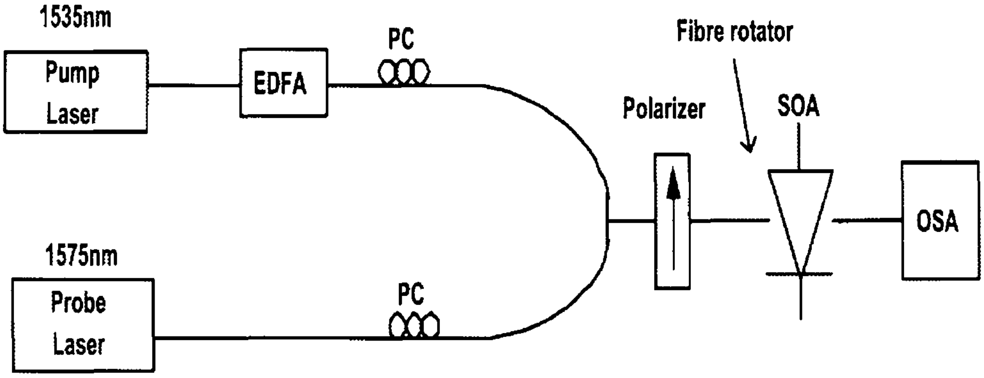

Fig. 6.7: Experimental setup for the FWM technique.

fast Kerr effects using this experimental setup, as the timeframes associated with these processes are beyond the resolution of the experiment. The polarization of both the pump and the probe was controlled using a PC and a polarizer. The polarizer ensured that both signals were co-polarized, a requirement for efficient FWM, as well as ensuring that the light was injected along the axis of the PM lensed fibre that was used to couple the light into the SOA. The PC's were used to align the light along the axis of the PM fibre.

The intensities of both the pump and probe were kept constant as a function of polarization. An OSA with a resolution bandwidth of 0.07 nm was used to observe the spectra at the output of the device. The EDFA was used to amplify the pump signal, as a strong intensity was required in order to suppress the gain of the device. The pump power was maintained at 9 dBm for all measurements, whilst the probe power was constant at -4 dBm. This difference of 13 dB is close to the optimum difference used by other groups to produce the best results [38], [40]. The polarization of the co-polarized pump and probe was varied with respect to the axis of the device by physically rotating the fibre. The coupling from the lensed fibre to the SOA was maintained at a constant level as the polarization was varied.

An OSA spectrum in Fig. 6.8 shows the a) pump, b) probe and c) conjugate signals. The difference of approximately 13 dB between the pump and the probe can be seen in this figure. The conjugate signal is over 20 dB below the probe signal at this detuning. The pump and the probe are separated by 5 nm, and it can be seen that the generated conjugate signal is also located 5 nm from the pump. This detuning corresponds to a time resolution of 1.5 ps. In Fig. 6.8 a second conjugate signal is generated on the high wavelength side of the pump and probe signals, at a wavelength from the probe corressponding to the pump-probe detuning. This signal is not visible in Fig. 6.8 as this wavelength is far from the peak gain wavelength of the spectrum. For this reason the second conjugate is not amplified above the noise. The conjugate obtained in this experiment was frequency up-converted. Frequency down conversion was not possible at large detunings due to the mismatch in wavelengths between the EDFA and the SOA. This would result in the probe signal moving outside the range of the EDFA for large detunings.

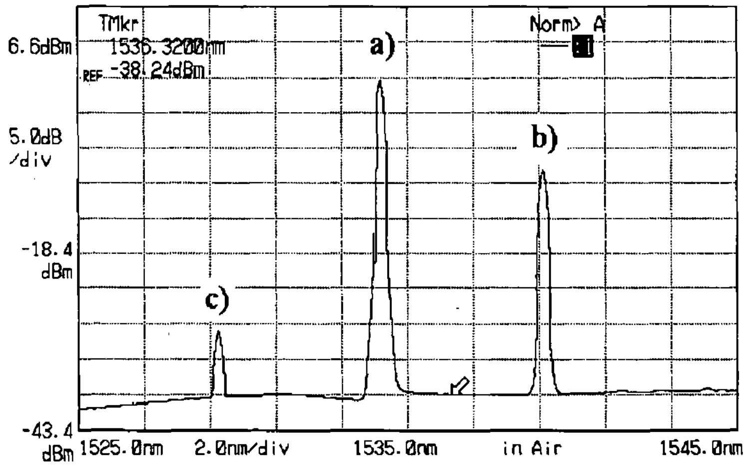

Fig. 6.8: OSA spectrum showing a) pump, b) probe and c) conjugate signals.

Several important considerations need to be taken into account when performing experiments of this nature. A result has been presented in the literature that examines the variation in the efficiency as a function of polarization [41]. A polarization dependence of the efficiency of over 10 dB was found for large detunings between the pump and the probe. The variation was attributed to the birefringence in the device. This result suggests that it would be difficult to determine the impact of a potential polarization dependence of the gain dynamics. However from this publication, and from results found experimentally using the setup of Fig. 6.7, it can be concluded that this birefringent effect is only significant for large frequency detuning in excess of approx. 3.5 THz, corresponding to a time resolution of approximately 300 fs. The polarization dependence of SHB cannot therefore be determined using this experiment. Results have been presented in the literature that measure the SHB using the FWM technique, however no polarization resolved measurements can be taken for this effect due to the birefringence at such large detunings.

It has been reported that in order to accurately describe the FWM process the wavelength dependence of the gain should also be taken into consideration [36]. However, over the 3.5 THz frequency detuning of interest in the present experiment the gain varies by less than 1 dB. For this reason the spectral dependence of the gain was neglected in the measurements. This small variation of the gain over the detuning range is due to the large spectral width the SOA under test, which was discussed in Sec. 2.12.1.

6.3.2 Parameter extraction

The aim of the experiment was to obtain the efficiency data as a function of the wavelength detuning between the pump and the probe. As the detuning was increased the gain of the SOA was modulated on smaller and smaller timescales. The efficiency data was thus used to retrieve information related to the gain processes occurring on different timescales. The efficiency is a measure of the quality of the frequency conversion and was measured experimentally using the following expression:

$$\rho_{exp} = \frac{P_{conj}}{P_{probe}} \tag{6.4}$$

A separate expression exists for the efficiency, which relates the FWM parameter to the different gain dynamics in the SOA. This theoretical expression is given by [42]:

$$\rho_{th} = S_0^2(L)|f_{cdp}(\Omega) + f_{ch}(\Omega) + f_{shb}(\Omega)|^2 \tag{6.5}$$

where S_0 represents the pump photon density and the contributions from carrier density pulsation (f_{cdp}), carrier heating (f_{ch}) and spectral-hole burning (f_{shb}) are defined as follows [43], [42]:

$$f_{cdp}(\Omega) = -\frac{1}{S_{sat}}\frac{1 - j\alpha_{cdp}}{2(1 - j\Omega\tau_{cdp})} \tag{6.6}$$

$$f_{ch}(\Omega) = -\frac{1}{S_{ch}}\frac{1 - j\alpha_{ch}}{(1 - j\Omega\tau_{ch})(1 - j\Omega\tau_{shb})} \tag{6.7}$$

$$f_{shb}(\Omega) = -\frac{1}{S_{shb}}\frac{1 - j\alpha_{shb}}{1 - j\Omega\tau_{shb}} \tag{6.8}$$

where the α_i parameters refer to the LEFs, the τ_i parameters refer to the recovery times and the S_i parameters refer to the characteristic power associated with each process. The angular frequency detuning is represented by Ω. The LEF for SHB is considered to be 0 because a spectral hole symmetrically depletes the gain only around the emission wavelength, in such a situation no refractive-index change results, [38] and [42]. As already discussed SHB may not be determined as a function of polarization. For this reason SHB recovery time was given a constant value of 70 fs which was previously determined for FWM measurements using a similar device [38]. The value for S_0 is also fixed as the pump signal is maintained at a constant power for all measurements. The next step involved using a minimization technique in order to minimize the error between the experimental efficiency data and the theoretical efficiency, defined in Eqns. (6.6)-(6.8). The parameters in these equations were given initial values and six of these parameters were set as variables of the minimization function and were varied in order to reduce the error between the experimental and theoretical efficiency. This fitting was performed as a function of angular frequency detuning for the following parameters: S_{sat}, α_{cdp}, τ_{cdp}, S_{ch}, α_{ch} and τ_{ch}. These six parameters were given initial estimates based on standard values for these parameters [38]. Using this technique it was possible to obtain values for the timescales and LEF's corresponding to CDP and CH processes as a function of polarization.

The experimental efficiency and the fitted efficiency are plotted as a function of detuning in Fig. 6.9 for an angle of 30^o, together with the calculated contribution from CDP and CH. The accuracy of the fitting can be seen on the graph. For a small frequency detuning CDP has the largest effect on the efficiency, as expected. CDP decreases by approximately 20 dB/decade, and CH becomes more important as the detuning is increased. This is due to the gain of the device becoming modulated on shorter timescales. Below an angular frequency of 0.3 THz the carrier density is the dominate mechanism, corresponding to a time of approx. 3 ps. At times shorter than 3 ps CH dominates the gain of the SOA. This result is in relatively close agreement with an independent time-resolved result presented in the literature which found that the ultra-fast gain dynamics dominate the recovery of the gain below 10 ps [12]. CH continues to be the dominant mechanism until at even larger detunings the SHB, TPA and ultra-fast Kerr effects have the largest effect on the efficiency. As already explained these faster effects are beyond the resolution of this experiment.

The fitting was performed for a range of injection polarizations between -30^o and 90^o. The accuracy of the fitting may be gauged by considering the variance between the experimental data and the fitted data. The variance was calculated from the following expression:

$$Var = \frac{\sum(\rho_{exp} - \rho_{th})^2}{N-1} \tag{6.9}$$

where ρ_{exp} and ρ_{calc} represent the experimentally measured efficiency and the calculated efficiency respectively, and N represents the number of experimental points under consideration. The variance calculated for each angle of polarization considered in the experiment is shown in Table 6.3.2. These values for the variance indicate excellent fitting between the experimental and calculated efficiency, with a maximum variance of 0.8% found using Eqn. (6.9).

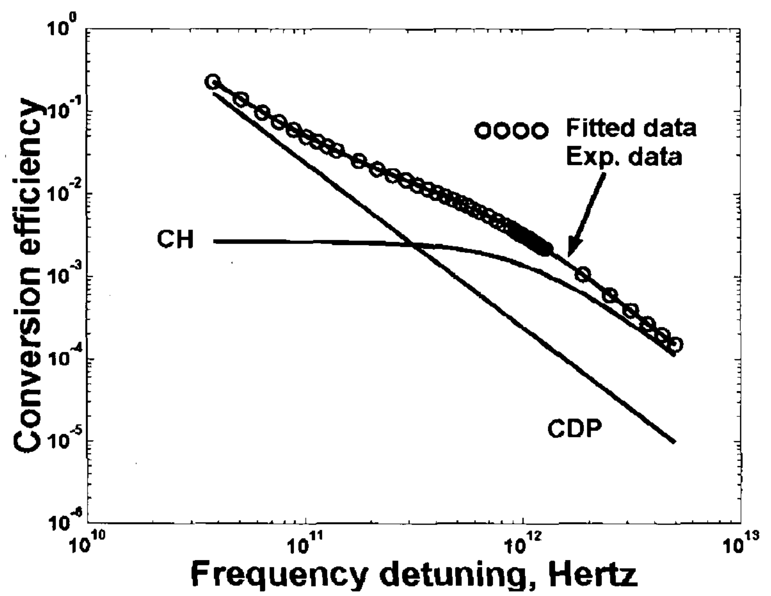

Fig. 6.9: Experimental data used and curves extracted from fitting for different gain processes at an angle of 30°.

Angle	Variance
-30	0.0039
0	0.0049
30	0.0079
45	0.0024
60	0.0037
90	0.0055

Tab. 6.4: Variance recorded between experimental and fitted curves as a function of polarization.

6.3.3 Analysis of results

Carrier density pulsation (CDP) parameters

Fig. 6.10 shows the extracted values for the LEF, α_{cdp}, and the carrier recovery time, τ_{cdp}, associated with CDP as a function of the polarization angle. α_{cdp} varies from a value of 4.5 at -30^o up to a peak of 6.5 at 60^o. Similarly the carrier recovery time varies from 50 ps to 230 ps, with the maximum also corresponding to the injected polarization state of 60^o.

For a tensile strained bulk device there are more TM transitions than TE transitions due to the shifting of the subbands in the valence band, as discussed in Sec. 4.5.2. The LHs, which give rise to TM transitions are favoured under such strain. The result of this is a larger TM gain and so a greater depletion of carriers for light polarized along the TM axis. So TM light results in a lower carrier density population, this leads to a longer carrier recovery time due to the fact that the carrier lifetime is inversely proportional to carrier density.

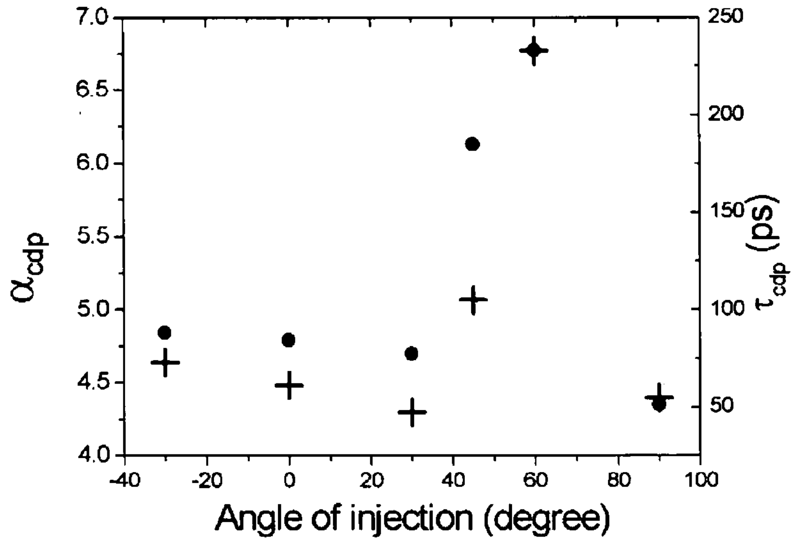

Fig. 6.10: The extracted data for CDP: LEF (+) and recovery time (•) as a function of the angle of injection.

From Sec. 4.6, under conditions of low CW injection, the axis of the device was found to occur at angles of 0°, for the TE axis, and 90°, for the TM axis. The results in Fig. 6.10 show that the longest recovery time occurs for light polarized at 60°, indicating that the largest number of recombinations occurs for this angle of polarization. This result suggests that 60° is closer to the TM axis of the device for the large level of intensity injected into the device in this experiment. One possible explanation for this result is a modification of the optical axis of the device. This phenomenon has received attention in the literature, although measurement of the exact angle of the new axis was not determined in these studies [44], [45]. For large carrier variations in the device the induced refractive index change results in an effective shift in the axis of the device. The reason why the axis of the device should shift to 60° rather than any other angle is unclear. Due to the fact that the TM gain is higher than the TE gain in the tensile strained case, there would also be a larger shift towards lower wavelengths for the TM mode, as carriers in higher electron states would participate in the gain under such circumstances. As α_{cdp} is inversely proportional to the wavelength the result is that α_{cdp} would shift towards larger values for light polarized along the TM direction as observed in Fig. 6.10.

Carrier heating (CH) parameters

Fig. 6.11 shows the LEF, α_{ch}, and the recovery time, τ_{ch}, associated with CH, as a function of injection angle. α_{ch} is approximately 1 at -30^o and peaks at 60^o with a value of almost 3. The expression used to calculate α_{ch} was defined in Sec. 2.10.2 by Eqn. (2.24). α_{ch} has been reported in the literature as having a value of approx. 1 and is generally 5 times smaller than α_{cdp} [38]. Fig. 6.11 indicates that this is the case for an angle of 0^o, but as the angle is increased towards the TM axis the magnitude of α_{ch} increases and there will be a significant contribution to the phase modulation due to CH. This result is in agreement with results obtained from the same device shown in Fig. 6.6, where it can be seen that the largest birefringent effect occurs at 60^o, which may represent the TM axis under conditions of high intensity injection.

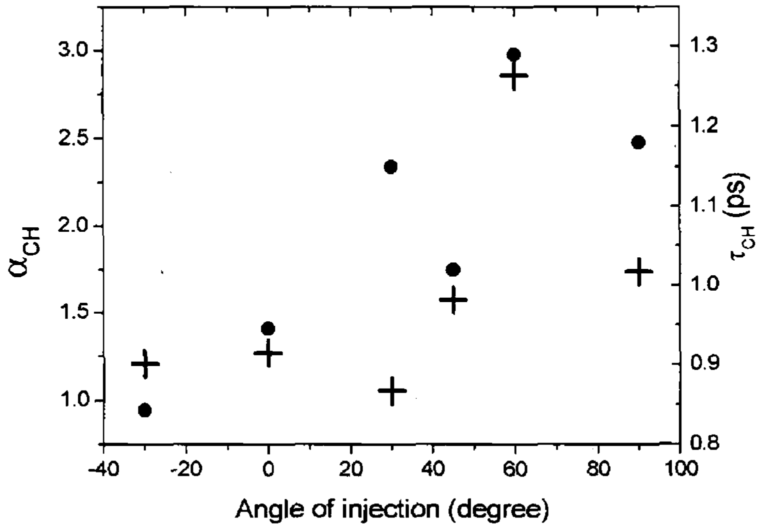

Fig. 6.11: The extracted data for CH: LEF (+) and recovery time (•) as a function of the angle of injection.

In Sec. 2.10.2 it was stated that the main contributions to CH are from FCA and the removal of cold carriers through stimulated emission. The reason that α_{ch} is greatest for TM polarization is due to the fact that the removal of cold carriers is greatest at this angle of polarization. This effect leads to a reduction in the $\partial g_m/\partial T_c$ term in Eqn. (2.24), due to the increased change in the temperature, resulting in an increase in α_{ch} as the angle of polarization is varied from TE to TM. This would further support the hypothesis that the effective TM axis is rotated to 60^o under conditions of injected power. As can be seen this angle again corresponds to the largest recovery time, with a recovery time of 1.3 ps found at 60^o as opposed to a time of 1 ps at -30^o. This result is also consistent with the polarization resolved 2 ps pulse propagation experiments presented in Sec. 6.2, in which the largest pulse broadening and chirp was observed for an injected linear polarization state at 60^o [18].

In this section an experiment was presented to investigate the polarization dependence of CDP and CH. A comparison between theory and experiment was performed that allowed the recovery times and LEFs for these processes to be extracted. The values that were extracted are within the range of those previously reported in the literature. Many groups present results that claim to have achieved polarization independence by applying a tensile strain to the SOA. This may be true for the steady state case, but the results presented in this section point to a large polarization dependence of the dynamic gain processes in the SOA. The polarization dependence of the LEF and recovery time for CDP and CH were found to have peak values for an injected angle of 60^o. This suggests that there may be a new effective TM axis under conditions of high intensity signal injection, indicating a possible modification of the optical axes of the SOA.

6.4 Conclusions

Results have been presented in this chapter which demonstrate the polarization dependence of the gain dynamics in the SOA. This dependence has two consequences. Firstly, the potential for ultra-fast NPR due to the polarization dependence of the CH is determined, which leads to the possibility to perform all-optical signal processing in the THz regime. Secondly, for pulses below 10 ps, there will be a polarization dependence introduced due to the CH, which may effect pulse propagation in SOAs employed in optical networks. The first experiment presented in this chapter was based on the propagation of 2 ps pulses through a bulk SOA in both linear and nonlinear regimes of operation. It has been shown in the literature that the recovery of the gain is dominated by intra-band effects for pulses below 10 ps. The pulses were measured after propagation through the SOA using the FROG technique. Using this technique it was possible to measure the pulse in both temporal and spectral domains. The results show that very little polarization dependence was introduced to the pulses when they were linearly amplified through the device. However, when the gain of the SOA was suppressed by means of a CW signal a large polarization dependence was introduced. Temporally this resulted in the increased significance of pedestals located in the wings of the pulse. A large polarization dependence of the amplification of these pedestals was found, indicating a polarization dependence of the gain suppression. A variation of 3 dB was recorded in the amplification of the pedestals as a function of polarization for an injected CW signal of 4 mW. For the same level of CW injection a variation of 143 GHz was found in the magnitude of the chirp as a function of polarization. This large polarization dependence may have implications for optical systems employing 2 ps pulses in the nonlinear gain regime of the SOA. This experiment demonstrates that the FROG measurement system is a good tool for performing polarization dependent measurements of chirp and pulsewidth.

Although there are several reported studies on the polarization dependence of the gain dynamics in a bulk SOA [8], [9], no work has been presented to measure this effect in a quantifiable manner. In order to examine this effect a second experiment was presented in this chapter, in which the characteristic times and LEFs related to CH, as well as the carrier lifetime, were determined using a FWM technique. As the frequency detuning between the pump and the probe was increased different gain processes were modulated. These different gain processes were analyzed by examination of the efficiency of the conversion. The frequency detuning was then related to time in order to estimate the recovery time of the different gain processes. The LEFs of the considered gain processes were also found using this technique. It was found that as the recovery times of the gain processes decreased, the LEF also decreased. This reduction in the modulation of the phase makes it more difficult to perform efficient XPM, as discussed in the literature [3]. The lower LEF also indicates that a smaller level of frequency chirp will be introduced at higher data rates. These results indicate that the FWM technique is a simple and effective technique for the measurement of the polarization dependence of the gain dynamics in the SOA. Consistency was found between the two experiments presented in this chapter. The largest contribution from CH was found to occur at an angle of 60° in both cases. This result suggests that there may be a modification in the optical axis of the device for large values of injected power. This phenomena has been reported previously in the literature.

BIBLIOGRAPHY

[1] D. Cotter, R.J. Manning, K.J. Blow, A.D. Ellis, A.E. Kelly, D. Nesset, I.D. Phillips, A.J. Poustie, D.C. Rogers. "Nonlinear optics for high-speed digital information processing". *Science*, vol.286:pp.1523–1528, 1999.

[2] K.L. Hall, G. Lenz, A.M. Darwish, and E.P. Ippen. "Subpicosecond gain and index nonlinearities in InGaAsP diode lasers". *Optics Comms.*, vol.111:pp.589–612, 1994.

[3] R.P. Schreieck, M.H. Kwakernaak, H. Jackel, and H. Melchior. "All-optical switching at multi-100-Gb/s data rates with Mach-Zehnder interferometer switches". *IEEE J. Quantum Electronics*, vol.38(no.8):pp.1053–1061, 2002.

[4] V.V. Lysak, H. Kawaguchi, I.A. Sukhoivanov, T. Katayama, and A.V. Shulika. "Ultrafast gain dynamics in asymmetrical multiple quantum-well semiconductor optical amplifiers". *IEEE J. Quantum Electronics*, vol.41(no.6):pp.797–807, 2005.

[5] H.J.S Dorren, X.Yang, D.Lenstra, H. de Waardt, G.D Khoe, T. Simoyama, H. Ishikawa, H. Kawashima, and T. Hasama. "Ultrafast refractive-index dynamics in a multiquantum-well semiconductor optical amplifier". *IEEE J Quantum Electronics*, vol.15(no.6):pp.792–794, 2003.

[6] H.J.S Dorren, X.Yang, A.K. Mishra, Z. Li, H. Ju, H. de Waardt, G.D Khoe, T. Simoyama, H. Ishikawa, H. Kawashima, and T. Hasama. "All-optical logic based on ultrafast gain and index dynamics in a semiconductor optical amplifier". *IEEE J. Sel. Areas Quantum Electronics*, vol.10(no.5):pp.1079–1091, 2004.

[7] L. Schares, C. Schubert, C. Schmidt, H.G. Weber, L. Occhi, and G. Guekos. "Phase dynamics of semiconductor optical amplifiers at 10-40 GHz". *IEEE J. Quantum Electronics*, vol.39:pp.1394–1408, 2003.

[8] X. Yang, D. Lenstra, G.D. Khoe, and H.J.S. Dorren. "Nonlinear polarization rotation induced by ultrashort optical pulses in a semiconductor optical amplifier". *Optics Communications*, vol.223:pp.169–179, 2003.

[9] Z. Li, X. Yang, E. Tangdiongga, H. Ju, G.D. Khoe, H.J.S. Dorren, and D. Lenstra. "Simulation of mode-locking by nonlinear polarization in a semiconductor optical amplifier". *IEEE J. Quantum Electronics*, vol.41(no.6):pp.808–816, 2005.

[10] J.M. Tang, and K.A. Shore. "Strong picosecond optical pulse propagation in semiconductor optical amplifiers at transparency". *IEEE J. Quantum Electronics*, vol.34(no.7):pp.1263–1269, 1998.

[11] M.Y. Hong, Y.H. Chang, A. Dienes, J.P. Heritage, and P.J. Delfyett. "Subpicosecond pulse amplification in semiconductor laser amplifiers: Theory and experiments". *IEEE J. Quantum Electronics*, vol.30(no.4):pp.1122–1131, 1994.

[12] P. Borri, S. Scaffetti, J. Mørk, W. Langbein, J.M. Hvam, A. Mecozzi, and F. Martelli. "Measurement and calculation of the critical pulsewidth for gain saturation in semiconductor optical amplifiers". *Optics Communications*, vol.164:pp.51–55, 1999.

[13] J.M. Tang, P.S. Spencer, and K.A. Shore. "Analysis of operating characteristics of TOADs using gain saturation and nonlinear gain in SOAs". *IEE proc. Optoelectronics*, vol.145(no.1):pp.83–87, 1998.

[14] H.J.S. Dorren, G.D. Khoe, and D. Lenstra. "All-optical switching of an ultrashort pulse using a semiconductor optical amplifier in a Sagnac-interferometer arrangement". *Optics Communications*, vol.205:pp.247–252, 2002.

[15] F. Romstad, P. Borri, W. Langbein, J. Mørk, and J.M. Hvam. "Measurement of pulse amplitude and phase distortion in a semiconductor optical amplifier: From pulse compression to breakup". *IEEE Phot. Tech. Lett.*, vol.12(no.12):pp.1674–1676, 2000.

[16] P.J. Delfyett, H. Shi, S. Gee, I. Nitta, J.C. Connolly, and G.A. Alphonse. "Joint time-frequency measurements of mode-locked semiconductor diode lasers and dynamics using frequency resolved optical gating". *IEEE J. Quantum Electronics*, vol.35(no.4):pp.487–500, 1999.

[17] A.M. Clarke, M.J. Connelly, P. Anandarajah, L.P. Barry, and D. Reid. "Investigation of pulse pedestal and dynamic chirp formation on picosecond pulses after propagation through an SOA". *IEEE Photonics Tech. Letters*, vol.17(no.9):pp.1800–1802, 2005.

[18] B.F. Kennedy, S. Philippe, H. Soto , A.L.Bradley, and P. Landais. "Temporal and spectoral dependence on polarization of the input signal in a semiconductor optical amplifier". *Proc. OSA Optical Amplifiers and their Applications, San Francisco, USA*, 2004.

[19] Daniel J. Kane and Rick Trebino. "Characterization of arbitrary femtosecond pulses using frequency-resolved optical gating". *IEEE J. Quantum Electronics*, vol.29(no.2):pp.571–579, 1993.

[20] D.J. Kane, A.J. Taylor, R. Trebino, and K.W. DeLong. "Single-shot measurement of the intensity and phase of femtosecond UV laser pulse using frequency-resolved optical gating". *Opt. Lett.*, vol.19:pp.1061–1063, 1994.

[21] B. Kohler, V.V. Yakovlev, K.R. Wilson, J. Squier, K.W. DeLong, and R. Trebino. "Phase and intensity characterization of femtosecond pulses from a chirped pulse amplifier by frequency-resolved optical gating". *Optics Letters*, vol.20:pp.483–485, 1995.

[22] J.M. Dudley, L.P. Barry, J.D. Harvey, M.D. Thomson, B.C. Thomsen, P.G. Bollond, and R. Leonhardt. "Complete characterization of ultrashort pulse sources at 1550 nm". *IEEE J. Quantum Electronics*, vol.34(no.4):pp.441–450, 1999.

[23] S. Haykin. "Communication systems". *Wiley*, pages 242–249, 1994, 3rd edition.

[24] R. Trebino, K.W. Long, D.N. Fittinghoff, J.N. Sweetser, M.A. Krumbugel, and B.A. Richman. "Measuring ultrashort laser pulses in the time-frequency domain using frequency resolved optical gating". *Rev. Sci. Instrum.*, vol.68:pp.3277–3295, 1997.

[25] H.A. Haus. "Mode-locking of lasers". *IEEE J. Sel. Top. in Quantum Electronics*, vol.6(no.6):pp.1173–1185, 2000.

[26] G.P. Agrawal, and N. A. Olsson. "Self-phase modulation and spectral broadening of optical pulses in semiconductor laser amplifiers". *IEEE J. Quantum Electronics*, vol.25(no.11):pp.2297–2306, 1989.

[27] H. Ghafouri-Shiraz, P.W. Tan, and T. Aruga. "Picosecond pulse amplification in tapered-waveguide laser-diode amplifiers". *IEEE J. Sel. Topics in Quantum Electronics*, vol.3(no.2):210–217, 1997.

[28] R.J. Manning, A. Antonopoulos, R. Le Roux, and A.E. Kelly. "Experimental measurement of nonlinear polarisation rotation in semiconductor optical amplifiers". *IEE Electronic Letters*, vol.37(no.4):pp.229–231, 2001.

[29] X. Yang, D. Lenstra, A.K. Mishra, H. D. Waardt, G.D. Khoe, and H.J.S. Dorren. "Propagation of ultrashort optical pulses in a semiconductor optical amplifier amplifier: Simulations and experiments". *ICTON 2003*, pages pp.47–53, 2003.

[30] L.F. Tiemeijer. "Effects of nonlinear gain on four-wave mixing and asymmetric gain saturation in a semiconductor laser amplifier". *Applied Physics Letters*, vol.59(no.5):pp.499–501, 1991.

[31] K. Kikuchi, M. Amano, C.E. Zah, and T.P. Lee. "Analysis of origin of nonlinear gain in 1.5 μm semiconductor active layers by highly nondegenerate four-wave mixing". *Applied Physics Letters*, vol.64(no.5):pp.548–550, 1994.

[32] A. Mecozzi. "Analytical theory of four-wave mixing in semiconductor amplifiers". *Optics Letters*, vol.19(no.12):pp.892–894, 1994.

[33] A. Mecozzi, A. D'Ottavi, F. Cara Romeo, P. Spano, R. Dall'Ara, G. Guekos, J. Eckner. "High saturation behavior of the four-wave mixing signal in semiconductor amplifiers". *Applied Physics Letters*, vol.66(no.10):pp.1184–1186, 1995.

[34] A. Mecozzi, S. Scotti, A. D'Ottavi, E. Iannone, and P. Spano. "Four-wave mixing in travelling-wave semiconductor amplifiers". *IEEE J. Quantum Electronics*, vol.31(no.4):pp.689–1199, 1995.

[35] I. Koltchanov, S. Kindt, K. Petermann, S. Diez, R. Ludwig, R. Schnabel, and H.G. Weber. "Gain dispersion and saturation effect in four-wave mixing in semiconductor laser amplifiers". *IEEE J. Quantum Electronics*, vol.32(no.4):pp.712–720, 1996.

[36] K. Obermann, I. Koltchanov, K. Petermann, S. Diez, R. Ludwig, and H.G. Weber. "Noise analysis of frequency converters utilizing semiconductor-laser amplifiers". *IEEE J. Quantum Electronics*, vol.33(no.1):pp.81–88, 1997.

[37] S. Diez, C. Schimt, R Ludwig, H.G. Weber, K. Obermann, S. Kindt, I. Koltchanov, and K. Petermann. "Four-wave mixing in semiconductor optical amplifiers for frequency conversion and fast optical switching". *IEEE J. Sel. Top. Quantum Electronics*, vol.3(no.5):pp.1131–1145, 1997.

[38] S. Scotti, L. Graziani, A. D'Ottavi, F. Martelli, A. Mecozzi, P. Spano, R. Dall'Ara, F. Girandin, and G. Guekos. "Effects of ultrafast processes on frequency converters based on four-wave mixing in semiconductor optical amplifiers". *IEEE J. Sel. Top. in Quantum Electronics*, vol.3(no.5):pp.1156–1161, 1997.

[39] A. Mecozzi, and J. Mørk. "Saturation effects in nondegenerate four-wave mixing between short optical pulses in semiconductor laser amplifiers". *IEEE J. Sel. Top. Quantum Electronics*, vol.3(no.5):pp.1190–1206, 1997.

[40] A. D'Ottavi, F. Girardin, L. Graziani, F. Martelli, P. Spano, A. Mecozzi, S. Scotti, R. Dall'Ara, J. Eckner, and G. Guekos. "Four-wave mixing in semiconductor optical amplifiers: A practical tool for wavelength conversion". *IEEE J. Quantum Electronics*, vol.3(no.2):pp.522–528, 1997.

[41] S. Diez, C. Schimt, R Ludwig, H.G. Weber, P. Doussiere, and T. Duceiller. "Effect of birefringence in bulk semiconductor optical amplifiers on FWM". *IEEE Photonics Tech. Letters*, vol.10(no.2):pp.212–214, 1998.

[42] F. Girardin. "Contribution a letude des phenomenes non-lineaires dans les lasers a semi-conducteurs". *PhD Thesis*, pages pp.93–109, 1995.

[43] A. Uskov, J. Mørk, and J. Mark. "Wavelength mixing in semiconductor laser amplifiers due to carrier heating and spectral-hole burning". *IEEE J. Quantum Electronics*, vol.30(no.8):pp.1769–1781, 1994.

[44] H. Soto, D. Erasme and G. Guekos. "Cross polarization modulation in semiconductor optical amplifiers". *IEEE Photonics Tech. Letters*, vol.11:pp.970–972, 1999.

[45] H. Soto, J.C. Dominguez, D. Erasme and G.Guekos. "Demonstration of an all-optical switch using cross polarization modulation in semiconductor optical amplifiers". *Microw. and Optic. Tech. Letters*, vol.29(no.3):pp.205–209, 2001.

7. CONCLUSIONS

The demand for higher bandwidth in our society due to the continued expansion of the internet, mobile services and interactive media, to name but a few, shows no sign of reducing. These developments put pressure on the present communication systems, due to the speed limitation introduced by electronic devices. Commercial systems exist, using such technology, that operate at speeds of 10 Gb/s. Systems operating at 40 Gb/s have also been developed and will be commercially available in the near future. However, as the demand for speed increases a fundamental restriction due to the electronics is imposed. If systems can be developed to perform signal processing in the optical domain it will be possible to remove the electronic bottleneck and thus develop systems which operate at much higher data rates.

One of the most promising techniques put forward to perform all-optical signal processing is the application of the semiconductor optical amplifier (SOA). This is due to its small-size, cost efficiency, large nonlinearities and integratibility. The most common techniques of performing signal processing using SOAs are Cross-Gain Modulation (XGM), Cross-Phase Modulation (XPM) and Four-Wave Mixing (FWM). XGM is the simplest technique to implement. However, the effect of the spontaneous emission can lead to a large degradation of the extinction ratio. Furthermore, it is not possible to achieve a non-inverted output using this technique. XPM can overcome several of the shortfalls associated with XGM. Less chirp is introduced by this technique. High extinction ratios can be achieved and it is possible to obtain a non-inverted output. A major drawback of XPM is the complexity of its implementation. FWM has also received a lot of attention for all-optical signal processing. However, this technique has very poor performance at large detunings between input signals. All three of these techniques, particularly FWM, are limited by a sensitivity to polarization. Recently a new technique has begun to receive a lot of attention in the literature. This technique is based on Nonlinear Polarization Rotation (NPR) in the SOA and takes advantage of the inherent polarization dependence in the SOA. Using NPR it is possible to obtain both inverted and non-inverted outputs with a high extinction ratio. This can be achieved over a larger range of wavelengths using a system setup that is as easy to implement as XGM. The NPR effect, as a means to perform all-optical signal processing, is the focus of the work presented in this thesis.

As outlined above the SOA is a very attractive device for all-optical signal processing. The operation of the SOA is very similar to a semiconductor laser. The SOA is prevented from lasing, however, by suppressing the reflections in the cavity. An analysis of the operation of the laser was presented before the methods used to suppress the reflections in the cavity were discussed. The particular SOAs used in this thesis were then introduced before the experimental characterization of the SOAs was presented. This experimental characterization was found to agree well with the specifications provided by the manufacturer. The characterization is of vital importance in assessing the performance of the devices in optical systems, and is referred to throughout the thesis.

After establishing a general understanding of the SOA a theoretical model was developed in order to obtain a more advanced understanding of the device. This model was first developed in the steady-state regime of operation and was then extended for operation in the dynamic regime, where the propagation of 15 ps was analyzed. The model was based on a travelling-wave description of the electric field in the amplifier cavity, which was split into a number of sections allowing the carrier density rate equation to be solved in each section of the device. The carrier density was given the same initial value in each section. Boundary conditions were then defined in order to determine the propagation of the signal from one section to the next. This sectioning allows for a more realistic analysis of the operation of the SOA then a single section model. After the equations used to model the propagation of the signal had been defined a thorough theoretical characterization of the SOA was performed and compared to the experimental characterization, in order to confirm the accuracy of the model. Good agreement was found. Using the model it was possible to analyze the propagation of optical signals in the device as a function of position in the SOA. This analysis could not be performed using experimental results. It would be straightforward to extend the operation of the model to the analysis of sub-picosecond pulses. This would involve the implementation of a model for the gain capable of accounting for the gain dynamics occuring on this timescale. The propagation of optical pulses along orthogonal axes in the SOA was also analyzed using the model. A large polarization dependence was determined. Off-axis angles of polarization were not considered in this analysis. It would be possible to model any angle of linearly polarized light by considering othhogonal components to be independent signals linked through the gain suppression. This method has been applied in the literature.

Having developed a detailed physical understanding of the SOA the main section of the work was undertaken. The idea is to use the nonlinear nature of the polarization dependence of the SOA in order to perform all-optical signal processing. Several phenomenon in the SOA cause a rotation in the state of polarization of a signal injected into the device. These include birefringence, polarization dependent gain and a shift in the optical axes of the device. The rotation of the state of polarization is nonlinear in nature. This allows for the polarization of a signal at the output of the device to be determined by the intensity of a second signal in the SOA. Experimental results were obtained using novel techniques to investigate the contribution of the different phenomena to the change in state of the polarization. This analysis was performed both in the case when no external optical signal was injected, and also in the case where a signal was injected. It was possible to compare the inherent polarization rotation with the induced rotation in the device. These are the first results in which such a comparison was performed. Under the condition of no injection a variation in refractive indicies of 8×10^{-2} was found between Transverse Electric (TE) and Transverse Magnetic (TM) modes. The gain was found to be equal within the resolution of the experiment when no signal was injected. Upon injection of an optical signal a polarization dependence of the gain was introduced. A ratio of 1.11 was found between the gain along orthogonal axes for an injected intensity of 450 μW. The phase difference was found to increase by 45^o over the same range of intensities. No modification of the axes of the device was found for the level of optical power injected into the device. Consistency was found between both experimental conditions.

A Continuous-Wave (CW) pump-probe experiment was also presented to examine the change in polarization of one signal due to the polarization and intensity of a second signal. Most pump-probe studies presented on NPR have focussed on the intensity variation introduced by the rotation in the state of polarization. Results were obtained in this thesis to observe the exact change in both the ellipticity and the orientation induced on a probe signal due to a contra-propagating probe signal. A large variation of approximately 0.26 was found for the ellipticity and a variation of approximately 28^o was found for the orientation. A polarimeter was used to accurately measure the polarization in this experiment. These experiments were performed in free space in order to ensure that the polarization of the signals was maintained during propagation.

The next section of the work involved utilizing the results obtained on the underlying causes of NPR in order to perform wavelength conversion. This technique to perform wavelength conversion is known as Cross-Polarization Modulation (XPolM). This was achieved in an optical system employing standard Single-Mode Fibre (SMF) using a Non-Return To Zero (NRZ) data signal with a Pseudo-Random Bit Stream (PBRS) of length $2^7 - 1$. It was possible to obtain both inverted and non-inverted conversion using this setup. Results have been presented in the literature to perform all-optical switching using XPolM in both co- and contra-propagation schemes. It is unclear which scheme is most efficient for this technique. For the first time, a detailed comparison between the two setups was presented in this thesis. It was found that the least power penalty was introduced for the inverted contra-propagation scheme. The penalty introduced for this setup was 0.5 dBm. However, wavelength independent conversion over a span of 35 nm was obtained for the non-inverted co-propagation setup, although a power penalty of approximately 6 dBm was measured for this setup. This wavelength independence has not been previously reported for XPolM. The span of the wavelength conversion was limited to 35 nm due to the Erbium Doped Fibre Amplifier (EDFA) in the system, which was limited to operation of the C-band. The spectral bandwidth of the SOA was 70 nm, which implies that a larger tunability can be expected. A larger impact from the NPR was found for the contra-propagation setup. An improvement in the power penalty of 6 dBm was found for the non-inverted conversion using the contra-propagation setup. It may be concluded that the choice of co- or contra-propagation setup is dependent on the system requirements. If wavelength independence is important then the co-propagation setup is suitable. If a low power penalty is desired then contra-propagation provides better results.

Experimental results were also taken for the XGM setup, in order to perform a comparison between the two techniques in the same device. It was possible to match the performance of XGM using XPolM in an SOA designed to be polarization independent. It may be possible to achieve superior wavelength conversion using the XPolM technique if a Polarizing Beam Splitter (PBS) with a greater extinction ratio is used. The experiments presented were limited by the PBS to an extinction ratio of 20 dB. The regeneration introduced during the conversion process was determined and was found to be similar to the regeneration introduced by XGM.

The XPolM was further tested by varying the polarization of the pump and the probe and recording the variation in the extinction ratio of the converted signal in each case. It was found that varying the polarization of the pump introduced a maximum change of 1.5

in the extinction ratio measured at the probe output. The main contribution of the pump was to deplete carriers in the active region of the device. However, a large variation in the extinction ratio measured at the probe output was found when the polarization of the probe at the input was changed. A variation in the extinction ratio of 6 dB was found with the contra-propagating setup.

The experiments presented for wavelength conversion were performed at a data rate of 2.5 GHz. The polarization dependence introduced at this data rate is due to the inter-band carrier recombinations. There is a fundamental limit to the speed that can be obtained using this mechanism. In order to perform all-optical signal processing at data rates in excess of approximately 200 GHz a new mechanism is required. One potential solution is to use the intra-band gain processes in order to perform signal processing in the THz regime. Results have already been presented to do this using XGM, XPM and FWM. There are also several investigations in the literature which point to a polarization dependence of the intra-band processes. However, the extent of this dependence has not been determined. Furthermore, any polarization dependence of the intra-band effects will limit the propagation of pulses below 10 ps in an SOA used for purposes other than NPR. The polarization dependent propagation of 2 ps pulses was determined in both the temporal and spectral domains, using the Frequency Resolved Optical Gating (FROG) technique. At low levels of injected intensity the propagation of 2 ps pulses was found to be polarization independent. The polarization dependence of the chirp magnitude in this situation was 10 GHz. However, as the intensity increased the propagation of these pulses developed a large dependence on polarization, due to the polarization dependent suppression of the gain in the SOA. This resulted in the increased significance of pulse pedestals in the wings on the pulses. The pedestals were most prominent for an angle of 60^o. In the case when a 4 mW CW signal was injected into the device in co-propagation with the 2 ps pulses, a polarization dependence in the chirp magnitude of 143 GHz was found. This result would have an impact for SOA based optical systems employing 2 ps pulses in the nonlinear regime. The large suppression of the gain introduced at high levels of injected power indicates a polarization dependence of the ultra-fast gain processes. This experiment also demonstrates the capability of the FROG to perform polarization resolved measurements on 2 ps pulses.

In order to measure the exact polarization dependence of the Carrier Density Pulsations (CDP) and the Carrier Heating (CH) an experiment was performed, which was based on FWM. This is a standard technique for measuring the gain dynamics of SOAs, but this approach has never been used to determine the polarization dependence of these effects. The frequency detuning between a pump and a probe was varied so that the gain dynamics could be analyzed on different timescales. The polarization dependence of faster processes, e.g. Spectral-Hole Burning (SHB), could not be determined using the FWM technique because of the increased impact of birefringence at large detunings. There is also a large degradation in the conversion efficiency of FWM at large detunings, which further limits the analysis of the faster gain dynamics. A large polarization dependence of both CH and CDP was found. Both the recovery time and the Linewidth Enhancement Factors (LEFs) associated with these processes were determined. The polarization dependence is attributed to the asymmetry introduced to the material gain of the device due to tensile strain. The polarization dependence of CH suggests that it will be possible to develop optical communications systems in the THz regime using NPR in the SOA. In both the experiment performed using the FROG technique and the experiment performed using FWM the largest contribution of the CH was found at an angle of 60°. This result suggests a possible modification in the optical axes of the device which has been reported previously in the literature.

In terms of polarization sensitivity of bulk SOAs, the results obtained suggest that care must be taken in analyzing this parameter. Many characterizations of this phenomenon in the SOA are performed in a CW setup. In this case it is possible to achieve very small polarization dependence as the effects of an asymmetric waveguide and of tensile strain may be balanced. An important consideration is that the dynamic response of the device may not have a low polarization sensitivity in this case if the symmetry is removed from the material gain due to tensile strain.

APPENDIX

A. VARIABLES USED IN THE MODEL

Subscript ’m’	section number
$\mathbf{E}$	Electric field
r_1, r_2	Facet reflectivity
E^{in}	Input electric field
K	Wavenumber
N	Carrier density
c	Speed of light
n_e	Effective index
Γ	Confinement factor
g_m	Material gain
α_i	Internal loss
ω_{k0}	Optical angular frequency
n_g	Group index
L	Active region length
F	Electric field
G_s	Single-pass gain
ϕ	Phase shift
τ_m	Section transit time
ω_{p0}	Gain peak angular frequency
N_r	Reference carrier density
F^{in}	Injected electric field
n_1	Active region refractive index
f_{k0}	Optical frequency
m_e	Conduction band heavy-hole mass
m_{hh}	Valence band heavy-hole mass
h	Planck’s constant
$\hbar$	$h/2\pi$
E_g	Bandgap energy
f_c	Fermi-Dirac distribution in the conduction band

f_v	Fermi-Dirac distribution in valence band
I	Bias current
e	Charge on an electron
V	Volume
R	Recombination rate
S_{sig}	Stimulated photon density
a_m	Gain factor
N_0	Carrier density at transparency
S_{spon}	Spontaneous photon density
c_1	Linear recombination coefficient
c_2	Bimolecular recombination coefficient
c_3	Auger recombination coefficient
I_{sp}	Spontaneous intensity
β	Spontaneous emission factor
P_{out}	Output optical power
P_{in}	Input optical power
F_{in}	Input electric field
P_{pulse}	Pulse power
P_0	Maximum power in the pulse
T_b	Pulsewidth
T_r	Risetime of the pulse
t	Time

B. PUBLICATIONS

B.1 Refereed journals

B.F. Kennedy, S. Philippe, P. Landais, A.L. Bradley and H. Soto, "Experimental investigation of polarization rotation in SOAs," IEE Proc. Optoelectronics, vol. 151, No.2, April 2004

B.2 Reviewed conference papers

B.F. Kennedy, S. Philippe, P. Landais, A.L. Bradley and H. Soto, "Experimental investigation of polarization rotation in semiconductor optical amplifiers," SIOE, Cardiff, April 2003.

B.F. Kennedy, S. Philippe, P. Landais, A.L. Bradley and H. Soto, "Study of the polarization dependence of a signal injected into a semiconductor optical amplifier," SIOE, Cardiff, April 2004

B.F. Kennedy, S. Philippe, P. Landais, A.L. Bradley and H. Soto, "Temporal and spectral dependence on polarization of the input signal in a semiconductor optical amplifier," OSA-Optical amplifiers and their applications, San Francisco, June 2004.

B.F. Kennedy, S. Philippe, P. Landais, A.L. Bradley and H. Soto, "Measurement of the chirp introduced to a picosecond pulse injected into an SOA as a function of input polarization," ETOS, Cork, July 2004.

S. Philippe, B. Kennedy, M. Martinez-Rosas, A. L. Bradley, P. Landais, "Pump-probe studies of non-linear polarization rotation in semiconductor optical amplifiers," ETOS, Cork, July 2004.

B.F. Kennedy, P. Landais, F. Surre, and A.L. Bradley, "Dynamic model of a bulk semiconductor optical amplifier", SIOE, Cardiff, March 2005.

B.F. Kennedy and P. Landais, "Experimental analysis of polarization dependence of ultrafast gain dynamics in SOAs," SPIE Europe - Opto Ireland, Dublin, April 2005.

S. Philippe, A. L. Bradley, M. Martinez-Rosas, B. Kennedy and P. Landais, "Pump-probe studies of polarization effects in semiconductor optical amplifiers", SPIE Europe - Opto Ireland, Dublin, April 2005.

B.F. Kennedy, F. Surre, L.P. Barry and P. Landais, "Wavelength Conversion Using Polarization Rotation in a Bulk Semiconductor Optical Amplifier", Cleo Europe, Munich, Germany, June 2005

SEMICONDUCTOR OPTOELECTRONICS

Experimental investigation of polarisation rotation in semiconductor optical amplifiers

B.F. Kennedy, S. Philippe, P. Landais, A.L. Bradley and H. Soto

Abstract: An experimental study of polarisation rotation in a semiconductor optical amplifier is presented. Two techniques are used to investigate the gain and birefringence along the two eigenmodes of the component waveguide, with and without injection. The first investigation is based on the residual reflectivity of the facet mirrors. From the modulation depth of polarisation resolved spectra, the gain and the refractive indices of these modes are determined. The second investigation takes into account the variation of the eigenmode gain and refractive indices as a function of injected power over the range 83.3 to 413 μW. The results of these two experiments are compared, and it is determined that the refractive index and the single-pass gain along the horizontal axis of the waveguide are higher than those along the vertical axis. Both gain and refractive index differences increase as a function of injected power in the sample under test. Furthermore, it is concluded that polarisation rotation in this component is heavily influenced by the power dependence of the relative gain in the TE and TM modes and birefringence.

1 Introduction

To achieve all-optical signal processing, various configurations based on nonlinearities in semiconductor optical amplifiers (SOAs), e.g. crossgain modulation, crossphase modulation and four-wave mixing, have been presented [1–3]. Nonlinear polarisation rotation (NPR) has also been demonstrated [4–7], relating to a switch of the state of polarisation of a beam injected into the device. Thus far, considerable attention has focused on applications which may emerge from the NPR [6–9]. Some groups have looked at the underlying physical origins [4, 8, 9] but a full characterisation of the polarisation change has yet to be performed, to the best of the authors' knowledge. The aim of this paper is to provide a deeper analysis of the nonlinear polarisation rotation in an SOA by applying two different methods, which probe the polarisation dependent gain and birefringence, with and without signal injection. Measurements of the polarisation state, as achieved using a polarimeter, provide information on the ellipticity of the output signal. Using this novel method, information on the power dependence of the SOA birefringence and TE to TM gain ratio can be extracted, complementing earlier work by Manning *et al.* [4]. Experimental results are presented and discussed, following which conclusions are drawn.

2 Experimental investigation and discussion

The SOA under test is a commercially available component. It is a 1.5 mm long bulk InGaAsP active region surrounded by InP. This structure was grown by MOCVD and it is quoted as having low polarisation dependent gain. Both facets are anti-reflection (AR) coated, with a tilted output of 12° to reduce the Fabry–Perot resonance due to the residual reflectivity of the facets. For all the experiments the component is temperature regulated at 20°C. In Fig. 1 the light-output characteristic is presented. Below 220 mA, the SOA acts as an LED; above this current the spontaneous emission is amplified and guided in the active region; the component then acts as an amplifier. In the inset, the emission spectrum is shown at a bias current of 400 mA. It features a peak at 1574 nm and a 3 dB linewidth of 27 nm.

We focus on two possible origins of NPR: the gain discrepancy between the eigen-axes of the waveguide, and birefringence due to different values of refractive indices for the modes. In the first experiment, these effects are investigated without injected power, providing information on the underlying properties of the waveguide. In the next experiment they are studied as a function of injected power. Both set-ups are in free space, allowing optimum control and preservation of the state of polarisation of the injected and collected signals.

2.1 Gain and birefringence in SOA without injection

The light output is collected by a 0.25 NA AR coated microscope objective; it passes through a 50 dB extinction ratio polarisation beam splitter (PBS) precisely aligned along the eigenmodes of the SOA waveguide The polarisation resolved amplified spontaneous emission (ASE) spectra are recorded for both eigenmodes using an optical spectrum analyser (HP 86143A) with a resolution of 0.07 nm, as shown in Fig. 2. These eigenmodes are referred to as TE (horizontal) and TM (vertical) throughout this paper. From the ASE modulation depth, introduced by the

---

IEE Proceedings online no. 20040287

doi: 10.1049/ip-opt:20040287

Paper first received 16th June and in revised form 17th December 2003

B.F. Kennedy and P. Landais are with the School of Electronic Engineering, Dublin City University, Dublin 9, Ireland

S. Philippe and A.L. Bradley are with the Physics Department, Trinity College Dublin, Dublin 2, Ireland

H. Soto is with Centro de Investigación Científica y de Educación Superio de Ensenada, Km. 107 Carr., Tijuana-Ensenada, Ensenada, Baja California 22860, Mexico

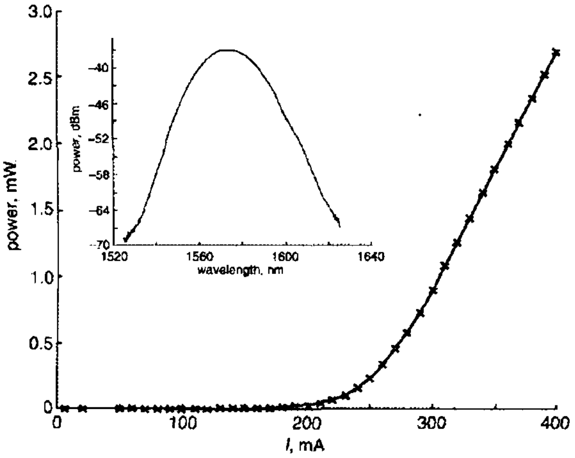

Fig. 1 *L/I characteristic of SOA under test*
Inset: ASE spectrum at 400 mA

Fabry–Perot resonance, we determine the wavelength dependence of the gain [10, 11] and the refractive index for TE and TM. The gain reflectivity product spectrum, γ, is calculated from the formula

$$\gamma(\lambda) = \frac{\sqrt{r(\lambda)} - 1}{\sqrt{r(\lambda)} + 1} \qquad (1)$$

where r, the modulation depth around the troughs, is given by $(P_{max\,1} + P_{max\,2})/(2P_{min})$, $P_{max\,1}$ and $P_{max\,2}$ represent neighbouring peak modulation power values and P_{min} the minimum power between these peaks. γ is linked to the single-pass gain, G, by

$$\gamma = \sqrt{R_1(\lambda)R_2(\lambda)}G(\lambda) \qquad (2)$$

where R_1 and R_2 are the reflectivities of the output facets. We assume that R_1 and R_2 are equal and constant over the spectral range of our study, in accordance with [12]. The single-pass gain is calculated from the TE and TM spectra, as shown in Fig. 2, using (1) and (2). Our investigation is limited to bias currents above 300 mA, as below this current the anti-reflection coatings and waveguide tilting minimise the ripples. Figure 3 shows four TM and TE single-pass gain spectra from 1565 nm to 1595 nm for bias currents of 300 mA, 350 mA, 400 mA and 450 mA. As the current increases, the peak value of the gain increases for both modes. It is noted that for bias currents from 350 mA to 450 mA, the maximum single-pass TE gain and the maximum single-pass TM gain are approximately equal. There is evidence of a small dip in the TE gain spectra at 1585 nm. This arises due to a decrease in the ripple modulation depth, which later recovers. It should be noted for later reference that the TE and TM gains at 1580 nm under bias of 400 mA are equal within error on the graph, and that the spectra obtained here are dependent on the value of the reflectivity. A change in these parameters would lead to a vertical shift in the spectra obtained, but would not change their profile. Confidence in the spectra presented in Fig. 3 is justified: the peak gain at each bias current is in agreement with the single-pass gain measured as a ratio of the power out to the power in.

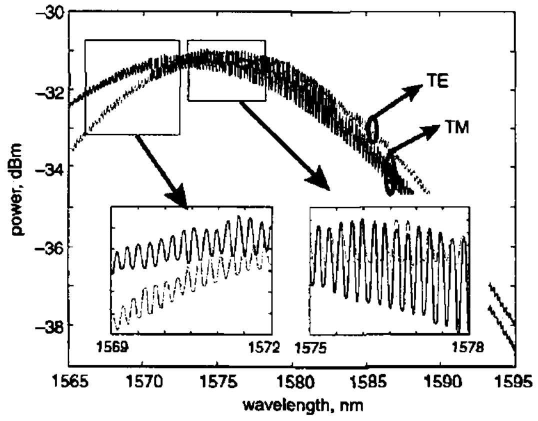

Fig. 2 *Polarisation resolved spectra*
Inset: ripples in phase and out of phase

Birefringence has also been considered as an effect responsible for NPR [4, 13]. To observe and quantify this effect, the refractive index is calculated for both the TE and TM modes. If there is a birefringent effect in the device then the period of the modulation ripples is different for both polarisations, as light travels at different speeds for each mode. In other words, the ripples in the ASE spectrum go in and out of phase with respect to each other, due to the small but finite difference in the periods of the ripple [14]. These effects can be seen in the insets of Fig. 2. Both modulations are in phase at 1577 nm. At 1570 nm, however, they are out of phase. This means that there are different refractive indices for the TE and TM modes, and that there must be birefringence in the device. The refractive index is measured using the ASE spectra recorded for the gain calculations. Using the definition of the free-spectral range in a Fabry–Perot resonator, the refractive index for both modes can be calculated:

$$\Delta\lambda = \frac{2n_{g,eff}L}{k} - \frac{2n_{g,eff}L}{k+1} = \frac{2n_{g,eff}L}{k(k+1)} \approx \frac{\lambda^2}{2n_{g,eff}L} \qquad (3)$$

where λ is the wavelength, $n_{g,eff}$ is the effective group refractive index, L is the length of the device and k is the wavevector. Using this equation we can extract $n_{g,eff}$ as a function of wavelength. $\Delta\lambda$ is the trough-to-trough wavelength separation, as measured from the ripples on the ASE spectra in Fig. 2, and λ is taken as the central wavelength from trough to trough. In this way, a refractive index can be calculated for each central wavelength. Figures 4*a* and *b* show the effective refractive index dependence from 1560 nm to 1590 nm at 400 mA for the TE and TM modes, respectively. The effective refractive index is found to be 4.03 for the TE mode and 3.95 in the TM mode, where the refractive index was averaged over the complete range of wavelengths, from 1560 nm to 1590 nm, providing quantitative evidence of the birefringence of the device under study. These values are consistent with previously documented results [15]. Furthermore, we can consider the dispersive nature of the semiconductor material and the dispersion parameter for each mode can be extracted using the following expression:

$$n_{g,eff} = n_{eff} - \lambda\frac{dn}{d\lambda} \qquad (4)$$

where $n_{g,eff}$ corresponds to the refractive index found from the free spectral range, n_{eff} is effective wavelength independent refractive index and $dn/d\lambda$ the dispersive term. It is found that the scatter of the refractive index data, in Fig. 4, is too large to extract a meaningful quantitative value. However, it is clear from the slope that the dispersion parameter for the TM mode is less than that of TE, in agreement with the results from [15]. Moreover the TE refractive index is higher than the TM refractive index and this difference between refractive indices decreases slightly

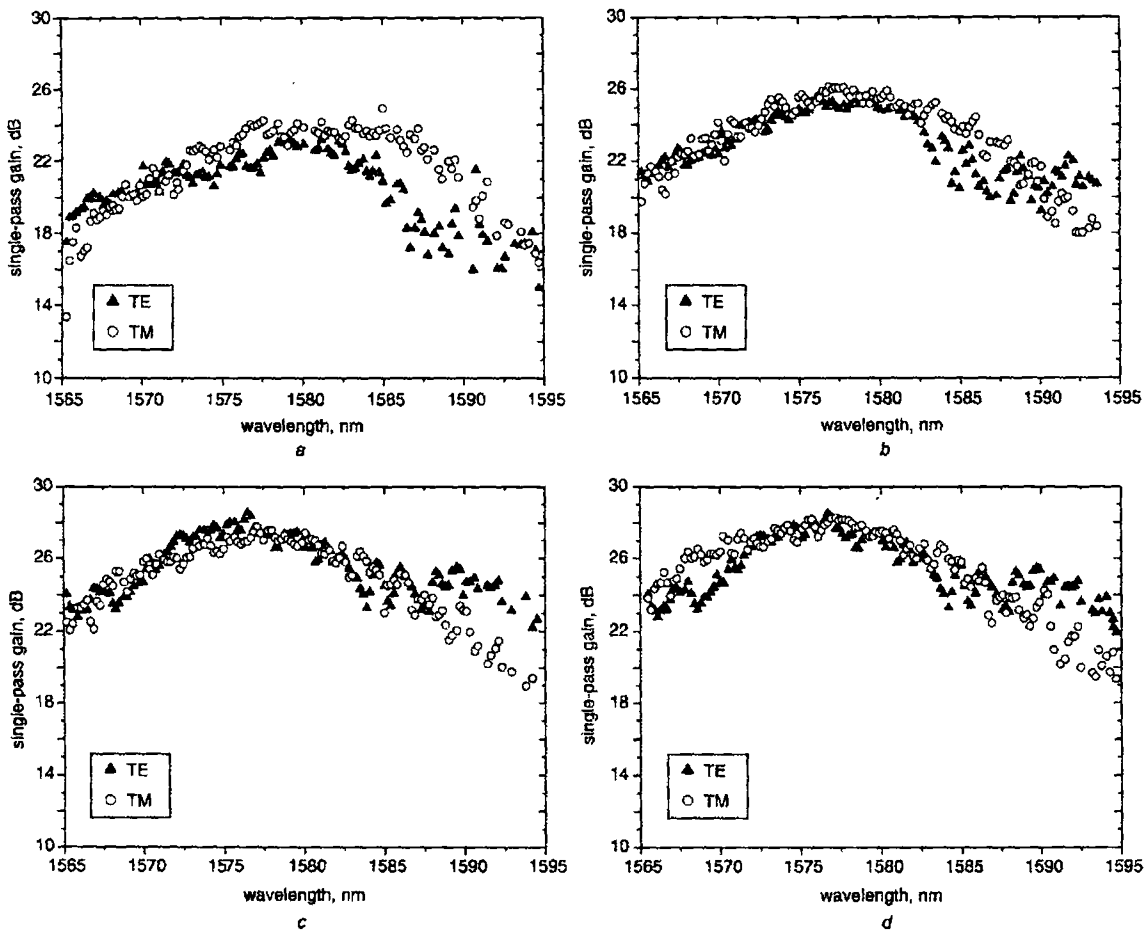

Fig. 3 *Polarisation resolved gain spectra for $I = 300\,mA$, $350\,mA$, $400\,mA$ and $450\,mA$*
a $I_{bias} = 300\,mA$
b $I_{bias} = 350\,mA$
c $I_{bias} = 400\,mA$
d $I_{bias} = 450\,mA$

with increasing wavelength. This birefringence is a second possible origin of the NPR in the SOA.

2.2 Gain and birefringence in SOA with injection

The experimental results discussed so far investigate possible sources of polarisation rotation due to the underlying properties of the waveguide. To validate the earlier results and to study the effect of the gain discrepancy and birefringence on the polarisation of an injected beam, a second set of experiments is undertaken. The ellipticity of the output amplified signal is measured as a function of the input orientation and power of a linearly polarised injected signal.

Figure 5 shows the experimental set-up. The probe signal is provided by a tunable laser source. The polarisation of the free space signal is controlled by several components: (i) a polariser, to achieve a linearly polarised signal, (ii) a half-wave plate, to rotate the linearly polarised signal; and (iii) a quarter-wave plate, to compensate the mismatch between the operating wavelength of the device and the operating wavelength of the plates. The optical signal is then launched into the SOA using a 0.25 NA AR microscope objective. The launching conditions are optimised using the two mirrors and micro-control lens mount. The ASE spectrum with 2.3 dBm injected power and without injected power can be seen in the inset of Fig. 5. From this, we can observe a suppression of more than 6 dB of the ASE indicating good injection has been achieved. A band-pass filter centred at 1580 nm with a bandwidth of 10 nm is placed in front of the polarimeter to reduce the influence of the random polarisation of the ASE. The polarimeter measures the ellipticity of the output signal. The ellipticity is defined as the ratio of the length of the minor axis of the polarisation ellipse by the length of the major axis. An ellipticity of zero means that the polarisation is linear. An ellipticity of -1 corresponds to circular polarisation since both lengths are equal; the negative sign is a convention to define the left-handed rotation.

The output ellipticity as a function of input orientation for a bias current of 350 mA and an injection wavelength of 1580 nm is shown in Fig. 6. This wavelength was specifically chosen since it corresponds to the peak gain of the TE and TM modes as shown in Fig. 3. The ellipticity is recorded for injected powers of 83.3, 166, 208 and 413 μW. As the injection angle increases, the ellipticity decreases, reaching a minimum at 48°, independently of input power. A minimum of -0.94 is achieved at 48° injection for 166 μW of injected power. At the minimum of ellipticity curves, the output is approaching a circular polarisation. The fact that the minimum is reached at an angle greater than 45° indicates that the TE gain must be greater than the TM gain. For example, at an input orientation of 48°, there will be more light injected into the TM mode than the TE mode and in order for the output to approach a circular polarisation the gain in TE mode must

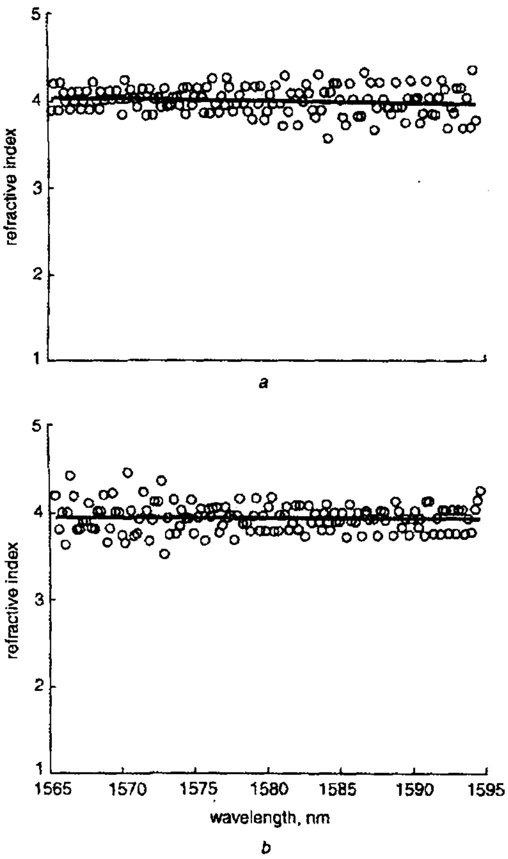

Fig. 4 *Refractive index dependence on wavelength at $I = 350\,mA$ for TE and TM modes*
a TE mode
b TM mode

compensate for the lower injected power. The negative sign shows that the output polarisation is of left-handed rotation, indicating that the TE axis is slower than the TM axis, in agreement with the result from the previous experiment with no injection. At 90° the ellipticity is zero, the linear input is injected along the TM mode, propagates and is amplified along this mode. This indicates that there is no modification of the principal axes over this power range.

To develop a more quantitative understanding of the experiment, we have written a model based on a propagating electric field, $\boldsymbol{E}$, having two components aligned along the modes of the waveguide:

$$\boldsymbol{E} = e^{i(\omega t - kz)}\left(\boldsymbol{E}_{0TE}e^{i\phi_{TE}} + \boldsymbol{E}_{0TM}e^{i\phi_{TM}}\right) \tag{5}$$

where $\boldsymbol{E}_{0TE(TM)}$ is the $\boldsymbol{E}$ component along the TE (TM) direction and its phase is $\phi_{TE(TM)}$. $\boldsymbol{E}_{TE}$ and $\boldsymbol{E}_{TM}$ are expressed as:

$$\begin{cases} \boldsymbol{E}_{0TE} = \rho E \cos(\theta)\boldsymbol{u}_{TE} \\ \boldsymbol{E}_{0TM} = E \sin(\theta)\boldsymbol{u}_{TM} \end{cases} \tag{6}$$

where ρ is the ratio of the single-pass gain in the TE mode to the single-pass gain in the TM mode, θ is the input angle and $\boldsymbol{u}_{TE(TM)}$ is the unit vector along the horizontal (vertical) axis. The amplitude E of the input field is taken to be unity in our model. The phases ϕ_{TE} and ϕ_{TM} are defined as follows:

$$\phi_{TE} = \frac{2\pi L n_{TE}}{\lambda} \text{ and } \phi_{TM} = \frac{2\pi L n_{TM}}{\lambda} \tag{7}$$

As shown in Fig. 6, our numerical results fit well the experimental data using only two parameters ρ and the phase difference, $\Delta\phi = \phi_{TM} - \phi_{TE}$. The ellipticity as a function of orientation is fitted using only one value of ρ and $\Delta\phi$ for each injected power. Figure 7 illustrates their power dependences. Within the range of injected power, the gain ratio increases up to a value of 1.25 for an injected power of 413 µW, indicating that the single-pass TE gain becomes increasingly greater than the single-pass TM gain. As the injected power is decreased to zero, ρ converges towards 1, indicating that the single-pass TE gain approximates to the single-pass TM gain. This is consistent with the results of Fig. 3, where the gain spectra are obtained under conditions of no injection.

The phase difference $\Delta\phi$ is negative, demonstrating that n_{TE} is larger than n_{TM}. As the injected power is increased, the difference between the TE and TM refractive indices increases nonlinearly. For future studies the polarimeter

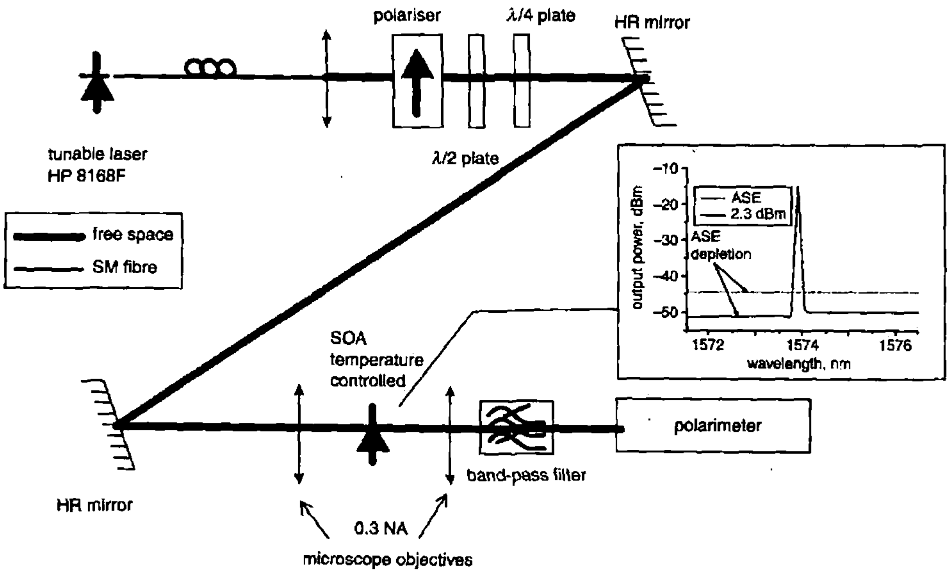

Fig. 5 *Experimental set-up of injection experiment*
Inset: spectra of ASE without and with injection

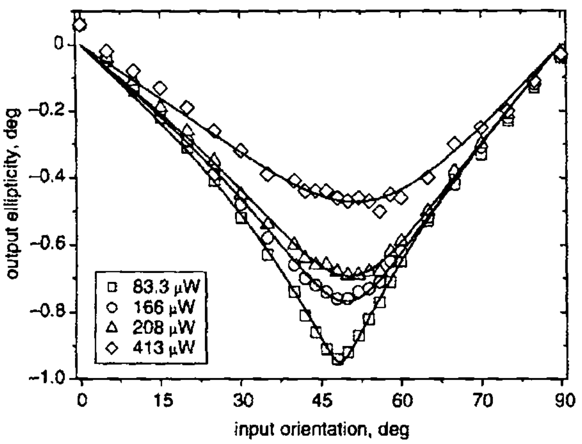

Fig. 6 *Output ellipticity as a function of angle of injection of a linearly polarised input for −10 dBm, −7 dBm, −6 dBm and −3 dBm*

Symbols represent experimental data; simulations are represented by lines
$I_{bias} = 350\,mA$; $\lambda = 1580\,nm$

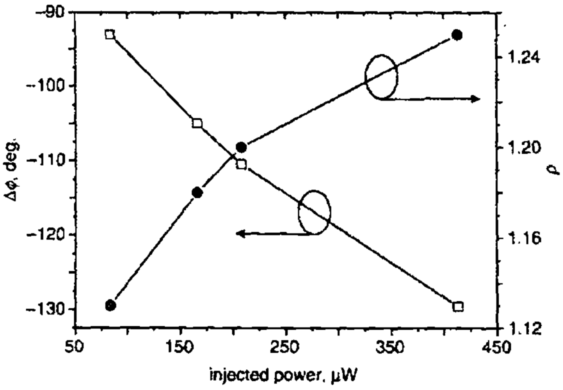

Fig. 7 *Gain ratio between TE and TM modes and phase difference as a function of input power*

Lines are a guide to the eye
$I_{bias} = 350\,mA$; $\lambda = 1580\,nm$

data can be considered more reliable as there are no assumptions made in the fitting, unlike the facet reflectivity in the gain spectrum analysis. However, this approach is limited, since only relative gain values can be extracted. Furthermore, due to the agreement between the two methods, we can have confidence in the gain spectra of Fig. 3.

3 Conclusions

We investigated the origin of the nonlinear polarisation rotation in semiconductor optical amplifiers, using two techniques Two phenomena were considered as sources of the NPR: asymmetric gain between the TE and TM and birefringence. In the first experiment, there is no injected signal, allowing for the underlying properties of the waveguide to be probed. Polarisation resolved ASE spectra were recorded and the gain and refractive index for the two eigenmodes of the SOA waveguide were calculated. It was found, using this method, that a difference in the refractive indices of the two modes could be determined, with that along the TE axis being greater than that along the TM axis. Furthermore, estimations of effective refractive indices of the two modes could be extracted. The values obtained are in agreement with the literature.

A new approach has been developed to investigate the gain and refractive index differences of the two eigenmodes. The change in polarisation state of an injected signal at the output of the device is measured using a polarimeter. From the fit of the experimental results, with a basic electric field propagation model, we are able to measure the TE and TM gain ratio and the birefringence as a function of injected power. It is found that, even though the TE and TM gains are close under low optical injection, consistent with the gain extracted from the analysis of the ASE spectra, the difference in gain between the two modes increases with increasing injected power. A higher refractive index for the TE axis compared to that of the TM is confirmed, in agreement with the spectral measurements. The birefringence is also seen to increase with increasing injected power.

4 Acknowledgment

This work is supported by Enterprise Ireland under the Research Innovation Fund, and S. Philippe would like to thank the Irish Research Council for Science, Engineering and Technology for its support.

5 References

1 Asghari, M., White, I.H., and Penty, R.V.: 'Wavelength conversion using semiconductor optical amplifiers', *J. Lightwave Technol.*, 1997, **15**, (7), pp. 1181–1190
2 Pastor, D., Martinez, A., Capmany, J., Sales, S., Ortega, B., and Munoz, P.: 'Experimental characterization of XGM-SOA-based wavelength converted SCM systems', *IEEE Photonics Technol. Lett.*, 2003, **15**, (1), pp. 114–116
3 Lee, S-L., Gong, P-M., and Yang, C-T.: 'Performance enhancement on SOA based four-wave mixing wavelength conversion using an assisted beam', *IEEE Photonics Technol. Lett.*, 2002, **14**, (12), pp. 1713–1715
4 Manning, R.J., Antonopoulos, A., Le Roux, R., and Kelly, A.E.: 'Experimental measurement of nonlinear polarization rotation in semiconductor optical amplifiers', *Electron. Lett.*, 2001, **37**, (4), pp. 229–231
5 Soto, H., Erasme, D., and Guekos, G.: 'Cross polarization modulation in semiconductor optical amplifiers', *IEEE Photonics Technol. Lett.*, 1999, **11**, pp. 970–972
6 Patrick, D.M., Ellis, A.D., Davies, D.A.O., Tatham, M.C., and Sherlock, G.: 'Demultiplexing using polarization rotation in a semiconductor laser amplifier', *Electron. Lett.*, 1994, **30**, (4), pp. 341–342
7 Stephens, M.F.C., Asghari, M., Penty, R.V., and White, I.H.: 'Demonstration of ultrafast all-optical wavelength conversion utilizing birefringence in semiconductor optical amplifiers', *IEEE Photonics Technol. Lett.*, 1997, **9**, (4), pp. 449–451
8 Liu, Y., Hill, M.T., Tangdiongga, E., de Waardt, H., Calabretta, N., Khoe, G.D., and Dorren, H.J.S.: 'Wavelength conversion using nonlinear polarization rotation in a single semiconductor optical amplifier', *IEEE Photonics Technol. Lett.*, 2003, **15**, (1), pp. 90–92
9 Dorren, H.J.S., Lenstra, D., Liu, Y., Hill, M.T., and Khoe, G.: 'Nonlinear polarization rotation in semiconductor optical amplifiers: theory and application to all-optical flip-flop memories', *IEEE J. Quantum Electron.*, 2003, **39**, (1), pp. 141–148
10 Hakki, B., and Paoli, T.: 'Gain spectra in GaAs double-heterostructure injection lasers', *J. Appl. Phys.*, 1975, **46**, (3), pp. 1299–1306
11 Merritt, S.A., Dauga, C., Fox, S., Wu, I.-F., and Dagenais, M.: 'Measurement of the facet modal reflectivity spectrum in high quality semiconductor travelling wave amplifiers', *J. Lightwave Technol.*, 1995, **13**, (3), pp. 430–433
12 Guekos, G.: 'Photonic devices for telecommunications' (Springer-Verlag, 1999), p. 329
13 Soto, H., Dominguez, J.C., Erasme, D., and Guekos, G.: 'Demonstration of an all-optical switch using cross-polarization modulation in semiconductor optical amplifiers', *Microw. Opt. Technol. Lett.*, 2001, **29**, (3), pp. 205–209
14 Diez, S., Schimt, C., Ludwig, R., Weber, H.G., Doussiere, P., and Duceiller, T.: 'Effect of birefringence in bulk semiconductor optical amplifier on FWM', *IEEE Photonics Technol. Lett.*, 1998, **10**, (2), pp. 212–214
15 Guekos, G. (Ed.): 'Photonic devices for telecommunications' (Springer-Verlag, 1999), pp. 144–145